Derivation of Spatiotemporal Landslide Activity for Large Areas Using Long-Term Multi-Sensor Satellite Time Series Data

vorgelegt von
Dipl. Geogr.
Robert Behling

Von der Fakultät VI–Planen Bauen Umwelt
der Technischen Universität Berlin
zur Erlangung des akademischen Grades
Doktor der Naturwissenschaften
Dr. rer. Nat.

genehmigte Dissertation

Promotionsausschuss:
Vorsitzender: Prof. Dr. Stefan Heiland
Gutachterin: Prof. Dr. Birgit Kleinschmit
Gutachter: Prof. Dr. Hermann Kaufmann
Gutachter: Prof. Dr. Luis Guanter

Tag der wissenschaftlichen Aussprache: 24.05.2016

Berlin, 2016

Abstract

The main principle in landslide hazard and risk assessment is that conditions of past and present landslide activity indicate future landslide occurrence. Hence, the probabilistic assessment of landslide hazard and risk requires a profound knowledge about spatiotemporal landslide activity over longer time spans and large areas. However, for most parts of the world such information is largely missing, because the identification of landslide activity still mainly relies on time-consuming and resource-intensive conventional methods (i.e. visual interpretation of optical data supported by comprehensive field surveys) and because all efforts to automate this landslide mapping procedure are hitherto limited to small areas and/or very short time periods or even single events.

This thesis presents the development of an automated approach for efficient multi-temporal identification of landslides based on optical satellite-based remote sensing time series data. The developed approach allows for retrospective analysis of long-term landslide occurrence and for monitoring recent landslide activity for large areas. For this purpose, a comprehensive optical remote sensing database has been created. To achieve best temporal resolution, data of multiple optical sensors are used simultaneously. In total, the database consists of 729 datasets acquired by Landsat-(E)TM, SPOT 1 & 5, IRS-1C (LISS3), ASTER, and RapidEye between 1986 and 2013 for a landslide-affected area of 12000 km² in Southern Kyrgyzstan, Central Asia.

The developed approach comprises automated multi-sensor pre-processing as well as knowledge-based and uncertainty-related multi-temporal change detection methods to enable efficient and robust spatiotemporal identification of landslides in a highly heterogeneous multi-sensor time series database. The change detection builds on the analysis of temporal NDVI-trajectories, representing footprints of vegetation changes over time. Landslide-specific trajectories are characterized by abrupt vegetation cover destruction and longer-term revegetation rates resulting from landslide-related disturbance and dislocation of the fertile soil cover. In combination with DEM-derivatives the developed approach enables automated identification of landslides of different sizes, shapes and in different stages of development under varying natural conditions.

The approach is applied to two scenarios. Firstly, the recent landslide activity (2009 – 2013) is identified by a RapidEye-based application of the approach in a 7500 km² area. Secondly, a long-term analysis (1986 - 2013) is performed on the basis of the multi-sensor database in a highly landslide-affected region of 2500 km². In both cases, the number of automatically mapped landslides exceeds the existing landslide records of the Kyrgyz authorities by more than a factor of ten. In total, almost 2000 landslides are mapped, whereas the size of the landslides ranges from 50 m² to 2.8 km². The identified landslide occurrence shows clear spatial patterns with highest activity along the foothills of the Tien-Shan mountain ranges. Temporally, the long-term analysis reveals a peak of landslide activity for the years 2003 and 2004. In these years, the annual landslide rate was more than five times higher than the identified long-term average rate of 57 landslides per annum. These

spatiotemporal activity patterns are evaluated against the morphological setting (predisposing factor) and the temporal variations of the precipitation (triggering factor), exemplarily showing the suitability of the achieved results to determine the individual or combined influence of specific landslide-causing factors in an analyzed region. For the derivation of the recent landslide activity, the approach takes advantage of the high spatial (5 m) and temporal resolution (acquisition intervals of up to several days/weeks) of the RapidEye data, allowing identification of small landslides that are often pre-cursors of subsequent more hazardous landslides. Thus, the approach can also provide valuable information for early warning applications in the context of a regular landslide monitoring system.

Overall, the presented approach identifies spatiotemporal landslide activity patterns to improve the regional landslide process understanding. This builds an important step to realize probabilistic landslide hazard and risk assessments in order to contribute to the mitigation of the landslide consequences for the local population of remote mountainous regions such as Southern Kyrgyzstan. Moreover, the multi-sensor applicability and uncertainty-related landslide change detection of the approach provides a great potential to be applied to other global landslide hotspots (e.g. South-East Asia and South America) as well as to new optical sensors (e.g. Sentinel-2), opening up new opportunities to establish a widely applicable large area landslide monitoring system.

Zusammenfassung

Zur Gefahreneinschätzung von Hangrutschungen greift man auf das grundlegende Prinzip zurück, dass zukünftige Hangrutschungen den gleichen Bedingungen unterliegen wie vergangene und gegenwärtige. Eine Voraussetzung für solche probabilistischen Gefährdungseinschätzungen sind daher fundierte Kenntnisse der raumzeitlichen Hangrutschungsaktivität über möglichst lange Zeiträume und große Gebiete. Allerdings fehlt solches Wissen in den meisten Regionen der Erde, da die Erfassung der Hangrutschungsaktivität nach wie vor meistens durch zeit- und arbeitsaufwendige Methoden erfolgt (d. h. visuelle Interpretation von optischen Fernerkundungsdaten und umfassenden Geländearbeiten) und weil Ansätze diese Hangrutschungsidentifizierung zu automatisieren sich bisher auf kleine Untersuchungsgebiete und/oder auf kurze Zeiträume beschränken.

In dieser Dissertation wird eine automatische Methode zur effizienten Hangrutschungsidentifizierung auf Basis von Zeitreihen optischer Satellitenfernerkundungsdaten entwickelt. Diese Methode erlaubt großflächig eine rückwirkende Analyse langzeitlichen Hangrutschungsvorkommens und ein Monitoring rezenter Hangrutschungsaktivität. Zu diesem Zweck wurde eine umfangreiche Datenbank optischer Fernerkundungsdaten erstellt, die, um eine möglichst hohe zeitliche Auflösung zu erreichen, Daten mehrerer optischer Sensoren einschließt. Insgesamt enthält die Datenbank 729 Datensätze sieben verschiedener optischer Satellitensysteme (Landsat-(E)TM, SPOT 1 & 5, IRS-1C (LISS3), ASTER und RapidEye). Die Aufnahmen erstrecken sich über einen Zeitraum von 1986 bis 2013 und über ein 12000 km² großes von Hangrutschungen betroffenes Gebiet im südlichen Kirgisistan (Zentralasien).

Die entwickelte Methode umfasst automatische multisensorale Vorverarbeitungsschritte sowie wissensbasierte und Unsicherheiten einbeziehende Algorithmen der multitemporalen Veränderungsdetektion um eine effiziente und robuste raumzeitliche Identifizierung von Hangrutschungen auf Basis einer stark heterogenen multisensoralen Datenzeitreihe zu ermöglichen. Die Algorithmen zur Veränderungsdetektion basieren auf der Analyse von zeitlichen NDVI-Trajektorien, welche ein Abbild zeitlicher Vegetationsveränderungen darstellen. Hangrutschungstypische Muster sind gekennzeichnet durch abrupte Vegetationszerstörung und einen langsamen Wiederbewuchs, da durch die Hangrutschungen fruchtbarer Oberboden gestört oder gar verlagert worden ist. In Verbindung mit reliefbeschreibenden Parametern erlaubt der entwickelte Ansatz somit die automatische Identifizierung von Hangrutschungen unterschiedlicher Größe, Form und Entwicklungsstadien unter verschiedenen natürlichen Bedingungen.

Die Methode wird auf zwei Szenarien angewendet. Zunächst wird die rezente Hangrutschungsdynamik auf Basis der RapidEye-Daten für ein Gebiet von 7500 km² untersucht. Anschließend erfolgt eine langzeitliche Analyse (1986-2013) eines 2500 km² großen stark von Hangrutschungen betroffenen Gebietes mittels der multisensoralen Datenbank. In beiden Fällen übersteigt die Anzahl der automatisch identifizierten Hangrutschungen jene offizieller kirgisischer Berichte um mehr als das Zehnfache. Insgesamt sind annähernd 2000 Hangrutschungen mit einer Größe von

50 m² bis 2.8 km² identifiziert worden. Das erfasste Hangrutschungsvorkommen zeigt deutliche räumliche Muster mit höchster Aktivität entlang der Hänge des Tien-Shan Gebirgsvorlandes. Zeitlich betrachtet hat die langzeitliche Analyse ein Aktivitätsmaximum in den Jahren 2003 und 2004 ergeben. Diese Jahre waren durch eine mehr als fünffach erhöhte Hangrutschungsaktivität gegenüber dem langjährigen Mittel von 57 Hangrutschungen gekennzeichnet. Diese raumzeitlichen Hangrutschungsaktivitätsmuster werden in der Dissertation der morphologischen Beschaffenheit (ursächlicher Faktor) und den zeitlichen Variationen des Niederschlages (auslösender Faktor) gegenübergestellt. So wird exemplarisch die Eignung der erzielten Identifizierungsergebnisse gezeigt, einzelne oder zusammenhängende Einflüsse von Hangrutschungen verursachenden Faktoren für ein Untersuchungsgebiet quantitativ zu bewerten. Für die Ableitung rezenter Hangrutschungsaktivität wird auf die RapidEye-Daten zurückgegriffen, die durch ihre hohe räumliche (5 m) und zeitliche Auflösung (Datenwiederholungsrate von bis zu wenigen Tagen und Wochen) eine Identifizierung von kleinen Rutschungen als Vorboten von größeren gefährlicheren Hangrutschungen zu ermöglichen. Dadurch kann die Methode innerhalb eines regelmäßigen Monitorings auch für Frühwarnsysteme nützliche Informationen liefern.

Die entwickelte Methode erlaubt die identifizierung von raumzeitliche Hangrutschungsaktivitätsmuster, welche zur Verbesserundie des regionalen Hangrutschungsprozessverständnis beitragen. Damit ist ein wichtiger Beitrag geschaffen zur Realisierung von Hangrutschungsgefährdungseinschätzungen, und damit zur potentiellen Reduzierung des Hangrutschungsrisikos für die lokale Bevölkerung von abgelegenen Gebirgsregionen wie im Falle Südkirgistans. Des Weiteren hat die Methode durch ihre sensorübergreifenden und Unsicherheiten einbeziehenden Analysealgorithmen ein großes Potential auf weitere hangrutschungsgefährdete Gebiete (wie bspw. Südostasien oder Südamerika) sowie auf neue optische Sensoren (z. B. Sentinel-2) angewandt zu werden, was Möglichkeiten für ein vielseitig und großflächig anwendbares Monitoringsystem eröffnet.

Contents

List of Figures

List of Tables

List of Abbreviations

AI ..... Area intersect (see Section II-5.3)
AU..... Area union (see Section II-5.3)
CIR..... Color infrared
CP ..... Check point
DEM ..... Digital elevation model
DGPS..... Differential global positioning system
DInSAR..... Differential interferometric synthetic aperture radar
DLR..... German Aerospace Center (*German: Deutsches Zentrum für Luft- und Raumfahrt e. V.*)
DN ..... Digital number
FN ..... False Negative
FP ..... False Positive
GCP ..... Ground Control Point
GFZ..... Helmholtz Centre Potsdam - German Research Centre for Geosciences (*German: Helmholtz-Zentrum Potsdam - Deutsches GeoForschungsZentrum*)
GIS ..... Geographic information system
GPS ..... Global positioning system
InSAR ..... Interferometric synthetic aperture radar
m.a.s.l..... Meters above sea level
MCHS..... Kyrgyz ministry of emergency situations
Mw ..... moment magnitude scale
NIR ..... Near-infrared
OOA ..... Object-oriented analysis
PE..... Position error (see Equation II-3)
RESA..... RapidEye Science Archive
SAR..... Synthetic aperture radar
SRTM..... Shuttle radar topography mission
TOA ..... Top of atmosphere
TP..... True positive
TS..... Time series data cube
USGS ..... United States Geological Survey

1 Introduction

1 Rationale and Structure

Landslides are a worldwide natural hazard causing thousands of fatalities and severe monetary losses every year (Highland & Brobowsky 2008; Nadim et al. 2006; Petley 2012). To predict and thus reduce landslide risk in the future, a profound knowledge about the past landslide activity is of utmost importance (Corominas & Moya 2008; Fell et al. 2008; Guzzetti et al. 2012; Varnes 1984). These records about past landslide activity have to be as complete as possible in time and space, in order to derive spatial and temporal probabilities of landslide occurrence as a crucial prerequisite of landslide hazard and risk assessment (Corominas et al. 2014; Guzzetti et al. 2005; van Westen et al. 2008). However, most regions, especially those with most fatalities in Asia (Petley 2010; Petley 2012), struggle with the limited availability of such comprehensive landslide records, because conventional mapping of landslides is an extremely time-consuming and labor-intensive task (Galli et al. 2008; Guzzetti et al. 2012; Wieczorek 1983). Thus, efficient strategies are needed for spatiotemporally precise mapping of landslide occurrence over large areas, which allow a retrospective derivation of long-term landslide activity as well as a regular monitoring of recent landslide activity.

In this context, the objective of the thesis is the development of a methodology enabling the utilization of long-available satellite remote sensing data (since the 1980s) for the automated analysis of the spatiotemporal landslide activity over large areas and long time spans. To be most precise in determining the temporal occurrence of landslides, each suitable dataset, regardless of the acquiring sensor, has to be integrated in the landslide analysis during the complete time span of satellite data availability. Consequently, this leads to comprehensive remote sensing time series databases of irregular temporal resolution and variable sensor characteristics. The mapping of landslides in such heterogeneous time series databases requires the development of efficient and robust methods for data pre-processing and multi-temporal landslide identification. The desired outcome of such an analysis is a multi-temporal landslide inventory, containing the location, extent and time of landslide occurrence, which serves as a basis for large-area probabilistic landslide hazard and risk assessment.

The thesis comprises five main chapters. Chapter I gives an overview of the general research background, presents the specific research framework and poses main research objectives and research questions. Chapters II-IV present consecutive stand-alone manuscripts, whose sub-objectives contribute to the overall thesis. Chapter II deals with the geometric normalization of the multi-sensor time series database, Chapter III with the monitoring of spatiotemporal landslide activity using RapidEye imagery, and Chapter IV with the derivation of long-term landslide activity based on multi-sensor optical satellite images. Chapter V discusses the overall research questions, considering the insights of Chapters II-IV. Figure I-1 illustrates the outline of the thesis and shows the main contributions of each chapter, whereas specific contributions and objectives of the individual manuscripts are presented in more detail in Section I-4.

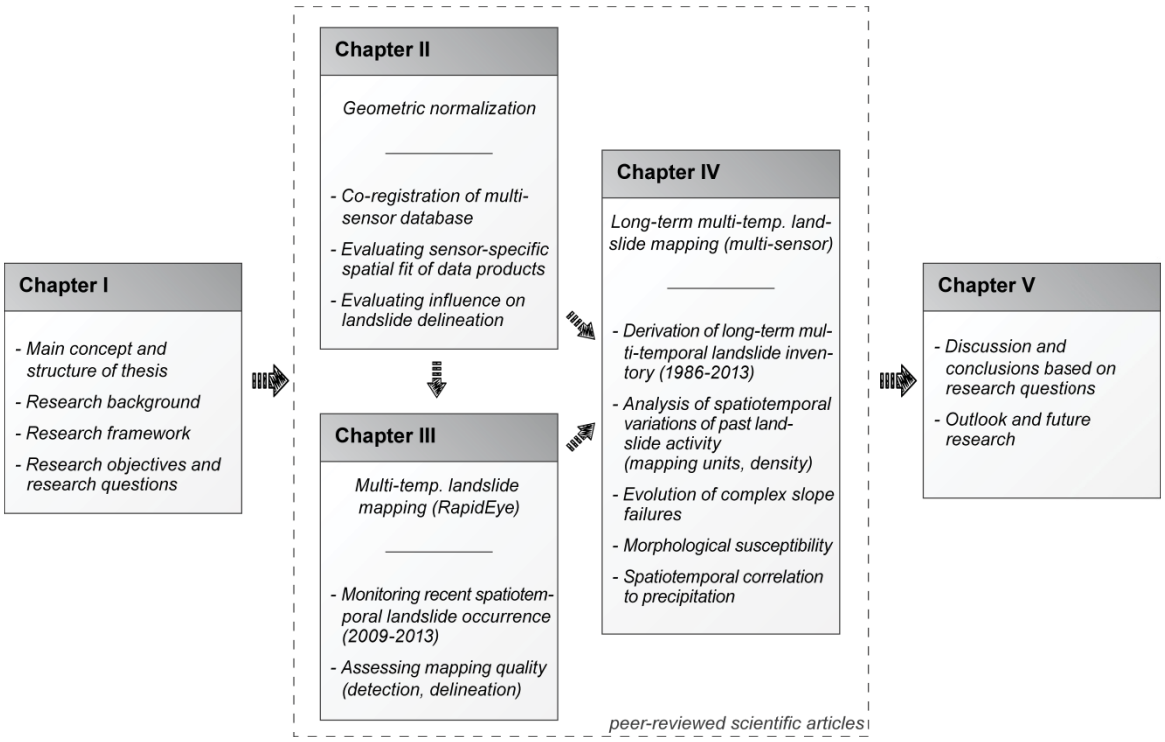

Figure I-1. Structure of the thesis. Chapters II-IV are subdivided into two parts: (top) method objectives and (bottom) application objectives (for more detail see Section I-4).

2 Research Background

The research background provides an overview of the landslide research in general (Section I-2.1) and the satellite-based remote sensing landslide investigations in particular (Section I-2.2).

2.1 Towards Landslide Hazard and Risk Assessments

This section summarizes the main concepts of landslide analysis and the related nomenclature the thesis is based on. More detailed information about further aspects of landslide research is provided by comprehensive overview articles (Corominas et al. 2014; Cruden 1993; Fell et al. 2008; Highland & Brobowsky 2008; Varnes 1978).

2.1.1 Landslide Processes and Landslide Inventory Types

Landslide is a generic term defining the downslope movement of a mass of rock, debris, or earth under the influence of gravity. Landslides can be classified into different types, based on a combination of the type of material (rock, soil, earth, mud, debris) and the type of movement (fall, topple, slide, spread, or flow). A complex landslide represents a slope failure in which one of the landslide types is followed by another type (or even types), such as a rock fall-debris flow. Landslides are further classified as deep-seated or shallow, depending on the type of movement and the depth of the disruption. A reactivation defines a landslide failure that occurs in place of a former landslide. A fresh failure is often specified as a landslide that occurs at a slope with missing signs of former failures. More information about the widely accepted definitions on landslide types and processes can be found in Cruden (1993), Cruden & Varnes (1996), Highland & Brobowsky (2008), and Varnes (1978). In this thesis, the generic terms “landslide”, “mass movement”, and “slope failure” are used interchangeably.

A landslide is a result of the interplay of predisposing and triggering factors. **Predisposing factors** – also called causative factors, environmental factors, and terrain factors – are characteristics of a slope determining the shear strength of the material. Commonly accepted predisposing factors are geology (lithological and structural properties), morphology (e.g. slope gradient, slope aspect, curvature), and land use (mainly described by the state and type of the vegetation surface cover). Predisposing factors are usually considered as static[1] conditions, defining a lower or higher probability of landslides. In contrast, **triggering factors** change the conditions on very short notice and set off the actual failure by exceeding a threshold where the shear stress is higher than the shear strength of the material[2]. Most frequent landslide triggers are precipitation (rainfall of different intensity and duration, snow melt, change of groundwater level) and seismic shaking (earthquakes of different magnitude peak ground acceleration) as well as volcanic activity (Clague 2013; Corominas et al. 2014; Corominas & Moya 2008; Guzzetti et al. 2012).

A **landslide inventory** contains the location of past landslides and their characteristics. The location is usually provided as point-based coordinates or as spatially explicit polygons. Where known, landslide characteristics include the date of occurrence, the landslide type, state of activity, dimension (e.g. area, width, length, volume, and depth), consequences (e.g. damage, fatalities), etc. The sets of recorded characteristics vary between the inventories due to different properties of the study areas as well as to different spatial scales and methods used to create the inventory. Landslide inventories can be differentiated into historical, event-based, seasonal and multi-temporal inventories (Fell et al. 2008; Guzzetti et al. 2012; Hervás 2013; Malamud et al. 2004; Van Den Eeckhaut & Hervás 2012; van Westen et al. 2008).

Historical inventories comprise the cumulative effect of landslides over a long period from tens to thousands of years. They usually comprise major landslides or landslide-prone slopes, whereas the age of the landslides is either unknown or given in relative terms, such as recent, old or historic (Murillo-Garcia et al. 2015; Wieczorek 1983).

Event inventories contain landslides that have been triggered by a single major triggering event such as intense tropical rainstorms or large earthquakes. Prominent landslide triggering events were the typhoon Morakot (Taiwan) and the Wenchuan earthquake (China). The typhoon Morakot hit central Taiwan on 7 August 2009 and triggered more than 20000 landslides that caused several hundreds of fatalities (Lin et al. 2011). The Wenchuan earthquake on 12 May 2008 with a magnitude of 7.9 Mw was one of the deadliest earthquakes in the recent past, whereas almost one third of the approximately 80000 fatalities have been caused by over 60000 triggered landslides (Huang & Fan 2013).

Seasonal inventories contain landslides related to multiple triggering events within one season of landslide activation. Such inventories are required for areas in which several events per season are likely to occur such as Southeast Asia, where landslide-prone areas are affected by several typhoons every year (Weng et al. 2011). For both, event and seasonal inventories the date of landslide occurrence is usually assigned to the date of the triggering event.

[1] The state of the predisposing factors is static to a certain extent only (depending on the observed time scale). Some factors can be considered as quasi-static (e.g. geology) and others are more dynamic such as human interference, which often affects the land use or soil properties of a slope.

[2] Many landslides also occur without the knowledge about distinct triggers. In such cases, slowly evolving changes of the conditions of the slope lead to a tipping point setting off the failing of the slope (Clague 2013).

Multi-temporal inventories are created by repeated documentation of landslides independently of specific triggering events during a longer period of time. The dates of occurrence are either precisely known or assigned to the time period between repeated documentation. Thus, these inventories provide detailed information about the past spatiotemporal landslide activity of a region (Galli et al. 2008; Saba et al. 2010).

2.1.2 Landslide Inventories as Requirement for Subsequent Landslide Investigations

"The past and present are keys to the future" (Varnes 1984) is a central principle in landslide research, expressing that future landslides occur under same or similar conditions that resulted in landslide failures in the past (Corominas & Moya 2008; Fell et al. 2008; Guzzetti et al. 2012). Thus, landslide inventories, representing the past and present landslide activity of a certain area, are the main prerequisite and the most important input dataset for the subsequent assessment of landslide susceptibility, hazard and risk (Cascini 2008; Corominas et al. 2014; Fell et al. 2008; Highland & Brobowsky 2008; van Westen et al. 2008). Figure I-2 illustrates the main steps from a landslide inventory to the prediction of landslide risk.

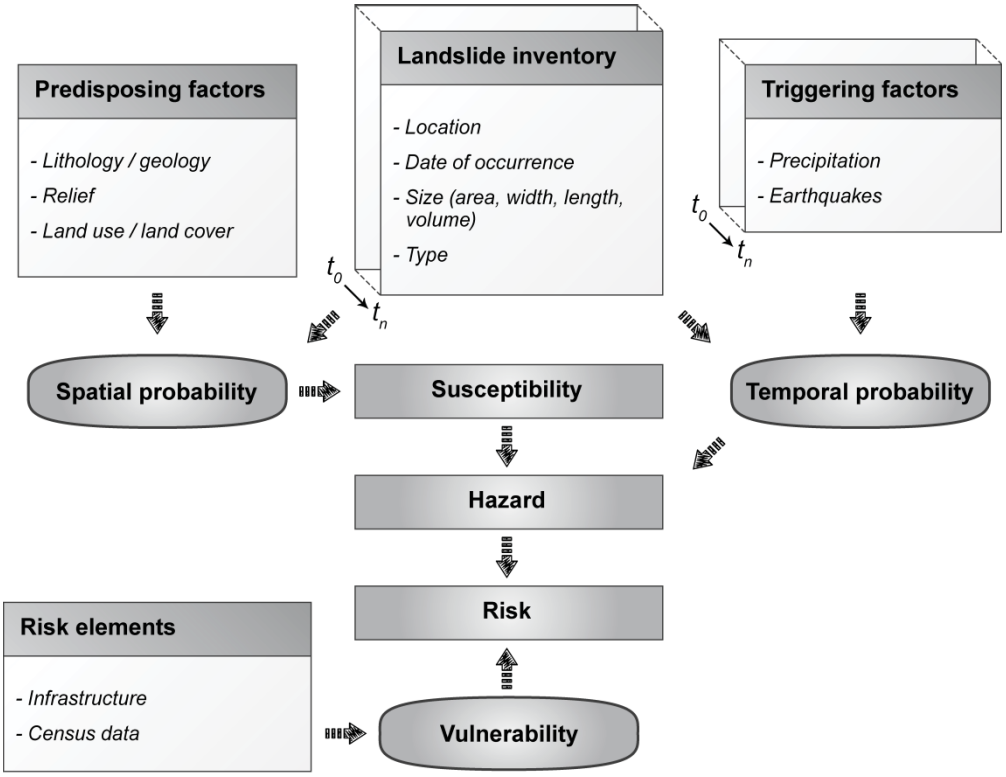

Figure I-2. Schematic representation of landslide risk assessment.

For the assessment of **landslide susceptibility** only predisposing factors are taken into account. For this purpose, the different factors and their characteristic combinations are analyzed against the spatial distribution of past landslide activity in order to map susceptible areas with the potential for future landslides. If available, this susceptibility assessment is performed for different sizes and types of landslides (Corominas et al. 2014; Fell et al. 2008; Guzzetti et al. 2005).

Landslide hazard assessment relates the temporal variations of landslides and triggering factors to determine the conditions that led to a certain frequency of landslides of different types and sizes (temporal landslide probability). In combination with the spatial distribution of the predisposing factors, a landslide hazard map shows the probability that a landslide of a certain type and intensity

will develop at a certain location in a given period of time (Corominas et al. 2014; Fell et al. 2008; Guzzetti et al. 2005; Peruccacci et al. 2012).

Landslide risk combines the probability information from a landslide hazard map with an analysis of all possible consequences (e.g. property damage, casualties, and loss of service). For this purpose, the elements at risk (e.g. infrastructure and population) are evaluated against their vulnerability to potential landslides. As a result landslide risk maps show for example how likely buildings will be destroyed or casualties can be expected in case of a landslide of a certain intensity, extent and downslope movement (Corominas et al. 2014; Fell et al. 2008; van Westen et al. 2008).

To allow comprehensive analysis of the conditions in which past landslides have occurred, the underlying landslide inventory is required to provide temporally and spatially precise information about the landslide failures for the longest possible period of time (Corominas & Moya 2008; Guzzetti et al. 2005; Guzzetti et al. 2012). However, despite their importance, such multi-temporal landslide inventories are largely unavailable or incomplete in space and time for most parts of the world (Guzzetti et al. 2012; Nadim et al. 2006). The main reason for this incompleteness in multi-temporal inventory availability is the high mapping effort, which such inventories usually require. Conventional mapping methods comprise the visual interpretation of high-resolution optical imagery and the mapping based on field surveys (Section I-2.1.3).

2.1.3 Landslide Mapping – Conventional Methods

Field-based mapping is commonly used to analyze single landslides in areas that are easy to access and where landslides have the potential to threaten local infrastructure and population. Field mapping contributes to the detailed characterization of the landslide process such as the description of material involved and movement type of the landslide. However, the suitability of the field-based methods for large area landslide mapping is hampered by the high mapping effort and the difficulties to access all parts of a study area. In addition, the detailed spatial delineation of the landslide is also very difficult, because the relief often impedes the ability to investigate all parts of a larger landslide from the viewing position at the bottom of a slope. Moreover, without additional information, the date of landslide occurrence is not precisely obtainable by visiting landslides after the failure and thus field-based mapping is inconvenient to map the temporal variations of the landslide activity retrospectively. In the context of landslide inventory mapping of large areas, the field-based methods are mainly used to validate other mapping procedures such as the visual or automated interpretation of remote sensing data (Galli et al. 2008; Guzzetti et al. 2012; Wieczorek 1983).

For several decades landslide inventory mapping has been largely based on the **visual interpretation** of aerial photographs or more recently of high resolution optical satellite imagery. Landslide failures usually disturb the Earth's surface, which leads to characteristic changes in surface cover and morphology that can be used as diagnostic features for landslide identification in panchromatic, multispectral and stereoscopic optical imagery. Especially fresh failures show distinct signs of surface disturbances that can be clearly distinguished from the undisturbed usually vegetated surroundings. As a result, optical imagery is suitable for the delineation of the outline of a landslide. If available, archived imagery can contribute to the retrospective analysis of spatiotemporal landslide activity by mapping the landslide failures between subsequent acquisitions. In practice, the labor-intensive and time-consuming visual interpretation hinders the multi-temporal mapping of landslides over large areas. However, optical imagery is often used to prepare a one-time landslide mapping based on a set of aerial photographs or high-resolution satellite data that have been acquired in the same period of time (Guzzetti et al. 2012; Michoud et al. 2010; van Westen et al. 2008).

2.2 Satellite Remote Sensing for Large-Area Landslide Investigations

This section provides a general insight in the remote sensing-based landslide research. The focus lies on satellite-based approaches that have the potential to contribute to large-area investigations in the context of landslide inventory mapping as a requirement for regional landslide risk assessments (cf. Section I-2.1). Although this thesis solely builds on optical satellite data (Section 2.2.2), the potential contribution of using radar remote sensing is also discussed (Section 2.2.1). For an overview of landslide applications based on other platforms (terrestrial and airborne remote sensing) or on how remote sensing techniques contribute to the characterization of predisposing or triggering factors there are comprehensive review articles: Guzzetti et al. (2012), Jaboyedoff et al. (2012), Michoud et al. (2010), Scaioni et al. (2014), Stumpf et al. (2010), Wasowski & Bovenga (2014), and van Westen et al. (2008).

2.2.1 Radar Data

Synthetic Aperture Radar (SAR) is widely used for landslide investigations, mainly focusing on the measurement of small surface deformations in the context of slow-moving landslides. SAR is an active system that records the phase and amplitude of the electromagnetic signal backscattered from the Earth's surface. Using two or more SAR images allows a generation of interferograms, representing images of the phase difference between two SAR images (Interferometric SAR - InSAR). For multi-temporal acquisitions the phase difference is a result of the topography, roughness, atmospheric effects, noise, and the possible ground displacement (e.g. due to slow-moving landslides) that occurred between the SAR image acquisitions along the line of sight (Scaioni et al. 2014; Wasowski & Bovenga 2014). Differential InSAR (DInSAR) techniques allow the extraction of the displacement component in an accuracy of several millimeters to centimeters by eliminating the other effects (Cascini et al. 2009; Hilley et al. 2004; Tofani et al. 2013). An extensive overview of DInSAR approaches used for the investigation of slow-moving landslides can be found in: Colesanti & Wasowski (2006), Delacourt et al. (2007), Scaioni et al. (2014), and Wasowski & Bovenga (2014).

In case of more rapidly moving landslides, their strong surface disturbances lead to a loss of coherence between the analyzed SAR images. This loss of coherence prevents the DInSAR analysis from providing meaningful results, and thus impedes the determination of the local surface displacements (Wasowski & Bovenga 2014). Recently published case studies use dual or full polarization SAR images to map rapid landslides after their failure. For this purpose, these studies analyze the dominant scattering mechanisms of the surface cover, which in case of a landslide is assumed to change from volume scattering (caused by the natural vegetation before failure) to surface scattering (caused by the bare soil after failure). However, so far, these studies have been designed to investigate the potential of polarimetric SAR data and thus have only been applied to specific test cases (Czuchlewski et al. 2003; Li et al. 2014; Plank et al. 2015; Shibayama & Yamaguchi 2014; Shimada et al. 2014; Yonezawa et al. 2012).

Main contributions to landslide research:

- Identification of very slow moving landslides or landslide parts.
- Measured displacement rates provide information about the state of activity of already known landslides or can indicate areas of potential onsets of rapid landslides.

2.2.2 Optical Data

In optical remote sensing, surface materials are differentiated by their spectral reflectance signature. In case of a landslide, this spectral signature is ambiguous and depends on the material that is exposed after a landslide failure. Strictly speaking, since these materials are not unique properties of landslides, the direct spectral identification of landslides is impracticable. Nevertheless, due to the high spectral and morphological contrast between landslide-related disturbances and their vegetated surroundings, landslides can still be clearly identified in optical imagery (Guzzetti et al. 2012; Metternicht et al. 2005; Roessner et al. 2005). As a result, a wide range of approaches have been published, dealing with the (semi-)automated detection of landslide failures in optical satellite images (recent review articles are: Guzzetti et al. (2012) and Scaioni et al. (2014)). Often, either the absence of the vegetation cover (mono-temporal approaches) or the loss or disturbance of vegetation cover (multi-temporal approaches) is used as the main diagnostic feature for landslide identification. Moreover, these approaches implement, albeit to different degrees, information about the local texture, shape properties of derived objects, and external data such as derivatives of a digital elevation model. This way, they are capable of the identification and the delineation of the surface cover disturbances that have been caused in the process of a landslide failure. Typical optical data used for the landslide investigations represent multi-spectral and panchromatic satellite remote sensing data with spatial resolutions from 30 m up to sub-meter resolution. Section I-2.2.3 provides a detailed overview of the existing approaches and shows how they contribute to landslide inventory mapping for different applications and scales.

A secondary field of application using optical data is the feature tracking method. Optical feature tracking aims at the precise comparison of corresponding areas between multi-temporal optical images. The displacements of these corresponding areas provide information about the rates of movement for targets such as slow-moving landslides. For optical satellite images, the minimum size of detectable displacement amounts approximately to 1/5 of the original pixels size, which is less detailed than the resolvable displacement achieved by most DInSAR approaches (Delacourt et al. 2007; Scaioni et al. 2014).

Main contributions to landslide research:

- Retrospective identification and delineation of landslides after failure.
- Potential for efficient landslide inventory generation for large areas.

2.2.3 Optical Satellite-Based Approaches for (Semi-)Automated Landslide Inventory Mapping

Due to the wide and long-term availability of optical remote sensing data as well as its proved potential to automate the landslide identification process (Section I-2.2.2) a large variety of optical remote sensing-based landslide mapping approaches have been published. This section provides an overview of the state of the art methods and identifies the needs for further methodological developments.

State of the Art

The developed (semi-)automated approaches can be loosely grouped by the geographical element (pixel or object) and by the number of data acquisitions (mono- or bi-temporal) used for landslide identification. An extensive list is given in the Table App-1.

The **pixel-oriented** approaches label areas that have been affected by landslide failures (e.g. Borghuis et al. 2007; Cheng et al. 2004), but are inadequate to relate the pixel-based results to individual slope failures. Thus, they do not allow the assessment of landslide dimensions and frequencies, which are a crucial requirement for subsequent landslide hazard and risk analysis. In recent years, an increasing

number of landslide mapping approaches has been published using **object-oriented** analysis (OOA). These approaches allow the derivation of these landslide dimensions and frequencies by assigning single objects to individual landslides (e.g. Barlow et al. 2006; Martha et al. 2010) or landslide parts (e.g Hölbling et al. 2015). Moreover, OOA allows the integration of contextual information (e.g. object direction in relation to local relief) to further improve the mapping reliability.

Mono-temporal approaches use single data acquisitions to identify preceding landslides based on supervised or unsupervised classification algorithms (e.g. Aksoy & Ercanoglu 2012; Stumpf & Kerle 2011). Since such approaches restrict their analysis to data of a single acquisition date, they cannot provide any information about the date of landslide occurrence. For this reason, the preparation of historical inventories is the most common application for mono-temporal approaches (e.g. Dou et al. 2015). However, some studies propose mono-temporal landslide identification also for event inventory mapping (cf. Table App-1). In such cases, a dataset acquired right after a landslide triggering event (post-event image) serves as the basis for landslide mapping, whereas the date of the detected landslides is assigned to the date of the triggering event. This usually results in an overestimation of the event-related landslide activity, because landslides prior to the triggering event might be mistaken as event-related.

Bi-temporal approaches identify landslides that have been occurred between the acquisitions of a bi-temporal image pair. They use analytical change detection algorithms (e.g. Mondini et al. 2011) or compare mono-temporal landslide classifications from both images (e.g. Lodhi 2011). If a bi-temporal image pair consists of image acquisitions right before and right after a landslide triggering event, these approaches are very suitable for event-based landslide inventory mapping (e.g. Parker et al. 2011; Tsai et al. 2010).

Research Gap

Despite the vast variety of developed landslide mapping approaches, little effort has been undertaken to promote automated multi-temporal inventory mapping, which is surprising, since it represents the most important requirement for landslide hazard and risk assessment (Section I-2.1). Multi-temporal inventories require the continuous mapping of the spatiotemporal landslide occurrence over a long period of time. So far, Martha et al. (2012, 2013) have applied a bi-temporal approach to subsequent image pairs of a multi-temporal database of annual data coverage from 1998 to 2009 for an area of 81 km² in the Indian Himalaya. This small case study shows the basic potential of existing bi-temporal approaches in the context of multi-temporal landslide mapping. However, there is still a strong need for an approach that allows:

- automated multi-temporal landslide mapping
- for large areas
- over longest possible time periods,

which enables the derivation of multi-temporal inventories

- of short update intervals
- and object-based results.

Such an approach requires a multi-temporal database of a large number of satellite remote sensing archive data as well as new methodological developments, which enable a robust multi-temporal landslide mapping by making efficient use of such comprehensive time series databases.

3 Research Framework

The thesis concentrates its methodological developments and spatiotemporal landslide investigations on a landslide-affected region in Southern Kyrgyzstan. To illustrate the research framework of the thesis, Section I-3 describes study area, the case areas used throughout the chapters, and lists the spatial data on which the methodological developments are based on.

3.1 Study Area

Natural Setting and Landslide Situation

Kyrgyzstan is located in Central Asia, a region of high tectonic activity (Reigber et al. 2001; Zubovich et al. 2010). Central Asia is part of the Indian-Eurasian collision zone, leading to the high mountain ranges of the Himalaya, Pamir and Tien Shan. Kyrgyzstan is almost completely covered by the W-E trending Tien Shan mountain ranges, whereas 90% of the country is located above 1000 m.a.s.l with peak elevations above 7000 m.a.s.l. This active mountain building frequently causes extreme natural events such as earthquakes, landslides, avalanches and floods. Due to the scarce living space in this mountainous country, the local population and infrastructure are often exposed to these extreme natural processes.

In this context, landslides represent one of the major natural hazards. For Kyrgyzstan more than 4500 landslide failures have been recorded, whereas the vast majority is concentrated in Southwest Kyrgyzstan along the eastern rim of the Fergana Basin (Ibatulin 2011). Between 1990 and 2009, landslides caused 421 fatalities and resulted in an annual average of economic loss of USD 2.5 million (Torgoev et al. 2008).

Landslides mainly occur in weakly consolidated sediments of the foothills of the high mountain ranges in elevations from 700 to 2000 m.a.s.l. A wide range of different landslide types are common in Southern Kyrgyzstan, whereas most of them occur in form of deep-seated rotational and translational slides in Quaternary and Tertiary sediments consisting of loess, sand- and siltstones, clays, loams and carbonates. Often, they also occur as complex landslides combining different types within an individual failure. Their size varies between several hundred and several million square meters, whereas large events of more than one million cubic meters of displaced material are a frequent phenomenon. The peak of landslide occurrence is observed in spring and early summer, however the annual landslide rates vary greatly. Most landslides are not directly caused by distinct major triggering events, but represent a result of complex interactions between geological, tectonic, seismic and hydrogeological factors, which are not well understood yet. Because of the high complexity of the landslide phenomena and their spatiotemporally sporadic occurrence over large areas, government agencies are very interested in the development of efficient and objective methods for improved landslide hazard and risk assessment in order to minimize casualties and economic loss (Golovko et al. 2015; Ibatulin 2011; Roessner et al. 2005; Wetzel et al. 2000).

Landslide Mapping in Kyrgyzstan

Up to now, the assessment of landslide hazard in Kyrgyzstan has relied on landslide inventories that have been manually prepared by local authorities. Starting in the 1950s, comprehensive field surveys have been undertaken to investigate landslides in most hazardous areas such as the Mailuu-Suu valley, which has been used for uranium mining and processing for the Soviet nuclear program and thus involves a great risk to the local population in case of landslide failures (Havenith et al. 2006). From the 1970s on, these field-based surveys have been accompanied by a more systematic landslide mapping based on the visual interpretation of aerial photographs (Yerokhin 1998). However, since the independence in 1991, Kyrgyz landslide investigations have been reduced to the vicinity of larger settlements due to a shortage of funding (Golovko et al. 2015). After 2002, even those efforts have further diminished and the landslide mapping basically relies on landslide reports from the local population. Moreover, most existing landslide information is available as point-based coordinates of limited geographical accuracy (Section I-3.2), which further constrains their use for subsequent analyses (Golovko et al. 2015).

Thus, Kyrgyzstan lacks a systematic landslide database, especially since its independence. However, such a database is indispensable for landslide hazard and risk assessment, since it provides information about the spatial and temporal variations of past landslide activity, on which such assessments are built on (Section I-2.1). Hence, this region could particularly benefit from methodological developments that allow a systematic assessment of spatiotemporal landslide activity, especially for the last two to three decades.

Case Areas

Figure I-3 gives an overview of the study area and the case areas this thesis is based on. The study area is located at the eastern rim of the Fergana Basin and is approximately 12000 km² in size. The figure also depicts known landslide failures (see Section I-3.2). The black dots represent landslides recorded by the systematic visual interpretation of aerial photographs with latest acquisitions in 1986, and the pink dots the landslide points available through field surveys and population reports since 1986.

The chapters of this thesis address different parts of the study area. In Chapter II a geometric preprocessing strategy is developed and applied to the remote sensing database (Section I-3.2) available for the complete study area. Chapter III and IV focus on the methodological developments towards a multi-temporal landslide mapping procedure enabling monitoring of recent landslide occurrence (Chapter III) and retrospective analysis of long-term spatiotemporal landslide activity (Chapter IV). For this purpose, these chapters address different subsets of the study area, which have been selected in respect of data availability and past landslide activity. This way, the methods of the thesis are developed, validated and applied to different parts of the study area and different remote sensing data allowing a comprehensive evaluation of the developed approach and achieved results of the thesis.

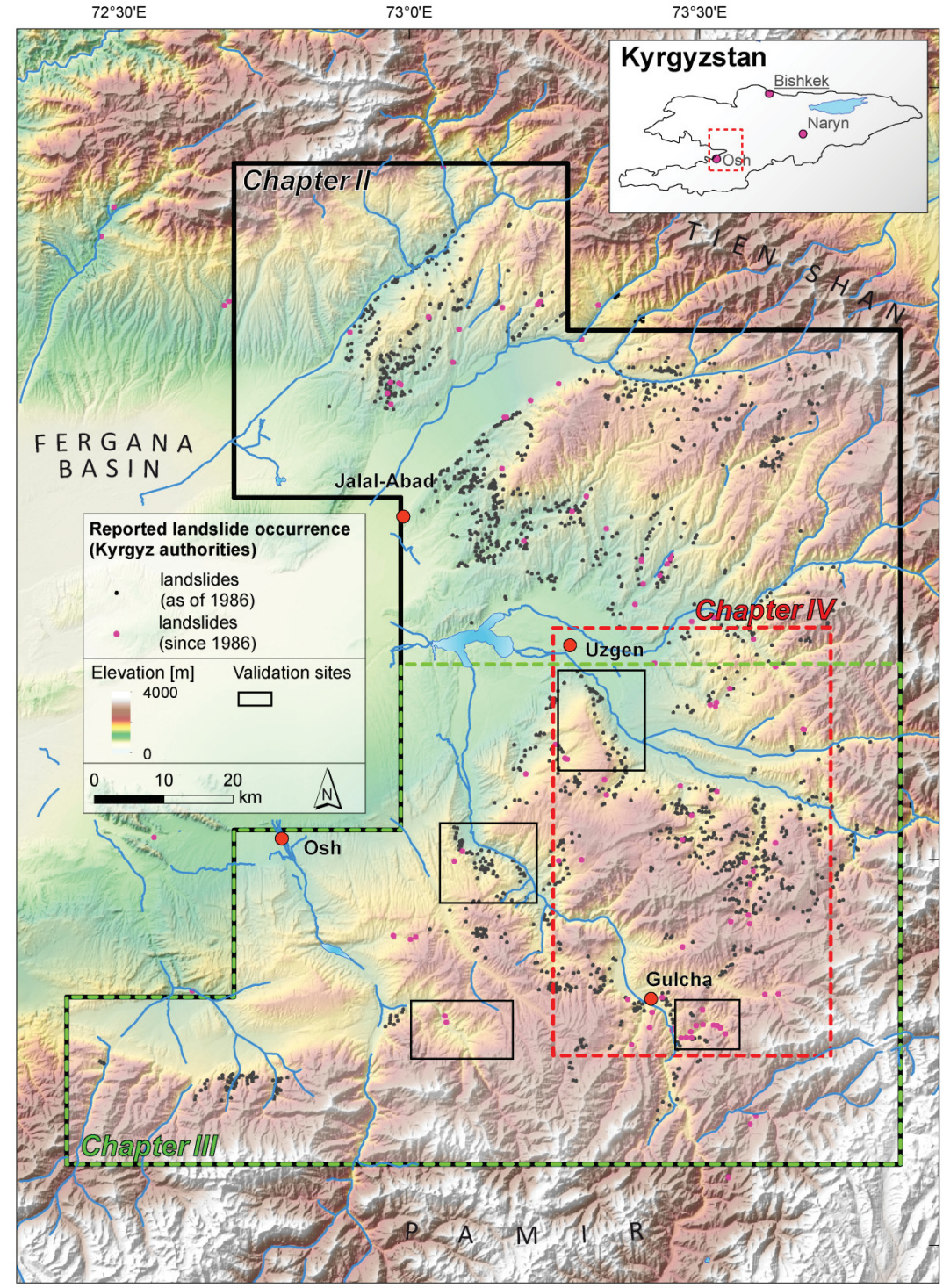

Figure I-3. Study area and case areas of individual Chapters II-IV.

3.2 Spatial Database

Remote Sensing Data

A multi-temporal database of optical remote sensing data has been established for the time period between 1986 and 2013. To achieve highest temporal resolution during these 27 years, the database combines images of seven optical sensors, i.e. SPOT 1 & 5, IRS1-C LISSIII, Landsat TM & ETM+, ASTER and RapidEye. These sensors vary in spatial resolution, ranging from 30 m for Landsat and 5 m for RapidEye data. They also cover different spectral ranges by varying spectral bands and resolutions, whereas all of them comprise the green, red and near-infrared bands as the lowest common spectral denominator. The imagery is obtained from the data providers as standard data products, which are radiometrically calibrated (at-sensor radiance) and geometrically registered (band-to-band co-registered and orthorectified[3]). In general, the datasets represent imagery from existing data archives. However, for the RapidEye data since 2011, the RESA (RapidEye Science Archive) data grant (project ID: 424) has allowed a pre-defined tasking of data acquisition during the landslide affected season, which resulted in a large amount of spatially and temporally high resolution data for the studied region (Sections II-2.2, III-2.2). Table I-1 provides an overview of the sensors used in this thesis and lists their sensor-specific characteristics and the amount of data available for the thesis.

In total, the database consists of 729 datasets. The temporal resolution varies between six years at the beginning and two weeks at the end of the time series, whereas since 1996 at least annual data coverage could be achieved with a small data gap in 2006. Due to the large study area and the mostly smaller swath of the remote sensing data (Table I-1), the temporal resolution varies also throughout the study area. Further details about the spatiotemporal data availability are given for the respective databases used in Chapters II-IV.

This multi-sensor time series database of irregular temporal and spatial resolution as well as spatially inconsistent data coverage builds the framework for the methodological developments towards a multi-temporal landslide mapping approach. In such a database, landslides appear highly variable depending on the data acquisition characteristics:

- *time of data acquisition* (season of acquisition, time passed after failure), and
- *sensor properties* (spatial, spectral and radiometric properties of the sensors)

as well as on the natural variability of the landslide phenomena throughout the large study area:

- *landslide activity* (fresh or reactivated failure), and
- *natural setting* (land cover, lithology and relief).

The challenges arising from the heterogeneity of the database and from the variability of landslide appearance are described comprehensively in the database sections of the Chapters II-IV.

[3] The data of the sensors SPOT 1 and SPOT 5 are obtained as radiometrically corrected only (product level 1A). They are automatically orthorectified based on orbital position parameters and a digital elevation model (Section II-2.2).

Table I-1. Optical satellite remote sensing database.

Sensor	Resolution (m)	Swath Width, Extent (km)	Spectral Range (nm)	No. of Bands	Time Period	Acquisition Dates	Datasets	Product Level	Provider
RapidEye	5	77, 25 × 25	440–850	5	2009–2013	65	631	3A	BlackBridge
SPOT 5	10	60, 60 × 60	500–1750	4	2006–2010	5	9	1A	SPOT IMAGE
ASTER	15–90	60, 60 × 60	520–2430	14	2000–2008	21	36	3A 01	ASTER GDS
SPOT 1	20	60, 60 × 60	500–890	3	1986	2	3	1A	SPOT IMAGE
IRS1C-LISS-III	23.6	141, 141 x 141	520-1700	4	1997	1	1	L1	Eurimage
Landsat TM	30	185, 185 × 170	450–2350	7	1989–1999 2009–2013	14	25	1T	USGS GLS
Landsat ETM+	30	185, 185 × 170	450–2350	8	1999–2003	13	24	1T	USGS GLS

Terrain Data

The study uses a digital elevation model (DEM) derived from the X-band data of the Shuttle Radar Topography Mission in February 2000 (Rabus et al. 2003). The DEM was obtained from the German Aerospace Center (DLR) in a spike-removed form. It is used to include landslide-related geomorphological information (e.g. angle and aspect of slopes) as contextual information for more reliable object-oriented landslide mapping.

Landslide Data

The most extensive and systematic source of landslide information is the report by Yerokhin (1998). This report represents the cumulative landslide mapping effort until 1986. It consists of 1532 landslides visually interpreted based on aerial photographs without specifying the sizes and dates of the documented slope failures. A more recent source is the report by Ibatulin (2011) containing descriptions of 67 selected major landslide failures that occurred between the 1970s and 2004 in the vicinity of settlements. These descriptions comprise precise temporal information of the date of occurrence, but do not include spatially explicit information on the location of the slope failures. Instead, verbal descriptions of topographic characteristics are given to convey locations. A third source is provided by the Kyrgyz Ministry of Emergency Situations (MCHS). Since 2002, employees of the MCHS visited 73 selected landslides in the vicinity of settlements and documented date of the visit, activity state of the landslide, and point-based coordinates of the landslide location.

In close cooperation, the MCHS and the Remote Sensing Section of the German Research Centre for Geosciences (GFZ) have been conducting field work in Southern Kyrgyzstan since 1998. Almost annually, sub-parts of the study area are visited and GPS-waypoints and field-photographs of selected landslides are documented. Moreover, these field surveys also include differential GPS measurements for selected topographic features and spatial reference points, which have been used for validation of the geometric pre-processing of Chapter II.

To allow the validation of the developed landslide mapping approach in Chapters III and IV, reference maps of spatiotemporal landslide occurrence are prepared for four selected validation sites (Figure I-3). The preparation of the reference maps is based on the available landslide data, the field-based surveys and the visual interpretation of the optical satellite remote sensing database.

4 Research Objectives and Research Questions

The main objective of the thesis is the development of an automated remote sensing-based approach that allows an efficient and robust derivation of a long-term and large area multi-temporal landslide inventory in order to derive spatiotemporal landslide frequencies as an important requirement for systematic landslide hazard and risk assessment. For this purpose, the large amount of multi-sensor time series data has to be efficiently pre-processed to serve as a basis for the methodological developments towards an automated multi-temporal landslide identification approach. This landslide identification approach is required for obtaining spatially explicit landslide objects with a precise as possible determination of their date of occurrence. A second objective is the application of the approach aiming at the precise assessment of the recent and long-term spatiotemporal landslide activity for large landslide-affected areas in Southern Kyrgyzstan.

Based on the objectives the following **research questions** will be addressed in this thesis:

Method perspective:

- *What are efficient and robust methods to utilize an optical multi-sensor satellite time series for large area and long-term multi-temporal landslide identification? What are the advances of the developed methods and the key differences to existing approaches?*

Application perspective:

- *What are essential applications of the developed approach and how can they contribute to an improved regional landslide process understanding? Which specific results can be achieved for Southern Kyrgyzstan and how can this region benefit from them?*

Specific Objectives per Chapter:

The stand-alone manuscripts of Chapters II-IV contribute to the overall objectives and deal with the main research questions. The synthesis in Chapter V provides overarching conclusions based on the research questions, considering the specific aspects of the individual manuscripts.

The stand-alone manuscripts of Chapters II-IV are published or submitted in international peer-reviewed scientific journals. For this purpose, each of these chapters is subdivided into the sections research background (introduction), research framework (study area and database), method, results, discussion, and conclusions. Consequently, recurring material cannot be avoided completely.

Neglecting adjustments in formatting, the three manuscripts are presented in the thesis unchanged. They were written originally by the first author. The co-authors contributed to discussions and revisions to clarify and improve the manuscripts. Further publications in the realm of the dissertation are listed in the appendix (Appendix E).

The next paragraphs briefly introduce the individual manuscripts in the overall context of the thesis by providing their objectives and main contributions (cf. Figure I-1). For each chapter, the publication information, the overall objective, the relations to the other manuscripts as well as its specific method and application objectives are given.

Chapter II: Database Generation for Multi-Temporal Landslide Analyses – Geometric Normalization

published as:

Behling, R., Roessner, S., Segl, K., Kleinschmit, B. & Kaufmann, H., (2014). Robust Automated Image Co-Registration of Optical Multi-Sensor Time Series Data: Database Generation for Multi-Temporal Landslide Detection. *Remote Sens.*, 6(3), pp.2572–2600.

The overall objective of this chapter is the development and application of a method for automated geometric co-registration in order to create a remote sensing database that is suitable for long-term automated landslide detection.

Method objectives:

- Development of a robust and efficient geometric normalization approach that allows:
  - the relative image-to-image co-registration of a large number of orthorectified standard data products acquired by different sensors and characterized by seasonal and long-term acquisition variations and
  - an absolute spatial fit of the co-registered remote sensing database, enabling the combined analysis with other spatial data (e.g. administrative data, geomorphology, geology, etc.).

Application objectives:

- Co-registration of the complete multi-sensor time series database.
- Determination of sensor-specific image-to-image location accuracies of the standard remote sensing data products.
- Evaluation of the co-registered database in regard to its suitability for the spatial delineation of landslide failures.

Chapter III: Monitoring of Recent Landslide Activity – RapidEye-Based Time Series Analysis

published as:

Behling, R., Roessner, S., Kaufmann, H. & Kleinschmit, B., (2014). Automated Spatiotemporal Landslide Mapping over Large Areas Using RapidEye Time Series Data. *Remote Sens.*, 6(9), pp.8026–8055.

This chapter aims at the development of an automated approach for the spatiotemporally precise mapping of recent landslide activity using RapidEye time series data of high temporal resolution.

Chapter III is based on the co-registered RapidEye data of Chapter II.

Method objectives:

- Development of a multi-temporal landslide mapping approach that allows:
  - landslide recognition by efficiently utilizing a high temporal resolution RapidEye time series,
  - object-oriented landslide identification,
  - precise determination of the time period of landslide occurrence, and
  - the possibility for regular updates (monitoring).

Application objectives:

- Derivation of a multi-temporal inventory of recent landslide activity (2009-2013) for an area of 7500 km².
- Precise and quantified evaluation of the landslide mapping quality.

Chapter IV: Retrospective Assessment of Long-Term Landslide Activity – Multi-Sensor Time Series Analysis

submitted as:

Behling, R., Roessner, S., Golovko, D. & Kleinschmit, B., (submitted on 02 September 2015). Derivation of Long-Term Spatiotemporal Landslide Activity–An Automated Multi-Sensor Time Series Approach. *Remote Sens. Environ.*

This chapter addresses the automated mapping and evaluation of long-term multi-temporal landslide activity.

Chapter IV is based on the co-registered multi-sensor database of Chapter II and on the methodological principles developed in Chapter III.

Method objectives:

- Comprehensive extension of the RapidEye-based multi-temporal landslide mapping approach into a multi-sensor approach, additionally allowing:
  - the extension of the time span of landslide identification to the beginning of suitable optical multi-spectral satellite data availability in the 1980s,
  - landslide identification in remote sensing data of different spectral and spatial sensor characteristics,
  - landslide object-specific image integration for most precise determination of the time period of landslide occurrence, and
  - landslide identification in a highly irregular remote sensing time series of variable data intervals (few weeks to several years) as well as seasonally differing acquisitions.

Application objectives:

- Derivation of a multi-temporal landslide inventory covering 27 years (1986-2013) for an area of 2500 km².
- Evaluation and exemplary demonstration of the potential of the derived inventory to serve as a basis for systematic hazard assessment, including:
  - the derivation of spatial and temporal variations in past landslide activity (landslide density, landslide occurrence rates, temporal evolution of landslides, etc.) and
  - the evaluation against morphological settings and against temporal variations of the triggering factor precipitation.

II Geometric Normalization

Behling, R., Roessner, S., Segl, K., Kleinschmit, B. & Kaufmann, H., (2014). Robust Automated Image Co-Registration of Optical Multi-Sensor Time Series Data: Database Generation for Multi-Temporal Landslide Detection. *Remote Sens.*, 6(3), pp.2572–2600.

© 2014 by the authors; licensee MDPI, Basel, Switzerland. This article is an open access article distributed under the terms and conditions of the Creative Commons Attribution license (http://creativecommons.org/licenses/by/3.0/).

Received: 9 October 2013; in revised form: 13 March 2014 / Accepted: 17 March 2014 /
Published: 21 March 2014 (doi:10.3390/rs6032572)

Abstract

Reliable multi-temporal landslide detection over longer periods of time requires multi-sensor time series data characterized by high internal geometric stability, as well as high relative and absolute accuracy. For this purpose, a new methodology for fully automated co-registration has been developed allowing efficient and robust spatial alignment of standard orthorectified data products originating from a multitude of optical satellite remote sensing data of varying spatial resolution. Correlation-based co-registration uses world-wide available terrain corrected Landsat Level 1T time series data as the spatial reference, ensuring global applicability. The developed approach has been applied to a multi-sensor time series of 592 remote sensing datasets covering an approximately 12000 km^2 area in Southern Kyrgyzstan (Central Asia) strongly affected by landslides. The database contains images acquired during the last 26 years by Landsat (E)TM, ASTER, SPOT and RapidEye sensors. Analysis of the spatial shifts obtained from co-registration has revealed sensor-specific alignments ranging between 5 m and more than 400 m. Overall accuracy assessment of these alignments has resulted in a high relative image-to-image accuracy of 17 m (RMSE) and a high absolute accuracy of 23 m (RMSE) for the whole co-registered database, making it suitable for multi-temporal landslide detection at a regional scale in Southern Kyrgyzstan.

1 Introduction

Landslides are a world-wide occurring natural hazard leading to severe loss of life and infrastructure. A global tendency towards steadily increasing landslide risk can be observed, because of the spreading of settlements in unfavorable regions and the consequences of climate change (Petley 2010; Petley 2012). Against this background, improved understanding of landslide processes in space and time is of great importance, requiring multi-temporal landslide inventories (Cascini 2008; Guzzetti et al. 2012; van Westen et al. 2008). So far, they have been largely missing for most parts of the world, because of their time and labor intense preparation using conventional mapping methods (Fiorucci et al. 2011; Guzzetti et al. 2012; Saba et al. 2010). In this context, the increasing availability of optical satellite remote sensing data has opened up new opportunities for spatiotemporal analysis of landslide occurrence covering large areas (Guzzetti et al. 2012; Metternicht et al. 2005; Othman & Gloaguen 2013; Roessner et al. 2005).

The completeness and quality of remote sensing-based landslide inventories depend on the used multi-temporal image database, whereas a high temporal repetition rate over the longest possible time period of data availability is required in order to perform longer term analysis of landslide occurrence, which is necessary for objective landslide hazard assessment (Cascini 2008; Guzzetti et al. 2012; van Westen et al. 2008). For this purpose, the global Landsat archive is of key importance, providing free access to the longest available time series of medium-resolution optical satellite remote sensing data (Wulder et al. 2012). However, in order to achieve the best possible temporal data coverage, multi-sensor data have to be used, resulting in a heterogeneous database of varying spatial and temporal resolution.

Despite this variability, precise image-to-image co-registration has to be ensured for all multi-temporal and multi-sensor datasets, because insufficient spatial fit leads to various ambiguities,

resulting in the detection of artifact changes (Sundaresan et al. 2007; Townshend et al. 1992), as well as incorrect spatial delineation of landslides. The creation of longer term inventories requires maintaining the geometric stability of the image database over several decades, taking into account seasonal and inter-annual landscape changes. Furthermore, the resulting multi-temporal remote sensing database has to be of sufficient absolute positional accuracy related to an external spatial reference system, allowing the combination of information derived from remote sensing analysis with other spatial data, such as GPS-based field measurements within a GIS environment in order to perform subsequent process and hazard analysis.

The overall goal of the presented study has been the development and application of a methodology for automated image-to-image co-registration in order to create an image database that is suitable for longer term automated landslide detection within a 12000 km^2 study area in Southern Kyrgyzstan (Central Asia) strongly affected by landslides (Roessner et al. 2005). The original image database for this area comprises almost 600 datasets acquired by the multispectral Landsat-(E)TM, SPOT, ASTER and RapidEye satellite systems during the last 26 years. Most of these images were obtained in the form of orthorectified standard data products from the respective satellite data providers. Initial evaluation of the relative spatial fit between these higher-level data products has revealed that significant spatial offsets occur between most of them, including data acquired by the same sensor.

Against this background, the objective has been the development of a co-registration methodology that is suitable to correct for the spatial offsets between large amounts of orthorectified standard data products comprising longer term multi-sensor time series. Thus, the approach has to be able to handle various multi-sensor effects, such as differences between the spatial, spectral and radiometric properties of the image data, as well as multi-temporal effects, such as varying atmospheric, solar and land cover conditions, resulting from seasonal and long-term variability between the image datasets (Le Moigne et al. 2011b; Gao et al. 2009; Gianinetto 2012). Despite the large number of existing methods for automated co-registration, which are comprehensively discussed in Le Moigne et al., 2011 (Le Moigne et al. 2011b), Dawn et al., 2010 (Dawn et al. 2010) and Zitova and Flusser, 2003 (Zitova & Flusser 2003), only a few of these methods are capable of dealing with multi-sensor and multi-temporal effects at the same time.

In general, the existing co-registration methods are classified into two main categories comprising feature-based and area-based techniques (Zitova & Flusser 2003). For accommodating multi-sensor effects during co-registration, feature-based techniques, such as scale-invariant feature transform (SIFT) (Lowe 2004) and speeded-up robust features (SURF) (Bay et al. 2008), are considered to be more suitable, because these techniques use salient features, such as edges, corners, intersections of linear structures and centroids of distinct geometric objects. These features are expected to be geometrically stable despite the sensor-related variability of the image data (Huang & Li 2010; Cao et al. 2013; Brook & Ben-Dor 2011; Bouchiha & Besbes 2013). However, in rural mountainous areas, like Southern Kyrgyzstan, such distinct time-invariant features are often scarce and unevenly distributed, which largely increases the likelihood for significant co-registration errors (Chen et al. 2003; Huang & Li 2010). For such environments, area-based methods are considered to be more suitable, because co-registration is based on identifying distinctive properties for image matching using intensity information rather than local features (Chen et al. 2003; Huang & Li 2010). Hence, area-based methods aim at identifying image areas that are similar in

intensity, whereas the commonly used similarity measures are cross-correlation and sequential similarity detection (Fonseca & Manjunath 1996; Zitova & Flusser 2003).

Independent of the used co-registration method, most of the already existing approaches have not been developed for fully automated and efficient processing of big amounts of multi-sensor and multi-temporal image data covering large areas over longer periods of time. Therefore, the practical usability of these methods is often limited, because of the high methodological complexity, the big computational effort, as well as additional requirements specific to the analyzed datasets (Cao et al. 2013; Dawn et al. 2010; Gao et al. 2009). The presented study aims at the development of a robust and globally applicable methodology for automated co-registration, which is suitable for efficient correction of spatial offsets between orthorectified standard data products representing multi-sensor time series.

In this context, a spatially and temporally consistent spatial reference system is required, allowing spatial alignment of all datasets with sufficient relative and absolute accuracy. For this purpose, globally available Landsat Level 1T time series data have been selected as a common spatial reference. They are characterized by sub-pixel image-to-image co-registration accuracy throughout the whole time series (Kennedy et al. 2010; Lee et al. 2004; Storey et al. 2008), whereas the absolute accuracy of the global Landsat Level 1T database has been estimated to 15 m (Storey et al. 2008). Both accuracies are considered to be sufficient for landslide detection at a regional scale. Moreover, Landsat data represent the only source of spatial reference information consistently and repeatedly covering the whole study area, allowing consistent spatial alignment of all time-series datasets, which, in part, are irregularly and patchily distributed over the large study area.

The developed co-registration approach is described in Section 3. The results of spatial alignment are presented in Section 4, comprising sensor-specific analysis for the complete database. In Section 5, the relative and absolute accuracy of the achieved co-registration is analyzed for the whole database, including its influence on the multi-temporal delineation of landslides. The developed methodology is comprehensively discussed in Section 6, focusing on achievable accuracy and overall applicability.

2 Study Area and Spatial Database

2.1 Study Area in Southern Kyrgyzstan (Central Asia)

The study area is located in Southern Kyrgyzstan in Central Asia and covers approximately 12000 km^2 (Figure 1), whereas landslide occurrence is especially concentrated along the Eastern rim of the Fergana Basin in the foothills of the surrounding Tien Shan and Pamir mountain ranges. In this area of high tectonic activity and pronounced topographic relief, landslides are a widespread phenomenon, representing one of the most severe natural hazards to the local population. Landslides vary widely in their sizes, ranging between a few hundred square meters for small events and several hundred thousands or even millions of square meters for large failures (Roessner et al. 2005; Schlögel et al. 2011).

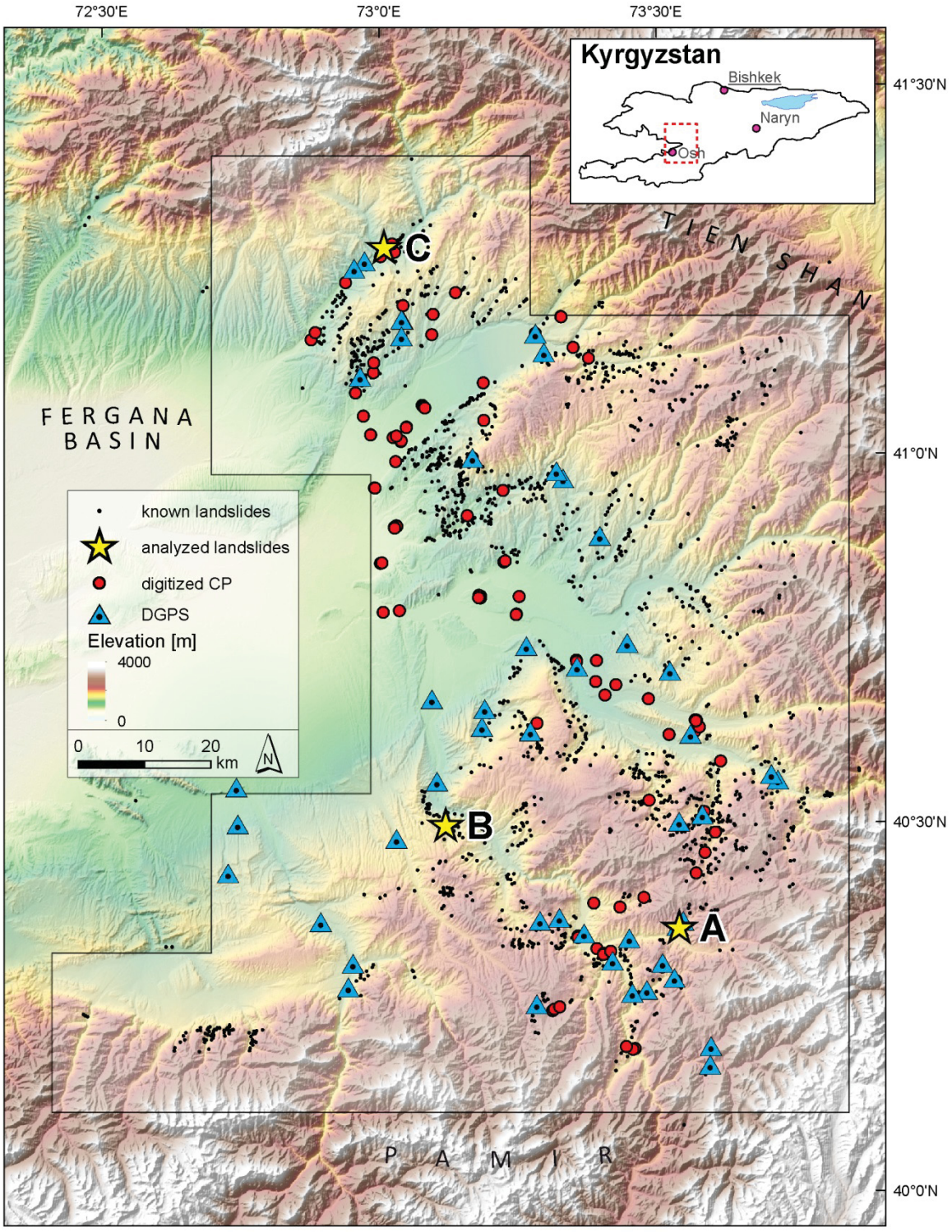

Figure II-1. Study area in Southern Kyrgyzstan. (Inset) The location within Kyrgyzstan (depicted as a red dashed line). (Main figure) The location of known landslides and reference information for accuracy assessment in Section 5 (check points (CPs), differential GPS (DGPS) points and analyzed landslides) within the study area, depicted as a transparent polygon overlay.

Since most of these landslides belong to the rotational and translational types, they cause widespread destruction of the mostly vegetated surface cover and, thus, are well detectable in optical imagery in general (Lacroix et al. 2013; Roessner et al. 2005). Most of these landslides are caused by complex interactions between geological, tectonic, seismic and hydrogeological factors, which have not been well understood, yet. As a result, landslides occur frequently, but at the same time,

irregularly throughout the whole study area and cannot be related to distinct triggering events, such as earthquakes and intense rainstorms (Roessner et al. 2005).

In this region, landslides have been investigated since the 1950s, whereas approximately 3000 landslides have been documented (Figure 1). However, regular monitoring has been limited to the time period between 1968 and 1992, focusing on larger settlements and their surroundings, whereas for most of the landslides, coordinate-based geographic locations are missing. Against this background, there is a great need for creating a spatiotemporal landslide inventory covering the whole area (Figure 1).

2.2 Satellite Remote Sensing Database

A multi-temporal database of optical remote sensing data has been created for the study area in Southern Kyrgyzstan. This multi-temporal database consists of 592 multispectral mid- and high-resolution satellite remote sensing images acquired by the Landsat-TM and ETM+, SPOT 1 and -5, ASTER and RapidEye sensors during the last 26 years (Table 1). The spatial resolutions of the contributing sensors range between 30 m for Landsat and 5 m for RapidEye data. They also cover different spectral ranges by varying spectral bands and resolutions. However, all of these sensors represent multispectral instruments comprising the green, red and near-infrared (NIR) spectral bands as the lowest common spectral denominator, allowing comprehensive multi-sensor analysis of landslide-related surface changes.

Almost all of the remote sensing datasets were obtained from the respective satellite data providers in the form of orthorectified standard data products (Table 1) in order to minimize geometric pre-processing efforts and to facilitate the applicability of the developed methodology independent of local ground-truth information, such as GCPs. In the case of SPOT, radiometrically-calibrated Level 1A data were automatically orthorectified using standard orthorectification routines of the ENVI software, which are based on orbital position parameters and a digital elevation model (SRTM). As a result, the established multi-temporal and multi-sensor satellite remote sensing database solely contains orthorectified datasets.

Table II-1. Optical satellite remote sensing database.

Sensor	Resolution (m)	Swath Width, Extent (km)	Spectral Range (nm)	No. of Bands	Time Period	Acquisition Dates	Datasets	Product Level	Provider
RapidEye	5	77, 25 × 25	440–850	5	2009–2012	51	503	3A	BlackBridge
SPOT-5	10	60, 60 × 60	500–1750	4	2006–2010	5	9	1A	SPOT IMAGE
ASTER	15–90	60, 60 × 60	520–2430	14	2000–2008	20	30	3A 01	ASTER GDS
SPOT-1	20	60, 60 × 60	500–890	3	1986	2	3	1A	SPOT IMAGE
Landsat TM	30	185, 185 × 170	450–2350	7	1989–1999 2009–2012	14	25	1T	USGS GLS
Landsat ETM+	30	185, 185 × 170	450–2350	8	1999–2003	13	24	1T	USGS GLS

Except for RapidEye, all other datasets have been contained in satellite remote sensing data archives. RapidEye data have been acquired in the frame of the RESA (RapidEye Science Archive) program, allowing customized tasking of data acquisition during pre-defined time periods. Due to the five independent satellites of the RapidEye system (Chander et al. 2013), a database of high spatial and temporal resolution could be created for the whole region of interest. In total, the database comprises 503 Level 3A standard orthorectified data products characterized by a 5-m pixel size, resulting from cubic convolution resampling of the original 6.5-m RapidEye data. Each of these datasets belongs to one of the fixed 21 RapidEye tiles (Blackbridge 2014) covering the study area (Figure 2).

Datasets acquired by different sensors vary in their spatial extent between 185 × 170 km² for Landsat and 25 × 25 km² for a single RapidEye tile. Therefore, for each sensor, varying numbers of datasets are required to cover the whole region of interest. Figure 2 illustrates the spatiotemporal coverage for the different sensors, whereas the numbers of temporal repetitions are color-coded. The diagrams at the bottom show the number of temporal repetition and their areal coverage of the study area, with maximum and minimum values depicted in grey.

In the case of Landsat, the database contains 49 scenes covering 100% of the study area at least for 23 different acquisition dates, whereas the maximum temporal repetition of 27 acquisition dates could be achieved for 80% of the area during the time period between 1989 and 2012. ASTER (30 scenes) and SPOT (10 scenes) have significantly lower temporal repetitions, with spatial coverage of the study area of 91% and 77%, respectively. RapidEye comprises the highest number of datasets, due to the high temporal repetition and the orthorectified datasets of a relatively small size (25 × 25 km²), resulting in a high number of datasets for a single acquisition date. Temporal repetition varies between 13 and 28 coverages for the different parts of the study area and is almost as high as for Landsat, despite the much shorter acquisition period (4 *versus* 19 years). Overall, spatial and temporal coverage differs within the study area, because of its large size and the variety of used sensors, representing a challenge to co-registration, since the whole image database has to be transferred into one consistent spatial system. For this purpose, the Landsat Level 1T database has been selected, because it repeatedly covers the whole study area in a spatially consistent way (Section 2.3).

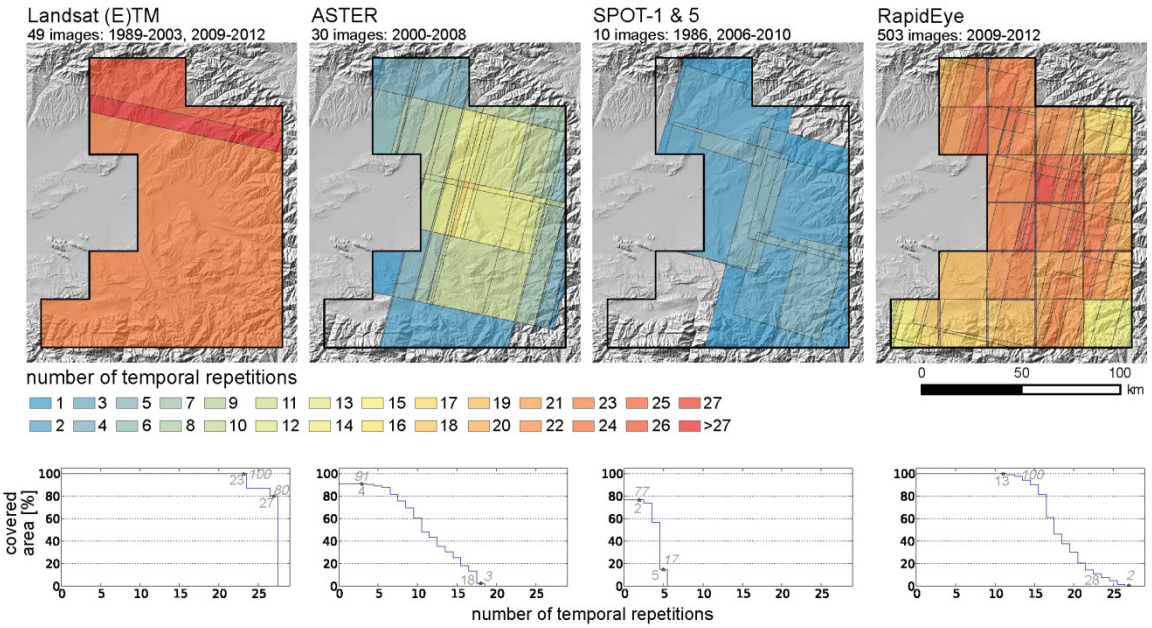

Figure II-2. Sensor-specific spatiotemporal coverage of the study area. Diagrams show the number of temporal repetitions and the related areal coverage of the study area.

The multi-temporal database is characterized by high seasonal and inter-annual variability of land cover, comprising additional challenges to co-registration. In Figure 3, this variability is exemplarily illustrated for a 6.8 × 7.2 km² subset of the study area showing color infrared (CIR) visualizations of the image data of all sensors contained in the database acquired during different seasons between 1986 and 2011. Seasonal variability mainly originates from differences in vegetation cover, whereas the period of most intense vegetation development lasts from May until early August, peaking in June. Another seasonal change is the decline of discharge in the river bed dur-

ing the depicted time span (April–September). Besides these regularly occurring changes, episodic changes can be observed, which are caused by agricultural land use and landslide occurrence. During the depicted period of time, the highest landslide activity can be observed between 2002 and 2004, resulting in a significant increase of landslide affected slopes (yellow ellipses in Figure 3), comparing the datasets acquired in 2004 and 1986.

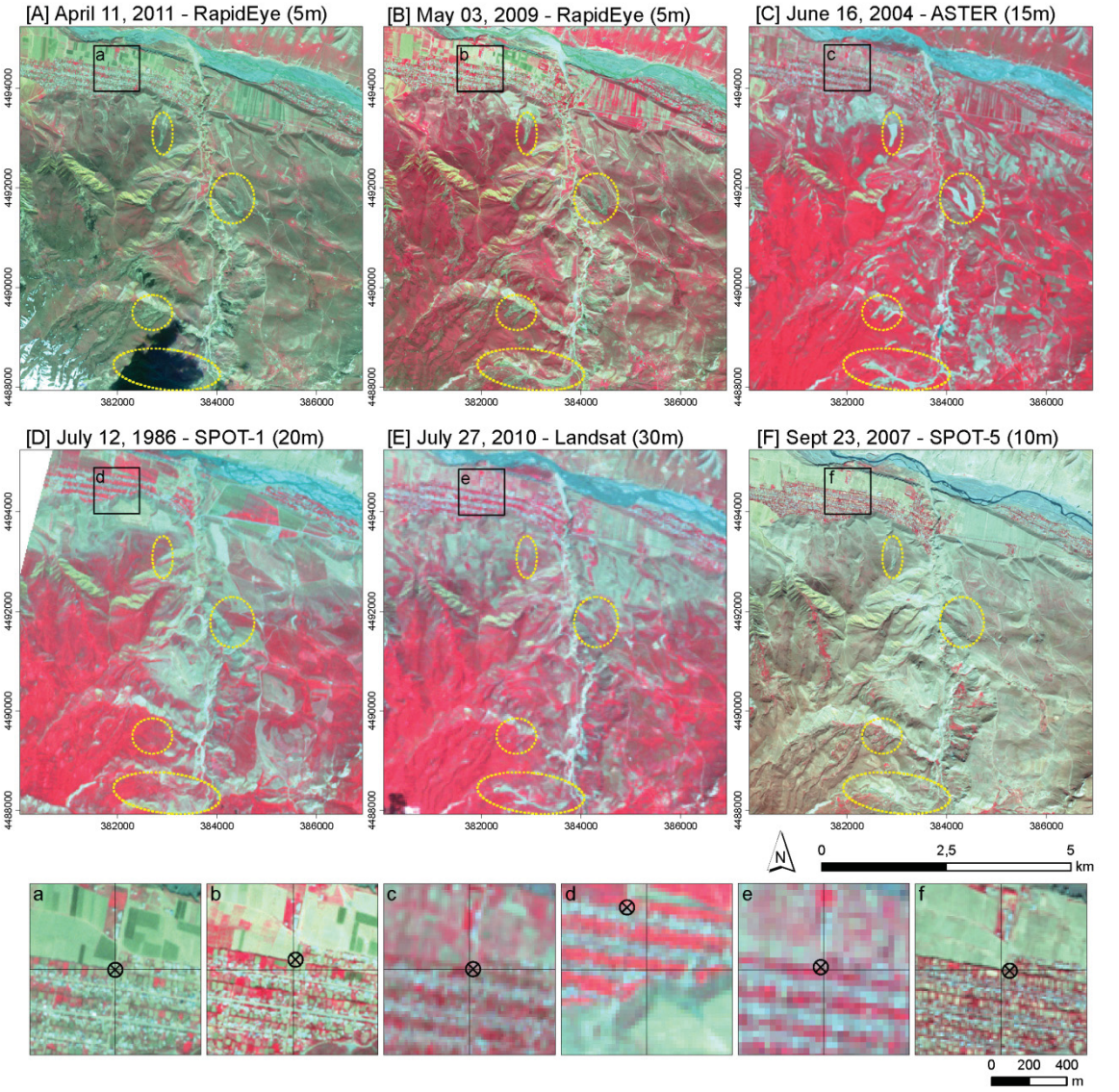

*Figure II-3. Exemplary representation of multi-temporal time series (1986–2011). (**A**–**F**) Color infrared (CIR) visualization of seasonal differing multi-sensor datasets; selected landslide prone areas are depicted by yellow dashed ellipses. (**a**–**f**) The geometric offsets within the time series.*

The small subsets (Figure 3a–f) depicted at the bottom of Figure 3 illustrate the initial spatial offsets occurring between standard orthorectified datasets. The black cross hairs represent the center coordinates of the subsets, whereas the circle-shaped markers indicate an identical point represented by a road crossing. In Figure 3a, the cross hair and the marked point have the same position, whereas for all other subsets, a relative offset can be observed, amounting to a maximum of almost 400 m in the case of SPOT 1 (Figure 3d). This maximum geometric offset is caused by the applied orthorectification procedure that is solely based on orbital position parameters, which

have been less accurate for SPOT 1 than for the later SPOT 5. Although, in the case of the other sensors, these offsets are less pronounced, they still amount to up to 60 m and need to be corrected in the process of automated co-registration.

2.3 Spatial Reference Information

2.3.1 Spatial Reference for Co-Registration

In this study, terrain corrected Landsat Level 1T data are used as the spatial reference, while at the same time, they are part of the satellite remote sensing database (Section 2.2). They have been selected because they are freely and widely available and because they represent the only spatially consistent reference information for the whole study area. In contrast, datasets acquired by other sensors either do not cover the complete study area or require many datasets of different acquisition dates and swaths (Figure 2). Such multiple acquisitions result in a spatially and temporally inconsistent data coverage, which is not suitable as the spatial reference. However, since the Landsat reference represents the lowest spatial resolution of the whole database, the co-registration procedure needs to support sub-pixel alignment in order to enable precise co-registration of higher resolution images (Section 3.2).

The Landsat Level 1T data are characterized by sub-pixel image-to-image registration accuracy (Kennedy et al. 2010; Lee et al. 2004; Storey et al. 2008), enabling the introduction of multiple reference scenes in the co-registration process. Using the reference scenes of different acquisition dates is advantageous, because it accommodates the multi-temporal variability caused by seasonal and long-term land cover changes, which often reduces the accuracy of co-registration (Gao et al. 2009). Moreover, Landsat Level 1T data are characterized by an absolute geolocation accuracy of 15 m (Storey et al. 2008) and, thus, are suitable as the external spatial reference.

Out of all 49 Landsat Level 1T datasets contained in the database, six scenes of three seasonally differing acquisition dates have been selected as the spatial reference. They comprise three mosaics of Landsat ETM+ scenes (path 151; row 31 and 32), which have been acquired on 24 August 2000, 26 May 2002, and 27 April 2003 comprising the main seasonal contrast between abundant green vegetation in spring and mostly dry vegetation in late summer. The Landsat scenes of 24 August 2000, have been identified as the primary spatial reference, which is used as the default. If co-registration to these scenes fails, one of the two other mosaics is selected.

2.3.2 Image-Based Check Points for Relative Accuracy Assessment

The relative accuracy of the co-registration approach is determined by assessing image-to-image accuracy between the single datasets of the remote sensing database. For this purpose, time invariant check points (CPs) were digitized in the Landsat reference. Because of its low spatial resolution of 30 m, only 21 CPs could be identified throughout the mountainous study area. To overcome this limitation, high resolution (5 m and 2.5 m) panchromatic orthorectified SPOT datasets, which are not part of the multi-temporal database, have been manually co-registered to the Landsat reference using the 21 CPs as tie points. Based on these co-registered SPOT images, an additional 65 CPs could be identified in areas of insufficient CP coverage, resulting in a total of 86 CPs. They are mostly represented by streets, intersections and corners of buildings, which were identified in settlements throughout the whole study area (Figure 1). Based on these CPs, the spatial offset of a dataset in relation to Landsat is determined before and after co-registration (Section 5.1).

2.3.3 Differential GPS Points for Absolute Accuracy Assessment

The absolute accuracy of the co-registered remote sensing database is assessed using high accuracy differential GPS (DGPS) points, which were measured in the field in the years 2011 and 2012 with a geolocation accuracy of a few centimeters by a Topcon GB-1000 receiver. This way, the spatial fit of the co-registered image database with spatial information from other sources, such as the results from GPS-based field mapping, can be evaluated. The measured 46 DGPS points (Figure 1) represent corners of buildings and road crossings. However, due to the dominating rural character of the study area, these structures are rather small and, thus, can only be precisely identified in remote sensing data of higher spatial resolution. Therefore, absolute accuracy assessment is only carried out for the co-registered SPOT 5 and RapidEye datasets with a spatial resolution of 10 m and 5 m, respectively (Section 5.2).

2.3.4 Time Series of Digitized Landslides

In order to evaluate the influence of co-registration accuracy on the multi-temporal spatial delineation of landslides, three landslides have been selected, which have not changed their extent since initial failure. These stationary landslides are situated far apart from each other in different parts of the study area (Figure 1). They have been manually digitized in all available multi-temporal datasets before and after co-registration. First, each landslide was digitized in a high-resolution RapidEye dataset. The resulting polygons were used as spatial templates, which, in a second step, have been manually overlaid on the landslide representations in all of the other datasets. This way, errors introduced by multiple manual digitization in datasets of varying spatial resolutions have been omitted, which otherwise would have influenced accuracy assessment (Section 5.3). The number of datasets that were available for multi-temporal digitization differs between the landslides depending on temporal data coverage after failure. Landslides A and B (Figure 1) occurred in 2009. Landslide A could be identified in 25 datasets acquired by three sensors (RapidEye, Landsat, SPOT 5) and Landslide B in 24 datasets acquired by two sensors (RapidEye, Landsat). Landslide C failed in 1999, resulting in its presence in 39 datasets acquired by the Landsat, ASTER, SPOT and RapidEye sensors.

3 Co-Registration of Multi-Temporal and Multi-Sensor Optical Satellite Data

3.1 Overall Approach

Image-to-image co-registration aims at the spatial alignment of the whole database (Section 2.2) to a common spatial reference represented by the Landsat Level 1T data (Section 2.3.1). The developed co-registration approach (Section 3.2) is based on the assumption that the orthorectified standard data products of the various sensors only differ by constant spatial offsets, which can be corrected by applying image-specific shifts. Checking the fulfillment of this condition for each dataset is an integral part of the co-registration approach, which is depicted in its overall structure in Figure 4.

In order to accommodate the needs originating from the diversity of datasets contained in the comprehensive satellite remote sensing database, two modes have been implemented. The first one enables co-registration of single datasets to the Landsat reference representing the standard case. This mode gets applied if datasets of the same sensor have very small or non-existing spatial overlaps and, thus, cannot be reliably co-registered to each other before aligning them to the Landsat

reference. The second mode is applied to data stacks of high temporal and spatial resolution acquired by the same sensor. This two-step mode starts with sensor-internal co-registration of the datasets before they are co-registered en bloc to the Landsat reference using the average of all shifts calculated for the single images of the sensor-internal data stack by the same procedure as in Mode 1. This way, high-accuracy spatial fit between datasets of the same sensor can be achieved or maintained avoiding the uncertainties that get introduced by the co-registration of individual images to a spatial reference of a largely differing spatial resolution. In this study, the second mode has been applied to the RapidEye data, since they are characterized by much higher temporal and spatial resolutions than the Landsat reference and the other medium-resolution satellite remote sensing data, which are co-registered using the first mode.

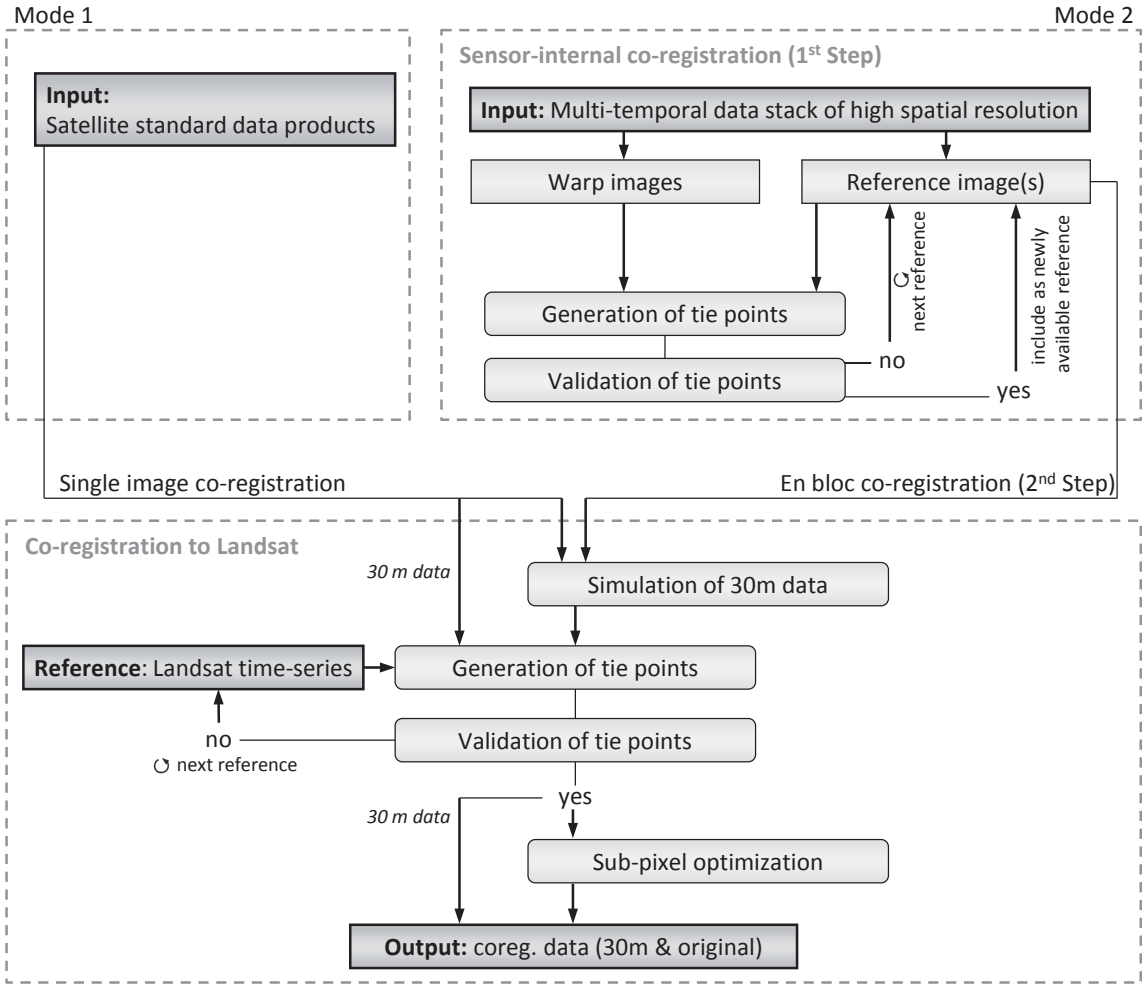

Figure II-4. Overall structure of the developed co-registration approach.

3.2 Co-Registration to Landsat Reference

Co-registration builds on area-based cross-correlation (Dawn et al. 2010; Fonseca & Manjunath 1996; Zitova & Flusser 2003) that requires the same spatial resolution for the reference image and the warp image. Thus, spatial resampling is a critical step for the performance of the correlation process. In order to get comparable results, downsampling the higher resolution dataset to the lower resolution one is applied, since upsampling of the lower resolution image to the higher resolution one does not allow the reconstruction of spectral details, which are only present in the higher resolution image and, thus, not suitable for correlation purposes. In contrast, downsampling enables the simulation of the spectral signatures of lower resolution data by mixing the spectral information of the higher resolution image. In this study, the warp images of higher spatial resolution are resampled to realistic Landsat pixels by applying a Gaussian filter kernel, which takes into account the spatial resolution of both sensors (Mueller & Segl 1999). The used approach defines the full width at half maximum (FWHM) of the Gaussian kernel as the ratio between the pixel size of the Landsat reference and the pixel size of the warp image. Once both images have the same spatial resolution, the warp image is shifted to the spatial grid of the Landsat reference as a basis for the following correlation.

Using the cross-correlation method, the warp image is co-registered to the reference image by correlating the intensity values within corresponding subsets of the images defined by a moving window. The subset of maximum correlation corresponds to the displacement that is stored in a tie point. In the presented approach, the red and the near infrared (NIR) bands of the input images are used simultaneously, providing a combined overall correlation value. The selection of these bands is performed in an automated way, as long as respective wavelength information is contained in the header files of the warp and reference images. Since the combination of these two bands reacts very sensitively to changes in vegetation cover, high correlation values can only be obtained for temporarily stable vegetated and non-vegetated areas. Moreover, for the correlation window, a relatively large size (51 × 51 pixels) is selected in order to minimize local ambiguities and further increase the robustness of the approach.

The tie point generation process iteratively selects random pixel positions for centering the correlation windows. The correlation coefficient is calculated for each pixel position within a predefined search range, which, by default, is constrained to five pixels, making the approach more robust and computationally less intense. However, this range can be changed depending on the expected offset. If a correlation coefficient is higher than the empirically determined threshold of 0.93, the offset value is stored as the tie point. This process is repeated, until 100 tie points are identified per image pair or 10% of all image pixels have been checked.

In order to validate the identified tie points and to exclude potential outliers, an affine transformation (translation, rotation, scaling) between both images is assumed, because global translation cannot be introduced as an *a priori* hypothesis. The biggest outliers in regard to the affine model are excluded in an iterative process, until the RMSE is less than one pixel. In the next step, the obtained optimized affine model allows for validating the initial assumption of a global translation. If the scaling or rotation factors of the affine model are negligibly small, i.e. additional offsets at the image corners are less than 1.5 pixels, the global translation transformation is used for co-registration.

If the validation process fails (e.g. due to an unfavorable tie point constellation) or less than 10 tie points per scene remain after the removal of outliers, one of the two other Landsat reference mosaics (Section 2.3) is selected, starting with the one that is seasonally closer to the warp image acquisition date (Figure 4). If none of the reference images meets these quality criteria, the warp image is excluded from the automated processing chain and has to be checked by the user with the option of interactively choosing an affine transformation for image wrapping based on the selected tie points.

In the case of a successful correlation, a final sub-pixel optimization is performed for images of significantly higher spatial resolution than the Landsat reference. In the initial simulation of the 30-m warp image, only one possible centering of the Gaussian filter kernel has been used for resampling to the 30-m resolution warp image. However, in principle, the number of possibilities amounts to the number of original warp image pixels fitting within a single reference pixel, e.g. a 10-m resolution SPOT image results in nine different possibilities for centering the Gaussian filter kernel. Hence, the Gaussian filter kernel is moved in single pixel steps over the original warp image grid around the first centering position of the initial resampling step in order to derive all spatial variations of the 30-m warp image. Then, the correlation process is repeated for all of the resampled 30-m warp images at the position of the already identified tie points. The image characterized by maximized overall correlation represents the sub-pixel optimized co-registered warp image at 30-m resolution.

The final shift comprises the sum of the shifts used to align the warp image grid to the Landsat grid, the 30-m pixel shift resulting from the initial correlation and the original resolution pixel shift originating from the sub-pixel optimization. In the last step, this shift is used to co-register the warp image using a global translation. As a result, two co-registered warp images are produced: one in the spatial resolution of the Landsat reference (the best correlation result) and one in the spatial resolution of the original image data. In the case of the original resolution warp image, the shift is used to update the coordinate reference point, and thus, the image is corrected without any resampling, which maintains the original spectral information of the image after co-registration. Both images are aligned to the Landsat reference grid. The simulated 30-m warp image has exactly the same spatial grid as the reference, whereas in the case of the original warp image, the upper left coordinate is aligned to the reference grid. The achievable accuracy of the approach is determined by the spatial resolution of the original data. If the original datasets have the same spatial resolution as the reference, the steps for simulating the reference resolution and sub-pixel optimization are omitted.

3.3 Sensor-Internal Co-Registration

In Mode 2 of the developed approach, sensor-internal co-registration is performed as the first step before the whole data stack is co-registered en bloc to the Landsat reference. For this purpose, a single dataset is selected from the data stack representing the sensor-internal spatial reference. All of the remaining images of the data stack are co-registered to this reference using the image-to-image area-based correlation algorithm implemented in the first mode without performing the simulation of 30-m data and the following sub-pixel optimization. If a dataset cannot be co-registered (due to a failed validation process or less than 10 identified tie points), it is iteratively correlated with already co-registered images of former iterations, until a good co-registration result can be achieved (Figure 4). This iterative approach allows the co-registration of seasonally differing datasets, resulting in a sensor-internal geometrically-consistent data stack, which is then

co-registered en bloc to the Landsat reference. For this purpose, the procedure of Mode 1 is applied to each of the datasets contained in the stack in order to determine the average values for all shifts, which then are used for the en bloc co-registration of the whole data stack.

4 Sensor-Specific Results of the Estimated Shifts

The developed co-registration approach has been applied to all of the 592 image datasets. All of them have passed the validation step, which means that the original orthorectified images have a consistent internal image geometry, which is free of significant distortions. In the following, the shifts obtained by automated co-registration are analyzed separately for each sensor.

4.1 Landsat Datasets

Applying the developed approach to the remaining 43 Landsat Level 1T datasets has resulted in no need for integer pixel shifts, confirming the sub-pixel image-to-image registration accuracy known from the literature (Kennedy et al. 2010; Lee et al. 2004; Storey et al. 2008). Co-registration was performed in the standard way (Section 3.2) for all of the datasets, which shows that the datasets are free of internal distortions. This also proves the robustness of the developed approach, accommodating the variability of the image data caused by the presence of clouds and snow, as well as inter-annual and seasonal changes introduced by the time series between 1989 and 2012 and long annual acquisition periods ranging from February to November.

4.2 ASTER and SPOT Datasets

ⓐ

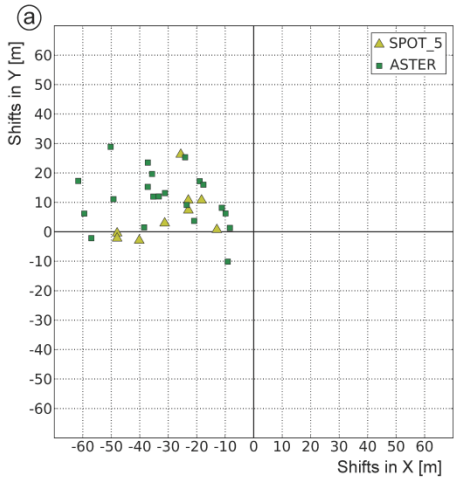

ⓑ

Number of images	SPOT-1 (20m) 3		SPOT-5 (10m) 9		ASTER (15m) 30	
Applied shifts [m]:	X	Y	X	Y	X	Y
Mean	67	-414	-30	6	-31	14
Stdev	52	32	13	9	17	9
Min	30	-434	-48	-3	-62	-10
Max	126	-377	-13	26	-8	29

*Figure II-5. Shifts applied during co-registration to Landsat reference (in rounded meters), X: east-west; Y: north-south. (**a**) The scatterplot of the shifts contains all individual datasets; (**b**) The sensor-specific statistics of applied shifts.*

In this study, 42 datasets of ASTER and SPOT have been co-registered to the Landsat reference using Mode 1 of the developed approach. It was possible to co-register all datasets in the standard way, whereas the applied global shifts range between −62 m and +126 m in the east-west direction (X) and between −434 m and +29 m in the north-south direction (Y) (Figure 5). The largest shifts have been obtained for the SPOT 1 images, reflecting the limited accuracy of the standard orthorectification process (Section 2.2). For visualization purposes, these maximum shifts have not

been included in Figure 5a, showing all other individual shifts applied to the ASTER and SPOT 5 images.

From the depicted data points, it can be seen that only westward shifts have been applied. Thus, all of the images were originally located east of the Landsat reference with maximum offsets of 48 m for SPOT 5 and 62 m for ASTER datasets (Figure 5b). Furthermore, the analysis of the applied shifts allows for assessing the sensor-internal spatial fit before co-registration. The range of the applied shifts represents the largest spatial difference before co-registration and amounts to approximately three pixels of the original resolution (SPOT 5 (10 m resolution): X: 35 m, Y: 29 m; ASTER (15 m resolution): X: 54 m, Y: 39 m). The standard deviation of the applied shifts for co-registering the images to the Landsat reference can be interpreted as the standard deviation between the orthorectified data products of each sensor before co-registration. It amounts to approximately one original pixel (SPOT 5: X: 13 m, Y: 9 m; ASTER: X: 17 m, Y: 9 m). These results show that for both sensors, the original sensor-internal spatial fit is better in the Y direction than in the X direction.

4.3 RapidEye Datasets

Co-registration of the RapidEye datasets has been performed by applying Mode 2 of the developed approach (Section 3.3). In the first step, sensor-internal co-registration has been carried out. For this purpose, for each of the 21 tiles, one RapidEye dataset was selected as the spatial reference. All of these reference datasets were acquired in May 2011. In the second step, each of the 21 sensor-internal co-registered data stacks were co-registered en bloc to the Landsat reference.

Figure 6 depicts the obtained sensor-internal shifts for all of the 482 co-registered images related to their respective acquisition years (Figure 6a–d), whereas (X) represents shifts in the east-west and (Y) in north-south direction. Part e of Figure 6 summarizes the statistics for all of the applied shifts. Since the original orthorectified RapidEye standard data products are located in a fixed pixel reference grid, only integer pixel shifts have been applied in order to fit the warp image to the sensor-internal RapidEye reference image. The number of datasets with the same applied shift is coded by color and the size of the circle symbols.

Figure 6 shows that the sensor-internal spatial fit between the orthorectified data products was less accurate in 2009 at the beginning of the operational RapidEye mission than in the following years. Maximum shift values amount up to 65 m (13 RapidEye pixels), and large ranges are observed in the X (40 m) and Y (75 m) directions with a strong systematic component in the Y direction. For the datasets acquired in 2010, these ranges are significantly smaller (X: 25 m, Y: 30 m) and less systematic. For most of the datasets acquired during the years of 2011 and 2012 (80% and 66%, respectively), no shift or a maximum shift of one pixel (5 m) has been applied, indicating a greatly improved sensor-internal spatial fit for these years, whereas in Figure 6c and d, hardly any systematic component can be observed. In the diagrams of Figure 6, all datasets with maximum shifts of one pixel are depicted within the black rectangles centered at the origin of the diagrams. Moreover, for the years 2011 and 2012, low standard deviation values of approximately 5 m confirm the high geometric stability of the standard orthorectified data products. Figure 6e also shows that during the whole acquisition period, the spatial fit in the X direction has been more accurate than in the Y direction, which is the opposite of the results obtained for the datasets acquired by the ASTER and SPOT sensors.

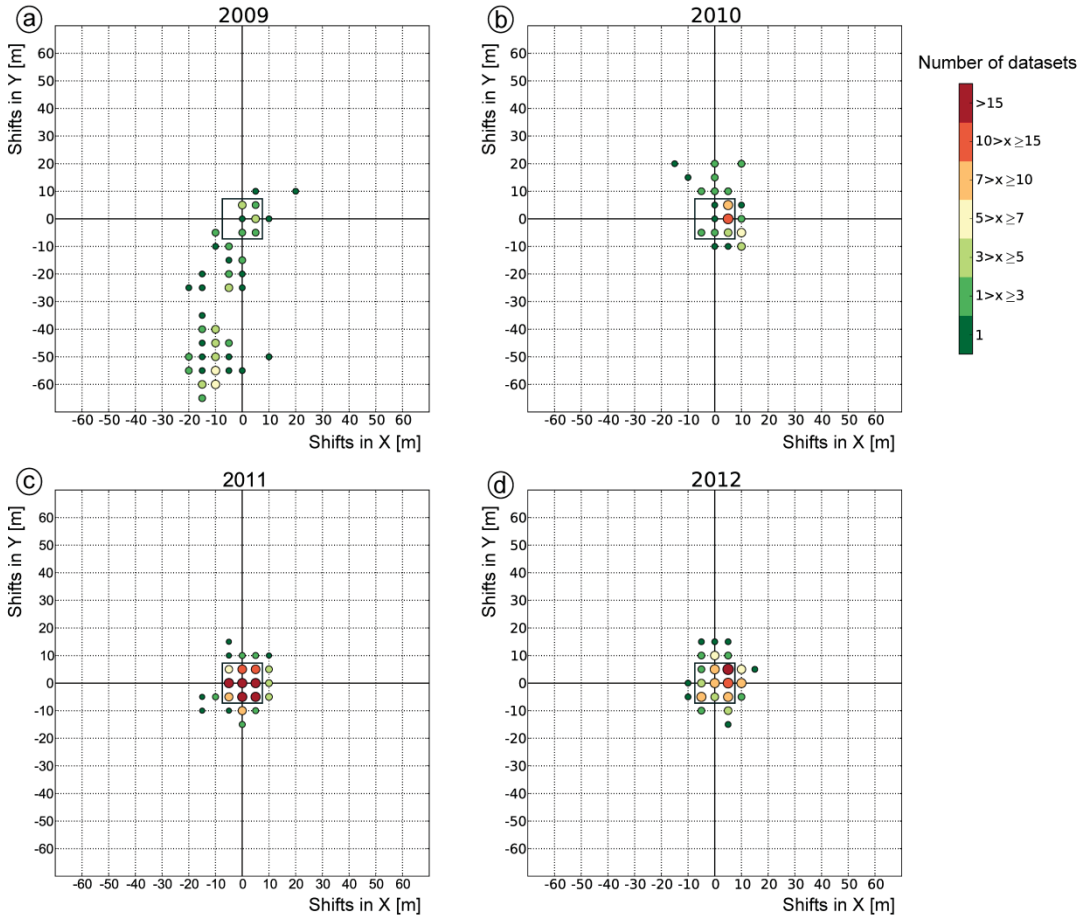

e

	2009		2010		2011		2012		All	
Number of images	90		62		209		121		482	
Applied shifts [m]:	X	Y	X	Y	X	Y	X	Y	X	Y
Mean	-6,7	-32,4	4,2	1,9	1,3	-1,3	2,8	1,2	0,5	-5,8
Stdev	7,9	23,2	5,3	8,6	4,6	5,1	5,1	5,7	6,5	16,7
Min	-20	-65	-15	-10	-15	-15	-10	-15	-20	-65
Max	20	10	10	20	10	15	15	15	20	20
Median	-10	-40	5	0	0	0	5	0	0	0
Shifts of 1 pixel or less [%]	19		48		80		66		61	

*Figure II-6. Applied shifts for sensor-internal co-registration of RapidEye. (**a**–**d**) The obtained shifts are related to the acquisition year. The number of images with the same shift is indicated by the color and size of the circle symbols. All symbols falling within the black rectangles represent datasets shifted by one pixel or less. (**e**) The table of statistics.*

Figure 7a summarizes the shifts that have been applied to the 21 sensor-internally co-registered data stacks during the second step; en bloc co-registration to the Landsat reference. In Figure 7b, these shifts are depicted as scaled arrows for each of the 21 tiles. For six data stacks comprising 154 images, the applied shifts amount to 10 m in the western direction and 15 m in the northern direction. The mean shift for all data stacks amounts to 9 m in the western direction and 20 m in the northern direction. Figure 7b shows that all of the applied shifts have a northwestern orientation, indicating that the selected RapidEye reference datasets used for sensor-internal co-registration in Step 1 are systematically offset from the Landsat reference. However, all of the applied shifts are smaller than the spatial resolution of the Landsat reference, and most of the tiles are characterized by rather similar shifts, reflecting the high geometric stability of the selected RapidEye sensor-internal reference datasets throughout the whole study area.

ⓐ

Tiles	Images	X [m]	Y [m]	Color
6	154	-10	15	
4	82	-10	20	
3	77	-5	20	
3	65	-15	25	
2	55	-10	25	
2	39	-5	25	
1	31	-5	15	
21	503			
Range of shifts		10	10	
Mean shift		-9	20	

ⓑ

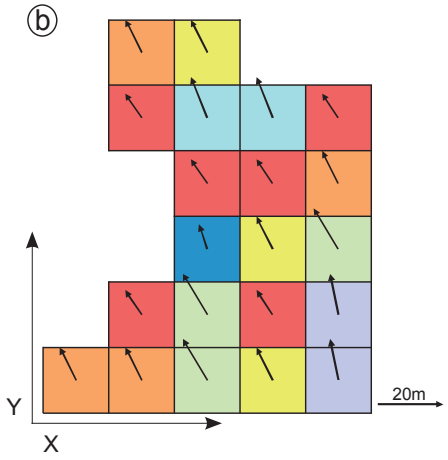

*Figure II-7. En bloc shifts applied to RapidEye data stacks represented by Level-3A tiles: (**a**) The number of data stacks (tiles) and related images with that particular shift; (**b**) The direction and amount of shift for each data stack depicted by scaled arrows (tile size: 25 × 25 km²).*

5 Accuracy Assessment

5.1 Relative Image-to-Image Accuracy of the Database

The relative accuracy of the co-registered database is assessed at 86 time invariant check points (CPs) representing the location of the Landsat reference (Figure 1, Section 2.3.2). By using at least 6 CPs per image, the mean spatial offsets (Δx_{IM}, Δy_{IM}), the position error (PE_{IM}) and the root-mean-square error ($RMSE_{IM}$) is determined before and after co-registration. The position error amounts to the mean of the Euclidean distances between the image and the Landsat reference at the locations of the digitized CPs (Equation 3). The $RMSE_{IM}$ is represented by the square root of the mean of the squares of the position errors at each CP (Equation 4).

$$\Delta x_{\mathrm{IM}} = \frac{\sum \Delta x_{CP}}{\mathrm{n}} \qquad ;\Delta x_{CP} = x_{\mathrm{CP,warp}} - x_{\mathrm{CP,ref}} \tag{1}$$

$$\Delta y_{\mathrm{IM}} = \frac{\sum \Delta y_{CP}}{\mathrm{n}} \qquad ;\Delta y_{CP} = y_{\mathrm{CP,warp}} - y_{\mathrm{CP,ref}} \tag{2}$$

$$PE_{\mathrm{IM}} = \frac{\sum PE_{CP}}{\mathrm{n}} \qquad ;\mathrm{PE}_{CP} = \sqrt{\Delta x_{CP}{}^2 + \Delta y_{CP}{}^2} \tag{3}$$

$$\mathrm{R}MSE_{\mathrm{IM}} = \sqrt{\frac{\sum \left(PE_{CP}{}^2\right)}{\mathrm{n}}} \tag{4}$$

For evaluating the relative accuracy of the whole database, a representative subset of images has been selected. It comprises images of all sensors, which are characterized by varying offsets and are located in different parts of the study area. In total, three SPOT 5 images, three ASTER images and two SPOT 1 images have been selected. In the case of RapidEye, the representative datasets comprise 12 images, four images per data stack, for three out of the 21 RapidEye tiles.

The data points depicted in Figure 8 represent the mean spatial offsets of the selected images to the Landsat reference in the X and Y direction (Δx_{IM}, Δy_{IM}) before co-registration (Figure 8a) and after co-registration (Figure 8b). For visualization purposes, the datasets of SPOT 1 have not been included in Figure 8a, because of their large offsets of more than 400 m (Section 4.2). Statistics of the analyzed distance parameters (Δx_{IM}, Δy_{IM}, PE_{IM}, $RMSE_{IM}$) are shown in the table below (Figure 8c). Before co-registration (Figure 8a), the analyzed datasets are characterized by significantly larger offsets compared to the ones that have remained after co-registration (Figure 8b). After co-registration, all datasets are located closely to the Landsat reference, resulting in a mean PE_{IM} of 16 m, a mean $RMSE_{IM}$ of 17 m and absolute maximum offsets of approximately 20 m in the X and Y directions (Δx_{IM}: −21 m, Δy_{IM}: 19 m).

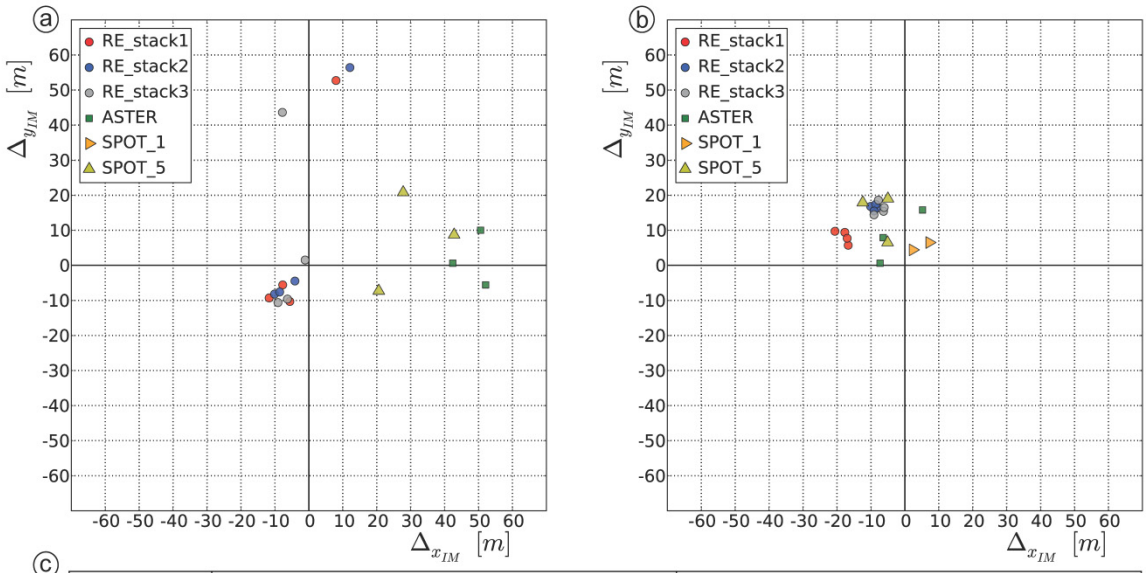

c

Errors [m]	Before coregistration				After coregistration			
	Δx_{IM}	Δy_{IM}	PE_{IM}	$RMSE_{IM}$	Δx_{IM}	Δy_{IM}	PE_{IM}	$RMSE_{IM}$
Mean	6	50	72	74	-8	12	16	17
Stdev	25	135	131	134	8	5	5	5
Max	52	440	441	441	7	19	23	23
Min	-36	-11	2	3	-21	1	7	9

*Figure II-8. Relative accuracy: the relative location of datasets to the Landsat reference (represented as the point of origin) (**a**) before co-registration and (**b**) after co-registration; (**c**) statistics of the offsets (in meters).*

All of these values are smaller than the spatial resolution of the used Landsat reference (30 m), indicating an overall sub-pixel accuracy. The achieved significant improvement in relative accuracy for the whole database is also revealed by comparing the after co-registration mean offset values with the ones obtained before co-registration (mean PE_{IM}: 72 m; mean $RMSE_{IM}$: 74 m; maximum offsets: Δx_{IM}: 52 m, Δy_{IM}: 440 m). Moreover, the offsets remaining after co-registration include a slight systematic error (mean values of Δx_{IM}: −8 m, Δy_{IM}: 12 m), which is also deducible from the scatterplot in Figure 8b. However, this distribution also shows high sensor-internal geometric stability as a result of co-registration, especially for the SPOT 5 and RapidEye datasets.

In order to evaluate the relative accuracy, which has been achieved by applying Mode 2, the results obtained for the RapidEye images have been analyzed in more detail. In Figure 8a, each data stack contains four images of different acquisition dates, including one image of early data acquisitions (2009) with offsets of up to 60 m in the Y direction. All other images are characterized by relatively

small before co-registration offsets in comparison with the SPOT 5 and ASTER datasets depicted in Figure 8a. After co-registration, the images belonging to the same data stack form clusters with internal offsets of approximately 5 m or less (Figure 8b), representing sub-pixel relative image-to-image registration accuracy, which has been achieved within the same data stack during the first step of co-registration. However, the cluster formed by images of Stack 1 differs in its offset from the offsets of the clusters representing Stacks 2 and 3, which are very similar to each other (Figure 8b). These results show the possibility for slight differences in relative accuracy between data stacks originating from the second step—en bloc co-registration. These differences could be related to the position of the data stack in the study area, which might lead to different land cover conditions influencing co-registration.

5.2 Absolute Accuracy of the Database

The absolute geolocation accuracy achievable by the developed approach is primarily determined by the absolute geolocation accuracy of the Landsat Level 1T reference, amounting to 15 m (RMSE) for Landsat Level 1T products located in areas of flat terrain with optimal ground-truth availability for the standard orthorectification process (Storey et al. 2008). For independent assessment of the absolute accuracy of the co-registered database, high accuracy differential GPS (DGPS) points have been used (Section 2.3.3). In 19 co-registered images acquired by the high spatial resolution RapidEye and SPOT 5 sensors, the offsets between DGPS points and their corresponding locations in the co-registered images have been manually determined.

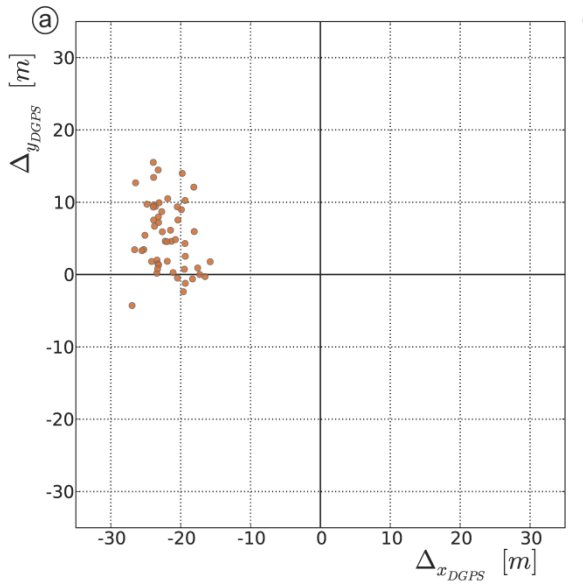

b

52 DGPS measurements			RMSE: 23 m
Errors [m]	Δx_{DGPS}	Δy_{DGPS}	PE_{DGPS}
Mean	-22	5	23
Stdev	3	5	3
Min	-27	-4	16
Max	-16	16	29
Max-Mean	6	10	
Min-Mean	-5	-10	

Figure II-9. Absolute accuracy: the location of the co-registered datasets in relation to the DGPS points (represented as the point of origin).

The results of 52 measurements are depicted in Figure 9a, whereas the point of origin represents the location of the DGPS point reference. Statistical analysis of the obtained offsets is shown in Figure 9b. The obtained RMSE of 23 m and the maximum absolute offsets (Δx_{DGPS}: 27 m, Δy_{DGPS}: 16 m, PE_{DGPS}: 29 m) reveal overall absolute accuracy in the sub-pixel range compared to the spatial resolution of the Landsat reference (30 m). The low standard deviations of 3 m (X) and 5 m (Y) reflect the high absolute geometric stability of the whole database. Furthermore, the results shown in Figure 9 depict a systematic error of 22 m in the western and 5 m in the northern direction, which implies that the Landsat reference is systematically offset in relation to the measured DGPS

points. Due to the high relative accuracy between the Landsat datasets (Section 4.1), this systematic error is assumed to be constant for the whole study area. Therefore, it can be corrected by applying a spatial shift to the whole database resulting from the inversion of the identified average offsets; in this case, 22 m towards the east and 5 m towards the south. As a result, maximum absolute offsets are reduced to approximately 6 m in the X and 10 m in the Y direction (Figure 9b), representing the remaining uncertainty resulting from the relative differences between the datasets.

5.3 Influence of Co-Registration on Spatial Delineation of Landslides

Reliable multi-temporal landslide delineation depends on the quality of the relative spatial fit between the datasets contained in the multi-temporal and multi-sensor database. In order to quantify the influence of the spatial fit on the delineation of landslides, multi-temporal digitization has been performed for three exemplary stationary landslides based on the available datasets before and after co-registration (Section 2.3.4). Figure 10 comprises the analysis of the spatial overlay of the multi-temporal digitized landslides in the form of the number of spatial overlaps between the digitized polygons. Figure 10b,c show the number of these overlaps by a color-coding scheme, where red depicts the area of overlap between all of the digitized landslide polygons and blue the area that is covered by only one of the digitized landslide polygons.

Moreover, a comparison between the spatial extents of the area of overlap between all landslide polygons (area intersect (AI)) and the whole area that is covered by all of the landslide polygons (area union (AU)) has been performed. The results are shown in Figure 10e and f and are quantified in the accompanying table. The AI area depicted in dark grey (10e,f) and red (10b,c) represents the area that is delineated as landslide in all of the multi-temporal datasets. For a stationary landslide, the ideal case of multi-temporal landslide delineation results in a seamless object, indicating spatial identity between AI and AU. A bigger spatial shift between the image data results in a larger AU, shown in light grey and blue colors.

Such an improved spatial fit can be observed for all three landslides depicted in Figure 10, implying that these findings are valid for the whole database. The significance of the achieved improvements mainly depends on the size of the landslide in relation to the offsets occurring between the multi-temporal datasets, whereas the bigger the size of a landslide, the lesser the influence of the spatial offset. In the case of Landslide B, with a length of 1.5 km and an area of approximately 250000 m^2, the offsets of the original datasets result in an AI that is considerably higher (69%) than for Landslide A (19%) and Landslide C (26%). Therefore, in the case of Landslide B, the relative improvement after co-registration only amounts to 26% and is significantly smaller compared to improvements of 65% and 62% for Landslides A and C, respectively.

Furthermore, the uncertainty in landslide delineation resulting from the quality of the spatial fit between datasets can be quantified by the maximum distance of AU (dashed line) to the original polygon shown in Figure 10c. This distance (Max_dist) represents the size of a landslide failure or the enlargement of a landslide that can reliably be detected within the multi-temporal database. In the case of the three analyzed landslides, the uncertainty remaining after co-registration ranges between 6 m and 9 m, representing a significant improvement compared to the uncertainty contained in the original database comprising values between 43 m and 59 m. The remaining uncertainty reflects the relative accuracy of co-registration, which has been achieved for the datasets used for multi-temporal landslide delineation.

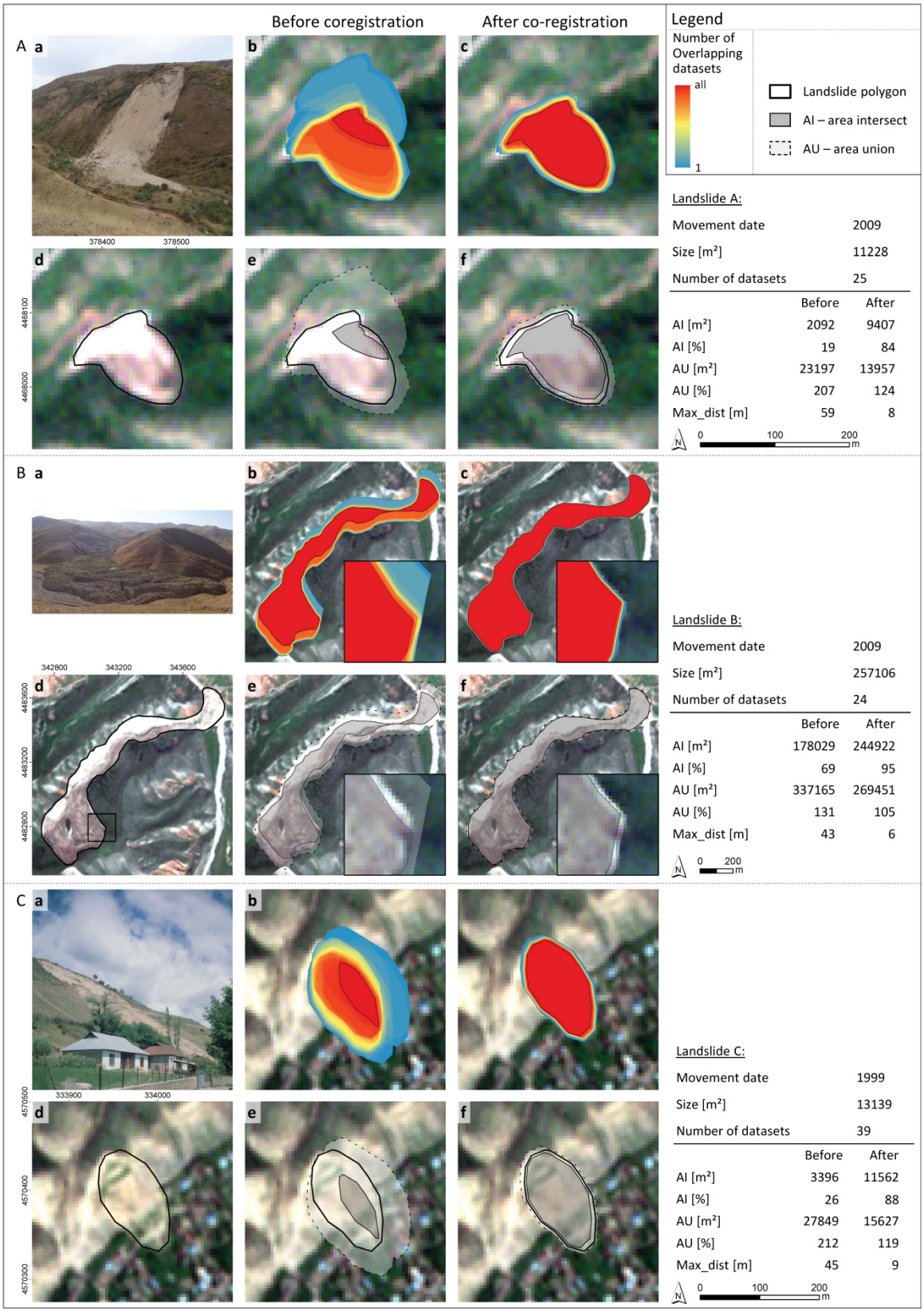

Figure II-10. Influence of co-registration on multi-temporal landslide delineation for three stationary landslides before and after co-registration. (a) Field photo; (d) Digitized landslide; (b,c) The number of overlapping datasets; (e,f) Overlapping area of all datasets (area intersect (AI)); area covered by all landslide polygons (area union (AU)). Image: RapidEye 2 May 2011.

6 Discussion

6.1 Applicability of Approach

Validation as part of the co-registration approach has revealed that the developed procedure of image-to-image co-registration using image-specific global shifts in the X and Y directions could be applied to all of the 592 datasets contained in the database, showing the high internal geometric stability of the orthorectified standard data products. The application of the global shift method results in the preservation of the original spectral properties of the standard data products, since there is no need for performing another resampling step.

Automated spatial alignment has mostly resulted in shifts of several tens of meters, whereas maximum offsets have been obtained in the case of SPOT 1, amounting to more than 400 m. These results show that the developed approach is capable of handling a wide range of offsets occurring in images of various spatial resolutions ranging between 5 m for RapidEye and 30 m for Landsat data. The successful application of the approach to all datasets also proves its robustness against the variability of image data caused by different multi-sensor and multi-temporal effects, which have the potential for impeding the applicability of co-registration, as well as reducing the achievable accuracy (Le Moigne et al. 2011b; Gao et al. 2009; Gianinetto 2012).

Sensor-specific analysis of the applied shifts (Section 4) allows for evaluating the sensor-internal spatial fit between standard data products generated by external providers. In the case of Landsat data, no integer pixel shifts have been applied (Section 4.1), confirming the sub-pixel image-to-image accuracy stated in the literature (Kennedy et al. 2010; Lee et al. 2004; Storey et al. 2008). For ASTER and SPOT 5 data, the standard deviations of the applied shifts are less than the respective pixel sizes, and the largest spatial offsets amount to approximately three pixels of the original resolutions (Section 4.2). Sensor-internal RapidEye co-registration (Figure 6) has revealed a steadily improving spatial fit between the datasets since the start of operational data acquisition in 2009, cumulating in offsets of one pixel or less for most of the images acquired in 2011 and 2012. These results are in accordance with the findings of a study assessing the geometric accuracy of the RapidEye constellation (Chander et al. 2013).

6.2 Accuracy Assessment

Assessment of the relative image-to-image co-registration accuracy based on time-invariant check points (CPs) has resulted in an overall accuracy of 17 m (RMSE) and the maximum remaining offsets to the Landsat reference amounting to 20 m (Section 5.1). Taking into account the 30-m resolution of the Landsat reference, these results indicate the sub-pixel relative accuracy of the whole multi-sensor database. Sensor-specific analysis of the achieved relative accuracy shows high sensor-internal spatial fit for the SPOT 5 and RapidEye datasets, which exceeds the accuracy obtained in relation to the Landsat reference. In the case of RapidEye, the results show that implementation of Mode 2 allows for generating (Step 1) and maintaining (Step 2) high image-to-image accuracies within sensor-internal data stacks during multi-sensor co-registration.

Moreover, it is noticeable that after co-registration, the majority of images still show a small northwestern shift in regard to the Landsat reference (Figure 8b), implying a systematic offset, which is of a significantly lesser amount than one Landsat pixel (mean values of Δx_{IM}: –8 m, Δy_{IM}: 12 m). Such a bias could not be observed for the co-registration of the Landsat time series (Section 4.1) and also not for sensor-internal RapidEye co-registration using Step 1 of Mode 2

(Figure 6). Therefore, it is assumed that this small bias is caused by a systematic offset between the Landsat reference and the CPs digitized in panchromatic SPOT 5 datasets, which have been manually co-registered to the Landsat reference (Section 2.3.2). In this case, the detected bias most likely originates from the manual co-registration step and, thus, is not a result of the co-registration approach itself. Direct determination of this offset has not been possible, because of the big difference in spatial resolution between the Landsat reference (30 m) and the panchromatic SPOT 5 datasets (2.5 m and 5 m).

Overall, the achieved relative image-to-image accuracies are comparable or, in parts, even better than the accuracies obtained by other studies dealing with the co-registration of optical time series data. The approach proposed by Gianinetto for automatic co-registration of Level 1A ASTER time series data (Gianinetto 2012) has resulted in RMSE values of less than two pixels. Liu and Chen (Liu & Chen 2009) have co-registered multi-temporal Formosat-2 Level 1A images (8-m resolution), achieving a RMSE of approximately 1.5 pixels in flat terrain and 2.2 pixels in mountainous areas. Barazetti et al. (Barazzetti et al. 2014) automatically co-registered 13 Landsat TM datasets acquired over a 30-year period mainly by correcting sub-pixel translation errors, resulting in a relative accuracy of sub-pixel RMSE values. Although, accuracy requirements for co-registration depend on the targets and methods used for change detection (Bruzzone et al. 2007; Sundaresan et al. 2007), in general, accuracies (RMSE) of less than one pixel are considered suitable for subsequent change detection (Jianya et al. 2008).

The absolute accuracy of the whole co-registered database, which has been assessed based on DGPS point measurements (Section 2.3.3), amounts to an RMSE of 23 m and a maximum position error of 29 m, whereas a clear systematic error of 22 m in the western and 5 m in the northern direction could be observed. These results indicate that the Landsat reference is systematically offset to the high accuracy DGPS points. This assumption is further supported by the low standard deviation of the derived absolute offsets (X: 3 m, Y: 5 m), implying a high relative accuracy between images, which is of primary importance for subsequent multi-temporal landslide detection.

Due to the availability of the field measured DGPS points and the high geometric stability of the multi-temporal Landsat reference, it is possible to correct for this systematic offset by applying a constant spatial shift. This procedure has resulted in remaining maximum absolute errors of approximately 6 m in the X and 10 m in the Y direction (Section 5.2). However, even the uncorrected absolute offsets are considered to be negligibly small, taking into account the near global availability of the Landsat reference, allowing for the world-wide application of the developed approach without requiring any ground control information. This is especially the case for large area analysis, such as landslide detection at a regional scale.

6.3 Accuracy of Multi-Temporal Landslide Delineation

Multi-temporal digitization of three stationary landslides within all datasets covering the landslides before and after co-registration (Section 5.3) has revealed a significant improvement in the relative spatial fit of landslide delineation, reducing the maximum offset from 59 m before co-registration to 9 m after co-registration (Figure 10). These relative accuracies correspond to the maximum absolute offsets, which can be derived for the whole database after correcting for the systematic error introduced by the Landsat reference. These findings indicate that the relative accuracy improvements, which can be observed for all three landslides after co-registration are valid for the whole study area. The remaining relative uncertainty of about 10 m forms a suitable basis

for reliable multi-temporal landslide detection, as well as the identification of changes within already existing landslides.

Besides the discussed relative accuracy of landslide delineation, sufficient absolute accuracy is also important for the integration of information derived from remote sensing analysis into a GIS environment for further landslide hazard and risk analysis. Comparing the achieved absolute accuracy of 23 m (RMSE) with the United States National Map Accuracy Standards (USGS 1947) has shown that the approach meets the requirements for a mapping scale of 1:50000 and smaller, which is suitable for landslide analysis at a regional scale.

6.4 Methodological Aspects

It could be shown that the developed co-registration approach is suitable for the efficient spatial alignment of a large database containing numerous multi-temporal and multi-sensor standard data products. Incorporation of three seasonally differing Landsat reference datasets has allowed for successful matching of images characterized by high multi-temporal variability. The implementation of a special resampling procedure (Mueller & Segl 1999) transforming the spatial resolution of the warp image to the one of the Landsat reference enables the application of area-based cross-correlation to images of varying spatial resolution acquired by different optical sensors.

The methodological constraints of the developed co-registration approach are related to the applied area-based cross-correlation, which is restricted to matching images of only slight affine distortions (Zitova & Flusser 2003), as well as by the implemented geometric transformation only supporting co-registration based on image-specific two-dimensional shifts. These constraints are attributed to the goal of developing a robust and efficient co-registration approach that can be applied in a fully automatic way to a large number of higher level standard data products, which, in general, are characterized by high internal geometric stability. This assumption could be confirmed for all of the 592 analyzed datasets by an initial validation procedure as part of the co-registration approach. The automatically detected tie points forming the basis for calculating the two-dimensional shifts could also be used in the frame of higher-degree transformation methods, which would allow for correcting more complex local distortions. However, it also needs to be taken into account that higher-degree transformations tend to produce local errors, depending on the spatial distribution and the number of tie points, which has to be larger in order to solve these transformation functions. Furthermore, the use of the two-dimensional shift transformation is more robust against localization errors related to the detected tie points.

In order to preserve the spectral information of the original image datasets for subsequent spectral image analysis, the co-registration approach aligns the original images to the Landsat pixel grid without any further resampling. Thus, the achievable accuracy of the approach is determined by the spatial resolution of the original warp image, allowing for sub-pixel accuracy related to the spatial resolution of the Landsat reference (e.g. 0.16 pixels for 5-m RapidEye data). The implementation of sub-pixel image matching techniques would result in the need for resampling the spectral information of the original warp images and lead to much longer processing times, which would impede the efficient usability of the approach for larger amounts of data.

Compared to other approaches, such as AROP (Gao et al. 2009), TARA (Le Moigne et al. 2011a) and COSI-CORR (Leprince et al. 2007) aiming at the precise correction of complex geometric distortions, the developed co-registration approach represents a less sophisticated, yet robust and

efficient, methodology, which can be applied in a fully automated way to large amounts of multi-sensor time series data, resulting in high relative and absolute accuracy.

7 Conclusions and Outlook

In this study, a new methodology for fully automated co-registration of optical satellite remote sensing data has been developed, allowing for the efficient and robust spatial alignment of big amounts of orthorectified standard data products acquired during the last 26 years for Southern Kyrgyzstan. The co-registration approach is capable of accommodating high image data variability resulting from varying spatial resolutions, as well as seasonal and inter-annual land cover variability. Applying co-registration to the whole database of 592 datasets from five different sensors has resulted in image-specific shifts ranging between 5 m and more than 400 m, showing the robustness of the approach and its suitability for the evaluation of relative spatial fit between standard data products. Moreover, spatial alignment is performed without any further resampling of the initial datasets, maintaining their original spectral information, which is advantageous for subsequent automated image analysis.

Due to the use of freely and globally available Landsat Level 1T data as the spatial reference, the developed methodology is independent of local geometric reference information and can be used in any part of the world covered by suitable Landsat Level 1T data. In this context, the launch of the Landsat-8 Operational Land Imager (OLI) on 11 February 2013, as well as the future Sentinel-2 mission (Drusch et al. 2012) will ensure its future applicability. The overall relative accuracy of 17 m, as well as the absolute accuracy of 23 m (RMSE) represent sub-pixel accuracy in regard to the 30-m resolution of the Landsat reference. These achieved accuracies make the co-registered database suitable for subsequent multi-temporal change detection and for combination with other spatial data within a GIS environment.

The analysis of co-registration accuracy in relation to multi-temporal landslide delineation has revealed maximum relative spatial offsets of six to 9 m between the otherwise unchanged landslides within the multi-temporal database. These offsets correspond to the minimal size of detectable landslide-related changes. However, since this size is also determined by the coarsest resolution of the used datasets, amounting to 30 m, only changes with an extent of more than 900 m^2 can reliably be detected. This is more than sufficient for a region dominated by medium-sized to large failures, such as Southern Kyrgyzstan. Achievable relative image-to-image accuracies of the developed co-registration approach could be further improved by using only higher resolution data (e.g. SPOT 5: 10 m and RapidEye: 5 m). Hence, it would be possible to reliably analyze even smaller changes mostly related to the reactivation of already existing landslides.

Altogether, these findings show that the developed methodology is suitable for robust and efficient co-registration of multi-sensor standard orthorectified data products acquired during longer periods of time. The resulting co-registered datasets of high and medium spatial resolution allow for automated landslide detection at a regional scale. Thus, they have the potential for being used for long-term spatiotemporal analysis, as well as for the monitoring of ongoing landslide activity, both contributing to more complete landslide inventories. However, the developed approach cannot only be used for database generation for landslide detection, but also for spatial alignment of any suitable satellite remote sensing time series data in order to perform subsequent analysis of long-

term land cover changes in many parts of the world. This way, the developed co-registration methodology supports remote sensing-based analysis of Earth surface processes, which is important for many applied tasks, such as hazard assessment, environmental monitoring and land-use management.

Acknowledgments

The authors gratefully acknowledge the many helpful comments and suggestions from several anonymous reviewers that substantially contributed to clarifying and improving the manuscript. The authors also thank the German Aerospace Agency (DLR) for providing RapidEye data by the RESA (RapidEye Science Archive) program. This work was funded by the German Federal Ministry of Research and Technology (BMBF) within the framework of PROGRESS (Potsdam Research Cluster for Georisk Analysis, Environmental Change and Sustainability).

Author Contributions

Robert Behling and Sigrid Roessner developed the overall approach. Karl Segl and Robert Behling contributed to the methodological development and programming. Robert Behling conducted the image processing and analysis. Robert Behling and Sigrid Roessner prepared the manuscript. Birgit Kleinschmit and Hermann Kaufmann contributed to the discussion and general paper review.

Conflicts of Interest

The authors declare no conflict of interest.

III Monitoring Recent Landslide Activity (RapidEye)

Behling, R., Roessner, S., Kaufmann, H. & Kleinschmit, B., (2014). Automated Spatiotemporal Landslide Mapping over Large Areas Using RapidEye Time Series Data. *Remote Sens.*, 6(9), pp.8026–8055.

© 2014 by the authors; licensee MDPI, Basel, Switzerland. This article is an open access article distributed under the terms and conditions of the Creative Commons Attribution license (http://creativecommons.org/licenses/by/3.0/).

Received: 28 May 2014; in revised form: 31 July 2014 / Accepted: 11 August 2014 /
Published: 27 August 2014 (doi:10.3390/rs6098026)

Abstract

In the past, different approaches for automated landslide identification based on multispectral satellite remote sensing were developed to focus on the analysis of the spatial distribution of landslide occurrences related to distinct triggering events. However, many regions, including southern Kyrgyzstan, experience ongoing process activity requiring continual multi-temporal analysis. For this purpose, an automated object-oriented landslide mapping approach has been developed based on RapidEye time series data complemented by relief information. The approach builds on analyzing temporal NDVI-trajectories for the separation between landslide-related surface changes and other land cover changes. To accommodate the variety of landslide phenomena occurring in the 7500 km^2 study area, a combination of pixel-based multiple thresholds and object-oriented analysis has been implemented including the discrimination of uncertainty-related landslide likelihood classes. Applying the approach to the whole study area for the time period between 2009 and 2013 has resulted in the multi-temporal identification of 471 landslide objects. A quantitative accuracy assessment for two independent validation sites has revealed overall high mapping accuracy (*Quality Percentage*: 80%), proving the suitability of the developed approach for efficient spatiotemporal landslide mapping over large areas, representing an important prerequisite for objective landslide hazard and risk assessment at the regional scale.

1 Introduction

Landslides are a major natural hazard causing serious damage to buildings and technical infrastructure, as well as severe loss of life in many mountainous regions worldwide (Kjekstad & Highland 2009; Nadim et al. 2006; Petley 2012). Against this background, landslide hazard and risk assessment is of great importance requiring the assessment of past process activity in the form of landslide inventories containing spatiotemporal information about occurrence and characteristics of landslides (Cascini 2008; Guzzetti et al. 2012; Nefeslioglu et al. 2011; Pradhan & Lee 2010a; van Westen et al. 2008). Since such inventories have to be as complete and precise as possible in time and space, multi-temporal inventories are needed, especially in regions of frequently occurring landslides (Guzzetti et al. 2012). The generation of these multi-temporal inventories requires efficient methods for landslide mapping which allow analyzing large areas with high temporal resolution over long periods of time. Traditional mapping methods, such as field surveys supported by visual interpretation of remote sensing data (Casson et al. 2003; Guzzetti et al. 2000), are time consuming and resource intensive. As a result, for many regions of the world, comprehensive landslide inventories are missing or the existing ones are limited in their spatial extent and temporal resolution (Fiorucci et al. 2011; Guzzetti et al. 2012; Saba et al. 2010). In this context, the use of multi-temporal satellite remote sensing data opens up the opportunity for the development of efficient methods for systematic spatiotemporal mapping of landslides over large areas. For the purpose of post-failure mapping, mainly optical remote sensing data have been used, as most of the landslide processes lead to disturbance of the Earth's surface resulting in significant changes in the reflectance characteristics of these surfaces(Guzzetti et al. 2012; Metternicht et al. 2005; Roessner et al. 2005).

Southern Kyrgyzstan represents such a region of high landslide activity where large events frequently cause damage to human settlements and infrastructure and also lead to loss of human lives. Past landslide investigations in this area have resulted in a comprehensive principle process understanding, thereby revealing that most of the landslides are caused by complex interactions between tectonic, geological, geomorphological and hydro-meteorological factors(Roessner et al. 2005), whereas the highest process activity can be observed in spring with large variations between the years. Most of these landslides cannot be related to major triggering events, such as intense rainstorms or strong earthquakes. Thus, an improvement of the spatiotemporal understanding of landslide processes in this region requires a systematic assessment of landslide events in the form of multi-temporal landslide inventories forming the basis for objective and spatially differentiated analyses of landslide hazard and risk (Fiorucci et al. 2011; Klimeš 2013; Rossi et al. 2010; Weng et al. 2011; Wu & Chen 2013).

In this context, the goal of this study has been the development of an automated approach for landslide mapping over large areas based on optical satellite remote sensing data which allows the establishment of multi-temporal landslide inventories, including the possibility for regular updates. This goal requires the availability of optical remote sensing data with high temporal and spatial resolution for the whole area of interest (Figure 1). Moreover, the approach needs to enable object-oriented and efficient automated mapping of landslide events using the available time series database. This includes the identification of landslides of different types and spatial extents occurring in varying land cover surroundings, lithological conditions and relief positions that are frequently changing throughout a large mountainous region. Furthermore, the generation of multi-temporal landslide inventories requires mapping results in an object-based form for subsequent GIS-based derivation of landslide characteristics.

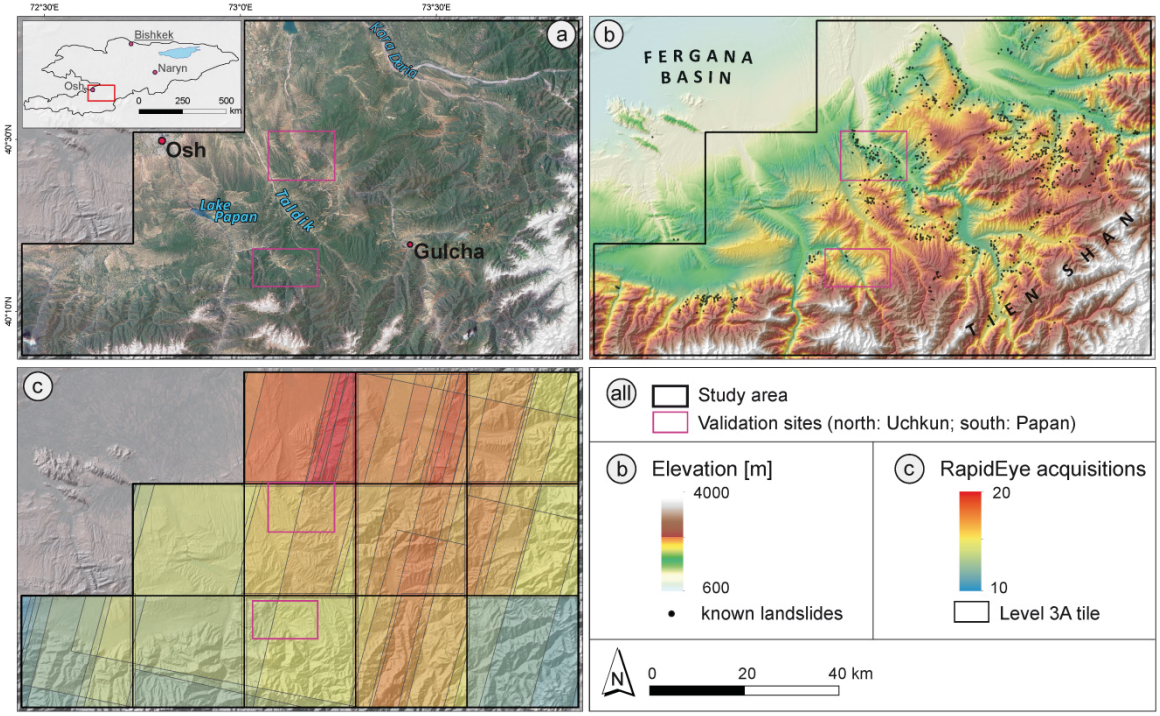

*Figure III-1. Overview of study area. (**a**) Extent of study area represented by true color RapidEye mosaic acquired in June 2013; (**b**) Topographic relief overlaid by previously known Landslide events; (**c**) RapidEye spatiotemporal data coverage between 2009 and 2013.*

Most of the existing automated methods using optical remote sensing data have been developed for one-time landslide mapping after a single major triggering event. These methods are based on either a single post-event classification (e.g. Aksoy & Ercanoglu 2012; Barlow et al. 2006; Borghuis et al. 2007; Mondini et al. 2013; Othman & Gloaguen 2013) or a bi-temporal change detection between an image pair acquired before and after the triggering event (e.g. Cheng et al. 2004; Nichol & Wong 2005; Rosin & Hervas 2005). Single post-event classification approaches assume that all of the mapped landslides have been caused by the analyzed triggering event without further specifying the time period of landslide occurrence. Bi-temporal approaches allow the derivation of the time period of landslide occurrence determined by the acquisition dates of the analyzed image pair. Thus far, only Martha et al. (2012, 2013) have proposed a semi-automated approach for generating a multi-temporal landslide inventory of annual temporal resolution for the time period between 1998 and 2009 for a 81 km^2 region in India. However, this approach had been initially developed for event-based one-time analysis and therefore does not use efficiently the full temporal information content of the available time series data. Furthermore, in most of the published studies, the methods have been applied to rather small test sites of 100 km^2 or less. In only two recent studies (Lacroix et al. 2013; Tsai et al. 2010) have the proposed methods been developed for study areas of more than 1000 km^2. During the last years, an increasing number of studies has proposed methods for object-oriented landslide mapping (e.g. Barlow et al. 2006; Kurtz et al. 2014; Lu et al. 2011; Martha et al. 2010; Park & Chi 2008; Stumpf et al. 2014; Stumpf & Kerle 2011), which is required for landslide inventories and also for the integration of additional contextual information in order to further improve the mapping reliability (Martha et al. 2010). However, there is still a lack of approaches allowing object-oriented landslide analysis over large areas, while making efficient use of time series data for multi-temporal landslide mapping with best possible temporal resolution.

Against this background, the methodological goal of this study is the development of an automated approach for object-oriented landslide mapping of large areas which is suitable for generating multi-temporal landslide inventories, including the possibility for regular monitoring of spatio-temporal landslide activity. For this purpose, a multi-temporal RapidEye (Chander et al. 2013) remote sensing database of 5 m spatial resolution has been established for a 7500 km^2 landslide-affected area in southern Kyrgyzstan for the time period between 2009 and 2013 with up to six multi-temporal acquisitions per year between April and July (Figure 1c). The database contains standard orthorectified Level-3A data products to enable operational applicability of the approach requiring efficient analysis of large amounts of data independent from the availability of ground truth information. The landslide situation in the study area and the spatial database are described in more detail in Section 2, also showing the multi-temporal appearance of different landslide types occurring in the study area. Section 3 describes the developed approach for object-oriented multi-temporal landslide mapping based on temporal NDVI-trajectories covering the whole available time series. Section 4 presents the results obtained by applying this approach to the whole study area. Subsequent systematic accuracy assessment is performed for two independent validation sites that differ in landslide activity and natural conditions (Section 5). In Section 6, the developed approach is discussed in regards to its methodological specifics, achievable accuracy and principle applicability. These are followed by the concluding remarks of Section 7.

2 Study Area and Database

2.1 Study Area and Landslide Situation

In southern Kyrgyzstan, landslides are especially concentrated in the foothills of the high mountain ranges along the eastern rim of the Fergana Basin in an elevation range between 700 and 2000 m (Figure 1b). Most of these landslides occur in form of rotational and translational slides in weakly consolidated Quaternary and Tertiary sediments (Roessner et al. 2005). They represent complex failures and vary greatly in their size, ranging between several hundred and several million square meters, whereas large events of more than one million cubic meters of displaced material have been frequently occurring. Since the beginning of landslide investigations in the 1950s, about 3000 landslides have been reported by local authorities (Ibatulin 2011; Kalmetieva et al. 2009). However, these investigations have been mostly limited to areas in the vicinity of populated places and focused on major events with high destructive potential (Darya Golovko et al. 2014). Thus, the existing spatiotemporal knowledge on landslide events is incomplete and leaves the need for a systematic multi-temporal landslide inventory as a main prerequisite for objective hazard assessment.

The 7500 km^2 study area covered by 12 RapidEye tiles (Figure 1c) is strongly affected by landslides. This region experiences above-average precipitation due to its orographic position west of the topographically rising eastern rim of the Fergana Basin, thus forming a barrier against the prevailing westerlies. The resulting increased precipitation level represents the main factor for the mobilization of landslides in this region. However, this process takes place over longer periods of time and is not related to single triggering events, such as short-term intense rainstorms. The relatively high availability of water leads to a largely developed vegetation cover dominated by grasslands. Therefore, landslide failures cause significant vegetation removal resulting in a distinct contrast between landslides and their surroundings that is easily detectable in optical imagery. Figure 2 illustrates this situation in an exemplary way based on four landslides typical of the whole study area using four multi-temporal RapidEye images contained in the database. All of these landslides occurred in spring 2010 between the depicted RapidEye acquisitions of 26 May 2009 and 2 May 2011. All of them have caused major disturbance of the Earth's surface and large displacement of material consisting of top soil, as well as underlying weakly consolidated sediments. The resulting destruction of the original vegetated surface cover is clearly visible and largely preserved during the whole depicted post-failure time period.

Field work carried out in the entire study area has revealed that the degree of vegetation destruction and the rate of post-failure revegetation are variable and depend on a number of factors, such as initial vegetation cover, degree of soil disturbance, hydrometeorological conditions, lithology, and state of activity of the landslide. Fresh failures (*LS1a*,*b* and *LS2*) are characterized by a high degree of vegetation destruction due to an undisturbed dense initial vegetation coverage shown by the pre-event image of 26 May 2009. Conversely, reactivations (*LS3*) are associated with less vegetation destruction because they are typically characterized by sparse and patchy initial vegetation coverage as a result of a former landslide at this position. For all landslides, the post-failure revegetation is typically very slow, as the landslide masses are susceptible to erosion and reactivation processes. In the case of the depicted deep-seated landslide examples (*LS1a*,*b* and *LS3*), hardly any revegetation can be seen in the image acquired three years after the failure (18 May 2013), whereas the shallow landslide *LS2* is characterized by faster revegetation.

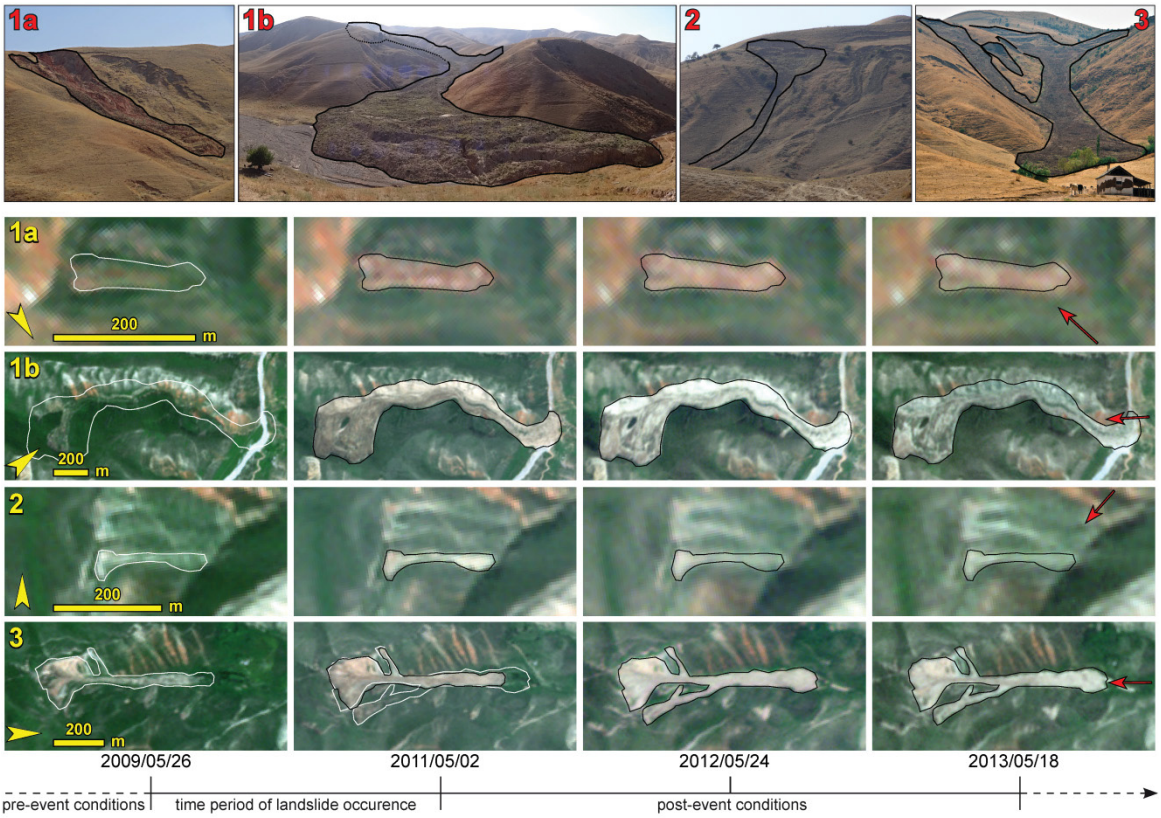

*Figure III-2. Multi-temporal development of landslides that occurred in spring 2010. Top: Field photos (September 2012). Bottom: RapidEye true color RGB images overlaid by outlines of landslides (Black: landslide occurred before acquisition date. White: landslide occurred after acquisition date). LS**1a**—deep-seated fresh failure of reddish sandstone; no revegetation; LS**1b**—deep-seated fresh failure of loess; slight revegetation; LS**2**—shallow fresh failure of loess; fast revegetation; LS**3**—deep-seated second reactivation of loess which occurred in 2012; no revegetation. (Red arrows: view direction of the field photos.)*

2.2 Remote Sensing Database

The multi-temporal optical remote sensing database consists of 216 orthorectified Level-3A RapidEye datasets delivered in the form of 25 × 25 km^2 tiles with 5 m pixel size. They have been provided by the RapidEye Science Archive (RESA) data grant program which has allowed customized data acquisition in pre-defined time periods of high landslide activity. As a result, a high temporal resolution of up to six acquisitions during the growing season between April and July could be achieved. Together with archive data acquired in 2009, there was a result of up to 20 acquisition dates between the years of 2009 and 2013, whereas no acquisitions were performed in 2010 (Figure 1c). The resulting high temporal resolution allows the determination of the time period of landslide occurrence up to several days and weeks, which is important for spatiotemporal analysis of landslide activity in respect to triggering and predisposing factors. Besides the multispectral remote sensing data, the developed landslide mapping approach is also based on a digital elevation model (DEM) of 30 m spatial resolution derived from the X-band data of the Shuttle Radar Topography Mission in February 2000 (Rabus et al. 2003). The DEM is used to derive landslide-related geomorphological information for the study area as contextual information for more reliable object-oriented landslide mapping (Section 3.2.3).

2.3 Pre-Processing of Remote Sensing Data

Pre-processing aims at the reduction of artifact changes in subsequent time series analysis. Such artifact changes are introduced by geometric mismatches and radiometric differences between the

image datasets, as well as pseudo-surface cover changes introduced by the temporary presence of clouds and snow (Coppin et al. 2004; Lu et al. 2010). To foster the potential for operational use and taking into account the high number of datasets, pre-processing has to be performed in an automated, robust and efficient way. For geometric adjustment, an image-to-image co-registration approach has been developed that allows automated spatial alignment of time series data comprising orthorectified standard data products (Behling et al. 2014b). As a result, geometric offsets of up to 60 m between the multi-temporal image data have been corrected and a relative image-to-image co-registration accuracy of less than one 5 m RapidEye pixel could be achieved for the complete multi-temporal database. To reduce the effects of radiometric differences between the images for subsequent change detection analysis, the developed landslide mapping approach (Section 3) is based on the temporal comparison of the normalized difference vegetation index (NDVI) derived from the standard corrected top-of-atmosphere radiance data. The remaining variability in NDVI values between the multi-temporal datasets needs to be compensated by the developed approach (Section 3.2). For masking clouds and snow, a threshold has been applied to the blue band of the RapidEye images ($Band1_{BLUE} > 1050\ W{\cdot}m^{-2}{\cdot}sr^{-1}{\cdot}\mu m^{-1}$). This threshold based approach has been extended by analyzing the whole time series in order to separate between permanent bright objects (e.g. sand and urban objects) and temporary ones (clouds and snow). In this context, it is assumed that a permanent bright object is present in all images of the time series, whereas clouds and snow are only temporarily present. This way even less thick cloud cover could be identified.

2.4 Reference Mapping for Validation Sites

To quantitatively assess the accuracy of object-oriented landslide mapping resulting from the developed approach, reference mapping has been carried out for two spatially independent validation sites which have been affected by recent multi-temporal landslide activity. They are outlined in Figure 1 and represent contrasting environments which are representative for the whole study area. The size of these validation sites amounts to approximately $14 \times 11\ km^2$ for the site *Uchkun* (Figure 3a) and $14 \times 8\ km^2$ for the site *Papan* (Figure 3b). The land use in these two sites is dominated by pastures and grassland. However, they also comprise several non-vegetated areas which could be mistaken for landslides, because of their similar appearance in optical remote sensing data. Both validation sites contain small settlements along the valleys close to the river beds. The *Uchkun* site further covers a bigger village in the southeastern part and an area of crop cultivation (western part), temporally without vegetation cover due to harvesting. The *Papan* site comprises a high percentage of permanently non-vegetated steep outcrops appearing as bright areas mainly in the center of the validation site. Furthermore, the two sites also differ in available remote sensing data, due to their location in different Level-3A RapidEye tiles (Figure 1c).

For both validation sites, a reference landslide inventory has been created by visual interpretation of the available RapidEye data acquired between 2009 and 2013, whereas the time period of occurrence of a mapped landslide is determined by the time period between the pre- and post-event RapidEye image. In Figure 3, these time periods are classified into full years, whereas the acquisition date of the post-event image defines the depicted year of occurrence. An exception is caused by the missing RapidEye acquisitions in 2010 resulting in a class of landslide occurrence between 2009 and 2011. Manual reference mapping has also been supported by spatially very high resolution satellite remote sensing data contained in the Google Earth™ archive with most recent images acquired in June 2013 for both validation sites. Furthermore, these inventories were validated during a field survey in September 2012. In total, 67 landslides were mapped—36 in the *Uchkun* and 31

in the *Papan* site. The size of these landslides ranges between 500 and 250000 m², whereas the total area affected by landslides amounts to approx. 1 km². Both sites are characterized by spatial and temporal concentrations in landslide occurrence, as well as areas and time periods without landslide activity. The *Uchkun* site is most strongly affected between the years 2009 and 2011, whereas for the *Papan* site highest landslide activity could be observed for 2012. Thus, the two selected validation sites differ in spatiotemporal landslide occurrence as well as in natural conditions and available RapidEye data coverage, thereby making them suitable for representative accuracy assessment of the developed approach.

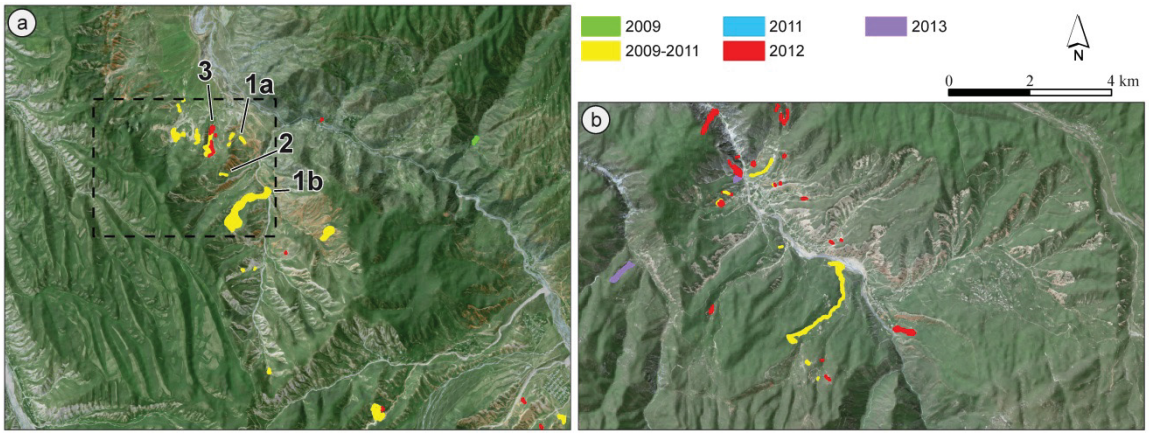

*Figure III-3. Reference mapping of landslide activity. (**a**) Validation site Uchkun including the subset illustrating the methodological descriptions of Section 3 (black dashed line). LS1-3: landslides shown in Figure 2; (**b**) Validation site Papan.*

3 Automated Approach for Multi-Temporal Landslide Mapping

The methodological developments aim at the automated multi-temporal mapping of landslides based on satellite remote sensing time series data. Thus, the approach needs to be able to identify landslide activations occurring at different times during the analyzed time span, whereas the determination of the time of landslide occurrence depends on the length of the time period between two subsequent images contained in the remote sensing time series database. To meet the goal of generating a multi-temporal landslide inventory, the approach is required to derive the occurring landslides as single objects for each of these time periods. In this context, the approach needs to take into account the natural variability of landslide phenomena occurring within the large study area.

To fulfill these requirements, the developed approach builds on a pixel- and object-oriented analysis of temporal NDVI-trajectories enabling the incorporation of rule-based knowledge about landslide-related surface cover changes. Furthermore, the approach comprises the possibility for the discrimination between uncertainty-related landslide likelihood classes to enable expert-aided evaluation of the results suitable for different applied tasks related to landslide investigations. For clarity, the descriptions of the basic idea (Section 3.1) and of the knowledge-based system (Section 3.2) are based on the exemplary analysis of the two subsequent RapidEye acquisitions (26 May 2009 and 2 May 2011) within the 8 × 4.5 km² subset depicted as dashed line in Figure 3a. In Section 3.3, the developed approach is extended to the whole time series available for this exemplary subset to demonstrate the derivation of the final results of multi-temporal landslide mapping. All methodological developments are realized using the open source programming language python.

3.1 Temporal NDVI-Trajectories for Landslide Identification

Temporal NDVI-trajectories represent specific temporal footprints of vegetation changes which are obtained for every pixel across the time span of the analyzed multi-temporal data stack. Figure 4 illustrates how these NDVI-trajectories can be used to distinguish between landslide-related vegetation changes (Figure 4(1)) and five other land cover changes (Figure 4(2–6)). In the case of the depicted landslide example *LS1b,* which occurred in the spring of 2010 (Figure 2(LS1b)), the failure caused a severe vegetation cover disturbance that is reflected in the abrupt decrease of the NDVI values between the RapidEye acquisitions of 26 May 2009 and 2 May 2011. These low post-failure NDVI values have been maintained for the following two years, indicating a slow revegetation rate in the area of the displaced landslide masses (Section 2.1). Based on the resulting distinct temporal NDVI-trajectory, landslides can be distinguished from permanently non-vegetated areas (Figure 4, bottom) characterized by permanent low NDVI values, as well as from temporally vegetated areas (Figure 4, top) characterized by a less distinct NDVI decrease and/or faster revegetation rates.

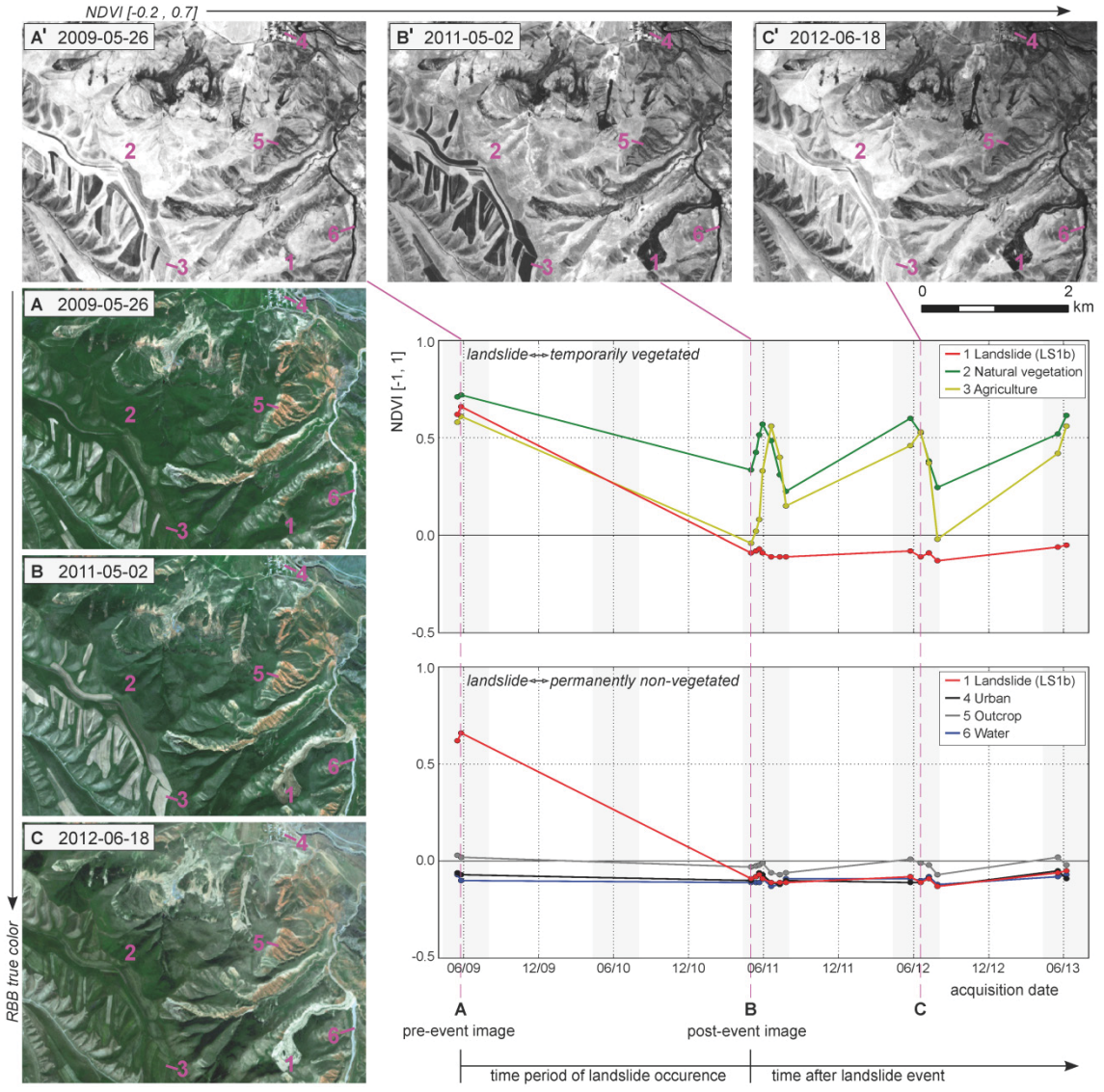

*Figure III-4. Temporal NDVI-trajectories used for differentiating landslides to other land cover changes. Images: NDVI illustrations (**A'–C'**) of exemplary RapidEye acquisitions (**A–C**) containing the position for the derived NDVI-trajectories 1–6. Diagrams: Comparison of the landslide trajectory (1) with vegetated surfaces (2,3) and with continually non-vegetated surfaces (4–6). Grey bars mark time periods of data availability focusing on the growing season.*

Compared to the ideal case of the fresh failure *LS1b,* other landslides may result in less distinct vegetation changes. Figure 5a illustrates such less-pronounced differences by depicting one characteristic NDVI-trajectory for each of the four landslide examples shown in Figure 2. If mass movements represent reactivations, which are typically occurring in areas of already existing landslides (Figure 2(LS3)), a smaller decrease of the NDVI values can be observed because of the sparser vegetation cover before failure. In the case of small shallow landslides (Figure 2(LS2)), the revegetation rate is often faster, because of the less severe soil disturbance. In the case of the deep-seated landslides (*LS1a* and *LS1b*), the NDVI-trajectories are very similar, showing their independence from the lithological properties of the material involved in the landslide failures. Besides the differences between the respective landslides, the temporal vegetation change characteristics also differ within a single landslide. Figure 5b depicts NDVI-trajectories for 20 pixels within landslide *LS1b* showing differences in the bi-temporal NDVI decrease and rate of post-failure revegetation. However, despite all of the described differences, the typical shape of a landslide-specific NDVI-trajectory is still maintained.

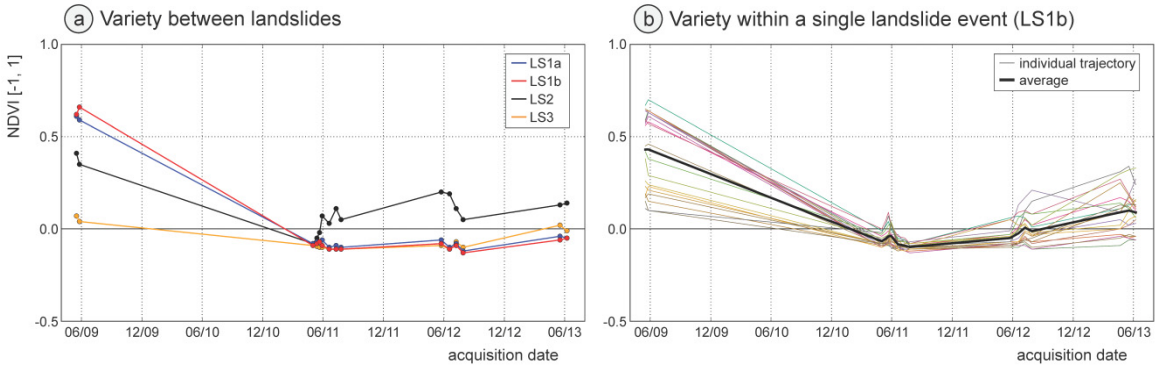

*Figure III-5. Variety of landslide-related NDVI-trajectories. (**a**) Differences between landslide types shown in Figure 2; (**b**) Differences within a single landslide event demonstrated by 20 NDVI-trajectories derived at various pixel positions within Landslide LS1b.*

3.2 Processing System for Knowledge-Based Landslide Identification

Based on the temporal NDVI-trajectories, a combined pixel- and object-oriented approach has been developed for the automated identification of landslide occurrence for subsequent image pairs, taking into account the entire available time series. For this purpose, the approach analyzes the degree of bi-temporal vegetation changes serving as the basis for the segmentation of landslide candidate objects for each time period (Section 3.2.1). In the following, these landslide candidate objects are evaluated regarding their plausibility in terms of post-event multi-temporal revegetation (Section 3.2.2) and relief-oriented parameters (Section 3.2.3). Figure 6 exemplarily illustrates the derivation of parameters that are used in the temporal NDVI-trajectory analysis. Figure 7 shows the overall processing scheme of the developed approach subdividing these three major parts into the processing steps A–F. The description in Section 3.2 follows steps A–F, whereas the empirically determined thresholds for each step are listed at the right of Figure 7. Figure 8 illustrates the results of each processing step based on the subset area shown in Figure 4. In the final step of the approach (Section 3.2.4), the object-oriented results are evaluated by the introduction of a reliability classification in the form of the overall landslide likelihood.

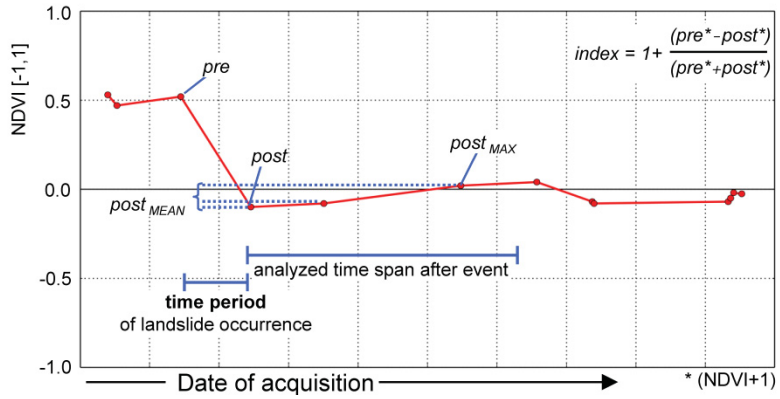

Figure III-6. Trajectory parameters for an exemplary landslide-related NDVI-trajectory.

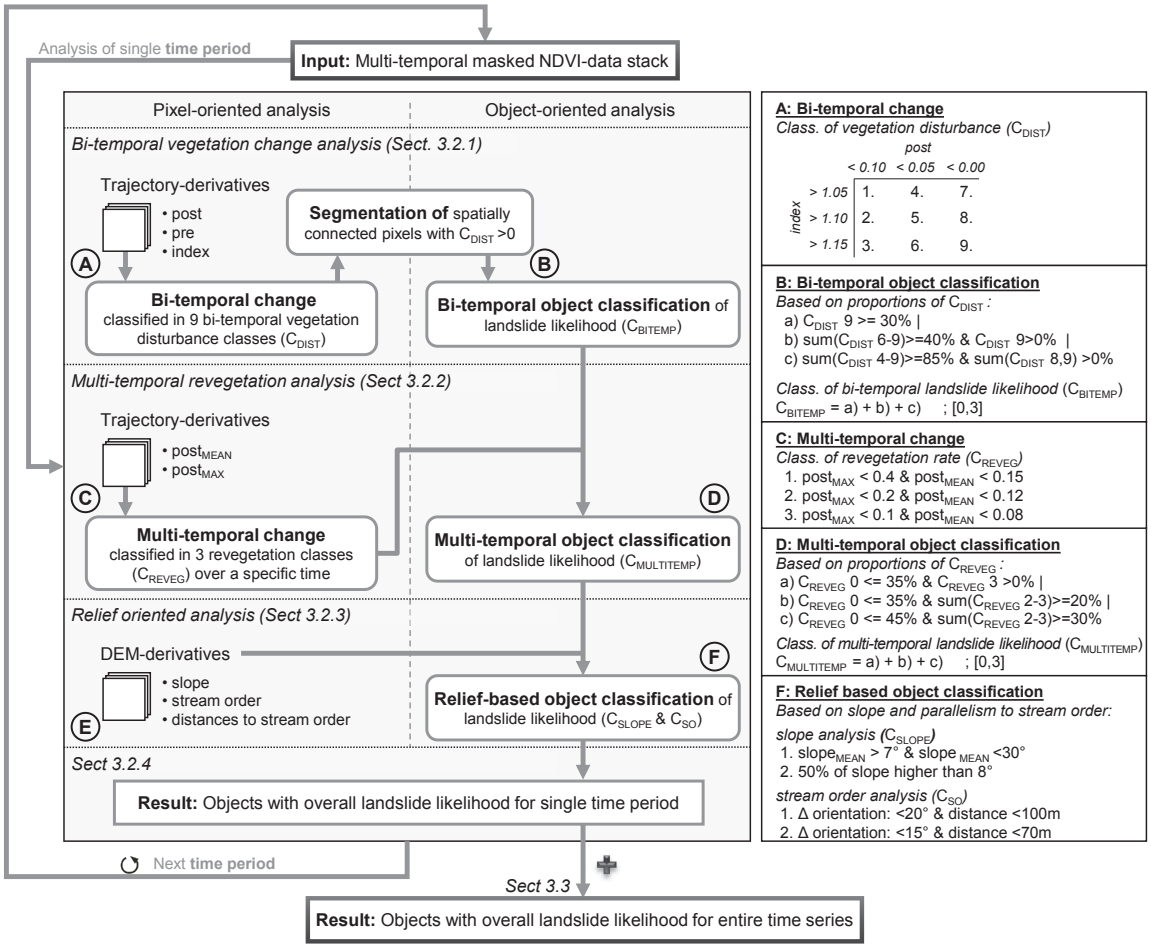

*Figure III-7. Multi-temporal landslide identification approach based on temporal NDVI-trajectories and relief oriented analysis. **(Left)** Processing scheme; **(Right)** Implemented thresholds for steps A to F.*

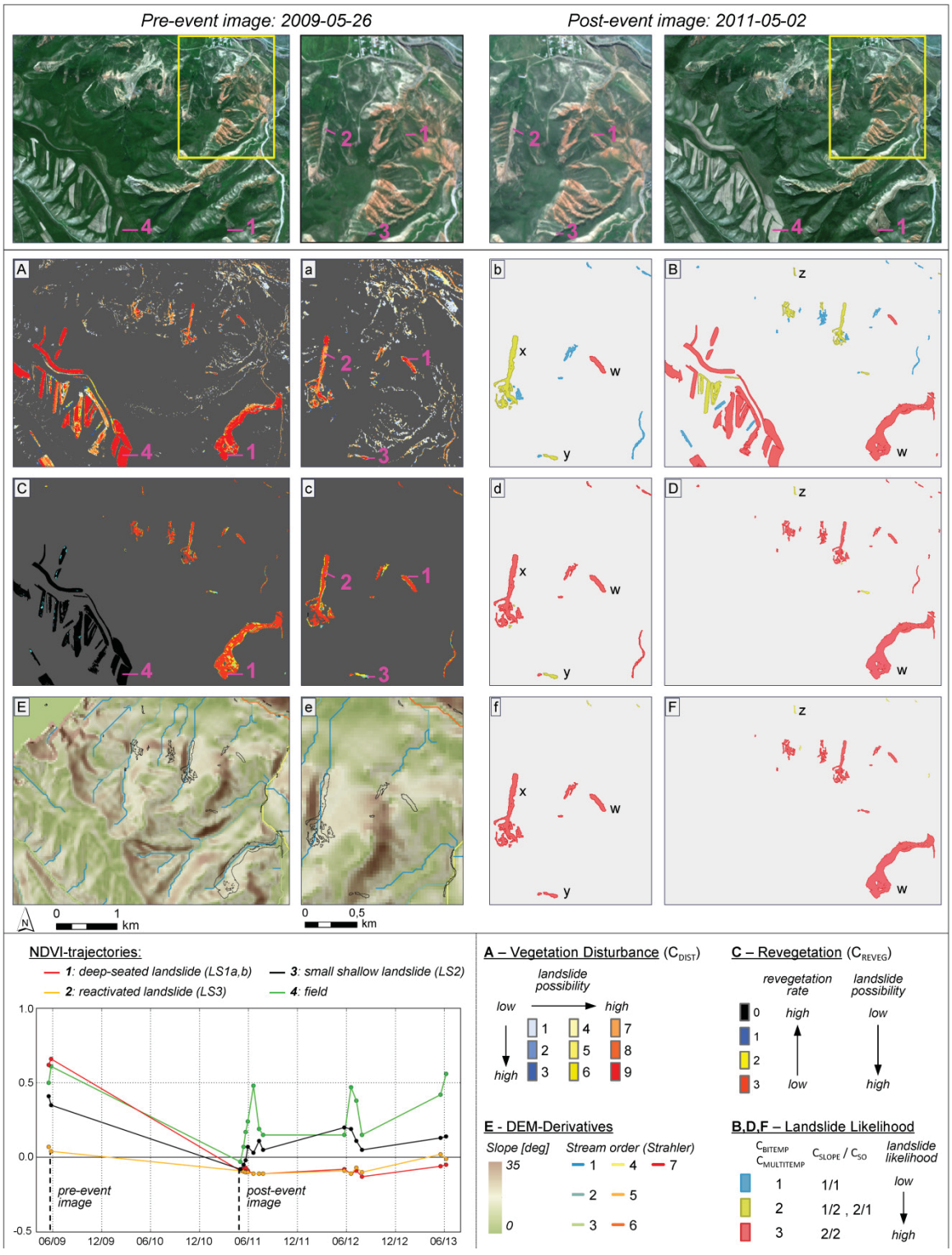

*Figure III-8. Landslide mapping approach for two subsequent RapidEye data acquisitions within the multi-temporal data stack. (**A–F**) Processing steps with zoom ins, (**a–f**) which are indicated by yellow rectangles, w,z: exemplarily described objects.*

3.2.1 Derivation of Landslide Candidate Objects Based on Bi-Temporal Vegetation Change Analysis

A: Pixel-Oriented Bi-Temporal Change Detection

To classify the bi-temporal vegetation disturbance for each pixel (C_{DIST}) in regards to the possibility of landslide occurrence, the NDVI values after an expected landslide (*post*) and the normalized index of the NDVI values of the pre-event and post-event image (*index*) are used in combination

(Figures 6 and 7). As shown in Figure 4, landslides usually cause the total loss of previously existing vegetation, which results in high *index* values and *post* values of less than zero representing bare soil. However, to accommodate the variety of landslide processes (Figure 5), the bi-temporal analysis of vegetation disturbance (C_{DIST}) is performed on a scale of 9 classes (Figure 7). The main idea of this multiple threshold-based analysis is adapted from the robust differencing approach developed by Castilla et al. (2009). The usage of multiple thresholds also enables the identification of less-pronounced surface cover changes related to landslide occurrence, e.g. if the vegetation cover is already less dense before the landslide event (e.g. Figure 2(LS3)). Figure 8A illustrates the results of this classification. The pixels representing deep-seated landslides (Figure 8(1)) have been classified with the highest C_{DIST} class of 9 and the landslide pixels characterized by less distinct bi-temporal vegetation changes (Figure 8(2,3)) have been assigned to lower C_{DIST} classes. However, the classification has also led to a high percentage of false-positive pixels that are introduced by slight vegetation changes in sparsely vegetated areas mainly in the northeastern part and by a distinct vegetation loss in the area of harvested fields in the western part of the subset shown in Figure 8. The exemplary NDVI-trajectory for harvested fields (Figure 8(4)) shows bi-temporal changes that are very similar to the ones of the deep-seated landslides (Figure 8(1)) and thus results in the same C_{DIST} classes.

B: Object-Oriented Classification of Bi-Temporal Landslide Likelihood

Based on the pixel-oriented results of the first step, a subsequent segmentation is performed that extracts individual segments from all of the spatially 8-connected pixels which have been assigned to a vegetation disturbance class ($C_{DIST} > 0$). The segments are classified regarding their bi-temporal landslide likelihood (C_{BITEMP}) by analyzing the frequency of the C_{DIST} classes for all pixels contained in the segment. If the segments do not meet any of the landslide likelihood criteria shown in Figure 7 ($C_{BITEMP} = 0$), they represent segments containing an excessively high percentage of pixels characterized by vegetation changes not typical for landslide occurrence; they are therefore eliminated. All other segments are kept as landslide candidate objects characterized by a three-step bi-temporal landslide likelihood ($C_{BITEMP} = 1–3$) of ascending order (Figure 8B). This procedure ensures the derivation of landslides as single objects even if in part they do not represent the optimal case of a significant vegetation disturbance. At the same time, this procedure reduces the high number of pixels with slight vegetation changes that can be considered as noise. Figure 8B shows that the deep-seated landslides (Figure 8(1,w)) are classified with the highest bi-temporal landslide likelihood ($C_{BITEMP} = 3$) because their segments consist of more than 30% of pixels with the highest bi-temporal vegetation disturbance class ($C_{DIST} = 9$). The reactivated landslide (Figure 8(2,x)) and the shallow landslide (Figure 8(3,y)) are classified with lower bi-temporal likelihood values ($C_{BITEMP} = 2$). Furthermore, Figure 8B shows the reduction of false-positive pixels, especially in the northeastern part of the subset.

3.2.2 Multi-Temporal Revegetation Analysis

C: Pixel-Oriented Multi-Temporal Change Detection

For each pixel contained in the identified objects, the revegetation is analyzed within a user-defined time span allowing the differentiation between landslide-related slow revegetation and other vegetation cover changes. In this study, this time span is limited to a maximum of three years, because the vegetation usually starts to recover in most parts of the landslides after these three years. Based on all post-event images available in this time span, the degree of revegetation is classified into four rates of revegetation (C_{REVEG}). They are based on the maximum ($post_{MAX}$) and

mean NDVI values ($post_{MEAN}$) derived from the NDVI-trajectory (Figure 6). The combination of $post_{MAX}$ and $post_{MEAN}$ allows a robust determination of the revegetation rate (Figure 7). In contrast, the single use of $post_{MAX}$ would be susceptible to co-registration errors, which could result in high NDVI values at the edge of landslide objects if the landslide is surrounded by vegetation. The single use of $post_{MEAN}$ would be more susceptible to the date of the image acquisitions and could result in rather low NDVI values for fields if the field is harvested in the majority of the acquired datasets. Figure 8C shows a reliable differentiation between landslide-related surface changes and fields resulting from the revegetation rate classification. The pixels of the fields are characterized by revegetation rates higher ($C_{REVEG} = 0$) than the landslide pixels ($C_{REVEG} = 2$ or 3).

D: Object-Oriented Classification of Multi-Temporal Landslide Likelihood

Based on the frequency of the pixel-oriented revegetation rate classes (C_{REVEG}), the landslide candidate objects are further characterized in regards to their multi-temporal landslide likelihood ($C_{MULTITEMP}$). Following the procedure described in (B), all landslide candidates are eliminated that do not meet any of the criteria shown in Figure 7 ($C_{MULTITEMP} = 0$) and the remaining objects are classified into three likelihood classes ($C_{MULTITEMP} = 1–3$). Thus, fields are eliminated from the landslide candidates, whereas landslides are maintained (Figure 8D). This way, landslides of low revegetation rates (Figure 8((1,w),(2,x))) and also landslides of faster natural revegetation (Figure 8(3,y)) could be distinguished from fields, whereas the shallow landslide (Figure 8(3,y)) is characterized by slightly lower multi-temporal landslide likelihood ($C_{MULTITEMP} = 2$).

3.2.3 Relief-Oriented Analysis

E, F: Pixel- and Object-Oriented Analysis of Relief Parameters

Landslide candidate objects are further evaluated in regards to relief-based plausibility based on the two parameters: slope and parallelism to streams (Figure 7). The first parameter slope has already been widely used for this purpose (Barlow et al. 2006; Borghuis et al. 2007; Cheng et al. 2004; Lacroix et al. 2013; Lu et al. 2011; Martha et al. 2012). It takes into account the fact that landslides require a certain initial relief contrast to allow the downward movement of material as a result of the onset of a slope failure. In this study, landslide objects are required to be characterized by an average slope ($slope_{MEAN}$), ranging between 7° and 30°. However, this range is only applicable to the source area of a landslide, since the accumulation zone can also comprise flatter parts resulting in slope values below the thresholds implemented for $slope_{MEAN}$. Therefore, the approach also analyzes the proportions of the slope values ($slope_{HIST}$) within the landslide object. If at least 50% of the slope values are larger than 8°, the object is still considered a landslide. Both parameters ($slope_{MEAN}$, $slope_{HIST}$) are combined to a slope-oriented parameter (C_{SLOPE}) for the evaluation of each landslide candidate object.

The second parameter, parallelism to streams, aims at eliminating false positives which occur if a river has flooded a formerly vegetated area or if local co-registration errors between the pre- and post-event images result in changes which have the same appearance as the ones in the flooded areas. An example is shown in the lower right part of Figure 8e. Analysis of a landslide object being parallel to streams is based on the distance and orientation of that object in regards to the stream network (Figure 7) derived from a DEM using the stream order by Strahler (1952). The orientation of the landslide object and the corresponding part of the adjacent stream is calculated by using the major axis of the ellipse, which is defined by the second central moment of the analyzed region (Burger & Burge 2009). First-order streams are excluded from this analysis because landslides are

often occurring alongside these topographically less pronounced valleys. For all other streams belonging to higher orders, the objects are evaluated in three steps (Figure 7) according to the degree of parallelism (C_{SO}), whereas C_{SO} = 2 represents the highest degree of being parallel. Both object parameters (C_{SLOPE}, C_{SO}) are combined into the relief-oriented landslide likelihood (C_{RELIEF}). If the landslide candidates are either clearly parallel to a stream (C_{SO} = 2) or do not meet any of the slope criteria (C_{SLOPE} = 0), they are classified as false positives. Applying this procedure, the object in the southeastern part of the enlarged zoom area of Figure 8e, which is parallel to a fourth-order stream, is eliminated from the identified landslide candidates shown in Figure 8f. The remaining landslide candidates are characterized by the three-step relief-oriented landslide likelihood parameter (C_{RELIEF}) illustrated in Figure 8F.

3.2.4 Classification of Overall Landslide Likelihood

To obtain meaningful results in the process of automated landslide identification—comprising the existing variability of landslide phenomena and the possibility for subsequent evaluation of the results by landslide experts—the identified landslide objects are classified into four (*I-IV*) classes representing different degrees of overall landslide likelihood (Figure 9). These classes are an expression of the level of uncertainty related to the automated identification of this particular landslide object using the three previously described parameters C_{BITEMP}, $C_{MULTITEMP}$ and C_{RELIEF}. Class *I* represents the ideal case of a deep-seated fresh failure which is characterized by high bi-temporal vegetation loss (C_{BITEMP} = 3), very low revegetation rates ($C_{MULTITEMP}$ = 3) and very high relief oriented landslide likelihood (C_{RELIEF} = 3). Both deep-seated fresh landslides *LS1a* and *LS1b* (object *w* in Figures 8 and 9) are characterized by the highest overall landslide likelihood. The reactivated landslide *LS3* (object: *x*) is characterized by less distinct vegetation loss (C_{BITEMP} = 2), but it still performs to an ideal in terms of the other two parameters and is thus classified into the overall landslide likelihood class *II*. Additionally to the non-ideal bi-temporal vegetation changes of class *II*, class *III* comprises also non-ideal revegetation rates. The small shallow landslide *LS2* (object: *y*) represents an example for this case, which is characterized by likelihood parameter values of 2 for both C_{BITEMP} and $C_{MULTITEMP}$. In the case of the lowest landslide likelihood class *IV*, objects are characterized by non-ideal values (<3) for all three parameters. The object *z* in Figures 8 and 9 represents an example for such cases. Overall, this demonstrates that these landslide likelihood classes represent the level of uncertainty as well as, to a certain degree, the type of landslide activation.

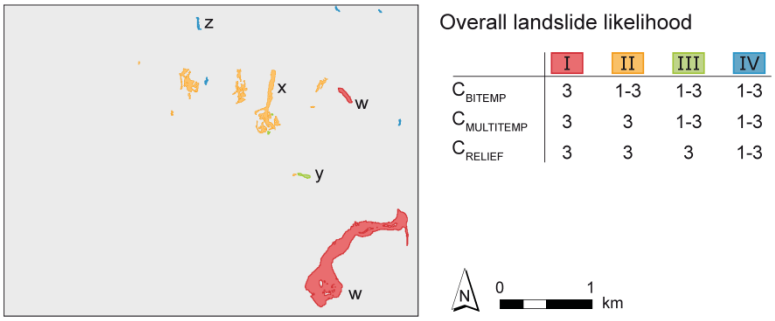

Figure III-9. Overall landslide likelihood derived for identified objects (cf. Figure 8F).

Furthermore, these overall landslide likelihood classes enable the separation of the automatically derived landslide mapping results into four selection categories (*I′–IV′*) representing a selection of the results of varying levels of strictness. In this context, the selection category *IV′* represents the

least strict selection and comprises all automatically mapped objects independent from the assigned overall landslide likelihood class. In contrast, category *I′* solely comprises the objects belonging to the highest landslide likelihood class representing the most strict selection. In Section 5, the results of these selection categories are evaluated in regards to mapping accuracy, thereby showing how these categories influence the approach in terms of automated or semi-automated usage.

3.3 Multi-Temporal Landslide Mapping for Whole Time Series

The application of the approach to the whole RapidEye time series has resulted in the identification of landslide events in four out of the 15 subsequent image pairs (Figure 10). The length of the identifiable time period of landslide occurrence depends on the temporal resolution of the available RapidEye time series data. In the case of the methodological subset, it varies between nine days (17 May 2009–26 May 2009) and two years (26 May 2009–2 May 2011). The results reveal the suitability of the approach for the identification of landslides representing fresh failures and reactivations (Section 2.1). In Figure 10, fresh failures are represented by the landslides *LS1a*, *LS1b*, and by the green polygon. Reactivations are shown by the polygons within the yellow ellipse and the landslide *LS3*. In the case of landslide *LS3,* two reactivations could be identified that both resulted in an enlargement of the crown area of the landslide and caused a further downward displacement of the already accumulated material. Moreover, Figure 10 also shows that the automated identification is independent from the lithology of the affected slopes, whereas the majority of the identified landslides occurred within loess (bright areas) and some within weakly consolidated reddish sedimentary rocks (e.g. *LS1a*).

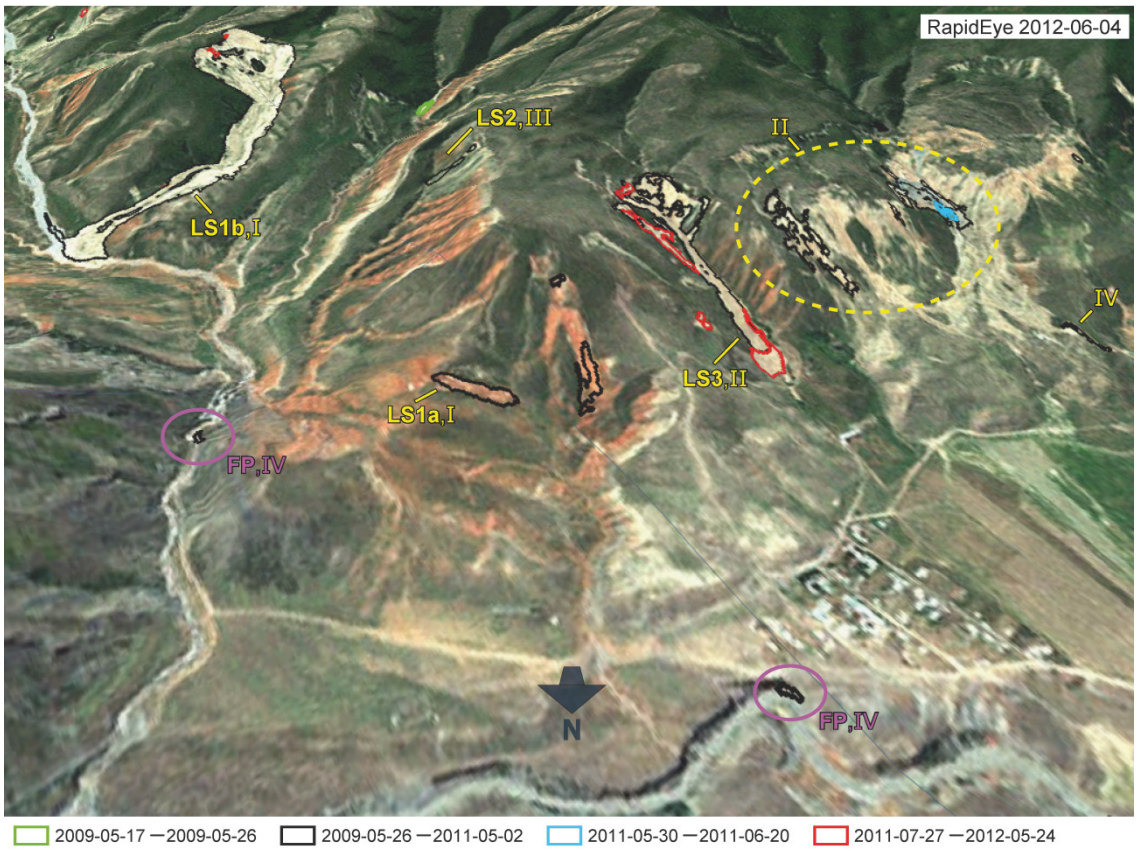

Figure III-10. Mapping results for the entire time period 2009–2013. Identified landslide objects are depicted according to their time period of occurrence and overlaid on a perspective view, together with a RapidEye image acquired at 4 June 2012. LS1–3: landslides shown in Figure 2; I–IV: overall landslide likelihood classes.

The exemplary results show that the approach is capable of reliable identification of landslides occurring during the analyzed time span (2009–2013) and distinguish them from older landslides that were already present. Furthermore, Figure 10 also confirms the suitability of analyzing temporal NDVI-trajectories for the separation between landslide objects and other non-vegetated areas, such as buildings, streets, outcrops and river beds. However, the purple ellipses shown in Figure 10 indicate two falsely identified landslide objects representing false positives (FP) in the specific form of small erosion features at a riverbank. To evaluate the influence of such identification errors on the overall quality of the automated landslide mapping result, a quantitative accuracy assessment was performed and is outlined in Section 5.

4 Application of Approach to Whole Study Area

Automated multi-temporal landslide mapping has been performed for the whole study area, which is characterized by variations in natural conditions and temporal RapidEye data coverage (Section 2). The complete mapping result, which includes objects of all overall landslide likelihood classes, has been visually validated by landslide experts to remove obvious false positives. All automatically identified landslides could therefore be included in the overall evaluation of the spatiotemporal landslide activity. As a result, 471 landslides have been identified, whose location, classified size, and time period of occurrence is depicted in Figure 11. During field investigations in September 2012, 120 of these identified landslides were visited, only revealing four false identifications. Each of these cases represented a manmade removal of construction material in the lower part of a slope.

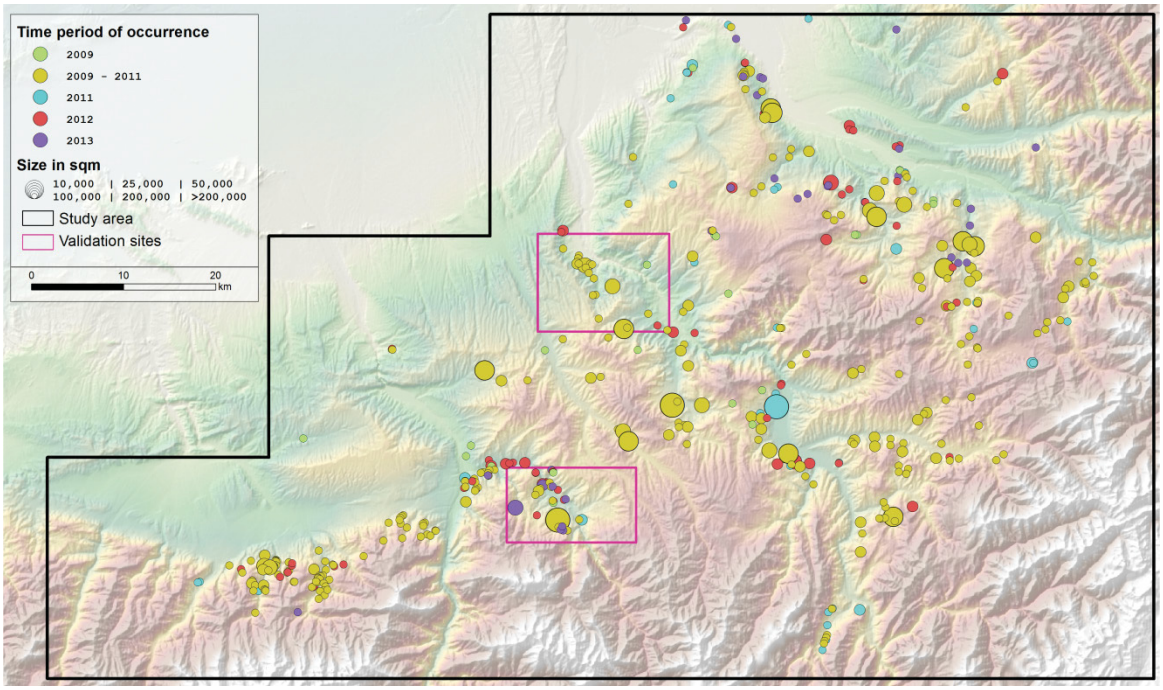

Figure III-11. Results of landslide mapping for the whole study area between 2009 and 2013. Landslide objects are depicted according to size and time period of occurrence. Background: color shaded relief (cf. Figure 1b).

The size of the identified landslides ranges between 125 and 750000 m^2, and the total area affected by these landslides amounts to 6.1 km^2 (Table 1). Table 1 also shows the distribution of the temporal landslide activity in respect to the classified time periods. The longest analyzed time period be-

tween 2009 and 2011 comprises 55% of all identified landslide objects. Landslide activity is less intense in the other analyzed years, varying between 6% of occurred landslide events in 2009 and 18% in 2012. These findings reveal a constantly ongoing landslide activity independent from major triggering events, such as intense rainstorms or larger earthquakes that did not happen in this region during the analyzed time period between 2009 and 2013. Moreover, the spatial distribution of the landslide objects depicted in Figure 11 shows clear spatial variations in landslide activity, including areas of distinct concentrations, whereas most landslides occurred at elevations between 900 and 2300 m. For this region, the obtained results comprise the first systematic assessment of spatiotemporal landslide activity, thus representing a main prerequisite for objective hazard and risk assessment.

Table III-1. Summary statistics of the landslide mapping results.

Time Period	N	N (%)	Area (m^2)	Area (%)	Min (m^2)	Max (m^2)	Mean (m^2)
2009	27	6	84,775	1	125	12,950	3140
2009–2011	260	55	3,732,712	61	400	242,900	14,357
2011	66	14	642,874	11	325	55,000	9741
2012	83	18	667,749	11	400	53,575	8045
2013	35	7	962,372	16	250	775,192	27,496
2009–2013	471	100	6,090,482	100	125	775,192	12,931

5 Accuracy Assessment

The systematic accuracy assessment of the developed approach is performed for two independent validation sites (Section 2.4). Section 5.1 assesses the influence of the landslide likelihood-based selection categories on the quantitative accuracy of the landslide mapping results. In Section 5.2, the accuracy assessment is complemented by the evaluation of the geometric quality of the automatically identified landslide objects.

5.1 Quantitative Landslide Mapping Accuracy

To obtain a comprehensive quantitative evaluation of the approach, the conformity between automated identification and reference mapping is analyzed for both validation sites and for each selection category (*I′–IV′*) in regards to the number of landslides and the area affected by these landslides. This comparison results in one of three relevant identification categories: true positive (TP), false negative (FN), and false positive (FP). TPs comprise the correctly mapped landslides, whereas the other two identification categories represent two types of identification errors. FNs correspond to reference landslides that have not been identified by the approach, and FPs are identified landslide objects which have not been mapped in the reference inventory. The fourth identification category of true negatives (TN) does not apply in the case of object-based single-target classifications (Martha et al. 2012).

To evaluate the performance of the landslide mapping approach the three relevant identification categories have to be considered in relation to each other. The best result is characterized by 100% TP and absent identification errors (0% FP and 0% FN). Based on this relation, the four accuracy metrics, *Detection Percentage*, *Omission Error*, *Commission Error* and *Quality Percentage* (Lee et al. 2003; Martha et al. 2012; Rau et al. 2014), are selected for the comprehensive accuracy assessment:

$$Detection\ Percentage = 100 \times \frac{TP}{TP + FN} \quad (1)$$

$$Quality\ Percentage = 100 \times \frac{TP}{TP + FN + FP} \quad (2)$$

$$Omission\ Error = 100 \times \frac{FN}{TP + FN} = 100 - Detection\ Percentage \quad (3)$$

$$Commission\ Error = 100 \times \frac{FP}{TP + FP} \quad (4)$$

The *Detection Percentage*—also called *True Positive Rate* or *Producer Accuracy*—represents the percentage of landslides which have been correctly identified by the automated approach. The *Commission Error* and the *Omission Error* describe separately the influence of the two possible identification errors FP and FN, respectively. The *Quality Percentage* represents an integrative indicator and relates the correctly mapped landslides to both possible identification errors, indicating how likely a landslide is correctly identified.

Figure 12 illustrates in a spatially explicit way the results of the four different selection categories for both validation sites in comparison to the reference mapping. At the bottom of Figure 12, the performance of each selection category is shown in terms of the four accuracy metrics (Equations 1–4), which are calculated based on the accuracy statistics shown in Table 2. The less strict selection categories result in higher *Detection Percentages* with a maximum of up to 95% correct identification of the landslide-affected area and more than 80% of the number of landslides achieved by selection category *IV′*. Thus, category *IV′* is most suitable to minimize missing identifications (FN) and to obtain results that comprise most of the landslide occurrences, including landslides that are characterized by very slight vegetation cover changes, represented by reactivations of already existing landslides or very small and shallow landslides. However, applying less strict selection categories, the number of FPs increases, which is expressed by the higher *Commission Error*s. Therefore, the mapping results of category *IV′* are most suitable for subsequent evaluation by a landslide expert who can interactively eliminate the FPs. This way, the least strict selection category minimizes the likelihood that potentially dangerous landslide objects are not included in the automated mapping result. In contrast, category *I′* results in the complete absence of FP for the *Papan* site and only a single FP object of 900 m² size for the *Uchkun* site. Thus, category *I* minimizes the number of FPs and limits the automated identification results to correctly identified landslide objects (TP) that are most likely to represent fresh landslide failures. Hence, if only landslide objects that represent most recently occurred new landslides are of interest, the selection category *I′* can be used.

Table III-2. Accuracy statistics according to the three different identification categories (TP, FN, FP) in regards to number of landslides (N) and landslide-affected area (given in m²).

Validation Site	Identification Category	I'		II'		III'		IV'	
		N	Area	N	Area	N	Area	N	Area
Uchkun	TP	3	272,590	30	533,552	31	535,046	33	540,184
	FN	33	284,751	6	23,790	5	22,296	3	17,158
	FP	1	900	32	71,854	32	71,854	85	143,807
Papan	TP	2	206,297	18	393,908	18	393,908	25	420,228
	FN	29	234,227	13	46,613	13	46,613	6	20,293
	FP	0	0	21	34,525	25	38,450	55	117,550

However, to apply the approach to large areas in a fully automated way, the approach needs to counterbalance the influence of the two identification errors (FP, FN). The integrative *Quality Percentage* takes this into account and shows the highest values for categories *II′* and *III′* in both validation sites. As a result, the application of these categories results in correct landslide identification for more than 90% of the landslide area, accompanied by *Omission* and *Commission Errors* of around 10%.

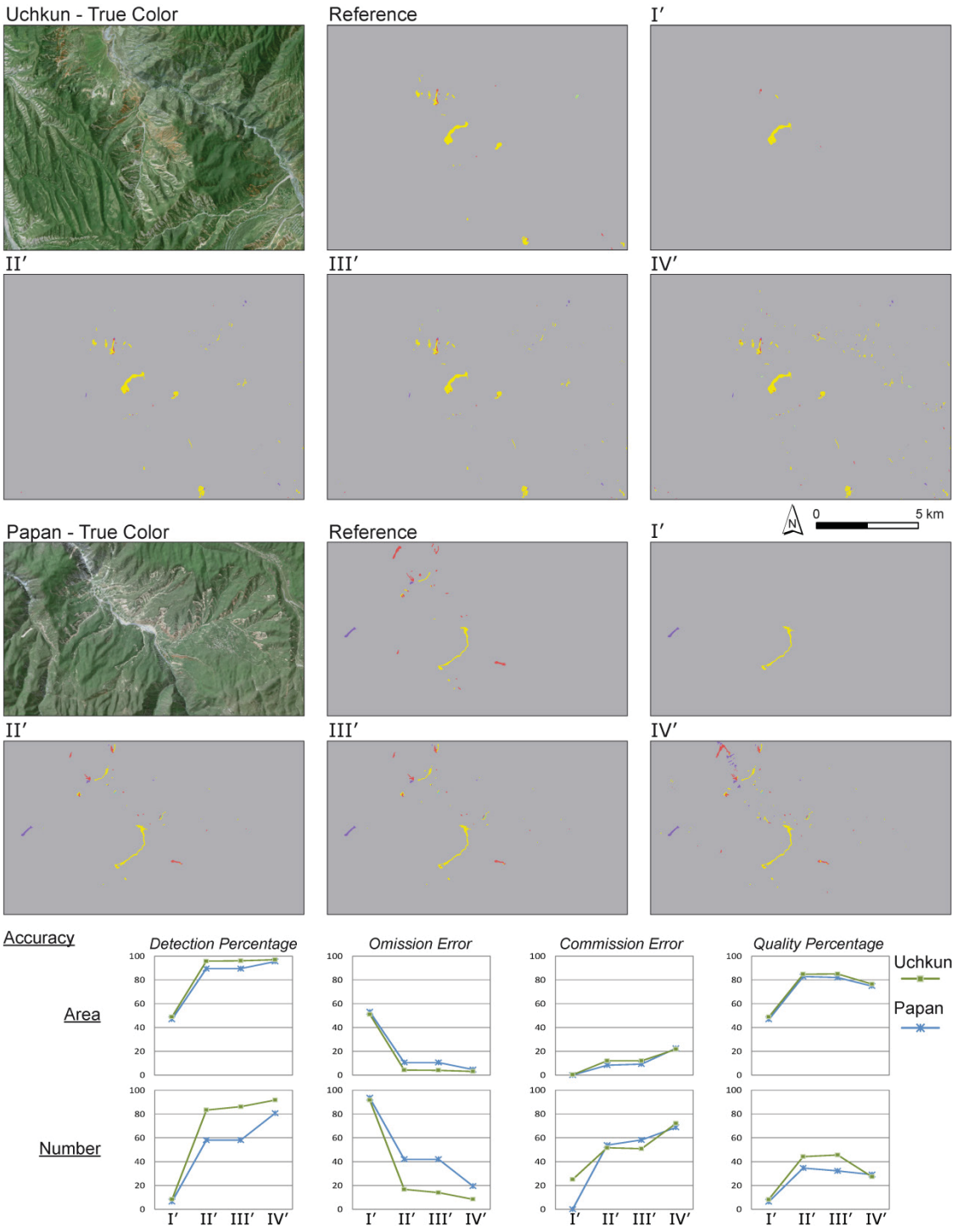

Figure III-12. Mapping results and accuracy for the four landslide likelihood selection categories (I′–IV′) of varying strictness (Time of landslide occurrence depicted by color—Legend: Figure 3).

Furthermore, the findings of the accuracy assessment show that the quality of the results is higher regarding the landslide-affected area than compared to the number of landslides. In the case of selection category *II',* the *Quality Percentage* amounts to approx. 80% for the area and approx. 40% for the number of landslides. This difference reveals that the approach identifies larger landslides with higher reliability and that both identification errors (FN, FP) are mostly caused by objects of smaller spatial extents.

5.2. Evaluation of the Geometric Quality of the Landslide Object Delineation

The correct spatial delineation of the automatically identified objects is important for the generation of high-quality multi-temporal landslide inventories which are required for subsequent objective hazard analysis. For this purpose, all of the 58 landslide objects which were correctly identified for the two validation sites have been individually compared to the reference mapping objects in regards to the degree of their spatial overlap (Figures 13 and 14). As a result, spatially explicit representations of the true positive (TP), false negative (FN) and false positive (FP) areas have been obtained for each object comparison (Figure 14). Their normalization by the size of the respective reference objects (sum of TP and FN) results in percentages for all of these three parameters. As such, the ideal spatial overlap between two objects is represented by 100% TP and 0% FP indicated by the star in the diagram of Figure 14 depicting the individual objects regarding their percentages of TP and FP. Based on this optimum situated at the origin of the diagram, three typical object delineation errors could be identified. Along the y-axis, the percentage of the correctly mapped landslide area is further reduced, thereby corresponding to a progressing underestimation of the size of the automatically derived objects compared to the size of the reference objects. Along the x-axis, the percentage of the FP area increases and results in an overestimation compared to the reference mapping. Along the line depicted in the diagram, the automatically mapped object corresponds in size to the reference object but differs either in shape or in position compared to the reference object.

Overall, the results depicted in Figure 14 show that most of the analyzed objects are located in the upper left part of the diagram close to the optimum point. The examples a and b in Figure 14 represent two cases of almost ideal object delineations. Another concentration can be seen along the depicted line of the diagram. It can be explained by the fact that automatically pixel-based object delineation always slightly differs from the manually digitized objects. This is especially evident in the case of small objects paradigmatically shown by the examples c and d of Figure 14. The examples e and f represent outliers of less exact object delineation for underestimation and overestimation, respectively. However, the diagram shows that for the vast majority of the analyzed landslide objects, the spatial overlap corresponds to at least 50% in regards to the original object contained in the reference mapping.

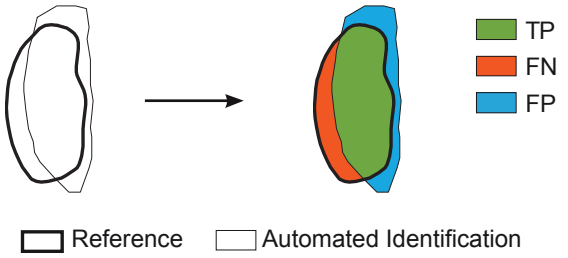

Figure III-13. Schematic view of TP, FN and FP areas resulting from comparing the spatial overlap between automatically and manually (reference) derived landslide objects.

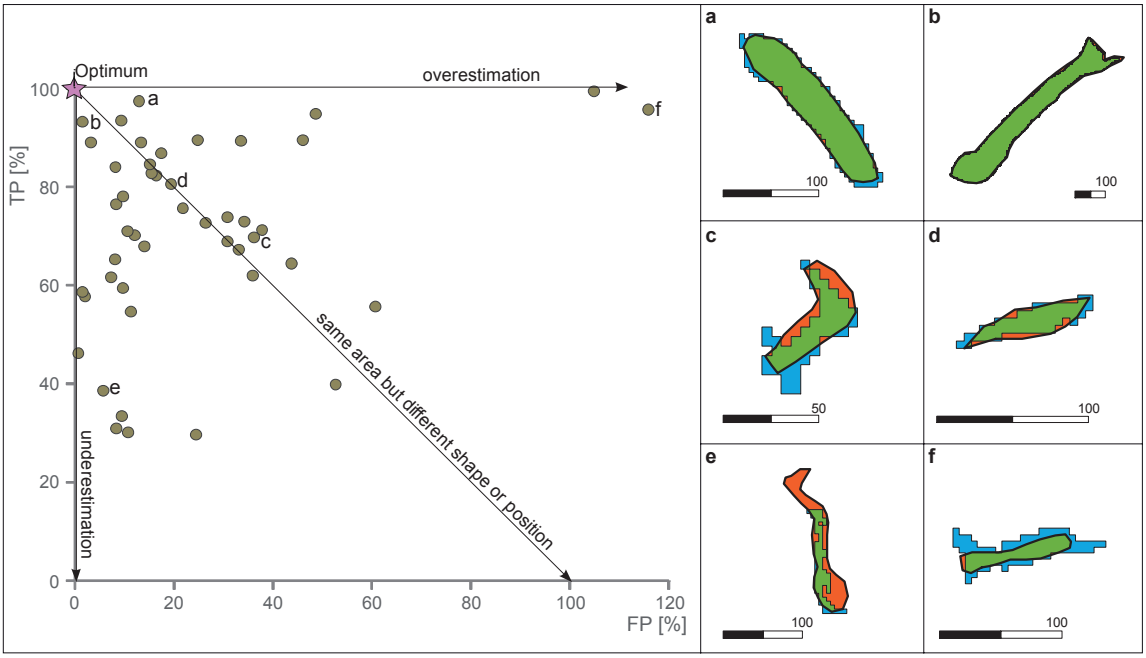

*Figure III-14. Comparison of automatically identified landslide objects with manually derived reference objects (cf. Figure 13). (**Left**) Diagram of the TP and FP percentages of each object comparison. (**Right**) Results depicted for six examples (same legend as for Figure 13).*

6 Discussion

The developed automated approach for spatiotemporal landslide mapping enables comprehensive assessment of landslide activity over longer periods of time. It is based on the analysis of landslide-specific vegetation changes using temporal NDVI-trajectories derived from optical remote sensing time series data complemented by relief parameters. To perform robustly over large areas, the approach considers the existing variability of vegetation change characteristics related to different types of landslides (Figure 5a) and to different parts within a single landslide (Figure 5b). This allows the identification of fresh and reactivated landslide occurrences including their separation from other surface changes not related to landslide processes (Figure 4). In this context, the approach differentiates the identified landslide objects by their overall landslide likelihood, enabling landslide experts to incorporate the level of uncertainty in the subsequent interpretation and evaluation of the results obtained by the automated analysis.

To meet the goal of assessing the multi-temporal landslide activity, the approach derives objects of landslide activations which occurred at different times during the time span of analysis. For this purpose, the segmentation of landslide candidate objects builds on the result of a specific multi-threshold-based change detection analysis considering distinct and less pronounced landslide-related vegetation cover changes between each subsequent image pair contained in the remote sensing time series database. In contrast, the existing object-oriented landslide mapping approaches use mono-temporal information for the segmentation procedure (Barlow et al. 2006; Kurtz et al. 2014; Lu et al. 2011; Martha et al. 2010; Stumpf et al. 2014; Stumpf & Kerle 2011) and thus are not designed to delineate active parts of a landslide. To evaluate the plausibility of the landslide candidate objects of the developed approach, they are further analyzed in regard to relief parameters and post-event rates of temporal revegetation. Analyzing landslides in regards to their relief position has long been a standard part of remote sensing-based landslide recognition (Barlow et al. 2003; Cheng et al. 2004). However, the incorporation of revegation rates, derived by the analysis of the temporal NDVI-trajectories, has firstly been applied and allows separation of slower revegetation rates typical for areas affected by landslides from other areas characterized by faster revegetation, as in the case of agricultural fields.

The application of the developed approach to the whole study area (Section 4) has confirmed its suitability for supporting the generation of multi-temporal landslide inventories for large areas. In this context, the approach enables the analysis of backdated landslide occurrence as well as the monitoring of ongoing landslide activity making it widely applicable in the frame of different applied tasks related to landslide investigations. However, the profound understanding of landslide processes also requires the assessment of information not derivable by the developed approach, such as landslide type, depth of sliding surface and volume of displaced material. They are mostly assessed during field investigations that are time- and resource-consuming and therefore often carried out less frequently than needed. The developed approach can thus facilitate a more efficient and systematic way of conducting such field work by providing reliable spatiotemporal information on landslide occurrence allowing more focused field investigations. This is especially important for regions like the study area in southern Kyrgyzstan, where large areas are affected by frequent, albeit sporadic, occurrences of landslides (Section 2.1).

Comprehensive accuracy assessment (Section 5) has been performed for two independent validation sites (Section 2.4) in order to assess the methodological performance of the approach including different parameterizations represented by the landslide likelihood-based selection categories. The highest accuracies have been obtained by applying the selection category *II'*, which comprises the landslide objects of very high and high landslide likelihood (*I* and *II*). For both validation sites, this category has resulted in a 90% correctly identified landslide-affected area (*Detection Percentage*), whereas *Omission* and *Commission Errors* of approximately 10% and *Quality Percentages* of 80% could be achieved (Figure 12II). These accuracies show that most of the automatically detected landslides are characterized by a high landslide likelihood, which reveals that the developed automated approach is able to reliably distinguish landslide-related surface cover changes from other land cover changes. This means that the approach robustly accommodates the variability of landslide phenomena occurring within the large study area, as well as the remaining geometric mismatches and the radiometric variability contained in the multi-temporal RapidEye database. The fact that the results are comparable for both validation sites, differing in temporal landslide activity patterns (Section 2.4), further indicates a reliable landslide identification independent from the time of landslide occurrence.

However, considering the number of identified landslides that have been obtained for the selection category *II′*, the results are less accurate (*Quality Percentage:* ≈ 40%) than for the areal extent of the landslides (Figure 12II). This difference indicates that mainly smaller objects are the source for both identification errors—not identified landslides (FN) and incorrectly identified landslides (FP). To further improve the automatically derived identification accuracies of selection category *II′*, the developed approach also allows for a semi-automated procedure. For this purpose, the selection category *IV′* has to be applied, thereby resulting in the consideration of all automatically identified landslide objects independent of their landslide likelihood. As a result, almost all of the reference landslides (30 out of 33 for the *Uchkun* and 25 out 31 for the *Papan* validation site) have been automatically identified (Table 2). However, at the same time, this category contains a higher number of FPs that could mostly be eliminated by subsequent expert-aided evaluation (Section 4). This way, even very small landslide occurrences, often characterized by less pronounced surface changes, have been contained by the landslide mapping result. The knowledge about such small activations can be very advantageous because they often represent precursors of subsequent large hazardous landslides.

For comparing these accuracies to accuracies that have been obtained by other automated approaches for object-oriented landslide mapping, a number of recent studies has been selected which use the same accuracy metrics. Rau et al. (2014) achieved *Detection Percentages* between 64.8% and 92.7% and *Quality Percentages* between 58% and 81.7% for three test sites by post-event classification of images acquired by different sensors of very high spatial resolution. Martha et al. (2012) used a bi-temporal approach for eight image pairs and reported for each time period individual accuracies ranging from 71.5% to 96.7% for the *Detection Percentage* and approx. from 50% to 90% for the *Quality Percentage*. These accuracy statistics are based on the areal extent of the identified landslides and are of comparable or in part lesser accuracy than the results that were achieved in this study for the automated usage of selection category *II′* (*Detection Percentages* of 88%–93% and *Quality Percentages* of 82.9%–84.8%). Martha et al. (2012) have also assessed the accuracy for the number of identified landslides resulting in *Quality Percentages* between approx. 20% and 70%, which are also comparable to the results of this study in showing lower accuracies for the identified number of landslides (*Quality Percentages* of 34.6%–44.1%).

Overall, the knowledge-based parameterization of the NDVI thresholds and the relief properties enabled a high mapping quality for both validation sites despite their differences in natural and land use conditions, RapidEye data coverage, and spatiotemporal landslide activity. This opens up the principle opportunity for applying the approach to other landslide-affected areas characterized by the presence of landslide-related changes in vegetation cover. In this context, the wider applicability of the developed approach also depends on the availability of suitable satellite remote sensing data. The RapidEye time series data used in this study represent an ideal database characterized by high spatial and temporal resolution. However, the approach also comprises the potential for the extension to data acquired by other satellite-based remote sensing systems, as it is primarily based on the NDVI representing a robust spectral index which can be calculated from most available multispectral satellite remote sensing data.

7 Conclusions

The developed automated approach is capable of object-oriented automated mapping of spatiotemporal landslide activity using optical satellite time series data and a digital elevation model. The approach builds on temporal NDVI-trajectories that represent pixel-based temporal footprints incorporating a variable number of multi-temporal data acquisitions. They enable the continual analysis of landslide-related surface cover changes over longer periods of time allowing their separation from other land cover changes based on differences in temporal evolution of the vegetation cover. To enable a meaningful evaluation of the automatically mapped landslide objects, they are characterized by uncertainty-related landslide likelihood classes. Based on these classes, the approach can be performed in a fully automated way if only objects of higher landslide likelihood are included or, in a semi-automated manner, if all identified landslide objects are considered independent from their landslide likelihood. This way, the knowledge-based approach accommodates different user needs and allows for efficient object-oriented automated landslide mapping.

The accuracy assessment of the presented approach has proven its suitability for multi-temporal mapping of landslides of different sizes, shapes, types, and activity styles under varying natural and land use conditions with a high mapping accuracy of a *Quality Percentage* of 80%. Thus, the approach enables detailed spatiotemporal assessment of landslide activity over large areas during longer periods of time. Its application to the 7500 km^2 study area in southern Kyrgyzstan has revealed a perpetual process activity in this area between 2009 and 2013 which could not be assessed by the local authorities solely relying on field-based landslide reporting and mapping. Consequently, the approach has enabled the monitoring of the recent spatiotemporal landslide activity, thereby contributing to the objective and reproducible generation of multi-temporal landslide inventories, which have been thus far largely missing for the analyzed region in southern Kyrgyzstan and many other parts of the world (Guzzetti et al. 2012; Petley 2012). The results of the spatiotemporal landslide mapping can also be further analyzed in relation to landslide triggering and predisposing factors in order to improve the regional process understanding as an important prerequisite for a spatially and temporally differentiated hazard assessment.

Since the approach is solely based on the NDVI, in principle it can be extended to a wide range of multispectral satellite remote sensing data comprising the required spectral bands. Taking into account the average size of approximately 13000 m^2 of the landslides that are identified in the study area in southern Kyrgyzstan, sensors with up to 30 m spatial resolution are considered to be suitable for automated landslide mapping in this region. Thus, the RapidEye time series database has been extended further into the past based on archived data of various multispectral systems, such as Landsat, SPOT and ASTER (Behling et al. 2014b). In this context new opportunities will open up with the upcoming launch of the Sentintel-2 system (Drusch et al. 2012). Its envisaged revisiting time of up to five days, the spatial resolution of 10 m, and the large swath width of 290 km will make the data of Sentinel-2 especially suitable for spatiotemporal monitoring of landslide activity in global hotspots (Nadim et al. 2006), such as South America (e.g. Brazil, Colombia) and Southeast Asia (e.g. Taiwan, Thailand, Philippines). However, the global transferability of the developed approach will require further methodological development in order to adapt it for regions where the natural environments largely differ from the conditions in Central Asia.

Acknowledgments

The authors acknowledge the helpful comments and suggestions from several anonymous reviewers that substantially contributed to clarifying and improving the manuscript. The authors also thank the German Aerospace Agency (DLR) for providing RapidEye data by the RESA (RapidEye Science Archive) program. This work was funded by the German Federal Ministry of Research and Technology (BMBF) within the framework of PROGRESS (Potsdam Research Cluster for Georisk Analysis, Environmental Change and Sustainability).

Author Contributions

Robert Behling and Sigrid Roessner designed the research. Robert Behling developed the approach, performed the programming and conducted the analysis. Robert Behling and Sigrid Roessner prepared the manuscript. Birgit Kleinschmit and Hermann Kaufmann contributed to the discussion and general paper review.

Conflicts of Interest

The authors declare no conflict of interest.

IV Long-Term Landslide Activity (Multi-Sensor Approach)

Behling, R., Roessner, S., Golovko, D. & Kleinschmit, B., (submitted). Derivation of Long-Term Spatiotemporal Landslide Activity–An Automated Multi-Sensor Time Series Approach. *Remote Sens. Environ.*

Received: 02 September 2015

Abstract

The main principle in landslide hazard and risk assessment is that conditions of past landslide activity indicate future landslide occurrence. To allow the analysis of past long-term spatiotemporal landslide frequencies, this paper presents an automated method for the derivation of multi-temporal landslide inventories, which have been the bottleneck in regional landslide hazard and risk assessment. The developed method uses globally archived satellite remote sensing data for a retrospective systematic assessment of past multi-temporal landslide activity. Landslides are automatically identified as spatially explicit objects based on landslide-specific vegetation cover changes using temporal NDVI-trajectories and complementary relief-oriented parameters. To enable long-term analysis of large areas with highest possible temporal resolution, the developed method facilitates the use of a large amount of optical multi-sensor time series data characterized by highly irregular temporal resolution. The database of this study consists of 212 datasets comprising the freely available Landsat TM & ETM+ data as well as SPOT 1 & 5, IRS1-C LISSIII, ASTER and RapidEye data. They have been acquired between 1986 and 2013 and cover a landslide-prone area of 2500 km² in Southern Kyrgyzstan. The application of the developed approach to this database led to the identification of 1583 landslide objects ranging in size between 50 m² and 2.8 km². Accuracy assessment of two independent validation sites resulted in Detection Percentages exceeding 90% and Quality Percentages of up to 80%. Spatiotemporal analysis of the landslides detected during these 27 years revealed constantly ongoing landslide activity of varying intensity. The highest overall landslide rates occurred in 2003 and 2004 exceeding the long-term annual average rate of 57 landslides per year by more than five times. The results of automated landslide detection also enabled the determination of areas of highest landslide activity, whereas most of them are persistent over time. Moreover, first statistical analyses of the spatiotemporal landslide frequencies revealed distinct dependencies to specific morphological settings as well as a moderate correlation with the triggering factor precipitation. Altogether, the developed automated approach has proven to be suitable for deriving multi-temporal landslide inventories in an efficient and reproducible way with a high degree of completeness, allowing the retrospective analysis of spatiotemporal landslide activity as an important prerequisite for probabilistic landslide hazard assessments at a regional scale.

1 Introduction

"The past and present are keys to the future," (Varnes 1984) is a long-standing principle in landslide hazard and risk assessment indicating that future landslides are more likely to occur under the same or similar conditions of past landslides (Corominas & Moya 2008; Fell et al. 2008; Guzzetti et al. 2012). To allow profound spatiotemporal analysis of past landslide activity, systematic and area-wide landslide inventories need to be established, which contain the location, extent and date of past landslides as well as other qualitative and quantitative parameters (Malamud et al. 2004; van Westen et al. 2008). Landslide inventories can be differentiated into historical, event-based, seasonal and multi-temporal inventories (Guzzetti et al. 2012). A historical inventory comprises landslides with very limited knowledge about the date and place of their occurrence. Event-based and seasonal inventories contain landslides that have been mapped related to either a single or multiple triggering events occurring within one season of landslide activation. Thereby, the date

of landslide occurrence is assigned to the date of the triggering event, such as earthquakes or intense rainstorms. In contrast, multi-temporal inventories are created by a repeated documentation of landslides independently of specific triggering events during a longer period of time, whereas the dates of occurrence are either precisely known or assigned to the time period between repeated documentation. Thus, multi-temporal landslide inventories represent an important requirement for probabilistic landslide hazard assessment, since their systematic spatiotemporal landslide documentation allows the determination of spatiotemporal variations of landslide frequencies (Guzzetti et al. 2005; van Westen et al. 2008). However, due to the very high mapping effort of such multi-temporal inventories, they are largely unavailable for most parts of the world (Guzzetti et al. 2012). The existing ones have mostly been prepared for relatively small areas (several tens of square kilometers) by combining field investigations, analysis of archival data and visual interpretation of optical remote sensing imagery, such as aerial photographs and high-resolution satellite data (Galli et al. 2008; Klimeš 2013; Ghosh et al. 2012; Fiorucci et al. 2011; Saba et al. 2010). In general, the temporal update rate of the existing inventories is often limited to several years or even decades. To improve the spatial and temporal completeness of such multi-temporal inventories, the development of efficient landslide mapping strategies is of utmost importance.

So far, several studies have demonstrated the potential of optical remote sensing for (semi-)automated mapping of landslide occurrence. They mostly aimed at the systematic assessment of spatial variations in landslide activity related to an individual well-known triggering event, such as earthquakes (Lacroix et al. 2013; Lodhi 2011; Parker et al. 2011; Yang & Chen 2010) and hydrometeorological extreme events (Borghuis et al. 2007; Mondini et al. 2011b; Tsai et al. 2010). For this purpose, either mono-temporal classification techniques have been applied to imagery of a single acquisition date after the triggering event (Barlow et al. 2006; Othman & Gloaguen 2013) or various change detection techniques have been used to identify landslide-related surface changes that occurred between pre-event and post-event data acquisitions (Hölbling et al. 2015; Lu et al. 2011; Nichol & Wong 2005; Stumpf & Kerle 2011).

Although optical remote sensing data have been widely used for identifying the spatial variability of event-based landslide activity, little attention has been paid to the systematic analysis of temporal variations in landslide activity over longer periods of time. To do so, efficient strategies are required that allow the automatic derivation of multi-temporal landslide inventories. By now, Martha et al. (2012, 2013) have presented a study for the semi-automatic derivation of a multi-temporal inventory. They applied an approach that had been initially designed for event-based mapping to a multi-temporal database of annual data coverage from 1998 to 2009 for an area of 81k m² in the Indian Himalaya. However, the evaluation of spatiotemporal landslide activity requires the analysis of larger areas with high temporal resolution. In the result, suitable image databases contain a large amount of data with variable image characteristics, originating from seasonal variations in data acquisition and the natural variability of the land surface and landslide phenomena throughout a larger natural environment. At the same time, such time series databases open up new opportunities to design landslide identification approaches taking into account the multi-temporal representation of landslide processes. We developed such an approach allowing automated detection of landslide objects based on the analysis of temporal trajectories of landslide-related vegetation changes using optical time series data in combination with relief-based parameters (Behling et al., 2014a). The approach enabled automated multi-temporal mapping of landslides for an area of 7500 km² in Southern Kyrgyzstan based on high temporal resolution RapidEye data of up to six acquisitions per year between 2009 and 2013. However, due to the availability of the

RapidEye data this analysis was limited to a time span of four years. Hence, it needs to be extended for the derivation of past landslide activity in a more comprehensive way to serve as suitable input information for subsequent probabilistic landslide hazard assessment.

Against this background, the objectives of this study are

- the development of an automated remote sensing based approach for retrospective long-term multi-temporal landslide mapping and
- the derivation of a large area multi-temporal landslide inventory including the evaluation of past spatiotemporal landslide activity in order to demonstrate its potential use for further systematic hazard assessment.

The objective of long-term multi-temporal landslide mapping requires the extension of the existing RapidEye based-approach into a multi-sensor approach that allows the analysis of longest possible time series using all available optical satellite imagery acquired by different sensors. In this study, we combine the freely available Landsat TM & ETM+ data with data acquired by the SPOT 1 & 5, IRS1-C LISSIII, ASTER, and RapidEye sensors. The Landsat archive provides the longest existing time series and therefore serves as a crucial data backbone in remote sensing data scarce regions including many global landslide hotspots, such as Central Asia, South America and Southeast Asia (Nadim et al. 2006). Since in many of these regions reliable spatial reference information is missing, we also used the terrain corrected multi-temporal datasets from the Landsat archive as the topographic reference for the development of an automated co-registration procedure between satellite remote sensing datasets of variable spatial resolution and origin (Behling et al. 2014b). For this study, the co-registration procedure is applied to a multi-sensor database of high temporal resolution for a 2500 km² area in Southern Kyrgyzstan, forming the basis for the development of the multi-sensor landslide mapping approach presented in this study. The required methodological developments deal with the challenges arising from irregular temporal resolutions inherent in the long-term time series data, the variability introduced by the implementation of multiple sensors, the high amount of variable datasets, and the irregular and patchy spatial availability of remote sensing data throughout the study area. Moreover, the presented study also includes the application of the developed approach to the complete database in order to derive an area-wide long-term multi-temporal landslide inventory. This inventory is analyzed regarding spatial and temporal variations in past landslide activity, whereas the derived spatiotemporal variability of landslide occurrence is further evaluated against the morphological setting and the temporal variations of precipitation as a triggering factor in order to demonstrate the potential of the developed approach to facilitate probabilistic and spatially differentiated landslide hazard assessment.

2 Study Area and Database

2.1 Study Area

The study area (Figure 1A) of 2500 km² is located in Southern Kyrgyzstan at the eastern rim of the Fergana Basin, where the foothills of the Tien Shan mountain ranges are largely affected by a high landslide activity (Golovko et al. 2015; Havenith et al. 2015; Roessner et al. 2005). Since this region is an important human living space in the mountainous country, landslides represent a major natural hazard causing fatalities and severe economic losses. Large mass movements mostly occur in form of deep-seated landslides within weakly consolidated Mesozoic and Cenozoic sediments, which have been subjected to ongoing tectonic deformation (Roessner et al. 2005). Observations of landslide activity in Southern Kyrgyzstan have been carried out by local organizations since the 1950s focusing on areas in the vicinity of settlements, whereas these efforts have largely decreased after the independence of Kyrgyzstan in 1991 (Ibatulin 2011; Kalmetieva et al. 2009).

2.2 Remote Sensing Database

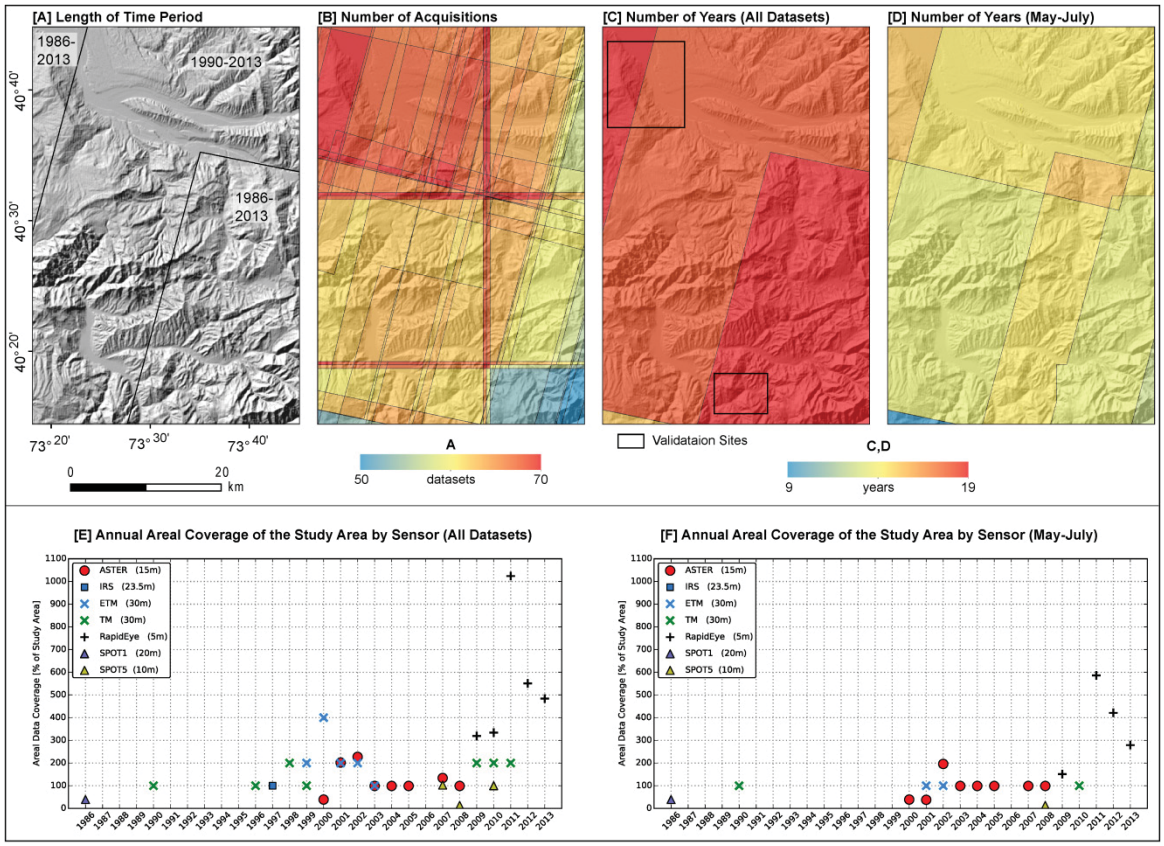

Figure IV-1. Time series database of optical multi-sensor data. A-D: Spatiotemporal distribution of the data within the study area. A: Length of time period. B: Number of repeated acquisitions. C: Number of years with available data coverage; location of validation sites. D: Number of years with data acquired in the growing season (May-July). E,F: Areal data coverage for the study area per year. Number of datasets: All: 212, May-July: 105.

To facilitate a comprehensive landslide mapping, a multi-temporal satellite remote sensing database has been established comprising data of seven optical sensors, i.e. SPOT 1 & 5, IRS1-C LISSIII, Landsat TM & ETM+, ASTER, and RapidEye. All datasets have been obtained in form of orthorectified standard data products in order to reduce preprocessing efforts (Behling et al. 2014b). The spatial resolution of the datasets ranges between 30 m for the Landsat and 5 m for the RapidEye

sensors (Figures 1E,F). A comprehensive overview of the used data including sensor characteristics can be found in Behling et al. (2014b). The database consists of 212 datasets covering a time span from 1986 to 2013. Since the first datasets, acquired by the SPOT 1 sensor (Figure 1E), cover only subsets of the study area, the analyzed time span starts in 1990 for the remaining parts (Figure 1A). In total, the database contains data acquisitions for at least 18 different years (Figure 1C), whereas the temporal resolution is variable in different parts of the study area and in different periods of the covered time span. The number of acquisitions varies between 50 and 70 datasets (Figure 1B), depending on the location within the study area. The time intervals between subsequent acquisitions range from six years (1990-1996) in the beginning of the time series (Figure 1E) to two weeks between the high temporal resolution data of the RapidEye sensor acquired between 2009 and 2013. Besides the multispectral remote sensing data, the study used a digital elevation model (DEM) of 30 m spatial resolution derived from the X-band data of the Shuttle Radar Topography Mission in February 2000 (Rabus et al. 2003).

2.3 Appearance of Landslides in the Multi-Sensor Time Series Database

In the existing multi-sensor database, landslide appearance is highly variable depending on the temporal acquisition characteristics and the spatial resolution of the data. In terms of temporal acquisition characteristics, two main aspects have to be considered, i.e. the season of data acquisition and the temporal gap between the failure and the first available data acquisition after the failure. In Figure 2A differences in landslide appearance between images acquired in the growing season and in the dry season are shown in an exemplary way. During the growing season, the removal of vegetation cover caused by landslide occurrence results in a much higher spectral contrast to the undisturbed vegetated surroundings than in case of the dry season. In the study area, the growing season usually spans from May to July. Towards the end of July, the amount of rainfall significantly decreases, and in combination with high temperatures, the vegetation cover experiences an increasing drought stress. Thus, the period between May and July is the most suitable one to identify landslide failures in optical satellite data acquisitions. Figure 1F shows the annual areal coverage of such ideal data acquisitions, whereas Figure 1D shows the number of years for which such coverage could be achieved. However, the database also comprises data acquisitions outside this optimal period (Figures 1C,E). They represent a valuable extension due to temporal and spatial shifts of the phenology between the years as well as time-independent spatial variations in the vegetation cover characteristics. They also reduce the length of the interval between subsequent data acquisitions within which a landslide could be automatically identified.

Figure 2B shows that a landslide is most evident right after the failure, whereas in the following years its appearance becomes less distinct because of the onset of revegetation. However, due to the typically rather deep disturbance of the affected Earth's surface and its increased susceptibility to erosion processes, most parts of the landslide stay largely unvegetated for several years. These revegetation processes show spatiotemporal variations caused by multiple factors, such as the type and size of the landslide, the depths of the active sliding plane and the intensity of subsequent reactivations. Deep-seated landslides often lead to a complete removal of the top soil and thus experience a slow subsequent revegetation and a long preservation of the largely unvegetated land surface, whereas shallow landslides and flows are characterized by less severe soil disturbance and thus a faster revegetation (Behling et al. 2014a).

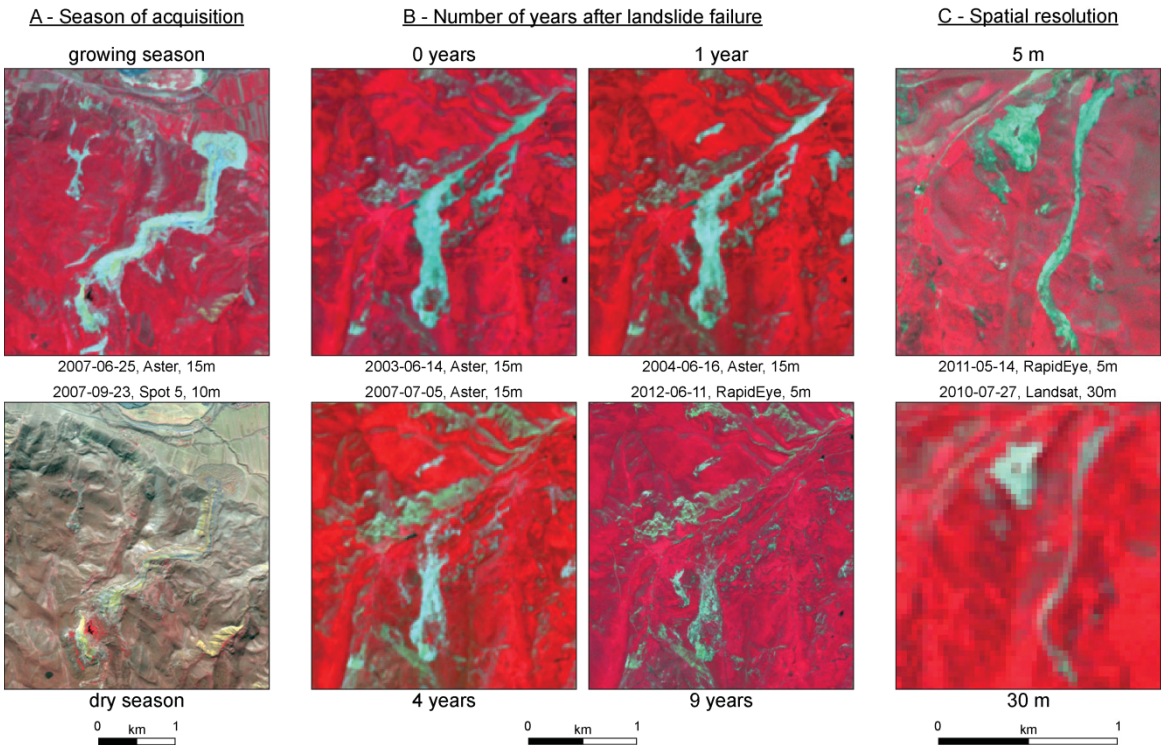

Figure IV-2. Comparison of landslide appearance in selected optical satellite remote sensing data of different characteristics.

Figure 2C shows the influence of the spatial resolution of the imagery on the landslide appearance by comparing the highest (5 m) and lowest (30 m) spatial resolution dataset contained in the database. The subset of Figure 2C shows a set of two landslides that are representative for the study area. The left one represents a rotational slide and the right one a combination of a slide and a flow. Both landslides are clearly visible in both spatial resolutions, whereas their spatial delineation is less precise in the lower resolution image. Moreover, Figure 2C shows that the lengthy shape of the flow reduces its detectability in the lower resolution data, whereas the compact shape of the rotational slide is better preserved in the lower resolution image. In general, the reliability of landslide detection is determined by the pixel size in relation to the landslide dimension, whereas the pixel size should not exceed the minimum dimension (length or width) of the landslide. Thus, the most common landslides of the study area (Figure 2C) are detectable in all available spatial resolutions, whereas the very small activations and narrow flows are better detectable in the datasets with spatial resolutions of 15 m or better (i.e. ASTER, SPOT 5, RapidEye). Since these small activations play a minor role in regional hazard assessment, the database is suitable for reliable spatiotemporal landslide detection in Southern Kyrgyzstan in terms of spatial resolution.

Overall, data acquisitions of high spatial resolution acquired in the growing season right after failure are most suitable for detecting the different types of landslide failures occurring in the study area. Furthermore, the interval between subsequent acquisitions needs to be as short as possible in order to achieve data acquisitions right after the landslide failures and to maximize the precision in determining the period of landslide occurrence. These different requirements result in a highly diverse database in terms of (i) spatial and spectral characteristics of the used data, (ii) variable time intervals between subsequent acquisitions, and (iii) differences in seasonal data acquisition, which all have to be considered in the method development (Section 3).

3 Method

The goal is the development of a methodology for automated multi-temporal mapping of landslides using a comprehensive and highly diverse multi-sensor time series database. For this purpose, the already developed multi-temporal landslide mapping approach (Behling et al. 2014a) needs to be extended to meet the requirements originating from the multi-sensor time series database covering several decades of data acquisitions in variable seasons with a highly irregular temporal and spatial resolution (Section 2). Thus, the approach needs to enable a robust and efficient identification of landslide objects independent from the spatial and spectral properties of the sensor as well as the year and season of data acquisition.

The methodology automatically identifies landslides by analyzing characteristic temporal vegetation cover changes that are related to the process of a landslide failure. Typically, landslides are represented by an abrupt disturbance of the vegetation cover due to the actual failure and by less distinct changes due to revegetation after the failure. This focus on vegetation changes allows for a cross-sensor comparison, since common multispectral satellite sensors comprise the spectral range of visual and near infrared, which is very suitable for vegetation-related issues. Thus, the temporal variations of the NDVI are used to separate landslide-specific vegetation changes from other temporal variations of the vegetation cover (e.g. changes in natural vegetation or in agricultural areas) as well as from permanently non-vegetated areas (e.g. urban structures, water bodies, outcrops).

Figure 3 depicts the overall approach for automated multi-temporal landslide mapping using long-term multi-sensor optical time series data. All of the methodological developments have been realized using the open source programming language Python. The developed system consists of three major parts. For each part, Figure 3 lists the specific processing steps in a dashed box and schematically shows the main features of the NDVI-based temporal analysis. Part 1 comprises the preprocessing procedures aiming at data homogenization as a prerequisite for subsequent multi-temporal change detection (Section 3.1). Part 2 deals with the construction of the NDVI time series data cubes (Section 3.2) forming the input data for the automated identification of landslide objects performed in part 3, which builds on the derived temporal NDVI-trajectories and relief-based properties (Section 3.3). In the following, these three parts are described in more detail focusing on the extensions that were made in order to accommodate the needs for automated multi-sensor analysis of longer time periods. The output of the extended approach is presented in an exemplary way in Section 3.4.

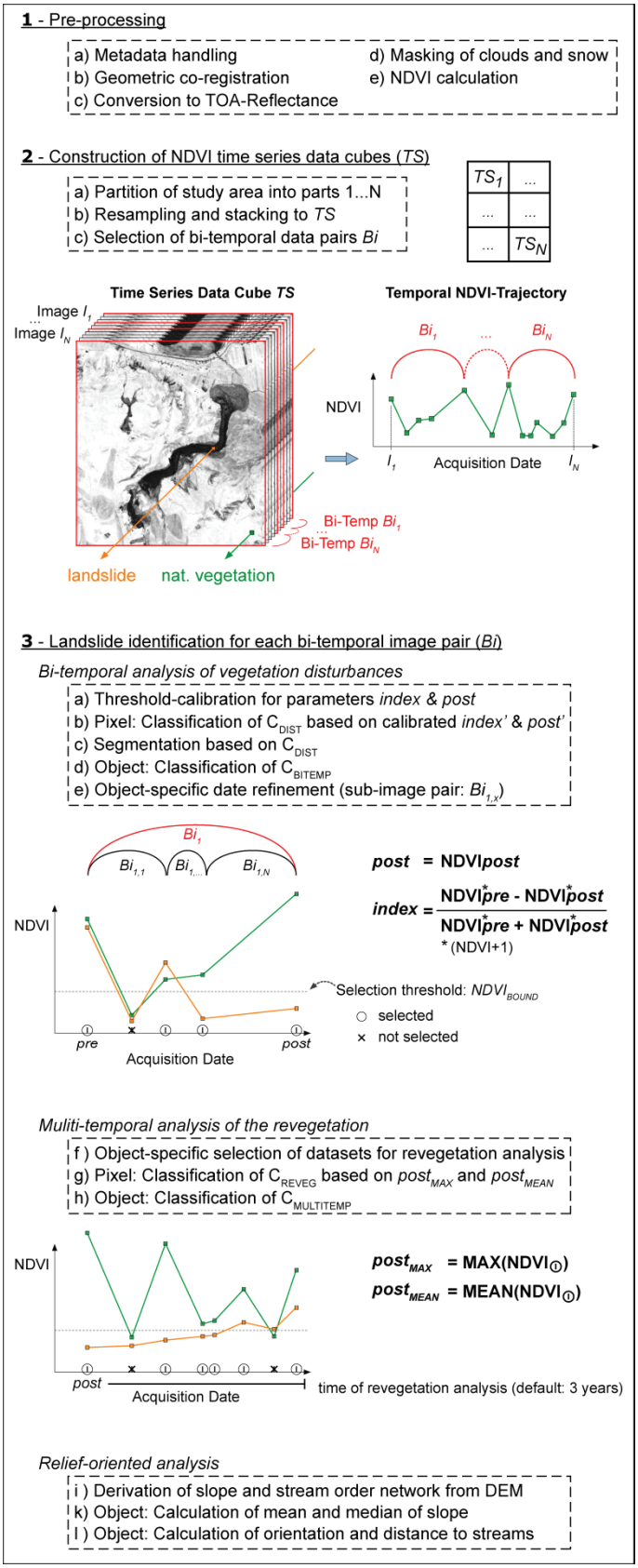

Figure IV-3. Schematic overview of the overall approach. For each part (1-3), the specific processing steps are listed in a dashed box. Main features and parameters of the processing steps are illustrated schematically. The specific values of the parameters are listed in Table 1. (important developed extensions compared to Behling et al. (2014a): 1a,c, 2a,b,c and 3a,e,f)

Table IV-1. Parameters implemented in the automated landslide mapping approach. (The gradient indicates landslide possibility. The higher the saturation the higher the landslide probability of the specific parameter.)

	Pixel-based classification		Object-based classification	
	Class	**Value**	**Class**	**Value**
Bi-temporal vegetation disturbance	C_{DIST}*	post: < 0.26 / < 0.21 / < 0.17 index: > 1.04 → 1 / 4 / 7 > 1.08 → 2 / 5 / 8 > 1.13 → 3 / 6 / 9	C_{BITEMP}	3: C_{DIST} 9 ≥ 30% 2: sum(C_{DIST} 6-9) ≥ 40% & C_{DIST} 9 ≥ 30% 1: sum(C_{DIST} 4-9) ≥ 85% & sum(C_{DIST} 8-9) > 0%
Multi-temporal revegetation	C_{REVEG}	$post_{MAX}$: < 0.53 / < 0.35 / < 0.26 $post_{MEAN}$: < 0.30 → 1 < 0.28 → 2 < 0.24 → 3	$C_{MULTITEMP}$	3: C_{REVEG} 0 ≤ 35% & C_{REVEG} 3 > 0% 2: C_{REVEG} 0 ≤ 35% & sum(C_{REVEG} 2-3) ≥ 20% 1: C_{REVEG} 0 ≤ 45% & sum(C_{REVEG} 2-3) ≥ 30%
Relief position			C_{RELIEF}	3: C_{SLOPE} (mean: 7°-30° & median >8°) & C_{SO} (Δorientation>20° & distance >100m) 2: C_{SLOPE} (mean: 7°-30° | median >8°) & C_{SO}(Δorientation>15° & distance >70m) | C_{SLOPE} (mean: 7°-30° & median >8°) & C_{SO} (Δorientation>20° & distance >100m) 1: C_{SLOPE} (mean: 7°-30° | median >8°) & C_{SO} (Δorientation>15° & distance >100m)
Overall Landslide Likelihood			LL	C_{BITEMP} / $C_{MULTITEMP}$ / C_{RELIEF} I: 3 / 3 / 3 — Fresh landslide failure with slow revegetation** II: 1-3 / 3 / 3 — Reactivated landslide with slow revegetation** III: 1-3 / 1-3 / 3 — Landslide with higher revegetation rate** IV: 1-3 / 1-3 / 1-3 — Landslide with higher revegetation rate on gentle slope**

* Default threshold values of *post* and *index*. (might change due to a preceding bi-temporal calibration step.)
** Landslide phenomena typically associated to specific overall landslide likelihood class (*I-IV*)

3.1 Pre-Processing

In time series analysis, pre-processing aims at minimizing artifact changes that are induced by geometric mismatches and radiometric differences between the images, as well as the temporary presence of clouds and snow (Coppin et al. 2004; Hussain et al. 2013). In terms of efficiency, the approach requires automated and robust pre-processing procedures that are suitable for handling such a large and heterogeneous database. For this purpose, the approach comprises customized automated routines for data import and metadata homogenization in order to deal with the different data structures of the standard data products. For geometric adjustment, an automated correlation-based image-to-image co-registration approach has been developed (Behling et al. 2014b). This approach aligns orthorectified standard data products of different optical sensors and of different seasonal and annual acquisition dates. This alignment is performed by determining and correcting for the spatial offsets between the datasets and a common spatial reference represented by the globally available terrain-corrected Landsat (L1T) time series data. An accuracy assessment of the aligned database has revealed an overall relative accuracy of 17 m and an absolute accuracy of 23 m (RMSE), which is considered to be sufficient for multi-temporal landslide detection and subsequent GIS-based analysis of the results in combination with other geospatial data (Behling et al. 2014b).

To reduce the radiometric differences between the images, a conversion of DN to TOA-reflectance is carried out. This conversion adjusts for radiometric scene variations caused by solar illumination differences, sensor specific gains and offsets as well as differences in seasonality (Earth-Sun distance). The influence of the remaining radiometric variability mainly caused by differences in atmospheric conditions is further reduced by using the normalized difference vegetation index (NDVI) as the basis for time series analysis.

The masking of clouds and snow is carried out by a threshold-based approach classifying pixels of clear or possible cloud/snow coverage in the green spectral bands of all the images contained in the time series database. If the classified pixels are spatially connected, they are segmented to objects.

The decision whether such an object is included in the mask is based on specific object characteristics, i.e. proportion of clear pixels within the segment, the size of the segment, as well as the temporal stability of the segment (presence throughout the time series). This way the approach is able to separate between permanent bright objects (e.g. sand and urban objects) that are defined by high temporal stability and a relatively small size, and temporary ones (e.g. clouds and snow).

3.2 Construction of Temporal NDVI Data Cubes

The spatially and temporally inhomogeneous database of masked NDVI images are compiled to NDVI data cubes forming the basis for efficient landslide identification. In a first step, the study area is divided in a user-defined number of sub-parts (1…N), which on the one hand reduces the required main storage for data processing and, more important, allows the adaption of the landslide identification approach to large variations of natural conditions within the study area. This adaption is done by calibrating the bi-temporal change detection procedure (Section 3.3.1) to the vegetation cover characteristics of this sub-part. In this study, we divided the study area in six tiles, based on the RapidEye tile structure (25x25 km² tiles). The next step is the construction of the complete NDVI time series data cube for each sub-part ($TS_{I,N}$). For this purpose, the datasets available for each sub-part are resampled to a common spatial resolution and stacked to a *TS*. In this study, the common spatial resolution is defined by the highest spatial resolution available in the multi-sensor database, i.e. 5 m pixel size of the RapidEye data.

After the construction of the *TS*, the approach yields the opportunity to preselect data acquisitions from the complete time series that are most suitable in terms of identifying landslide-related land surface changes. As stated in Section 2, suitable datasets are those, which have been acquired in the growing season and are characterized by a higher spatial resolution. The selected images define the subsequent bi-temporal image pairs (*Bi*) forming the basis for the identification of potential landslide objects. One of the selected images serves as a calibration dataset representing the typical vegetation cover characteristics during the growing season for the area covered by the respective *TS*. The unselected images are used for a subsequent refinement of the time period of landslide occurrences (Section 3.3.1). In case of the database at hand, high-resolution data acquisitions during the growing season are available since 2009 (5 m resolution RapidEye data). For the 2000s, datasets of the ASTER and the SPOT 5 sensors form a suitable time series with spatial resolutions of 15 m and 10 m, respectively. For the years before, data of lower resolution and in part acquired outside of the main growing season (e.g. Landsat image of 11 Aug. 1998) had to be selected in order to maintain a high temporal resolution throughout the complete time series. The calibration images of the NDVI time series data cubes (*TS*) are defined by RapidEye datasets that have been acquired in May 2011. Overall, the decision which datasets are selected varies for each *TS* due to the differing spatial availability of individual image datasets throughout the study area.

3.3 Automated Landslide Identification

The resulting temporal NDVI data cubes with their preselected datasets are the basis for the NDVI-trajectory-based identification of multi-temporal landslide occurrence. The preselected datasets represent bi-temporal data pairs (*Bi*) in which landslide occurrence can be identified. For each data pair the approach analyzes the degree of landslide-related bi-temporal vegetation changes serving as the basis for the segmentation of landslide candidate objects. Afterwards, the remaining datasets that have been acquired in between the dates of the initial bi-temporal data pair are included to refine the time period of landslide occurrence. The resulting landslide candidate

objects (Section 3.3.1) are further evaluated in regard to their plausibility considering multi-temporal revegetation and relief-oriented parameters (Section 3.3.2) to reduce the likelihood of false identifications. For this purpose, we developed a rule-based landslide identification approach, which builds on multiple pixel- and object-based parameters to analyze the landslide-related vegetation changes and relief properties (Table 1). This parameterization is based on multiple thresholds, in order to allow for uncertainty-related analysis (adapted from Castilla et al., 2009) facilitating the approach to accommodate the natural variability of the landslide phenomena evident within a single landslide object as well as between different landslide types, which is in detail described in Behling et al. 2014a.

3.3.1 Identification of Landslide Candidate Objects

In our previously developed approach (Behling et al. 2014a), the identification and segmentation of landslide candidate objects is based on change detection algorithms using multiple thresholds to analyze the landslide-related vegetation disturbances (C_{DIST}) between a bi-temporal image pair (*Bi*) that has been acquired during the growing season. Since the long-term data archive also comprises images acquired outside the growing season, the images of a bi-temporal image pair may strongly differ in their vegetation conditions. Therefore, we implemented a calibration procedure that pre-calibrates the default threshold values of the *index* and *post* parameter (Figure 3, Table 1) used for classifying the landslide-related vegetation disturbances (C_{DIST}) occurring between a bi-temporal image pair (*Bi*). The *index* parameter describes the landslide-related NDVI decrease between the pre- and post-event image. The *post* parameter specifies typical NDVI values of a disturbed vegetation cover or bare soil, which are present in the post-event image after landslide failure. The calibration procedure is expressed by the following equations,

$$index' = index + \frac{VEG_{PRE} - VEG_{POST}}{VEG_{PRE} + VEG_{POST}} \quad (1)$$

$$post' = post + \left(VEG_{POST} - VEG_{CAL}\right) \quad (2)$$

whereas *VEG* represents the average NDVI value of the possibly vegetated pixels (pixels of NDVI > 0.17), which are contained in the pre-event (*PRE)*, the post-event image (*POST*), and the calibration image (*CAL*). This way, the parameters are calibrated by taking into account the vegetation cover characteristics inherent in the analyzed image datasets. The adaption of the *index* parameter corrects for the influence resulting from seasonal differences between the pre- and post-event image. The adaption of the *post* parameter corrects for seasonal differences between the post-event image and the calibration dataset of a NDVI data cube, which represents the typical vegetation cover characteristics for the growing season. This way the differentiation between the landslide-related disturbed vegetation cover and the surrounding vegetation is adapted to the actual vegetation conditions in the post-event image.

Figure 4 exemplarily demonstrates the calibration procedure. It compares the default and calibrated bi-temporal identification of pixels that are affected by landslide related vegetation disturbance (C_{DIST}) and their subsequent segmentation to landslide candidate objects. Figure 4A represents the comparison of two images that have been acquired during the growing season. In this standard case, the default and calibrated thresholds perform very similarly, resulting in a reliable pixel-based identification of landslide-related bi-temporal vegetation change (C_{DIST}). This enables a robust segmentation of the spatially connected C_{DIST} pixels to landslide candidate objects. These candidate

objects are further classified regarding their bi-temporal landslide likelihood (C_{BITEMP}) based on the proportions of the C_{DIST} pixels within each object (Table 1). In case an object meets none of the criteria described in Table 1, it is classified as false positive (e.g. background noise) and will be removed from the selection of landslide candidate objects. Applying this procedure to the bi-temporal image pair of Figure 4A enables the identification and delineation of the three landslides that have occurred during the given time period. In Figures 4B,C the bi-temporal comparison includes an acquisition outside of the growing season, when the vegetation had already experienced a high drought stress. In Figure 4B, the dataset acquired under dryer conditions (represented by the Landsat TM image from 11 August 1998) serves as the post-event image and in Figure 4C as the pre-event image within the bi-temporal image pair (*Bi*). In case B, the dryer post-conditions result in an area-wide NDVI decrease for the bi-temporal image comparison. The default thresholds result in an overestimation of C_{DIST} pixels, because dried vegetation tends to be mistaken as landslide-related slight vegetation disturbances. In case C, the default values result in an underestimation of C_{DIST} pixels, because a landslide is characterized by a much lower NDVI decrease, due to the lower NDVI values of the dry pre-event condition. However, the application of the calibration procedure eliminates to a large degree these over and underestimations, and thus significantly improves the subsequent segmentation of landslide candidate objects and their classification regarding bi-temporal likelihood. As a result, the calibration allows for the correct identification and delineation of the single landslide depicted in Figure 4B as well as the two landslides shown in Figure 4C.

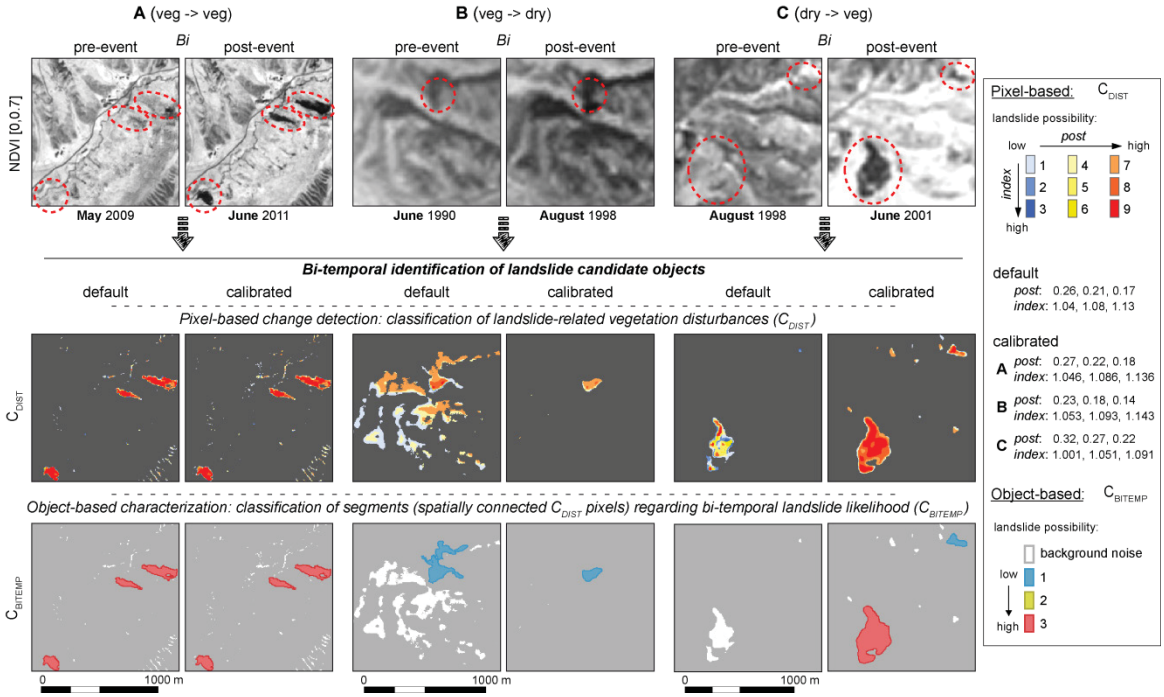

Figure IV-4. Bi-temporal calibration procedure. Comparison of calibrated thresholds to the default thresholds of Behling et al. (2014a) for three test cases (A-C). A: Pre- and post-event image are acquired in the growing season ranging from May and July (standard case). B: Pre-event = growing season, post-event = dry season. C: Pre-event = dry season, post-event = growing season. Red ellipses represent landslide occurrences during the time-period of the bi-temporal image pair.

The time period of occurrence for the resulting landslide candidate objects is determined by the acquisition dates of the analyzed image pair (*Bi*). However, the approach enables further temporal refinement for each landslide object by the subsequent selection of the bi-temporal sub-pair ($Bi_{x,x}$) that shows the first distinct evidence of that landslide. The procedure solely considers datasets with a significant vegetation cover surrounding the landslide object in order to ensure a correct refine-

ment. A dataset meets this criterion if the average NDVI in the surroundings of the object – defined by a 300 m buffer – is higher than the lowest default threshold of the *post* parameter (i.e. 0.26). After defining the image sub-pairs $Bi_{x,x}$ for each object, the bi-temporal change detection (C_{DIST}), is performed iteratively between the pre-event image of Bi_1 and the images of the sub-pairs ($Bi_{1,1...n}$). The first pair that shows a distinct landslide-related vegetation disturbance for the analyzed object, defined by an average C_{DIST} value of more than 1, determines the refined time period of landslide occurrence. Figure 5 illustrates the these steps of the refinement procedure in an exemplary way for a landslide that has been identified in a bi-temporal image pair (*Bi*) of two RapidEye datasets acquired 17 May 2009 and 14 May 2011. Between these RapidEye acquisitions, three further acquisitions are available, whereas two of them meet the criterion of significant vegetation cover around the identified object. Compared to the RapidEye acquisitions these datasets are characterized by a lower spatial resolution and/or less developed vegetation cover. Nevertheless, the refinement procedure allows the identification of the first evidence of the landslide in the Landsat image of 27 July 2010, resulting in a refined time period between 21 April 2010 and 27 July 2010. Thus, the approach uses the most comparable datasets to segment the landslide candidate objects and includes lower resolution images and/or images far outside the growing season for the refinement procedure without altering the shape of the identified object.

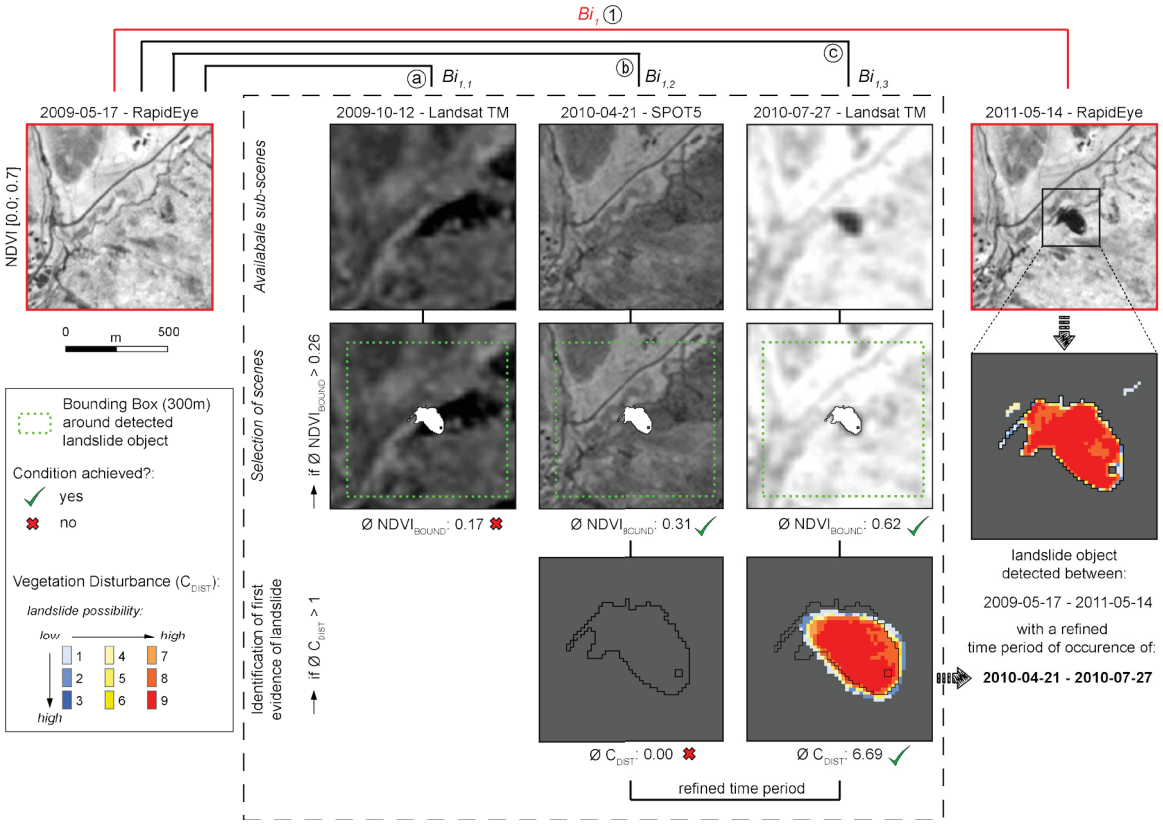

Figure IV-5. Refinement of the time period of landslide occurrence. 1: Bi-temporal vegetation analysis between bi-temporal image pairs (Bi) and subsequent segmentation to the landslide candidate object (black border). 1a)–1 c): Identification of Bi1,x that shows the first distinct evidence of that landslide.

3.3.2 Plausibility Check of the Landslide Candidate Objects in Respect to Revegetation Rates and Relief Position

The identified landslide candidate objects resulting from the bi-temporal change detection are further evaluated regarding their plausibility in terms of their revegetation characteristics and their relief position. The analysis of revegetation characteristics aims at the differentiation between landslides and similar bi-temporal vegetation changes, such as the ones caused by harvested fields. After landslide failure, the disturbed or removed material exposed to the surface experiences slow revegetation, whereas harvested fields are characterized by much higher revegetation rates. The approach evaluates the revegetation for the subsequent three years after the failure by classifying each pixel of the identified objects into four revegetation classes (C_{REVEG}) based on the combined use of the NDVI parameters $post_{MAX}$ and $post_{MEAN}$ (Figure 3, Table 1). For this purpose, an object-specific selection of datasets is carried out that follows the same procedure as described for the date refinement step (Section 3.3.1, Figure 5). This way, revegetation can be analyzed for each landslide object separately, allowing to include as many as possible datasets that are suitable for temporal vegetation change analysis and are available for the specific landslide object within three years after the failure. This object-specific data selection for pixel-based revegetation analysis (C_{REVEG}) represents an important extension of the approach compared to Behling et al. (2014a) in order to accommodate the seasonal and spatial variability of vegetation cover characteristics inherent in the multi-sensor database. Based on the proportions of the pixel-based C_{REVEG} classes, the landslide candidate objects are evaluated as a whole in respect to their revegetation status. As a result, objects with a very high revegetation rate are excluded from the landslide candidate objects and the remaining ones are classified into three classes of multi-temporal landslide likelihood ($C_{MULTITEMP}$) described in Table 1.

Furthermore, the landslide candidate objects are evaluated in respect to their relief position, which is characterized by statistics of the slope (C_{SLOPE}) and parallelism of the objects related to streams (C_{SO}). This way, the approach follows earlier developments of Behling et al. (2014a). This relief-based analysis aims at the elimination of false positives that are similar to landslide-related changes in terms of bi- and multi-temporal vegetation characteristics. The procedure allows for excluding false positives that are located on flat terrain and that are caused by flooded rivers or local co-registration errors mostly occurring in steep valleys. The remaining landslide candidate objects are classified into three classes of relief-oriented landslide likelihood (C_{RELIEF}) described in Table 1.

3.4 Output

After applying the landslide identification approach (Section 3.3) to all subsequent bi-temporal image pairs (*Bi*) included in the time series data cubes (*TS*), the results in form of the identified landslide objects are stored in a shapefile. For each object, several quantitative and qualitative characteristics are derived comprising the time period of landslide occurrence and the main landslide likelihood classes resulting from the automated identification process, i.e. C_{BITEMP}, $C_{MULTITEMP}$, C_{RELIEF}. Based on these three classes, each object is further characterized by an overall landslide likelihood (LL), describing the probability of that object being a landslide in respect to the automated identification process. This overall landslide likelihood is differentiated into the four classes I-IV (Table 1) and enables an uncertainty-related discrimination of the results in subsequent expert-based evaluations. Moreover, these classes also allow to a certain degree an interpretation of the landslide phenomena. For example, a landslide object of the highest overall landslide likelihood class I is characterized by high bi-temporal vegetation loss ($C_{BITEMP} = 3$), low revegetation rates ($C_{MULTITEMP} = 3$) and high relief-oriented landslide likelihood ($C_{RELIEF} = 3$), and therefore most

likely represents a deep-seated landslide failure of severe and long-lasting land surface disturbances. Table 1 lists these landslide-related interpretations for all of the four classes I-IV (further details can be found in Behling et al. (2014a)).

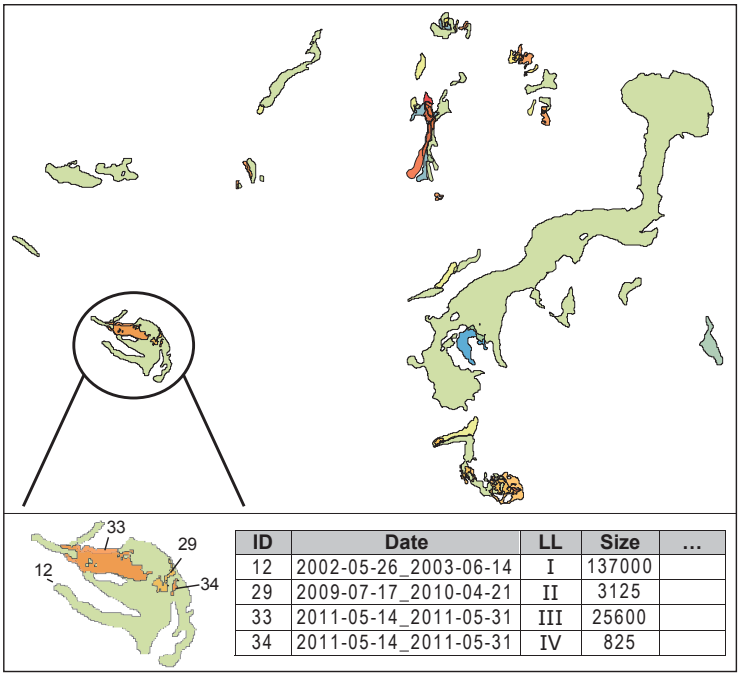

Figure IV-6. Exemplary output of the automated multi-temporal landslide mapping approach. Color of landslide objects represents the time period of occurrence. Bottom: Spatial subset of identified landslide objects with a selection of related attributes.

Additionally, the identified objects are characterized by quantitative landslide attributes, such as the size and the average slope of an object as well as by several object shape-oriented parameters such as length, compactness, entropy, etc. Figure 6 exemplarily shows the multi-temporal mapping results comprising landslides of different sizes, shapes and time periods of occurrence. The approach also allows the identification of reoccurring landslide activity resulting in spatially overlapping landslide objects originating from different time periods.

4 Accuracy Assessment

Systematic accuracy assessment is carried out for two spatially independent validation sites (outlined in Figures 1, 8) named *Uzgen* (12x14 km²) and *Kainama* (5.5x7.5 km²). They have been subject to long-term landslide activity and represent contrasting natural environments that are representative for the whole study area. Both sites are dominated by pastures and grassland, but are also covered by different types of non-vegetated areas, which are likely to be confused with landslides in optical remote sensing data. These non-vegetated areas comprise settlement areas (e.g. streets, buildings), rock outcrops, harvested fields, and water bodies. The specific spatial locations of the validation sites result in different multi-temporal remote sensing data coverages, which are available in the process of the automated landslide identification (Figure 1).

For both validation sites, landslide reference maps were produced by visual interpretation of the available remote sensing data complemented by comprehensive field surveys that have been carried out since 1998 by the GFZ Potsdam in cooperation with the Kyrgyz Ministry of Emergency

Situations. In total, 124 landslides were mapped in *Uzgen* and 94 in *Kainama*. The *Uzgen* site is characterized by constant landslide activity with peaks in 1990, 2003/04 and 2009/10. For the *Kainama* site, main peaks have been observed in 1998 and 2002-2004. The sizes of the landslides vary from 455 m² to 2.9 km² and 216 m² to 0.3k m² for *Uzgen* and *Kainama*, respectively.

The automatically identified landslide objects are validated against the landslide objects of the reference maps to derive a quantitative accuracy assessment. For each of the analyzed time periods, this comparison results in one of the three validation categories true positive (TP), false negative (FN) and false positive (FP). TPs represent spatially and temporally correct identifications, FNs are reference landslide objects that are missing in the automatic identification and FPs represent identified objects that are not present in the reference map. Based on the relation between these validation categories, the mapping accuracy of the approach is determined by the four accuracy metrics relevant for object-based single target classifications, i.e. *Detection Percentage*, *Omission Error*, *Commission Error* and *Quality Percentage*. The *Detection Percentage* represents the percentage of spatially and temporally correct landslide identifications, *Commission* and *Omission Error* provide information about the influence of the two possible identification errors FP and FN, and the *Quality Percentage* represents an integrative indicator, expressing how likely a landslide is to be correctly identified (Behling et al. 2014a; Lee et al. 2003; Martha et al. 2012; Rau et al. 2014).

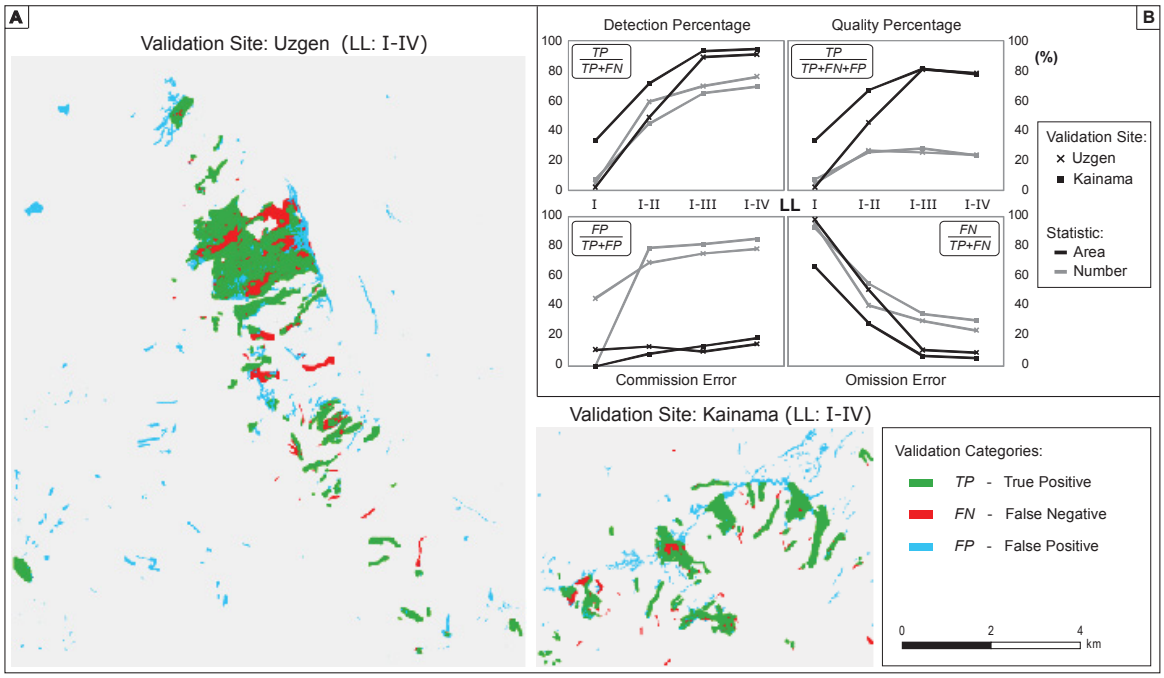

Figure IV-7. Results of accuracy assessment. A: Spatially explicit comparison of the automated mapping and the reference mapping for the two validation sites Uzgen and Kainama independent from the overall landslide likelihood LL. B: Accuracy metrics according to LL. (I-IV represents the complete mapping result of the approach, including all identified objects independent from LL; I-III: ignores objects of class IV; I-II: ignores objects of classes III and IV; I: ignores objects of classes II-IV.) Accuracy metrics are based on the validation categories TP, FN, FP (Table 2).

Figure 7A illustrates the spatially explicit comparison of the reference map and all automatically identified landslide objects regardless of the overall landslide likelihood (LL). Figure 7B shows graphs of the accuracy metrics for the area and number of the identified landslide objects. These accuracy metrics are derived for four different classes (I,I-II,I-III,I-IV)[4], whereas class I-IV corresponds to the complete mapping result and the other three to a sub-selection of the identified landslide results according to LL. For the complete mapping result (I-IV), high *Detection Percentages* of more than 90% for the landslide area and 70-80% for the number of landslides could be achieved. Missed landslides (FN) are mainly represented by small shallow landslides of longish shape and fast revegetation. The average size of the FN amounts to 20700 m², which is smaller than the average size of the reference landslides of 55400 m² (Table 2). The largest FN exist at the beginning of the analyzed time series during the long remote sensing data gaps from 1986 to 1990 and from 1990 to 1996. In these time periods, the approach missed eight landslides (FN) with sizes ranging from 12000 m² to 167000 m² with an average size of 84500 m². These rather large FN arise, because landslide failures at the beginning of such long time periods have already experienced a substantial revegetation before the acquisition of the post-event image (Figure 2B). Ignoring the landslide occurrences of these two long time periods reduces the average size of the FN to 7800 m² (Table 2).

Table IV-2. Statistics of the three validation categories (TP, FN, FP) in regard to number of landslides (N) and landslide-affected area (given in m²).

Validation Site	Validation Category	I		I-II		I-III		I-IV	
		N	Area	N	Area	N	Area	N	Area
Uzgen	TP	6	194,884	74	4,607,660	93	8,397,504	101	8,570,824
	FN	118	9,247,139	50	4,834,362	31	1,044,519	23	871,199
	FP	5	24,350	167	704,800	266	943,672	348	1,506,072
Kainama	TP	7	878,148	42	1,882,493	64	2,383,482	68	2,508,373
	FN	87	1,757,583	52	753,237	30	252,249	26	145,358
	FP	0	0	159	172,057	273	324,407	373	582,355

These high *Detection Percentages* are accompanied by low commission errors (<20%) for the areal statistics. However in case of landslide number statistics the commission errors are much higher (ca. 80%), which reveals a high influence of small FP. The average size of the FP of 2900 m² (Table 2) is much smaller than the average size of the landslide failures (55400 m²). Hence, the approach provides higher identification reliability for larger landslides, and both identification errors (FN, FP) are mostly related to objects of smaller spatial extents. For a fully automated usage, the approach needs to counterbalance the influence of these two identification errors. The integrative *Quality Percentage* takes this into account by relating the correctly identified landslides (TP) to both FN and FP. To achieve highest performance the approach allows to refine the multi-temporal mapping results by removing objects of lower landslide likelihood, which are more likely to be FP and therefore decreasing the overall mapping quality. In doing so, highest *Quality Percentages* could be achieved by reducing the landslide mapping results to the objects of the three highest overall landslide likelihood classes (I-III), amounting to 81% for the landslide-affected area and 30% for the landslide number for both validation sites. This comparable mapping accuracy between the validation sites is also apparent for the other result-subsets and accuracy metrics, indicating a mapping quality that is largely independent from the environmental setting, landslide characteristics and available remote sensing database of these sites.

[4] These four classes (I,I-II,I-III,I-IV) correspond to the selection categories (I',II',III',IV') of Chapter III (not in the manuscript).

5 Results

The developed approach has been applied to the whole study area and time period (1986-2013) using the complete multi-sensor database (Section 2). After an expert-based validation of the results, including the elimination of remaining false positives, the multi-temporal landslide inventory has been created (Section 5.1). This multi-temporal inventory is the basis for the analysis of spatiotemporal variations of the past landslide activity in Section 5.2. Furthermore, the potential of this multi-temporal inventory is analyzed in an exemplary way for the evaluation of the obtained spatiotemporal landslide activity in respect to predisposing (Section 5.3) and triggering factors (Section 5.4).

5.1 Multi-Temporal Landslide Inventory

In total, 1583 landslides were identified. Their sizes range from 50 m² to 2.8 km² and the total area affected by landslides amounts to 33.2 km² (Figure 8C). Figure 8A depicts the location of the individual landslides in combination with their size and temporal occurrence. The highest spatial concentration could be found at the lower parts of the slopes situated adjacent to the river valleys. In Figure 8B, the temporal statistics of the mapped landslides show the by far highest activity in 2003 and 2004. Compared to the long-term average the observed landslide rate of these years is up to 5.7 times higher for the number of landslides and 7.1 times higher for the landslide-affected area (Figure 8C). The years 1990, 1998, 2010 and 2011 are also characterized by significantly increased landslide number or area, at least twice the long-term average.

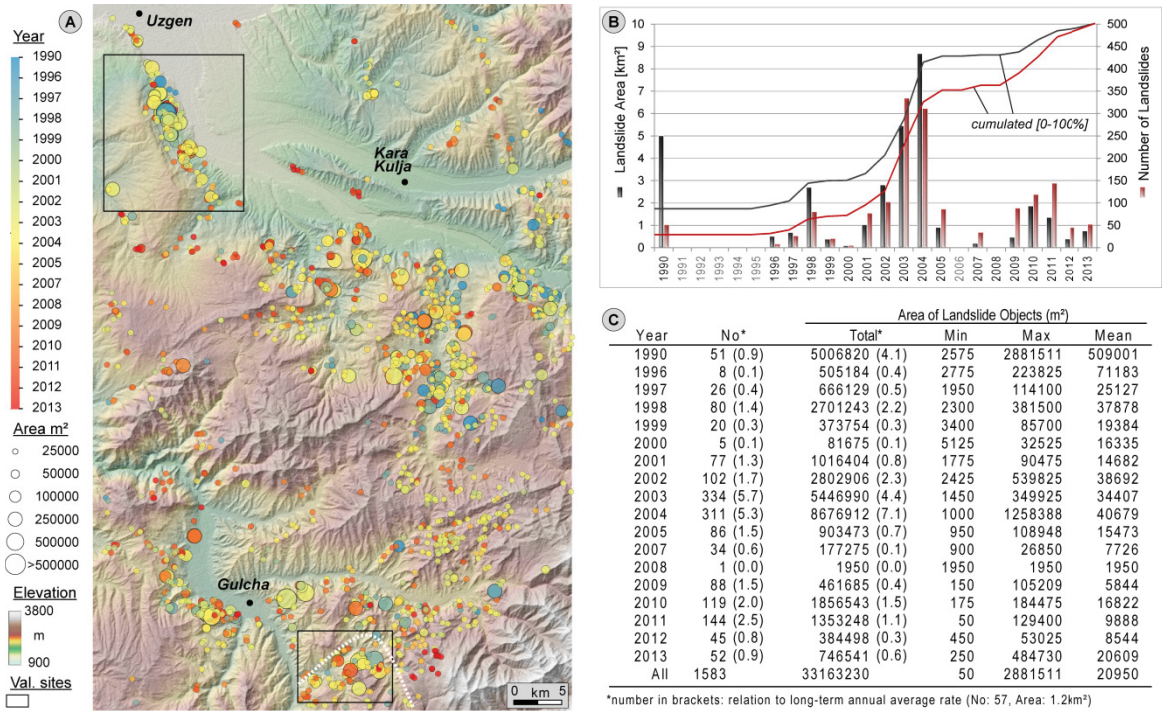

C

Year	No*	Area of Landslide Objects (m²) Total*	Min	Max	Mean
1990	51 (0.9)	5006820 (4.1)	2575	2881511	509001
1996	8 (0.1)	505184 (0.4)	2775	223825	71183
1997	26 (0.4)	666129 (0.5)	1950	114100	25127
1998	80 (1.4)	2701243 (2.2)	2300	381500	37878
1999	20 (0.3)	373754 (0.3)	3400	85700	19384
2000	5 (0.1)	81675 (0.1)	5125	32525	16335
2001	77 (1.3)	1016404 (0.8)	1775	90475	14682
2002	102 (1.7)	2802906 (2.3)	2425	539825	38692
2003	334 (5.7)	5446990 (4.4)	1450	349925	34407
2004	311 (5.3)	8676912 (7.1)	1000	1258388	40679
2005	86 (1.5)	903473 (0.7)	950	108948	15473
2007	34 (0.6)	177275 (0.1)	900	26850	7726
2008	1 (0.0)	1950 (0.0)	1950	1950	1950
2009	88 (1.5)	461685 (0.4)	150	105209	5844
2010	119 (2.0)	1856543 (1.5)	175	184475	16822
2011	144 (2.5)	1353248 (1.1)	50	129400	9888
2012	45 (0.8)	384498 (0.3)	450	53025	8544
2013	52 (0.9)	746541 (0.6)	250	484730	20609
All	1583	33163230	50	2881511	20950

*number in brackets: relation to long-term annual average rate (No: 57, Area: 1.2km²)

Figure IV-8. Automatically derived multi-temporal landslide inventory. Figure shows the spatiotemporal distribution of landslide objects related to size, location and year of occurrence. Year of occurrence corresponds to the year in which the first post-event image was acquired (for more detail on time determination see Section 3.3.1 and Figure 5). White dashed line indicates the area of the perspective view of Figure 9.

In Figure 9, the object-based multi-temporal landslide inventory is presented in more detail for the north-facing slopes of the Budalyk river valley. In this area, landslides of different sizes, shapes and

temporal occurrence could be identified (Figure 9A). The largest ones are represented by deep-seated failures affecting the uppermost loess cover and the underlying weakly consolidated Mesozoic sediments. Due to the large amount of initially displaced material they mostly transform into flows characterized by long runout zones (Danneels et al. 2008; Roessner et al. 2005). The resulting complex failures are often subject to multiple reactivations over time (Figure 9A-1), whereas the large hazardous displacements of material are often pre-dated by precursors in form of smaller failures (Figure 9A-1a). Figure 9B presents the development of the most disastrous slope failure of the analyzed time period - the "Kainama-landslide". In this case, the approach identified two small landslides occurred in 2003 (3700 m^2 and 5800 m^2) as precursors of the subsequent catastrophic failure from 26 April 2004. According to the remote sensing analysis, the displaced masses reached a maximum travel distance of 1360 m, and in parts covered and crossed the Budalyk River. They also destroyed 12 houses of the Kainama village located on the opposite side of the river causing 33 fatalities (Havenith et al. 2015; Ibatulin 2011; Kalmetieva et al. 2009). Ibatulin (2011) estimated the volume of the landslide to be $0.5x10^6$ m^3 and Danneels et al. (2008) reported a volume of $0.4x10^6$ m^3 and a size of 220000 m^2. The automated mapping approach precisely delineated this landslide object resulting in a size of 212000 m^2. Figure 9Bc shows the overlay of the derived landslide polygon on a very high-resolution image of GoogleEarth™ clearly revealing the houses that have been buried by the landslide masses. During the time period after the catastrophic failure, the approach detected a single reactivation in 2012 (22100 m^2) in the upper part of the slope close to the main scarp indicating that future larger failures might still occur.

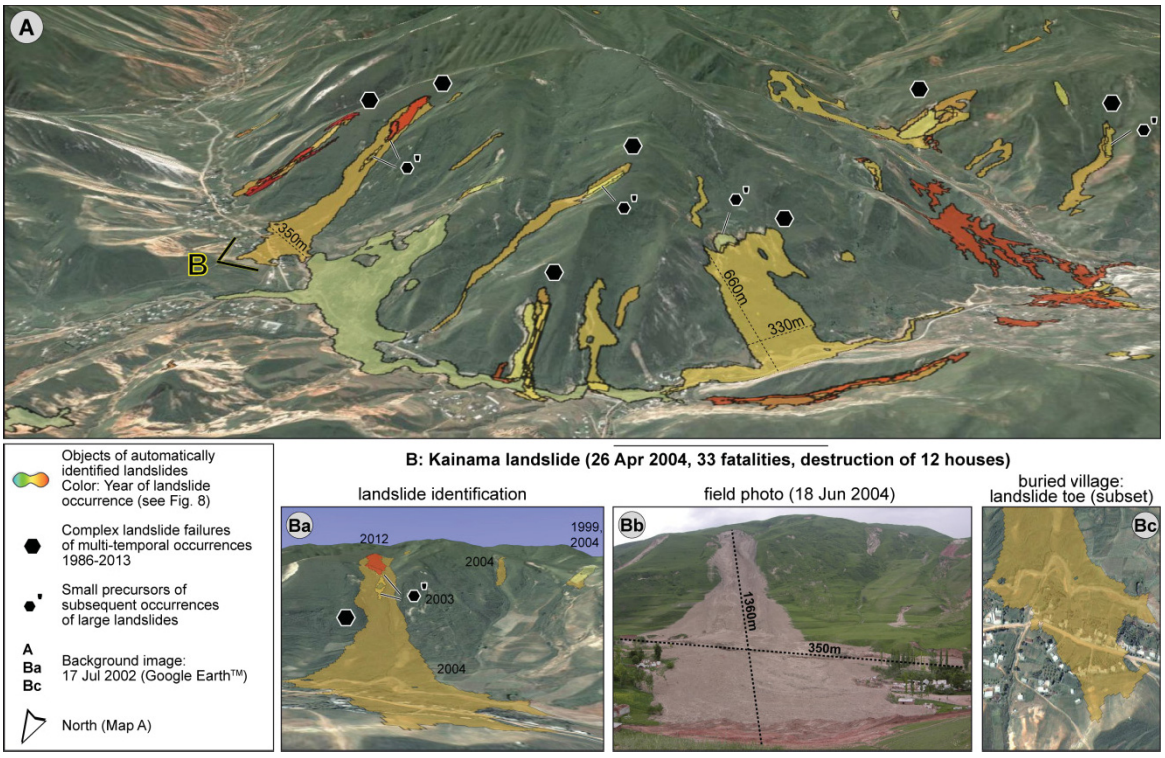

Figure IV-9. Object-based multi-temporal inventory for landslide-prone slopes along the Budalyk river valley (subset indicated in Figure 8). A: Perspective view of the object-based mapping results. B: Perspective view of Kainama landslide overlaid by automated mapping result (Ba). Field photo taken by GFZ Potsdam (Bb). Part of automatically detected landslide masses overlaid on GoogleEarthTM pre-vent image (Bc).

Figure 10 exemplarily illustrates the stepwise identification of such complex failures of multiple reactivations. Based on the multi-temporal satellite remote sensing database the approach identifies two single landslides in 2002, a reactivation of the western landslide in 2004, and a reactivation

of the eastern landslide in 2010. In contrast to the achieved spatiotemporal reconstruction of landslide evolution, commonly performed one-time landslide mapping based on mono-temporal high resolution images (Figure 10B) or field investigations (Figure 10C) are often not able to identify such evolutions, because the youngest failures have often already covered the older ones.

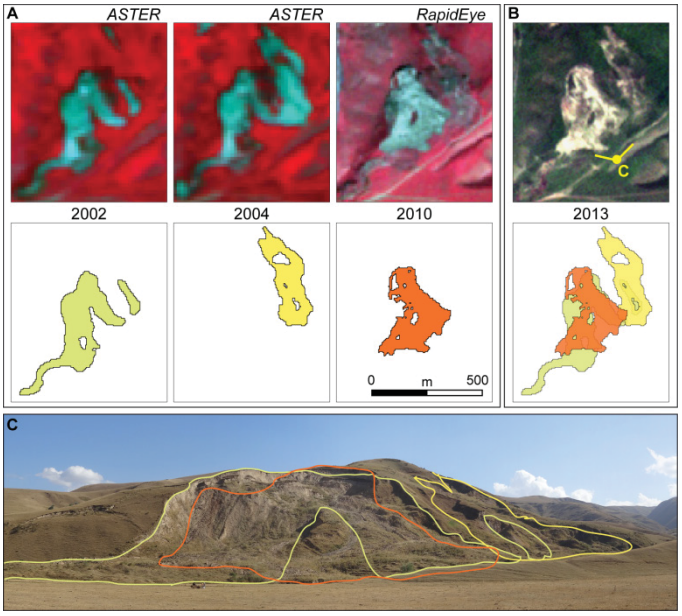

Figure IV-10. Temporal evolution of a complex landslide failure. A: CIR images (top) and the automatically identified landslide objects (bottom). B: Final situation (2013); top: true color RapidEye image of June 2013; bottom: multi-temporal overlay of all identified landslide objects. C: Field photo (Sept 2012) overlaid by the outlines of landslide objects.

The analysis of the derived landslide inventory has revealed that 670 out of 1583 landslide objects (42%) spatially overlap in at least one part with another landslide object. The largest frequency of overlaps amounts to four reoccurring landslide events during the analyzed time span (1986-2013). Table 3 lists the areal coverage of these overlapping landslides, differentiated according to the number of overlaps. It shows that 70.5% (23.38 km²) of the landslide area has been affected once and 29.5% (9.79 km²) twice or more. In case of a one-time mapping these repeatedly affected areas would be delineated only once, which would underestimate the landslide-affected area by 5.28 km² ($LsArea_{MULT}$: 33.16 km²; $LsArea_{MONO}$: 27.88 km²).

Table IV-3. Statistics of spatially overlapping landslide areas

Overlaps	$LsArea_{MULT}$ [km²][a]	[%]	$LsArea_{MONO}$ [km²][b]	[%]
---	23.38	70.5	23.38	83.9
2	7.54	22.7	3.77	13.5
3	2.01	6.1	0.67	2.4
4	0.24	0.7	0.06	0.2
Sum	33.16		27.88	

[a] $LsArea_{MULT}$: Landslide-affected area identified by the multi-temporal mapping approach.[b] $LsArea_{MONO}$: Landslide-affected area of a one-time mapping, assuming a mapping of the same landslides ($LsArea_{MULT}$ / Overlaps)

5.2 Spatiotemporal Variations of Past Landslide Activity

The derived multi-temporal inventory showed that landslides in Southern Kyrgyzstan occur almost to a third repeatedly in the same areas, often representing reactivations of older landslides. This situation also becomes evident in the analysis of the relative landslide density and its changes over time. Figure 11 depicts landslide density maps for the complete time span (1986-2013) and for five-year intervals starting from 1990 (year of first available post-event image). These landslide

density maps reveal quite persistent spatial patterns of landslide occurrence. The interval of 1990 to 1994 (Figure 11B) represents the only exception showing a different spatial distribution of the landslide density. However, this difference is mainly caused by the incomplete satellite data coverage for that time period, largely missing pre-event imagery from 1986 (Figure 1). Overall, the spatiotemporal variations in landslide density reflect the repeated landslide activity, especially in areas of high landslide activity.

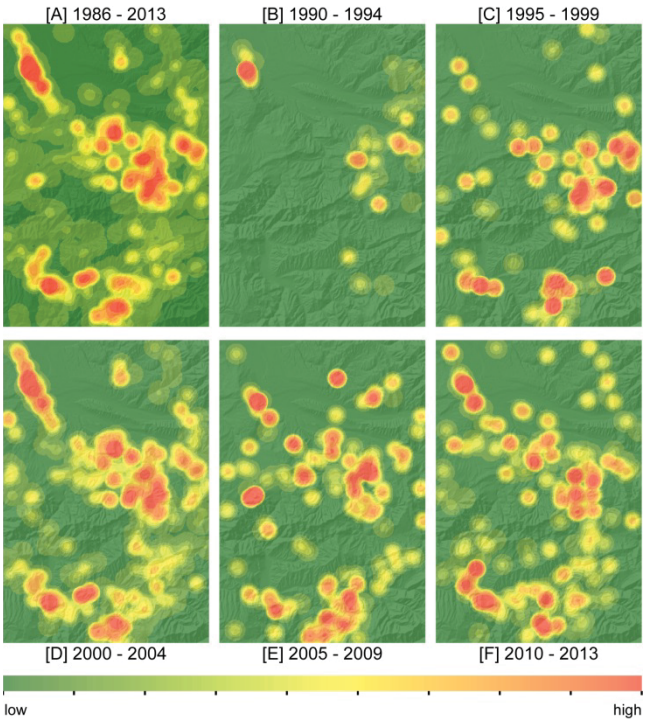

Figure IV-11. Spatiotemporal landslide density. Sum of landslide area for a moving quadratic-weighted Kernel of 2 km size for the complete time span (A) and for five-year intervals (B-F). Plotted in ten classes (decile for each time interval).

To perform a spatially more detailed analysis of landslide activity, the study area is subdivided into mapping units. Such mapping units represent spatial units that are characterized by specific ground conditions differing from the adjacent units. They form the basis for subsequent hazard analysis and can comprise administrative units, slope units, regular grid cells etc. (Erener & Düzgün 2012; Guzzetti et al. 1999; Van Den Eeckhaut et al. 2009). In this study, morphologically-based slope units, derived by Golovko et al. (2015), have been used as landslide mapping units. Figure 12 depicts the spatiotemporal variations in landslide activity related to these mapping units in respect to the areal coverage of landslides (Figure 12A), the number of landslides (Figure 12B) and number of years with landslide occurrence (Figure 12C). Three regions of particularly high landslide activity become evident: (i) the slope south of Uzgen, (ii) the eastern part of the study area south of Kara Kulja, and (iii) the southern region around and south east of Gulcha. These three spatial hotspots of landslide occurrence also correspond to the areas of highest landslide density shown in Figure 11A. Furthermore, Figure 12 also allows the characterization of different types of the landslide activity. For example, the mapping units east of Gulcha are largely affected (Figure 12A) by a relatively low number of landslides (Figure 12B), which occurred in only a few years (Figure 12C), indicating the presence of a few large landslides dominating that area. However, in most parts of the study area, the affected area, the number of landslides and the years of landslide occurrence are highly correlated. Besides the described areas of high landslide activity, a fairly large number of mapping units has not been affected by landslides at all corresponding to 51% of the analyzed area.

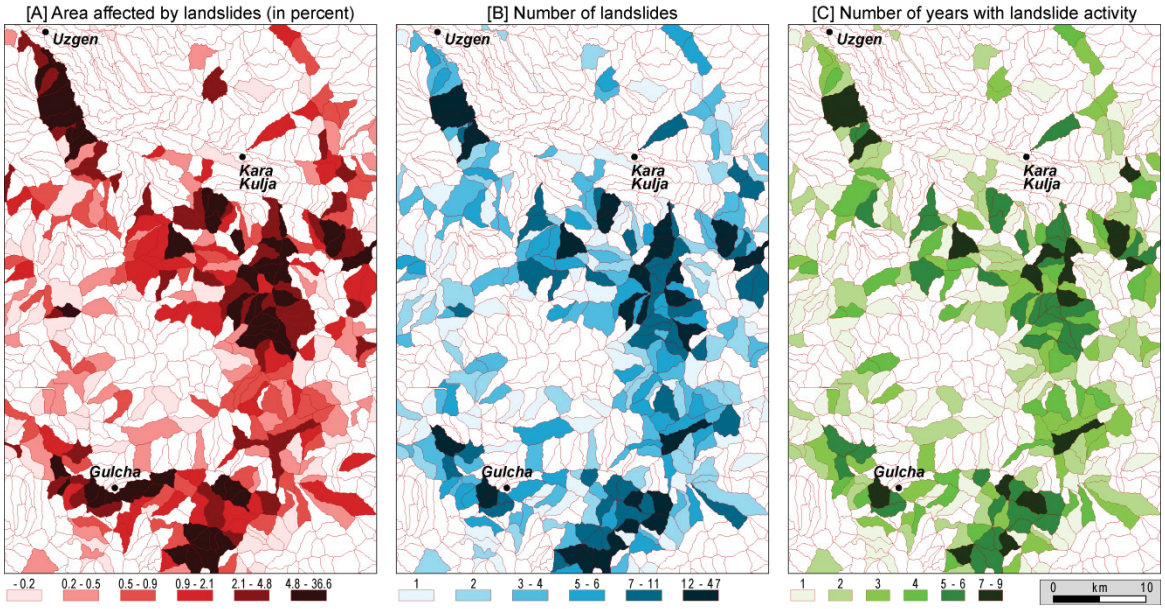

Figure IV-12. Spatiotemporal statistics of landslide occurrence based on mapping units. A: Percentage of mapping unit affected by landslides. B: Number of Landslides. C: Number of years with landslide occurrence. Plotted in six classes (sextile)

5.3 Morphological Landslide Susceptibility

Precise knowledge about the spatial distribution of landslide activity plays an essential role in the analysis of landslide susceptibility. For this purpose, the spatial variations of landslide occurrence are related to the spatial distribution of predisposing factors such as the morphological, geological and lithological setting (Van Den Eeckhaut et al. 2009). Most existing susceptibility studies base on a one-time landslide mapping to derive the spatial distribution of the landslide activity. In contrast, multi-temporal landslide inventories enable the analysis of the spatial landslide distribution over time and thus the consideration of reoccurring landslide activations. Since such reactivations frequently occur in the analyzed study area (Section 5.1), their omission would definitely influence the evaluation of the landslide susceptibility. In this study, we used the derived multi-temporal inventory for an exemplary assessment of the landslide susceptibility related to the morphological parameters elevation, slope and aspect. Figure 13 compares the frequency distributions of these three parameters (gray) with the corresponding landslide frequency (red). This reveals a particularly high landslide susceptibility of slopes that are characterized by an elevation range between 1700 and 2200 m.a.s.l., a slope between 16 and 32°, and an aspect in approx. northeastern direction. Besides these regions with above-average susceptibility it is also notable that landslide occurrence is not limited to a certain morphological setting. The identified landslides occur at all aspects and almost all inclinations and elevations. The most stable parts of the study area are regions with an elevation above 2800 m, very gentle slopes and slopes of southern aspect (SE-SW).

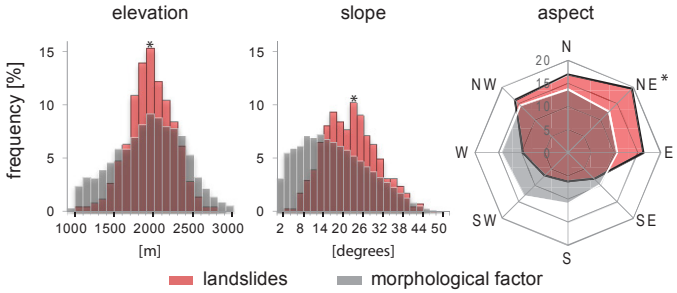

*Figure IV-13. Landslide susceptibility according to the morphological predisposing factors elevation (A), slope (B), and aspect (C). Red: Frequency of landslides per class (%). Gray: Frequency of morphological factor per class (%). *landslide frequency class of largest difference to the factor frequency.*

5.4 Investigation of Precipitation as a Potential Landslide Trigger

Whereas the predisposing factors determine the spatial susceptibility of landslide occurrence, the temporal occurrence of the actual failures is determined by the temporal variations of triggering factors such as hydrometeorological conditions and seismicity (Corominas & Moya 2008; Peruccacci et al. 2012; van Westen et al. 2008). For a better understanding of the role of the triggering factors at a regional scale, the relationship between the temporal variations of landslide activity and triggering factors has to be investigated. In this study, the triggering factor precipitation is analyzed in an exemplary way. For this purpose, we used the modeled precipitation estimates of Duethmann et al. (2013), which were derived from downscaled reanalysis and station gauge data. These estimates were available for the whole study area in form of daily precipitation data of 1 km spatial resolution for the years between 1998 and 2009. Figure 14 shows the seasonal variations in precipitation for this time span. The highest monthly rates have been observed for the months March through June (Figure 14A), whereas the maximum intensity of daily precipitation is more constant throughout the year (Figure 14B). Figure 15 shows the temporal variations of the daily precipitation for the whole time span of data availability (1998-2009). The annual sum of precipitation ranges between 450 mm and 1000 mm with peaks in the years 1998, 2002-2004 and 2009, whereas all of them correspond to years of increased landslide activity. Furthermore, the seasonality of precipitation varies between the years. In 1998, 2002, 2003 and 2009 a distinct peak of precipitation is apparent during the time period of highest landslide activity from March to July. In contrast, the peaks in 2000 and 2001 occur during the winter months. All of the remaining years are characterized by a more even distribution of precipitation throughout the year.

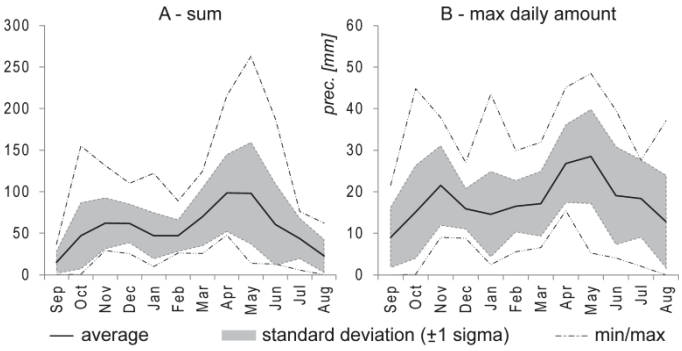

Figure IV-14. Seasonal variations of precipitation from 1998 to 2009. Left: Monthly sums. Right: Maximum daily amount of precipitation per month.

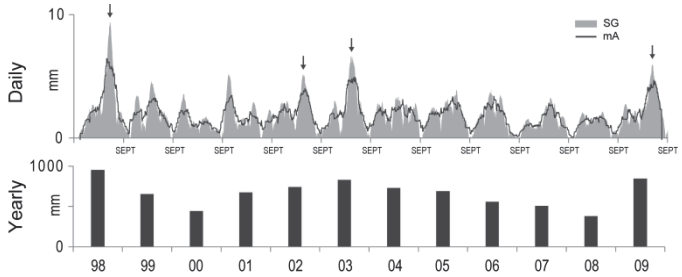

Figure IV-15. Temporal distribution of precipitation. Top: Smoothed daily data, SG – Savitzky-Golay filter (2nd order polynomial, 90 days window), mA –moving average (90 days); Arrows indicate maximum precipitation during the months of most landslide activity (March to July). Bottom: Sum of annual precipitation for the hydrological years (September through August).

Due to the different temporal characteristics of the precipitation data and the derived landslide data – daily information versus variable time periods – the comparison of precipitation and temporal landslide activity is performed on an annual basis. For landslides the year is assigned to the end of the identified time period (Figure 8) and for the precipitation data to the hydrological year spanning from September through August (e.g. September 2007 through August 2008 represents the year 2008). The hydrological year comprises the rainfall during the active landslide season as well as the snowfall in the preceding winter, which both are assumed to have an influence of landslide activity.

Figure 16 depicts the Pearson correlation between the temporal variations of four different precipitation parameters and the annual landslide area and number. Three of these four parameter (A,C,D) show a positive correlation. In general, they are stronger correlated to the number of landslides than to the area of landslides, implying that smaller landslides are more directly influenced by precipitation than larger ones. Accepting a *p*-value (permutation test) of less than 0.1, three of the correlations can be considered as statistically significant (highlighted in red). The correlation coefficient (*R*) of these significant correlations ranges between 0.52 and 0.57, which reveals a moderate positive correlation of landslide activity and precipitation statistics. To investigate the influence of seasonal variations in precipitation on landslide activity, the hydrological year has been sub-divided into a mainly snow-influenced winter period (October-February) and a mainly rain-influenced spring period (March-July). Table 4 compares the correlation of the four precipitation parameters for the complete hydrological year, the winter period, the spring period and the combined winter and spring period. This comparison shows highest correlations for the complete hydrological year, indicating that the landslide activity is more influenced by a combination of rain and snow fall/melt rather than by the individual influence of winter or spring precipitation. The precipitation parameter with highest correlations and lowest *p*-values is represented by the averaged daily precipitation (C). The fact that the average in daily precipitation is stronger correlated than the 95th percentile (D) implies that the landslide activity in Southern Kyrgyzstan is more likely to be triggered by longer periods of moderate rainfall than by a few days of intense precipitation.

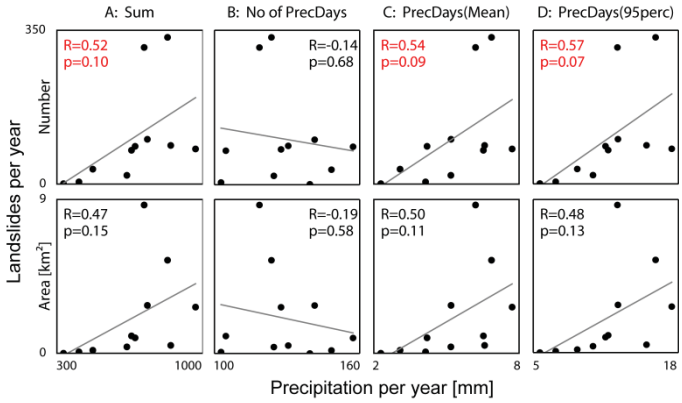

Figure IV-16. Pearson correlations of annual landslide number/area with four parameters of annual precipitation. A: Annual precipitation; B: Number of precipitation days; C: Average precipitation for precipitation days; D: 95th percentile of precipitation for precipitation days

Table IV-4. Pearson correlations of annual landslide number/area with four precipitation parameters (A-D). A-D are derived for the hydrological year (Year), the mainly snow-influenced winter period (Oct-Feb), the mainly rain-influenced spring period (Mar-Jul), and the combination of both periods (Oct-Jul).

	Area		Number			Area		Number	
	R	p	R	p		R	p	R	p
A Year	0.47	0.15	0.52	0.10	A Oct-Feb	0.29	0.38	0.33	0.33
B Year	-0.19	0.58	-0.14	0.68	B Oct-Feb	-0.24	0.48	-0.20	0.56
C Year	0.50	0.11	0.54	0.09	C Oct-Feb	0.29	0.38	0.28	0.40
D Year	0.48	0.13	0.57	0.07	D Oct-Feb	0.33	0.32	0.37	0.26
A Mar-Jul	0.34	0.31	0.39	0.23	A Oct-Jul	0.41	0.21	0.47	0.14
B Mar-Jul	-0.09	0.78	-0.09	0.79	B Oct-Jul	-0.22	0.51	-0.19	0.57
C Mar-Jul	0.48	0.14	0.54	0.08	C Oct-Jul	0.51	0.11	0.55	0.08
D Mar-Jul	0.44	0.17	0.48	0.14	D Oct-Jul	0.42	0.20	0.49	0.13

6 Discussion

We developed an approach for an automated derivation of a multi-temporal landslide inventory, allowing the retrospective assessment of spatiotemporal variations of landslide frequencies, which so far often represents the bottleneck in systematic regional landslide hazard and risk assessment (Guzzetti et al. 2012). Based on a multi-sensor time series database and a digital elevation model the approach derives objects of landslide occurrences during the time span of optical satellite remote sensing data availability, whereas the repeat rate of data acquisition determines the temporal precision of landslide identification.

6.1 Method

For best possible landslide identification in space and time, the whole variety of available multispectral sensors needs to be taken into account. Therefore, the NDVI as the least common spectral denominator is used to derive landslide-related vegetation changes representing diagnostic temporal features used in the identification of landslide failures. Focusing on the NDVI ensures a broad methodological transferability to most common multispectral optical satellite sensors, since they usually comprise the required bands in the red and near infrared (NIR) parts of the spectrum. However, due to sensor-specific spectral response functions for the red and NIR bands the NDVI slightly differs among the different sensors (Goetz 1997; Huang et al. 2013; Martinez-Beltran et al. 2009). Nevertheless, the application of the approach revealed that such cross-sensor NDVI variations could be neglected in the context of NDVI-based landslide identification, since they are

marginal in comparison to the distinct NDVI changes caused by landslide-related vegetation disturbances.

The capability to integrate multiple sensors in the methodological framework allows to establish optical time series databases of best temporal resolution, and thus to be most precise in the determination of the temporal occurrence of landslide failures. To benefit fully from the high temporal resolution the methodological developments comprise strategies to accommodate uncertainties arising from the highly variable multi-sensor time series database. A multiple threshold-based pixel- and object-oriented analysis generally reduces the sensitivity to small variations of the analyzed parameters throughout the whole identification process of bi-temporal detection of landslide-related vegetation disturbances, multi-temporal analysis of post-failure revegetation rates as well as relief-based evaluation. A calibration procedure specifically deals with the adaption of the NDVI-thresholds in respect to the vegetation cover conditions of a specific bi-temporal image pair, in order to identify areas of landslide-related vegetation disturbances serving as a basis for landslide object generation. A refinement procedure ensures reliable bi-temporal change detection and object segmentation by selecting suitable bi-temporal image pairs (i.e. images of comparable vegetation cover characteristics, similar spatial resolution, similar acquisition parameters such as the roll angle of the sensor) and a subsequent object-specific refinement of the time period of temporal landslide occurrence by involving less suitable images acquired in between. Overall, to the best knowledge of the authors, the approach is the first landslide identification approach, which allows multi-temporal landslide mapping in a large amount of data with irregular temporal resolution, different spatial resolution and irregular areal coverage.

Moreover, the developed approach assigns to each identified object an overall landslide likelihood of four classes (I-IV), enabling landslide experts to incorporate the level of uncertainty in their subsequent interpretation and evaluation of the results obtained by the automated analysis. The accuracy assessment of the automated analysis revealed correct identifications of more than 90% of the landslide-affected areas with *Omission* and *Commission Errors* below 20%. Highest accuracy is achieved by considering objects of likelihood classes I-III, which lowers the false positive rate and results in a *Quality Percentage* of approx. 80%. This way the developed approach is comparable to recently published studies for object-based landslide mapping showing *Quality Percentages* of 58% to 81.7% for event-based mapping (Rau et al. 2014) and 71.5% to 96.7% for different time periods of the multi-temporal mapping of Martha et al. (2012). These achieved accuracies reveal a suitability of the approach for automated application for the analysis of the spatiotemporal variations of landslide-affected area. In respect to the landslide number, the approach achieved lower *Quality Percentages* of approx. 30%, conforming with the lower *Quality Percentages* of Martha et al. (2012) ranging between approx. 20% and 70%. The lowered mapping accuracy of this study for the landslide number is mainly caused by the high repeat rate of the multi-temporal data coverage (Figure 1) and the relatively low number of landslide reference objects (approx. 100 for each validation site). Thus, even a small number of false positives in each analyzed bi-temporal image pair had a strong influence on the *Commission Error* and thus also on the *Quality Percentage*. However, the likelihood characterizations of the identified objects support a subsequent expert-based elimination of FP, resulting in a valuable database of multi-temporal landslide occurrence of spatially precise landslide delineation of high temporal precision.

6.2 Results

The application of the approach resulted in a regional multi-temporal landslide inventory for Southern Kyrgyzstan, containing 1583 landslide occurrences between 1986 and 2013 in an area of 2500 km². The temporal resolution of the obtained inventory ranges between six years (1990–1986) and two weeks during the RapidEye data acquisition (2012–2013), and provides at least annual coverage since 1996 with a gap in 2006. This exceeds the repeat rate at which most manual mapped multi-temporal inventories are updated. Typical update rates of existing multi-temporal inventories are several years to decades. Galli et al. (2008) mapped landslides in Italy at five dates between 1941 and 1997, Klimeš (2013) at eight dates between 1949 and 2009 in Peru. Since optical satellite data of high spatial resolution became available in the 2000s a few manually mapped multi-temporal landslide inventories are prepared that provide annual coverage (e.g. Saba et al. (2010): five data acquisitions between 2004 and 2008) or even intra-annual coverage (e.g. Weng et al. (2011): 16 data acquisitions between 2005 and 2009). However, due to the high manual mapping effort, these multi-temporal inventories cover very limited areas of several tens of square kilometers. In this context, the developed approach represents a substantial improvement since it allows for systematic landslide mapping at high temporal resolution for larger areas of several thousands of square kilometers.

For the study area, the number of automatically mapped landslides (1583) largely exceeds the number of landslides that have been reported by the Kyrgyz authorities (<100) in the same time period from 1986 to 2013 (Golovko et al. 2015). This demonstrates the potential contribution of the developed approach to the systematic spatiotemporal landslide investigations in Kyrgyzstan, which became especially important since the means for regular landslide monitoring have significantly decreased after the breakup of the Soviet Union in 1991. Before that, large efforts had been undertaken between 1956 and 1986 in the systematic investigation of landslide-prone areas in the vicinity of settlements (Yerokhin 1998). The report (as of 1986) compiled by Yerokhin (1998) contains 453 undated landslides for the study area, comprising those that occurred between 1956 and 1986 as well as historical slope failures. In comparison, the remote sensing based approach results in more than thrice as many landslide occurrences, providing landslide objects of known temporal occurrence throughout the complete study area. Moreover, the high temporal resolution of the achieved results enables the analysis of the evolution of reoccurring landslides, which is impossible by one-time mapping, such as the previously compiled field-based landslide documentation (Golovko et al., 2015). The results have shown that a substantial part of the landslide area (30%) is affected twice or more, confirming the importance of compiling multi-temporal landslide inventories as main prerequisite for the subsequent evaluation of landslide susceptibility and hazard.

Thus, this paper exemplarily analyzed the morphological landslide susceptibility for the study area of Southern Kyrgyzstan. The results indicated highest susceptibility in moderate slopes in N-NE direction within an elevation range of 1700 and 2200 m.a.s.l. Such moderate slopes are typical for weakly consolidated materials, which according to Roessner et al. (2005) are the main source of deep-seated landslides in Southern Kyrgyzstan.

The derived multi-temporal inventory also allows the analysis of the temporal variations in landslide activity. This knowledge represents a key factor in understanding the regional dynamics of landslide processes in Southern Kyrgyzstan which has been largely missing in the past (Havenith et al. 2015). The results have revealed a permanently ongoing landslide activity during the analyzed time period with main activity peaks in 2003 and 2004. It is notable that this continuous landslide

activity exists without the presence of major triggering events. According to the USGS earthquake catalog (USGS Earthquake Hazard Program, 2015) no severe earthquakes have been recorded in the analyzed time span. Moreover, Southern Kyrgyzstan represents an area of moderate precipitation (450-1000m m/a), where strong rainstorms which could serve as triggering events are largely missing. First investigations towards the relationship between the amount of precipitation and the observed landslide frequency have revealed that precipitation has a positive but moderate influence on the onset of slope failures in Southern Kyrgyzstan. This influence is less distinct compared to areas where landslide occurrence is primarily related to intense rainstorms, such as Southeast Asia (Mathew et al. 2014; Weng et al. 2011; Wu & Chen 2013). Thus, landslide occurrence in Southern Kyrgyzstan can only be in part explained by the derived precipitation characteristics, indicating that in this region landslide occurrence is most likely the result of a complex interplay between geological and geomorphological composition of the relief and the spatiotemporal characteristics of triggering factors (Havenith et al. 2015; Roessner et al. 2005).

These analyses of the spatiotemporal landslide frequencies to the morphological setting and the triggering factor precipitation revealed the suitability of the developed approach to provide a systematic long-term landslide information base, which is required for landslide hazard and risk assessment. Hence, the derived results open up the opportunity to perform multivariate analysis considering further pre-disposing factors (e.g. lithology and structural geology) and triggering factors (e.g. seismicity), in order to improve the regional landslide process understanding.

7 Conclusions and Outlook

This paper presented the methodological developments for an automated remote sensing-based approach for generating long-term multi-temporal landslide inventories using an optical multi-sensor satellite time series database and a digital elevation model. The developed approach is based on the analysis of landslide-related vegetation cover changes, which has been proven suitable for multi-temporal landslide identification using temporal irregular time series of remote sensing data comprising seasonal differing data acquisitions of various sensors.

Applied to a landslide-affected area of 2500 km² in Southern Kyrgyzstan, the approach allowed a retrospective systematic assessment of past spatiotemporal landslide occurrence for the time period of satellite data availability from 1986 to 2013. The resulting multi-temporal inventory contains spatially explicit landslide objects of high spatiotemporal consistency and completeness, representing a valuable database for analyzing variations long-term landslide frequencies at a regional scale. The obtained spatiotemporal landslide frequencies have been related to morphological parameters and to the triggering factor precipitation, demonstrating that the approach is capable of contributing to an improved understanding of landslide process at a regional scale and thus to the realization of subsequent probabilistic landslide hazard and risk assessment.

The developed approach, with its capability of integrating different optical sensors enables its principle transferability to other areas where landslide occurrence also leads to changes of the surface vegetation cover, which is the case for many other global landslide hotspots (Nadim et al. 2006) in South America (e.g. Brazil, Colombia) and Southeast Asia (e.g. Taiwan, Thailand, Philippines). Moreover, new opportunities for automated global landslide mapping using optical satellite remote sensing data have opened up with the launch of the Sentinel-2A system in June 2015 (2B is planned

for 2016). With revisiting times of up to five days, a spatial resolution of 10 m, a large swath of 290 km, and the free of charge data availability (Drusch et al. 2012) this system will be especially suitable for monitoring landslide occurrence over large areas with high temporal resolution enabling a more precise determination of the time period during which the landslide failure occurred.

Acknowledgments

The authors thank the German Aerospace Agency (DLR) for providing RapidEye data by the RESA (RapidEye Science Archive) program and Doris Duethmann for providing the daily precipitation data. This work was funded by the German Federal Ministry of Research and Technology (BMBF) within the framework of PROGRESS (Potsdam Research Cluster for Georisk Analysis, Environmental Change and Sustainability).

V Synthesis

1 Conclusions

The overarching goal of the thesis is the development and application of an automated multi-temporal landslide mapping approach to enable the spatiotemporal analysis of past landslide activity over large areas, which is a prerequisite for subsequent regional landslide hazard and risk assessments. This chapter discusses the results of the thesis in respect to the major research questions and research objectives described in Section I-4.

1.1 Method

Research Questions: What are efficient and robust methods to utilize an optical multi-sensor satellite time series for large area and long-term multi-temporal landslide identification? What are the advances of the developed methods and the key differences to existing approaches?

For evaluating the methodological developments, the individual aspects of Chapters II-IV are considered as a whole, jointly culminating in the multi-temporal and multi-sensor landslide mapping approach of Chapter IV. In general, the developed approach is based on the analysis of landslide-specific vegetation cover changes and relief-oriented parameters, allowing for automated mapping of spatiotemporal landslide activity over large areas and long time periods. Table App-1 compares the existing landslide mapping approaches (see also Section I-2.2.3) and the developed approach of this thesis in respect to methodological properties and scope of application. Figure V-1 illustrates this comparison by depicting the landslide mapping approaches against size of study area and number of temporal data acquisitions as well as methodological characteristics.

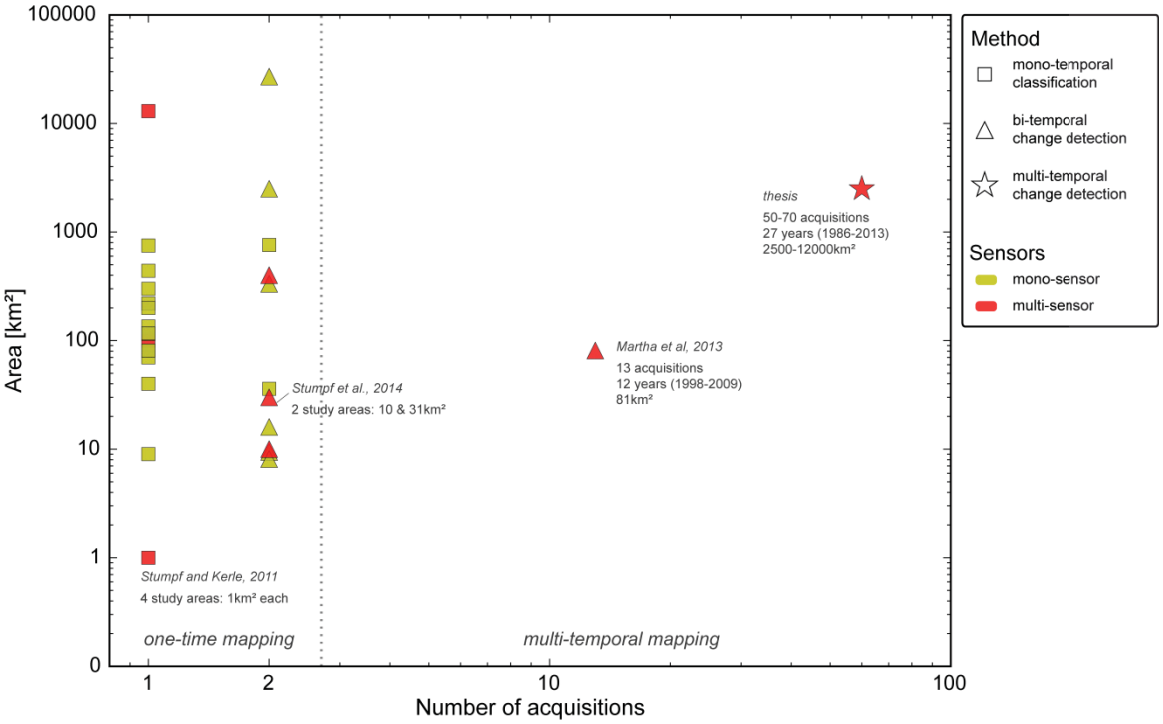

Figure V-1. Overview of remote sensing based landslide mapping approaches. Comparison of the developed automated approach (labeled with "thesis") with (semi-)automated approaches existing in the literature. The four labeled approaches are those that are applied to different scenarios (either multiple study areas or multi-temporal datasets). See also Table App-1 for further information.

The vast majority of the existing approaches are applied to one or two image acquisitions, providing a one-time landslide mapping (Figure V-1). Generally, these one-time mapping approaches also have the potential to be applied to multiple datasets and therefore serve as a tool for multi-temporal landslide mapping. However, most of them have only proved the applicability to a single test case (specific area and datasets) and thus miss the affirmation that their one-time characterization of the landslide-diagnostic parameters is transferable for different scenarios. Exceptions are Stumpf & Kerle (2011) and Stumpf et al. (2014) which tested their one-time mapping approach in different study areas and Martha et al. (2012, 2013) which applied their approach to 13 different data acquisitions of a time series database. However, they are of very limited areal coverage (Table App-1) and thus still remain test cases. In contrast, the developed approach has proved its applicability to rather large areas of 2500 km² (Chapter IV) and 7500 km² (Chapter III) as well as many time series data acquisitions (up to 70). For such an extensive analysis the landslide mapping approach has to be applicable for many different scenarios. Therefore, the thesis includes several methodological developments to accommodate the challenges originating from the comprehensive and variable multi-sensor time series database used for the long-term and large area analysis (Section I-3.2, II-2.2, III-2.2, IV-2.2).

One fundamental methodological innovation is the **implementation of multi-temporal information** within the landslide identification procedure, which goes beyond the existing mono- and bi-temporal approaches to date. This way, the landslide-specific vegetation characteristics, often representing the main diagnostic feature for landslide detection in optical remote sensing data (Section I-2.2.2), are considered over time instead of limiting the analysis to the absence of vegetation in mono-temporal approaches or to the loss of vegetation in bi-temporal approaches. The developed approach addresses the multi-temporal aspect by using temporal NDVI-trajectories allowing the analysis of bi-temporal vegetation disturbance and subsequent revegetation rates as landslide diagnostic parameters (Section III-3.1). Thus, landslide-related vegetation changes can be distinguished from permanently non-vegetated areas such as water, artificial surfaces, and outcrops as well as from other temporally non-vegetated areas such as harvested fields (Figure III-4). In the existing mono- and bi-temporal approaches these differentiations are usually assisted by various additional parameters, which can be broadly grouped into spectral, textural, morphometric, and contextual measures. However, most of the parameters are highly sensitive to differences in sensor characteristics and season of data acquisition, e.g. texture characterization is sensitive to the spatial resolution of the analyzed data (Benson & Mackenzie 1995; Ojala et al. 2002; Puissant et al. 2005). In this context, the introduction of multi-temporal information in the landslide identification process is advantageous, because it opens up the opportunity to reduce the use of required parameters and to focus on the analysis of the vegetation surface cover changes as a main landslide diagnostic property. Moreover, due to this focus on vegetation analysis, it is possible to integrate different optical sensors, since the NDVI (used for the vegetation analysis) can be derived for all common multispectral satellite sensors.

With the use of NDVI-trajectory analysis, the developed approach adopts the basic principle of time series analysis, analyzing the progression of specific information over time. In remote sensing, several trajectory-based algorithms have been published: BFAST (Verbesselt et al. 2010), TIMESAT (Jonsson & Eklundh 2004), DBEST (Jamali et al. 2015), LandTrendr (Kennedy et al. 2010), and TimeStats (Udelhoven 2011). They usually aim at the determination of short- and long-term vegetation trends as well as seasonality parameters (e.g. start and end of season). The temporal pattern of a landslide is described as short-term vegetation disturbance and long-term vegetation regrowth (Section III-3.1). However, for different parts of a landslide this temporal pat-

tern can vary greatly (Figure III-5B), e.g. revegetation rates are faster at the usually gentle slopes of the landslide deposits than at the upper more steeper parts, which are more susceptible to subsequent erosion processes. These differences of the temporal patterns within a single landslide failure hinder the existing pixel-oriented trajectory algorithms to derive homogenous results for an individual landslide failure and thus are inconvenient to obtain landslide-related objects. However, landslide hazard and risk assessments require object-oriented results for the statistical analysis of spatiotemporal landslide probabilities (Section I-2.1). For this purpose, the object segmentation procedure of the developed landslide identification approach focuses on the bi-temporal vegetation disturbance, which represents the most discernable landslide-related information in optical remote sensing data. Moreover, the applicability of the existing trajectory-based algorithms is further impeded by the irregular temporal resolution of the multi-sensor time series of the thesis (between six years and two weeks), because they are designed for regular and dense time series only. Thus, the developed hybrid approach of bi-temporal analysis of vegetation disturbances (used for object segmentation) and subsequent multi-temporal analysis of revegetation rates (plausibility control) represents an adaption of trajectory-based algorithms to the needs of object-oriented landslide mapping using irregular time series data.

The developed approach builds on a **multi-threshold-based analysis** to reduce its sensitivity to small variations of the implemented pixel- and object-based parameters for NDVI- and relief-oriented analysis (Table IV-1, Figures III-6, III-7, IV-3). The findings of the thesis reveal that this multi-threshold parametrization is very suitable to facilitate the detection and delineation of landslides despite their natural variability. Thus, the approach is able to identify deep-seated fresh failures as well as landslides that result in less pronounced vegetation changes such as reactivations and shallow landslides (Figures III-2, III-5A). Furthermore, the landslide object delineation could be achieved in high geometric quality regarding the shape and size of landslides (Figure III-14, Section III-5.2) although the vegetation change characteristics can vary greatly within an individual landslide failure (Figure III-5B). Overall, Chapters III and IV show that the approach is able to identify landslides of different sizes, shapes, activity state, and lithological properties of the involved material.

Based on the multi-threshold rules, the object-based results of the landslide identification are characterized by **landslide likelihood parameters** (i.e. C_{BITEMP}, $C_{MULTITEMP}$, C_{RELIEF}, and LL), describing the probability of that object being a landslide in respect to the automated identification process (Table IV-1, Sections III-3, IV-3). These likelihood classes enable an uncertainty-related discrimination of the results (Section III-3.2.4) and partly reflect the activation type of the landslide (Table IV-1), both advantageous in subsequent expert-aided interpretation and evaluation of the automatically derived spatiotemporal landslide occurrence.

A further substantial strength of the approach is the integration of a **refinement and calibration procedure** to fully benefit from the temporal resolution inherent in the complete time series database despite the data's sensor variability and temporal irregularity (Section IV-3.3.1). The refinement procedure comprises (i) the preselection of image data pairs, between which the landslide occurrence is identified and (ii) the refinement of that time period of landslide occurrence by subsequently analyzing all acquired images in between. Thus, landslide identification and landslide object segmentation can be performed most reliably on the basis of image pairs suitable for bi-temporal image change detection without losing temporal precision in the determination of the time period of landslide occurrence (Figure IV-5). Suitable image pairs are characterized by com-

parable vegetation cover (e.g. data acquisitions of the same season), similar sensor characteristics (e.g. spatial resolution), similar acquisition parameters (e.g. viewing angle of the sensor), minimal cloud and snow cover, and a short interval between data acquisitions. Since for most parts of the world archive data is usually less available before the late 1990s, the selection of suitable image data pairs before that is impeded by the lack of alternatives. However, to enable landslide identification nonetheless, a calibration procedure is introduced that allows improved change detection between image data pairs of less comparable data acquisitions. Said calibration procedure adapts the NDVI-thresholds with respect to the vegetation cover characteristics of a specific bi-temporal image pair. This threshold adaptation enables the approach to achieve robust identification of landslide-related vegetation disturbances and thus more reliable object segmentation for landslide failures that have occurred between image pairs of differing seasonal acquisitions (Figure IV-4).

The approach also comprises **automated pre-processing** strategies, which allow the efficient application of the developed landslide recognition and segmentation algorithms to a large multi-sensor remote sensing database. Generally, in time series analysis, the purpose of pre-processing is the homogenization of the database to the needs of the envisaged change detection methods (Coppin et al. 2004; Hussain et al. 2013). In this thesis, the priority has been the development of robust techniques suitable for operational use. For the spectral normalization, the datasets are converted to TOA-reflectance values before deriving the analyzed NDVI values (Section IV-3.1). Thus, the pre-processing neglects the variability introduced by differences in atmospheric conditions and the variable spectral response functions of the different sensors. However, the severe disturbance or loss of vegetation in case of a landslide causes strong changes in the NDVI, usually much stronger than those by the neglected factors. Moreover, the use of the spectral index NDVI as the basic landslide diagnostic parameter also reduces the atmospheric influences in the multi-temporal data comparison. Consequently, the signal-to-noise ratio can be considered sufficient to enable a robust mapping of landslide occurrence, especially in combination with the implemented uncertainty-related multi-threshold rules, which help in case of lower landslide signals to discriminate between landslides and background noise (Section III-3.2, Figure III-8). For the geometric normalization, an automated correlation-based image-to-image co-registration approach has been developed (Chapter II). It allows efficient and robust spatial alignment of orthorectified standard data products of varying spatial resolutions and of seasonal and inter-annual land cover differences. The usage of the multi-temporal terrain-corrected Landsat Level 1T data as spatial reference ensures a spatially consistent and widely available topographic reference for the alignment of the datasets of the multi-sensor time series database, irregularly and patchily distributed over the study area. The application of the co-registration approach allowed a multi-sensor relative image-to-image alignment (RMSE of 17 m) required for the subsequent NDVI-trajectory-based change detection as well as an absolute positional accuracy (RMSE: 23 m) that is sufficient for the mapping scale of 1:50000 and enables the subsequent analysis of the landslide identification results in combination with other spatial data within a GIS environment (Sections II-5, II-6.3). Apart from the spectral and geometric homogenization, the pre-processing facilitates the robust usage of the approach by further automatic routines for data input, metadata reading and homogenization, and masking of clouds and snow (Section IV-3.1).

Altogether, the thesis comprises the developments of automated pre-processing strategies and knowledge-based, uncertainty-related, and database-adaptable algorithms for landslide identification and delineation, in order to allow an optimized multi-temporal mapping of varying landslide phenomena within an irregular multi-sensor time series database covering large areas and long time periods.

1.2 Applications and Results

Research Questions: What are essential applications of the developed approach and how can they contribute to an improved regional landslide process understanding? Which specific results can be achieved for Southern Kyrgyzstan and how can this region benefit from them?

The developed landslide mapping approach allows the derivation of the spatiotemporal landslide activity based on available multi-temporal remote sensing data of various optical satellite-based sensors. The applications of the approach for long-term landslide investigations and for recent monitoring are discussed in the following. Then, the specific results, which have been achieved for Kyrgyzstan, are presented.

1.2.1 Retrospective Analysis of Long-Term Spatiotemporal Landslide Activity

For several decades, optical satellite remote sensing data have been acquired to monitor the Earth's surface. With the launch of Landsat 5 and SPOT 1 in the 1980s, data of spatial resolution of 30 m and higher are available. This is sufficient for the mapping of large and medium sized landslides representing system-relevant landslides in the context of regional hazard and risk assessment (Section II-7). In combination with the increased availability of high spatial resolution data since the 2000s, long and sufficiently dense time series databases can be established for large areas, such as the one of the thesis (Sections I-4.2, II-2.2, IV-2.2). With the developed landslide mapping approach at hand, it is now possible to utilize such time series to achieve comprehensive multi-temporal landslide inventories in retrospect for the complete time span of suitable satellite data availability.

Chapter IV shows the application of the approach to a time series between 1986 and 2013 covering an area of 2500 km². The derived multi-temporal landslide inventory contains the location, extent, and temporal occurrence of the landslide failures that happened during the analyzed 27-year period. Section IV-5 demonstrates that such remote sensing-based multi-temporal landslide inventories are suitable to obtain profound knowledge about spatiotemporal variations of past landslide activity (Figure IV-8). One important aspect is the analysis of the spatial landslide distribution in regard to the predisposing factors, which allows the derivation of spatial landslide probabilities required for the assessment of landslide susceptibility (Section I-2.1). In this context, the object-based nature of the results is advantageous, because it allows focusing on specific parts of a landslide such as its source area (Section IV-5.3), and thus the determination of process-relevant information of landslide occurrence, which cannot be achieved by point-based landslide inventories. Moreover, susceptibility analysis also benefits from the long-term multi-temporal analysis, enabling the identification of recurring landslides (Figure IV-10). So far, most susceptibility assessments are based on one-time landslide mappings (e.g. Erener & Düzgün 2012; Lee et al. 2007; Pourghasemi et al. 2013; Pradhan 2013; Pradhan & Lee 2010; Van Den Eeckhaut et al. 2009), by which such recurring landslide failures can usually not be identified, and thus have to be neglected within the landslide susceptibility analysis (Section IV-5.3).

A vital aspect in landslide hazard and risk investigations is the knowledge about temporal variations in past landslide activity (Section I-2.1). In this context, the derived long-term multi-temporal inventory forms a crucial information base, allowing the retrospective derivation of past landslide frequencies (Figure IV-8). In regions of incomplete or missing landslide records, such as the studied Southern Kyrgyzstan, the analysis of multi-temporal satellite archive data represents the only way to achieve such information in retrospect. With presently performed field- or imagery

based landslide mappings the reconstruction of past landslide failure dates is impossible or imprecise at best (e.g. recent, old or historic). For landslide hazard assessments such landslide frequency rates are analyzed in regard to the temporal variations of the triggering factors to determine the temporal probability of landslide occurrence (Figure I-2). With the derived multi-temporal landslide inventory, annual rates of landslide number and their affected area are achieved for the years since 1996, which allows a correlation of high temporal resolution with different parameters of the triggering factor precipitation (Section IV-5.4). Apart from the holistic area-wide analysis, the multi-temporal inventory also enables the examination of spatially differentiated landslide frequencies, such as the analysis based on landslide mapping units (Figure IV-12) and the derivation of temporal variations of landslide density (Figure IV-11). Furthermore, the analysis of the spatial and temporal landslide probability could be combined in such mapping units, which would facilitate a spatially differentiated landslide hazard assessment based on the achieved landslide mapping results (Cascini 2008; Corominas et al. 2014; Guzzetti et al. 2005).

1.2.2 Monitoring Recent Landslide Activity

With the opportunity of the customized tasking of RapidEye data acquisition within the RESA program (Sections I-4.2, II-2.2, III-2.2), the creation of a dense time series database between 2009 and 2013 has been possible. The application of the developed approach to this time series database shows its potential to create multi-temporal landslide inventories of high spatiotemporal completeness and precision (Chapter III). Hence, the approach can be used as part of a monitoring system allowing a systematic and continuous update of recent landslide inventories for large areas with repeat intervals of up to several days (Figure III-10). With the developed refinement procedure (Section IV-3.3.1), the temporal resolution can be further improved by closing possibly existing data gaps in the RapidEye time series with data of other sensors, even if they are characterized by lower spatial resolution (Figure IV-5). Thus, the multi-temporal landslide identifications have a great potential to contribute to the regional process understanding of current landslide activity over large areas. Putting this knowledge about current landslide activity into the context of long-term landslide variations facilitates an up to date assessment of landslide hazard and risk.

The spatiotemporal information about recent landslide activity could also help to organize landslide field surveys in a more systematic and focused way. This is particularly important in regions where landslides occur frequently, yet sporadically over large areas as is the case for the study area of Southern Kyrgyzstan. Hence, on-site investigations could be performed more efficiently, allowing to attain deeper insights into the local failure mechanisms of selected landslides, e.g. type of movement, involved material, and potential causes. Moreover, the RapidEye database with its high spatial and temporal resolution has proved to be suitable for the identification of small landslide activations that often represent precursors for larger and more hazardous landslides (Figure App-1). In practice, the detection of such small precursors could allow field investigations to take place before the potential onsets of hazardous landslides in order to conduct local risk assessments and, if needed, the realization of on-site landslide mitigation activities. Thus, provided that suitable high resolution remote sensing data are continuously available, the landslide mapping approach could be part of a landslide early warning system, especially in remote regions that are difficult to access.

1.2.3 Outcomes for Kyrgyzstan

Since the end of the 1980s, the landslide records in Southern Kyrgyzstan are very incomplete in time and space (Section I-3.1). Hence, this region particularly benefits from the multi-temporal landslide mapping, which is feasible since the first satellite data availability in 1986. The multi-sensor long-term analysis between 1986 and 2013 has revealed 1583 landslide failures in a 2500 km² large area (Figure IV-8). This number of identified landslides is more than fifteen times higher than the approx. 100 landslides that have been reported by the Kyrgyz authorities for this area over the same period of time. For the RapidEye-based analysis between 2009 and 2013 (Chapter III), similar discrepancies could be observed. In the analyzed 7500 km² large area the approach identified 471 landslides (Section III-4), whereas only 40 landslides are contained in the official reports.

This substantial increase in recorded landslides demonstrates the great potential of the developed approach to improve the knowledge about past landslide occurrence. Thereby, it has to be considered that the precision of the time period of landslide occurrence varies over time and space. With the database available for Southern Kyrgyzstan, the landslide activity can be analyzed at least annually since 1996 (with a data gap in 2006), whereas before that, less frequent repeat rates of remote sensing data acquisition could be achieved. Due to these longer repeat intervals, the completeness of the landslide inventory before 1996 might be reduced for two reasons. Firstly, landslides that have occurred at the beginning of such long intervals have usually already experienced vegetation regrowth, and thus show less disturbance signs in the post-event image, which greatly impedes their identifiability (Figure IV-2B). Secondly, recurrent landslide activations during such time periods cannot be identified. However, the influence of these effects could not be reliably quantified, due to the lack of external landslide reference information (Section IV-4). In absence of such external information, the manual reference mapping for the accuracy assessment had to be based on the same images as the automatic identification (Section III-2.4, IV-4). Thus, the manual landslide mapping underlies the same restrictions. This shows that limited data availability is a general constraint of retrospective landslide analysis and not specific to the developed landslide mapping approach. Nevertheless, the performed quantitative accuracy assessment (Section IV-4) showed that the automatic identification approach detected most manually mapped landslides (*Detection Percentages* up to more than 90% (Section III-5, IV-4)), revealing the suitability of the approach to perform reliable and consistent retrospective landslide mapping on the available remote sensing image data.

Since the independence of Kyrgyzstan in 1991, the existing landslide investigations have been concentrated on the vicinity of larger settlements, whereas most information is available as point-based coordinates only (Section I-4.1). In contrast, the derived multi-temporal landslide inventory provides area-wide and spatially explicit object-oriented information, allowing systematic and quantified analysis of past landslide activity. Additionally to the derivation of the multi-temporal inventory, the obtained landslide results are analyzed in respect to their spatiotemporal variations in order to demonstrate their suitability for achieving an improved process understanding of the regional landslide activity in Southern Kyrgyzstan.

For this purpose, the recent analysis based on RapidEye (Chapter III) has further been extended to the complete study area of 12000 km² (Figure App-2-7). In total, 625 landslides have been mapped between 2009 and 2013 with sizes ranging between 50 m² and 0.75 km², and an overall affected

area of 8.2 km². Most landslides have occurred in the time period between 2009 and 2011[5] (65%), which corresponds to the previous results of the 7500 km² studied region of Chapter III (Table III-1). In general, these four years of investigation showed a constantly ongoing landslide activity along the foothills of the Tien Shan mountain ranges throughout the complete study area, whereas the northern part of the study area has been less active than the south (Figures App-2-7). In detail, the distribution of the identified landslides reveals clear spatial patterns in landslide activity, including areas of distinct concentrations and non-affected areas. The most affected areas are located along the mountain ranges southeast of Uzgen and west and northwest of Gulcha (Figure App-6, 7).

The long-term analysis between 1986 and 2013 has been carried out for this recently most active region between Uzgen and Gulcha (Chapter IV). The 1583 identified landslides affected a total area of 33.2 km², whereas large landslides of up to 2.8 km² occurred in the 2500 km² area during the analyzed 27 year period (Figure IV-8). Spatiotemporal analysis of the detected landslides revealed constantly ongoing landslide activity of varying intensity. The long-term annual average rate amounts to 57 landslides and an affected area of 1.2 km² per year. The peak of activity has been recorded for the years 2003 and 2004, in which the observed landslide rates exceed the average rates by more than five times for the landslide number and up to seven times for the area that has been affected by landslides (Figure IV-8). Spatially, the landslide occurrence shows activity patterns that have been fairly persistent during the analyzed 27 years (Figure IV-11), whereas 30% of the landslide area has been affected even twice or more (Table IV-3). Such a spatial persistency indicates clear relations of landslide occurrence and local geological and morphological settings. This has been exemplarily evaluated by the analysis of the detected landslide objects in regard to three morphological parameters (Section IV-5.3), representing a selection of predisposing factors for landslide failures (Section I-2). This analysis unveiled highest susceptibility to landslides on slopes facing N-NE direction with an inclination of 16° to 32° at an elevation ranging from 1700 m.a.s.l. to 2200 m.a.s.l. (Figure IV-13). Moreover, it has been analyzed how temporal variations of landslide activity can be explained by variations of the triggering factor precipitation. Since the precipitation records, derived from downscaled reanalysis and station gauge data, have been available from 1998 to 2009 (Section IV-5.4), the multi-temporal landslide results allowed an annual correlation analysis between landslide occurrence and precipitation. The correlations show a positive but moderately significant trend (Figure IV-16, Table IV-4), indicating that the direct influence of precipitation only partly explains the onset of landslide occurrence. More likely, it is the result of a complex interrelation of different triggering factors and the local geological and geomorphological conditions, whereas the influence of precipitation could also be delayed in time.

Overall, these results demonstrate that the developed landslide mapping approach is able to derive a multi-temporal landslide inventory, which is suitable in spatial and temporal completeness, precision, and consistency to improve the regional landslide process understanding in Southern Kyrgyzstan and thus to facilitate the realization of subsequent hazard and risk assessments.

[5] The customized tasking of RapidEye data acquisition started in 2011 and allowed up to six acquisitions per year. Before that, RapidEye archive data of 2009 have been used (Section III-2.2), which caused a data gap in 2010 resulting in the two-year time period between 2009 and 2011.

2 Outlook

The thesis comprises the methodological development of the automated multi-temporal landslide mapping approach, its application to comprehensive time series remote sensing databases in Southern Kyrgyzstan, and the demonstration of its suitability for spatiotemporal landslide analyses. Naturally, there are numerous aspects worth researching beyond the objectives of this thesis. Out of these aspects, this section discusses prospective landslide investigations in Southern Kyrgyzstan, future potential methodological developments and the transferability of the approach to different sensors, natural environments, and applications.

2.1 Prospective Landslide Investigations in Southern Kyrgyzstan

By enabling the derivation and evaluation of long-term spatiotemporal landslide activity, the developed approach has proved its suitability to serve as valuable contribution to landslide hazard and risk assessments. However, to realize profound probabilistic analysis of landslide hazard, the exemplary analysis of the landslide occurrence relations to the morphological setting (Section IV-5.3) and to the temporal variations of the precipitation (Section IV-5.4) has to be extended to additional predisposing and triggering factors. Commonly used predisposing factors are morphological, geological, lithological, land use, and land cover properties (Corominas et al. 2014; Guzzetti et al. 2005; Van Den Eeckhaut et al. 2009). Landslide triggers are rainfall, snowmelt, seismicity, and volcanic activity (Corominas et al. 2014; van Westen et al. 2008), whereas in Kyrgyzstan the effect of active volcanism does not exist. To get a deeper insight which factors or combination of factors have an influence on the spatial and temporal variations of landslide occurrence, several univariate and multivariate methods exist (a recent review of such methods is given by Corominas et al. (2014)). Applying these methods on the basis of spatial mapping units (like those introduced in Section IV-5.2) to the identified multi-temporal landslide activity will allow achieving a quantified and spatially differentiated landslide hazard assessment for Southern Kyrgyzstan.

Until now, the long-term multi-temporal landslide mapping, as basis for such a probabilistic hazard assessment, could be achieved for a landslide active region of 2500 km² (Chapter IV). To broaden the analysis to the complete landslide prone area in Southern Kyrgyzstan, the application of the approach has to be extended to the remote sensing database of the whole study area of 12000 km². The proof that the approach is applicable for such large areas has already been given by the RapidEye-based analysis of recent landslide activity shown in Section V-1.2.3 (Figures App-2-7).

The remote sensing-based multi-temporal analysis allows the area-wide and systematic derivation of locations, extents, and temporal occurrence of landslides. This provides a comprehensive landslide database that would be unfeasible to derive with local field-based investigations. However, such field-based investigations often allow a more detailed characterization of the local failure mechanisms. In Kyrgyzstan, authorities have visited some major destructive landslides during the last decades (Section I-4.1) and recorded the caused damage, the movement type as well as other landslide-related descriptions, e.g. if the landslide deposit had formed a dam. Furthermore, information exists about landslides that occurred before the start of the satellite-based analysis in 1986 (Yerokhin 1998). Although the failure date of these landslides is unknown, these landslide records provide valuable information about the spatial distribution of historic landslide activity. Thus, the combination of the remote sensing-based results and the landslide information of local authorities could further improve the understanding of the regional landslide processes in Kyrgyzstan. To utilize these heterogeneous landslide data for quantitative analysis requires their homogenization and

integration in a combined multi-source landslide inventory. Such a multi-source inventory could be accomplished by Golovko et al. (2015), which combine the automatically derived RapidEye-based landslide mapping results with the locally available landslide information base for Southern Kyrgyzstan.

The RapidEye science archive (RESA) data grant, which has allowed pre-defined tasking of RapidEye data acquisition during the period between 2011 and 2013 (Section I-3.2), could be continued beyond 2013. Since 2014, the study area of the thesis could be established as a priority tasking area within the RESA program. The current tasking aims at a bi-monthly coverage during the active landslide season ranging from April to July. Thus, the RapidEye-based spatiotemporally precise analysis of the landslide activity, performed for the years 2009-2013 (Chapter III), can be pursued for the years 2014 and 2015. Moreover, the ongoing tasking ensures adequate remote sensing data availability for the area-wide landslide monitoring for upcoming years as long as the current data acquisition scheme can be continued[6].

2.2 Methodological Developments and Potential Synergies

The proposed landslide mapping approach is extensively automated, yet the preselection of bi-temporal image pairs remains a manual task (Section IV-3.2). This preselection step is implemented to utilize highly irregular time series of seasonally varying data acquisitions. It allows the approach to focus the landslide detection on datasets that are most comparable and to use the remaining datasets subsequently in the multi-temporal revegetation analysis as well as in a date refinement step (Section IV-3.3). Thus, the efficiency of the approach for operational use would benefit from the development of an optimization routine that automatically identifies most comparable datasets within the time series at hand. Said routine needs to consider the seasonality, spectral characteristics, spatial resolution, temporal intervals between acquisitions, and viewing angles of the different datasets, whereas comparable seasons and similar viewing angles are particularly important in mountainous regions that are characterized by short vegetation periods and rough terrain. Nevertheless, if the approach is applied to a time series of comparable datasets, it can be performed fully automated.

Some landslide identification studies (Barlow et al. 2006; Martha et al. 2010) aim at the classification of landslide types, which, depending on the achieved accuracy, enables type differentiated landslide hazard assessment (Corominas et al. 2014). For the discrimination of landslide types, they analyze shape, relief, and textural characteristics of detected landslide objects. Their landslide detection and classification is based on optical remote sensing data of high spatial resolution (6 m and better) and precise digital elevation models (DEM) derived from local topographic maps (Barlow et al. 2006) or from a stereo pair of the high resolution images (Martha et al. 2010). With less resolution data available (optical imagery or elevation data), the discrimination of the landslide types is less satisfactory (Barlow et al. 2003; Martin & Franklin 2005). Thus, the implementation of type classification routines into the multi-temporal landslide mapping approach of the thesis is hampered by the absence of a high-resolution DEM in Kyrgyzstan as well as by the lower resolution of the imagery available for the long-term analysis. However, the currently ongoing generation of the global WorldDEM™ (Riegler et al. 2015) will open up new opportunities in Kyrgyzstan for improved relief-based analysis. This new global DEM will exceed the spatial resolution and vertical accuracy of the currently available global DEMs (Avtar et al. 2015), i.e. ASTER GDEM V2

[6] The continuation of the RESA program is currently under discussion (as of 5 November 2015)

(Tachikawa et al. 2011) and the SRTM (Rabus et al. 2003). Thus, the WorldDEM™ facilitates a future extension of the landslide mapping approach towards the discrimination of landslide types at least for the recent analysis, e.g. based on RapidEye imagery.

A further promising field of investigation is the synergy between data of optical and radar sensors. As this thesis shows, optical remote sensing enables an efficient retrospective derivation of long-term multi-temporal landslide inventories. In contrast, radar contributes to the identification and quantification of slow moving parts of landslides (Section I-2.2.1). Put differently, optical remote sensing data enable the spatially explicit delineation of the landslide extent and the determination of the landslide failure date, whereas radar data provide information of how long and how much a landslide has moved before or after the onset of the failure. Thus, an efficient combination of these two complementing results has a great potential to further improve the landslide process understanding of a given region. In Southern Kyrgyzstan, recent studies of Motagh et al. (2013) and Teshebaeva et al. (2015) measured displacement rates of active slow-moving landslides for subsets of the study area using radar times series from 2009 to 2010 and from 2007 to 2010, respectively. Hence, future research could focus on the development of strategies to merge the existing results of optical and radar analysis and to extend the combined analysis to large areas and longer time spans (e.g. by a synergetic use of Sentinel-1 & 2).

In view of other time series applications (besides landslide mapping) it might be worthwhile to implement or develop further pre-processing strategies, e.g. spectral resampling and atmospheric correction routines (Bodart et al. 2011; Richter & Schlapfer 2002; Song et al. 2001; Tan et al. 2012). The realization of such routines is one objective of the currently ongoing project "GeoMultiSens" (GMS 2015)[7]. This project aims at an efficient homogenization and analysis of multi-sensor time series data in the petabyte range to enable monitoring of spatiotemporal Earth surface changes for large areas (GMS 2015). The imagery and partly the integrated pre-processing algorithms of this thesis are used within "GeoMultiSens" for the methodological developments towards a homogenized time series data cube as basis for time series analyses for various fields of application.

2.3 Transferability

The developed multi-temporal landslide identification procedure concentrates on landslide-related vegetation change characteristics, i.e. the vegetation disturbance due to the landslide failure and the slow revegetation rate after failure (Chapters III, IV). Thus, it enables general transferability to areas where landslide occurrence is also associated with changes to the surface vegetation cover. Most landslides are highly dependent on the existence of weakly consolidated material and substantial water supply, both factors facilitating vegetation growth. Hence, areas of high landslide activity very often correspond to vegetated areas, such as the global landslide hotspots (Nadim et al. 2006) in South America (e.g. Brazil, Colombia) and Southeast Asia (e.g. Taiwan, Thailand, Philippines). Landslides not or only barely associated with vegetation change occur in arid regions (Cardinali 1990), in very high mountain ranges (Stolle et al. 2015), and in extraterrestrial landscapes (Brunetti et al. 2014). However, in comparison to the usually vegetated global landslide hotspots such regions are less subject to hazardous landslides, due to sparse population and lower landslide rates. Thus, in general, the approach is widely applicable, especially for regions where the local population and infrastructure is most endangered by landslides.

[7] Project is funded by the Federal Ministry of Education and Research (BMBF) from September 2014 to August 2017.

The actual transfer of the approach requires the complete processing chain (pre-processing and landslide mapping) to be applicable to new datasets and new environmental conditions. The pre-processing is designed to perform robustly based on standard data products of common multi-spectral satellite sensors, without the need of external reference information such as reference spectra or GPS measurements (Chapter II, Section III-2.3, IV-3.1). Thus, it has the potential to work in other areas as well, without collecting reference data in advance. In fact, the geometric co-registration procedure has already shown its applicability in other studies, which analyzed multi-temporal RapidEye data stacks in Northern Germany for the derivation of agricultural soil patterns (Blasch et al. 2015) and for the reconstruction of lake level changes (Heine et al. 2015). The application of the landslide identification procedure to other areas may require the adaption of the implemented thresholds to possibly differing environmental conditions. For example, climatic conditions influence the rate of vegetation regrowth after a landslide failure, e.g. landslides in tropical environments are usually subject to faster revegetation than in Kyrgyzstan. Furthermore, the local relief might be different from the foothills of the Tien Shan mountain ranges and thus landslides may occur on steeper or gentler slopes. However, in principle the complete processing chain could be transferred to other areas without the need of any external data input or new methodological developments.

A further requirement for the application of the approach to other areas is the local availability of suitable remote sensing data. The data of the sensors used in this thesis (Section I-3.2) are usually widely available for most parts of the world and thus promote broad transferability of the approach. However, in some areas other remote sensing data might be more feasible to use. In Southeast Asia, landslide investigations are often based on the high-temporal resolution data of the multi-spectral Formosat-2 sensor (Mondini et al. 2011a; Mondini et al. 2013; Rau et al. 2014; Tsai et al. 2010; Weng et al. 2011). The potential to integrate such multi-spectral sensors in the multi-temporal landslide mapping procedure represents a substantial strength of the developed approach. In general, the focus on the NDVI-based analysis allows the approach to perform on all common multi-spectral sensors, since they usually comprise the required bands in the red and near infrared parts of the spectrum, which is also true for the Formosat-2 sensor. Furthermore, the successful application of the approach to seven sensors in Chapter IV could already show its suitability to accommodate for slight sensor-specific NDVI variations, which may exist between the sensors (Goetz 1997; Huang et al. 2013; Martinez-Beltran et al. 2009). This multi-sensor applicability also allows future extensions of the approach to upcoming sensors. In this context the freely available Sentinel-2[8] data with a temporal resolution of up to five days, a spatial resolution of 10 m and a swath of 290 km (Drusch et al. 2012) will open up new opportunities for automated large area landslide mapping using optical satellite remote sensing.

Besides monitoring and long-term spatiotemporal analysis, the event-based analysis is another important field of application for landslide mapping approaches. In case of major landslide triggering events such as large earthquakes or tropical rainstorms, rapid disaster response and coordination needs fast identification of the most affected areas. This requires landslide mapping approaches to perform on the first available satellite data acquired right after the event. For such a scenario, most landslide mapping approaches have been designed, using either a mono-temporal post-event image or a bi-temporal image pair consisting of a pre- and post-event image (Table App-1). Although the landslide mapping approach of this thesis is primarily developed to

[8] Sentinel-2 will be a system of two sensors in the same orbit with a phase delay of 180°. Sentinel-2A is launched on 23 June 2015 and Sentinel-2B is planned in 2016.

identify landslides within a time series database, it can also be applied to a bi-temporal image pair only, due to its sub-division in bi-temporal landslide identification and subsequent multi-temporal plausibility control (Section IV-3.3). Limiting the approach to the bi-temporal landslide identification step might increase the number of false positives, but has no influence on the landslide detection success. Moreover, the capability of the developed approach to perform on different sensors is advantageous in the context of rapid response mapping, because often the sensors of the data that are available before and after an event do not match and if large areas are affected, data of different sensors have to be used to cover the complete area.

A recent example of such a major landslide triggering event is the Nepal earthquake (also called Gorkha earthquake) on 25 April 2015 and the aftershock on 12 May 2015 with magnitudes of 7.8 Mw and 7.3 Mw, respectively (Gupta 2015). The earthquake killed almost 9000 people and destroyed more than half a million houses (OCHA 2015). According to the EWF (2015) the earthquake triggered approximately 5600 landslides and caused a widespread destabilization of slopes and building of cracks, which most likely lead to landslides during the subsequent summer monsoons (NEAU 2015a; NEAU 2015b). As a part of an international network of scientists, a GFZ funded and coordinated HART ("Hazard and Risk Team") initiative[9] investigates the aftereffects of the disastrous earthquakes in Nepal (Andermann et al. 2015). Based on this initiative, a RESA proposal could be realized (project ID: 165), allowing to achieve RapidEye data coverages after the two main shocks as well as before and after the summer monsoon in the upcoming two years. In this context, the landslide mapping approach has been tested within the earthquake-affected area for two scenarios. Firstly, the approach has been applied to a multi-sensor image pair consisting of a Landsat-OLI pre-event image and a RapidEye post-event image (Figures App-10,11). Secondly, a mono-sensor image pair of RapidEye data has been used (Figures App-8,9). In both test cases the approach resulted in reliable identification of the landslide-affected areas, however a quantitative accuracy assessment could not be performed yet. These first results demonstrate the general transferability of the approach to other natural environments, the successful transfer of the processing chain to other areas and other available data, and its suitability to operate within a rapid response application using mono- and multi-sensor analysis. Among others, future applications of the landslide mapping approach will focus on the investigation of the immediate landslide response to the earthquake (identification of co-seismically triggered landslides), and the monitoring of landslide rates in upcoming monsoon seasons, in order to evaluate the still not-well understood interrelation of earthquake-induced slope destabilization and intensity of increased landslide risk after earthquakes (Marc et al. 2015; NEAU 2015b).

Overall, the developed approach provides a great potential to be applied to different landslide-affected regions, optical sensors, and fields of application (e.g. long-term spatiotemporal landslide analysis, monitoring of recent landslide activity, event-related rapid response mapping, and as a part of early-warning systems by identifying precursors of hazardous landslides). Prerequisites are sufficient optical remote sensing data availability, a potentially required calibration of the implemented thresholds in case of naturally differing environments, and that landslide occurrence in the studied region corresponds to vegetation disturbance.

[9] The international network of the HART initiative includes scientists from Potsdam, Nancy, Zurich, Cambridge, Edinburgh, Utrecht and partners from Nepal. (https://idw-online.de/en/news631843, accessed 21 October 2015)

References

Aksoy, B. & Ercanoglu, M., (2012). Landslide identification and classification by object-based image analysis and fuzzy logic: An example from the Azdavay region (Kastamonu, Turkey). *Computers & Geosciences*, 38(1), pp.87–98.

Andermann, C., Behling, R., Cook, K.L., Emberson, R., Hovius, N., Marc, O., Motagh, M., Roessner, S., Sens-Schoenfelder, C. & Turowski, J. M., (2015). Landscape Response To The Mw7.9 Gorkha Earthquake. In GSA Annual Meeting in Baltimore, Maryland, USA (1-4 November 2015).

Avtar, R., Yunus, A.P., Kraines, S. & Yamamuro, M., (2015). Evaluation of DEM generation based on Interferometric SAR using TanDEM-X data in Tokyo. *Phys. Chem. Earth*.

Barazzetti, L., Scaioni, M. & Gianinetto, M., (2014). Automatic Co-registration of Satellite Time Series via Least Squares Adjustment. *Eur. J. Remote Sens.*, 47, pp.55–74.

Barlow, J., Franklin, S. & Martin, Y., (2006). High spatial resolution satellite imagery, DEM derivatives, and image segmentation for the detection of mass wasting processes. *Photogramm. Eng. Remote Sens.*, 72(6), pp.687–692.

Barlow, J., Martin, Y. & Franklin, S.E., (2003). Detecting translational landslide scars using segmentation of Landsat ETM+ and DEM data in the northern Cascade Mountains, British Columbia. *Can. J. Remote Sens.*, 29(4), pp.510–517.

Bay, H., Ess, A., Tuytelaars, T. & Van Gool, L., (2008). Speeded-Up Robust Features (SURF). *Comput. Vis. Image Und.*, 110(3), pp.346–359.

Behling, R., Roessner, S., Kaufmann, H. & Kleinschmit, B., (2014a). Automated Spatiotemporal Landslide Mapping over Large Areas Using RapidEye Time Series Data. *Remote Sens.*, 6(9), pp.8026–8055.

Behling, R., Roessner, S., Segl, K., Kleinschmit, B. & Kaufmann, H., (2014b). Robust Automated Image Co-Registration of Optical Multi-Sensor Time Series Data: Database Generation for Multi-Temporal Landslide Detection. *Remote Sens.*, 6(3), pp.2572–2600.

Benson, B. & Mackenzie, M., (1995). Effects of Sensor Spatial-Resolution on Landscape Structure Parameters. *Landsc. Ecol.*, 10(2), pp.113–120.

Blackbridge, (2014). BlackBridge: Delivering the World. http://www.blackbridge.com/rapideye/products/ortho.htm (accesed 05 November 2015)

Blasch, G., Spengler, D., Hohmann, C., Neumann, C., Itzerott, S. & Kaufmann, H., (2015). Multitemporal soil pattern analysis with multispectral remote sensing data at the field-scale. *Comput. Electron. Agric.*, 113, pp.1–13.

Blaschke, T., Feizizadeh, B. & Hoelbling, D., (2014). Object-Based Image Analysis and Digital Terrain Analysis for Locating Landslides in the Urmia Lake Basin, Iran. *IEEE J. Sel. Top. Appl. Earth Observ. Remote Sens.*, 7(12), pp.4806–4817.

Bodart, C., Eva, H., Beuchle, R., Rasi, R., Simonetti, D., Stibig, H.-J., Brink, A., Lindquist, E. & Achard, F., (2011). Pre-processing of a sample of multi-scene and multi-date Landsat imagery used to monitor forest cover changes over the tropics. *ISPRS-J. Photogramm. Remote Sens.*, 66(5), pp.555–563.

Borghuis, A.M., Chang, K. & Lee, H.Y., (2007). Comparison between automated and manual mapping of typhoon-triggered landslides from SPOT-5 imagery. *Int. J. Remote Sens.*, 28(8), pp.1843–1856.

Bouchiha, R. & Besbes, K., (2013). Automatic Remote-sensing Image Registration Using SURF. *IJCTE*, pp.88–92.

Brook, A. & Ben-Dor, E., (2011). Automatic Registration of Airborne and Spaceborne Images by Topology Map Matching with SURF Processor Algorithm. *Remote Sens.*, 3(1), pp.65–82.

Brunetti, M.T., Guzzetti, F., Cardinali, M., Fiorucci, F., Santangelo, M., Mancinelli, P., Komatsu, G. & Borselli, L., (2014). Analysis of a new geomorphological inventory of landslides in Valles Marineris, Mars. *Earth Planet. Sci. Lett.*, 405, pp.156–168.

Bruzzone, L., Bovolo, F. & Marchesi, S., (2007). A multiscale change detection technique robust to registration noise. In *Pattern Recognition and Machine Intelligence, Proceedings*. 2nd International Conference on Pattern Recognition and Machine Intelligence, DEC 18-22, 2007 Calcutta, INDIA. pp. 77–86.

Burger, W. & Burge, M.J., (2009). *Principles of Digital Image Processing: Core Algorithms*, London: Springer.

Cao, S., Jiang, J., Zhang, G. & Yuan, Y., (2013). An edge-based scale- and affine-invariant algorithm for remote sensing image registration. *Int. J. Remote Sens.*, 34(7), pp.2301–2326.

Cardinali, M., Guzzetti, F. & Brabb, E.E., (1990). Preliminary map showing landslide deposits and related features in New Mexico. USGS Open File Report 90/293, 4 sheets, scale 1:500,000.

Cascini, L., (2008). Applicability of landslide susceptibility and hazard zoning at different scales. *Eng. Geol.*, 102(3-4), pp.164–177.

Cascini, L., Fornaro, G. & Peduto, D., (2009). Analysis at medium scale of low-resolution DInSAR data in slow-moving landslide-affected areas. *ISPRS-J. Photogramm. Remote Sens.*, 64(6), pp.598–611.

Casson, B., Delacourt, C., Baratoux, D. & Allemand, P., (2003). Seventeen years of the "La Clapiere" landslide evolution analysed from ortho-rectified aerial photographs. *Eng. Geol.*, 68(1-2), pp.123–139.

Castilla, G., Guthrie, R.H. & Hay, G.J., (2009). The Land-cover Change Mapper (LCM) and its Application to Timber Harvest Monitoring in Western Canada. *Photogramm. Eng. Remote Sens.*, 75(8), pp.941–950.

Chander, G., Haque, M.O., Sampath, A., Brunn, A., Trosset, G., Hoffmann, D., Roloff, S., Thiele, M. & Anderson, C., (2013). Radiometric and geometric assessment of data from the RapidEye constellation of satellites. *Int. J. Remote Sens.*, 34(16), pp.5905–5925.

Cheng, K.S., Wei, C. & Chang, S.C., (2004). Locating landslides using multi-temporal satellite images. *Adv. Space Res.*, 33(3), pp.296–301.

Chen, H.M., Arora, M.K. & Varshney, P.K., (2003). Mutual information-based image registration for remote sensing data. *Int. J. Remote Sens.*, 24(18), pp.3701–3706.

Clague, J.J., (2013). Landslide. In P. T. Bobrowsky, ed. *Encyclopedia of Natural Hazards*. Encyclopedia of Earth Sciences Series. Springer Netherlands, pp. 594–602.

Colesanti, C. & Wasowski, J., (2006). Investigating landslides with space-borne synthetic aperture radar (SAR) interferometry. *Eng. Geol.*, 88(3-4), pp.173–199.

Coppin, P., Jonckheere, I., Nackaerts, K., Muys, B. & Lambin, E., (2004). Digital change detection methods in ecosystem monitoring: a review. *Int. J. Remote Sens.*, 25(9), pp.1565–1596.

Corominas, J. & Moya, J., (2008). A review of assessing landslide frequency for hazard zoning purposes. *Eng. Geol.*, 102(3-4), pp.193–213.

Corominas, J., van Westen, C., Frattini, P., Cascini, L., Malet, J.-P., Fotopoulou, S., Catani, F., Van Den Eeckhaut, M., Mavrouli, O., Agliardi, F., Pitilakis, K., Winter, M.G., Pastor, M., Ferlisi, S., Tofani, V., Hervas, J. & Smith, J.T., (2014). Recommendations for the quantitative analysis of landslide risk. *Bull. Eng. Geol. Environ.*, 73(2), pp.209–263.

Cruden, D.M., (1993). The multilingual landslide glossary. *The International Geotechnical Societies UNESCO Working Party for World Landslide Inventory*, 5.

Cruden, D.M. & Varnes, D.J., (1996). Landslide types and processes. *Landslides, Investigation and Mitigation*, pp.36–75.

Czuchlewski, K.R., Weissel, J.K. & Kim, Y., (2003). Polarimetric synthetic aperture radar study of the Tsaoling landslide generated by the 1999 Chi-Chi earthquake, Taiwan. *J. Geophys. Res.-Earth Surf.*, 108(F1).

Danneels, G., Bourdeau, C., Torgoev, I. & Havenith, H.-B., (2008). Geophysical investigation and dynamic modelling of unstable slopes: case-study of Kainama (Kyrgyzstan). *Geophys. J. Int.*, 175(1), pp.17–34.

Danneels, G., Pirard, E. & Havenith, H.B., (2007). Automatic landslide detection from remote sensing images using supervised classification methods. In *Geoscience and Remote Sensing Symposium, 2007. IGARSS 2007. IEEE International*. pp. 3014–3017.

Dawn, S., Saxena, V. & Sharma, B., (2010). Remote Sensing Image Registration Techniques: A Survey. *Image and Signal Processing*, pp.103–112.

Delacourt, C., Allemand, P., Berthier, E., Raucoules, D., Casson, B., Grandjean, P., Pambrun, C. & Varel, E., (2007). Remote-sensing techniques for analysing landslide kinematics: a review. *Bull. Soc. Geol. Fr.*, 178(2), pp.89–100.

Dou, J., Chang, K.-T., Chen, S., Yunus, A.P., Liu, J.-K., Xia, H. & Zhu, Z., (2015). Automatic Case-Based Reasoning Approach for Landslide Detection: Integration of Object-Oriented Image Analysis and a Genetic Algorithm. *Remote Sens.*, 7(4), pp.4318–4342.

Drusch, M., Del Bello, U., Carlier, S., Colin, O., Fernandez, V., Gascon, F., Hoersch, B., Isola, C., Laberinti, P., Martimort, P., Meygret, A., Spoto, F., Sy, O., Marchese, F. & Bargellini, P., (2012). Sentinel-2: ESA's Optical High-Resolution Mission for GMES Operational Services. *Remote Sens. Environ.*, 120, pp.25–36.

Duethmann, D., Zimmer, J., Gafurov, A., Guentner, A., Kriegel, D., Merz, B. & Vorogushyn, S., (2013). Evaluation of areal precipitation estimates based on downscaled reanalysis and station data by hydrological modelling. *Hydrol. Earth Syst. Sci.*, 17(7), pp.2415–2434.

Erener, A. & Düzgün, H.S.B., (2012). Landslide susceptibility assessment: what are the effects of mapping unit and mapping method? *Environ. Earth Sci.*, 66(3), pp.859–877.

EWF, (2015). UPDATED (30 June) landslide inventory following 25 April and 12 May Nepal earthquakes. *Earthquakes without Frontiers (EWF)*. http://ewf.nerc.ac.uk/2015/06/30/updated-30-june-landslide-inventory-following-25-april-and-12-may-nepal-earthquakes/ (accessed 21 Oct 2015)

Fell, R., Corominas, J., Bonnard, C., Cascini, L., Leroi, E. & Savage, W.Z., (2008). Guidelines for landslide susceptibility, hazard and risk zoning for land use planning. *Eng. Geol.*, 102(3-4), pp.85–98.

Fiorucci, F., Cardinali, M., Carlà, R., Rossi, M., Mondini, A.C., Santurri, L., Ardizzone, F. & Guzzetti, F., (2011). Seasonal landslide mapping and estimation of landslide mobilization rates using aerial and satellite images. *Geomorphology*, 129(1–2), pp.59–70.

Fonseca, L.M.. & Manjunath, B.S., (1996). Registration techniques for multisensor remotely sensed imagery. *Photogramm. Eng. Remote Sens.*, 62(9), pp.1049–1056.

Galli, M., Ardizzone, F., Cardinali, M., Guzzetti, F. & Reichenbach, P., (2008). Comparing landslide inventory maps. *Geomorphology*, 94(3–4), pp.268–289.

Gao, F., Masek, J. & Wolfe, R.E., (2009). Automated registration and orthorectification package for Landsat and Landsat-like data processing. *J. Appl. Remote Sens.*, 3(1), p.033515.

Ghosh, S., van Westen, C.J., Carranza, E.J.M., Jetten, V.G., Cardinali, M., Rossi, M. & Guzzetti, F., (2012). Generating event-based landslide maps in a data-scarce Himalayan environment for estimating temporal and magnitude probabilities. *Eng. Geol.*, 128, pp.49–62.

Gianinetto, M., (2012). Automatic Co-Registration of Satellite Time Series. *Photogramm. Rec.*, 27(140), pp.462–470.

GMS (2015): GeoMultiSens - Scalable Analysis of Big Remote Sensing Data. http://geomultisens.de/ (accessed 05 Nov 2015)

Goetz, S.J., (1997). Multi-sensor analysis of NDVI, surface temperature and biophysical variables at a mixed grassland site. *Int. J. Remote Sens.*, 18(1), pp.71–94.

Golovko, D., Roessner, S., Behling, R., Wetzel, H.-U. & Kaufmann, H., (2014). GIS-Based Integration of Heterogeneous Data for a Multi-temporal Landslide Inventory. In K. Sassa, P. Canuti, & Y. Yin, eds. *Landslide Science for a Safer Geoenvironment*. Springer International Publishing, pp. 799–804.

Golovko, D., Roessner, S., Behling, R., Wetzel, H.-U. & Kleinschmit, B., (2015). Development of Multi-Temporal Landslide Inventory Information System for Southern Kyrgyzstan Using GIS and Satellite Remote Sensing. *Photogramm. Fernerkund. Geoinf.*, (2), pp.157–172.

Gupta, H.K., (2015). The Mw 7.8 April 25, 2015 Nepal earthquake (End of a long-term seismic quiescence?). *J. Geol. Soc. India*, 85(6), pp.641–646.

Guzzetti, F., Cardinali, M., Reichenbach, P. & Carrara, A., (2000). Comparing landslide maps: A case study in the Upper Tiber River basin, central Italy. *Environ. Manage.*, 25(3), pp.247–263.

Guzzetti, F., Carrara, A., Cardinali, M. & Reichenbach, P., (1999). Landslide hazard evaluation: a review of current techniques and their application in a multi-scale study, Central Italy. *Geomorphology*, 31(1-4), pp.181–216.

Guzzetti, F., Mondini, A.C., Cardinali, M., Fiorucci, F., Santangelo, M. & Chang, K.-T., (2012). Landslide inventory maps: New tools for an old problem. *Earth-Sci. Rev.*, 112(1–2), pp.42–66.

Guzzetti, F., Reichenbach, P., Cardinali, M., Galli, M. & Ardizzone, F., (2005). Probabilistic landslide hazard assessment at the basin scale. *Geomorphology*, 72(1-4), pp.272–299.

Havenith, H.B., Strom, A., Torgoev, I., Torgoev, A., Lamair, L., Ischuk, A. & Abdrakhmatov, K., (2015). Tien Shan geohazards database: Earthquakes and landslides. *Geomorphology*.

Havenith, H.B., Torgoev, I., Meleshko, A., Alioshin, Y., Torgoev, A. & Danneels, G., (2006). Landslides in the Mailuu-Suu Valley, Kyrgyzstan—Hazards and Impacts. *Landslides*, 3(2), pp.137–147.

Heine, I., Stueve, P., Kleinschmit, B. & Itzerott, S., (2015). Reconstruction of Lake Level Changes of Groundwater-Fed Lakes in Northeastern Germany Using RapidEye Time Series. *Water*, 7(8), pp.4175–4199.

Hervás, J., (2013). Landslide Inventory. In P. T. Bobrowsky, ed. *Encyclopedia of Natural Hazards*. Encyclopedia of Earth Sciences Series. Springer Netherlands, pp. 610–611.

Highland, L. & Brobowsky, P., (2008). The Landslide Handbook— A Guide to Understanding Landslides. *US Geological Survey Circular*, 1325.

Hilley, G.E., Burgmann, R., Ferretti, A., Novali, F. & Rocca, F., (2004). Dynamics of slow-moving landslides from permanent scatterer analysis. *Science*, 304(5679), pp.1952–1955.

Hölbling, D., Friedl, B. & Eisank, C., (2015). An object-based approach for semi-automated landslide change detection and attribution of changes to landslide classes in northern Taiwan. *Earth Sci. Inform.*, pp.1–9.

Hölbling, D., Füreder, P., Antolini, F., Cigna, F., Casagli, N. & Lang, S., (2012). A Semi-Automated Object-Based Approach for Landslide Detection Validated by Persistent Scatterer Interferometry Measures and Landslide Inventories. *Remote Sens.*, 4(12), pp.1310–1336.

Huang, L. & Li, Z., (2010). Feature-based image registration using the shape context. *Int. J. Remote Sens.*, 31(8), pp.2169–2177.

Huang, R. & Fan, X., (2013). The landslide story. *Nat. Geosci.*, 6(5), pp.325–326.

Huang, W., Huang, J., Wang, X., Wang, F. & Shi, J., (2013). Comparability of Red/Near-Infrared Reflectance and NDVI Based on the Spectral Response Function between MODIS and 30 Other Satellite Sensors Using Rice Canopy Spectra. *Sensors*, 13(12), pp.16023–16050.

Hussain, M., Chen, D., Cheng, A., Wei, H. & Stanley, D., (2013). Change detection from remotely sensed images: From pixel-based to object-based approaches. *ISPRS-J. Photogramm. Remote Sens.*, 80, pp.91–106.

Ibatulin, K.V., (2011). *Monitoring of Landslides in Kyrgyzstan*, Bishkek, Kyrgyzstan: Ministry of Emergency Situations of the Kyrgyz Republic.

Jaboyedoff, M., Oppikofer, T., Abellan, A., Derron, M.-H., Loye, A., Metzger, R. & Pedrazzini, A., (2012). Use of LIDAR in landslide investigations: a review. *Nat. Hazards*, 61(1), pp.5–28.

Jamali, S., Jonsson, P., Eklundh, L., Ardo, J. & Seaquist, J., (2015). Detecting changes in vegetation trends using time series segmentation. *Remote Sens. Environ.*, 156, pp.182–195.

Jianya, G., Haigang, S., Guorui, M. & Qiming, Z., (2008). A review of multi-temporal remote sensing data change detection algorithms. *The International Archives of the Photogrammetry, Remote Sensing and Spatial Information Sciences*, 37(B7), pp.757–762.

Jonsson, P. & Eklundh, L., (2004). TIMESAT - a program for analyzing time-series of satellite sensor data. *Comput. Geosci.*, 30(8), pp.833–845.

Kalmetieva, Z.A., Mikolaichuk, A.V., Moldobekov, B.D., Meleshko, A.V., Jantaev, M.M. & Zubovich, A.V., (2009). *Atlas of earthquakes in Kyrgyzstan*, Bishkek, Kyrgyzstan: CAIAG.

Kennedy, R.E., Yang, Z. & Cohen, W.B., (2010). Detecting trends in forest disturbance and recovery using yearly Landsat time series: 1. LandTrendr — Temporal segmentation algorithms. *Remote Sens. Environ.*, 114(12), pp.2897–2910.

Kjekstad, O. & Highland, L., (2009). Economic and Social Impacts of Landslides. In K. Sassa & P. Canuti, eds. *Landslides – Disaster Risk Reduction*. Springer Berlin Heidelberg, pp. 573–587.

Klimeš, J., (2013). Landslide temporal analysis and susceptibility assessment as bases for landslide mitigation, Machu Picchu, Peru. *Environ. Earth Sci.*, 70(2), pp.913–925.

Kurtz, C., Stumpf, A., Malet, J.-P., Gançarski, P., Puissant, A. & Passat, N., (2014). Hierarchical extraction of landslides from multiresolution remotely sensed optical images. *ISPRS-J. Photogramm. Remote Sens.* , 87, pp.122–136.

Lacroix, P., Zavala, B., Berthier, E. & Audin, L., (2013). Supervised Method of Landslide Inventory Using Panchromatic SPOT5 Images and Application to the Earthquake-Triggered Landslides of Pisco (Peru, 2007, Mw8.0). *Remote Sens.*, 5(6), pp.2590–2616.

Lahousse, T., Chang, K.T. & Lin, Y.H., (2011). Landslide mapping with multi-scale object-based image analysis – a case study in the Baichi watershed, Taiwan. *Nat. Hazards Earth Syst. Sci.*, 11(10), pp.2715–2726.

Lee, D.S., Shan, J. & Bethel, J.S., (2003). Class-guided building extraction from Ikonos imagery. *Photogramm. Eng. Remote Sens.*, 69(2), pp.143–150.

Lee, D.S., Storey, J.C., Choate, M.J. & Hayes, R.W., (2004). Four years of Landsat-7 on-orbit geometric calibration and performance. *IEEE Trans. Geosci. Remote Sens.*, 42(12), pp.2786–2795.

Lee, S., Ryu, J.-H. & Kim, I.-S., (2007). Landslide susceptibility analysis and its verification using likelihood ratio, logistic regression, and artificial neural network models: case study of Youngin, Korea. *Landslides*, 4(4), pp.327–338.

Le Moigne, J., Cole-Rhodes, A.A., Eastman, R.D., Netanyahu, N.S., Stone, H.S., Zavorin, I. & Morisette, J.T., (2011a). Multitemporal and multisensor image registration. In J. LeMoigne, N. S. Netanyahu, & R. D. Eastman, eds. *Image Registration for Remote Sensing*. Cambridge: Cambridge Univ Press, pp. 293–338.

Le Moigne, J., Netanyahu, N.S. & Eastman, R.D. eds., (2011b). *Image Registration for Remote Sensing*, Cambridge: Cambridge Univ Press.

Leprince, S., Barbot, S., Ayoub, F. & Avouac, J.-P., (2007). Automatic and Precise Orthorectification, Coregistration, and Subpixel Correlation of Satellite Images, Application to Ground Deformation Measurements. *IEEE Trans. Geosci. Remote Sens.*, 45(6), pp.1529–1558.

Lin, C.-W., Chang, W.-S., Liu, S.-H., Tsai, T.-T., Lee, S.-P., Tsang, Y.-C., Shieh, C.-L. & Tseng, C.-M., (2011). Landslides triggered by the 7 August 2009 Typhoon Morakot in southern Taiwan. *Eng. Geol.*, 123(1-2), pp.3–12.

Li, N., Wang, R., Deng, Y., Liu, Y., Wang, C., Balz, T. & Li, B., (2014). Polarimetric Response of Landslides at X-Band Following the Wenchuan Earthquake. *IEEE Geosci. Remote Sens. Lett.*, 11(10), pp.1722–1726.

Liu, C.-C. & Chen, P.-L., (2009). Automatic extraction of ground control regions and orthorectification of remote sensing imagery. *Opt. Express*, 17(10), pp.7970–7984.

Lodhi, M.A., (2011). Earthquake-induced landslide mapping in the western Himalayas using medium resolution ASTER imagery. *Int. J. Remote Sens.*, 32(19), pp.5331–5346.

Lowe, D.G., (2004). Distinctive image features from scale-invariant keypoints. *Int. J. Comput. Vis.*, 60(2), pp.91–110.

Lu, D., Moran, E., Hetrick, S. & Li, G., (2010). Land-Use and Land-Cover Change Detection. In Q. Weng, ed. *Advances in Environmental Remote Sensing: Sensors, Algorithms, and Applications*. p. 273.

Lu, P., Stumpf, A., Kerle, N. & Casagli, N., (2011). Object-Oriented Change Detection for Landslide Rapid Mapping. *IEEE Geosci. Remote Sens. Lett.*, (99), pp.701–705.

Malamud, B.D., Turcotte, D.L., Guzzetti, F. & Reichenbach, P., (2004). Landslide inventories and their statistical properties. *Earth Surf. Proc. Land.*, 29(6), pp.687–711.

Marc, O., Hovius, N., Meunier, P., Uchida, T. & Hayashi, S., (2015). Transient changes of landslide rates after earthquakes. *Geology*, p.G36961.1.

Martha, T.R., Kerle, N., Jetten, V., van Westen, C.J. & Kumar, K.V., (2010). Characterising spectral, spatial and morphometric properties of landslides for semi-automatic detection using object-oriented methods. *Geomorphology*, 116(1-2), pp.24–36.

Martha, T.R., Kerle, N., van Westen, C.J., Jetten, V. & Vinod Kumar, K., (2012). Object-oriented analysis of multi-temporal panchromatic images for creation of historical landslide inventories. *ISPRS-J. Photogramm. Remote Sens.*, 67(0), pp.105–119.

Martha, T.R., van Westen, C.J., Kerle, N., Jetten, V. & Kumar, K.V., (2013). Landslide hazard and risk assessment using semi-automatically created landslide inventories. *Geomorphology*, 184, pp.139–150.

Martinez-Beltran, C., Osann Jochum, M.A., Calera, A. & Melia, J., (2009). Multisensor comparison of NDVI for a semi-arid environment in Spain. *Int. J. Remote Sens.*, 30(5), pp.1355–1384.

Martin, Y.E. & Franklin, S.E., (2005). Classification of soil- and bedrock-dominated landslides in British Columbia using segmentation of satellite imagery and DEM - data. *Int. J. Remote Sens.*, 26(7), pp.1505–1509.

Mathew, J., Babu, D.G., Kundu, S., Kumar, K.V. & Pant, C.C., (2014). Integrating intensity-duration-based rainfall threshold and antecedent rainfall-based probability estimate towards generating early warning for rainfall-induced landslides in parts of the Garhwal Himalaya, India. *Landslides*, 11(4), pp.575–588.

Metternicht, G., Hurni, L. & Gogu, R., (2005). Remote sensing of landslides: An analysis of the potential contribution to geo-spatial systems for hazard assessment in mountainous environments. *Remote Sens. Environ.*, 98(2-3), pp.284–303.

Michoud, C., Abellan, A., Derron, M.-H. & Jaboyedoff, M., (2010). *Review of Techniques for Landslide Detection, Fast Characterization, Rapid Mapping and Long-Term Monitoring*. Report: SafeLand Deliverable D4.1.

Moine, M., Puissant, A. & Malet, J.P., (2009). Detection of landslides from aerial and satellite images with a semi-automatic method. Application to the Barcelonnette basin (Alpes-de-Hautes-Provence, France). In *International Conference "Landslide Processes: from geomorpholgic mapping to dynamic modelling."*

Mondini, A.C., Chang, K.-T. & Yin, H.-Y., (2011a). Combining multiple change detection indices for mapping landslides triggered by typhoons. *Geomorphology*, 134(3-4), pp.440–451.

Mondini, A.C., Guzzetti, F., Reichenbach, P., Rossi, M., Cardinali, M. & Ardizzone, F., (2011b). Semi-automatic recognition and mapping of rainfall induced shallow landslides using optical satellite images. *Remote Sens. Environ.*, 115(7), pp.1743–1757.

Mondini, A.C., Marchesini, I., Rossi, M., Chang, K.-T., Pasquariello, G. & Guzzetti, F., (2013). Bayesian framework for mapping and classifying shallow landslides exploiting remote sensing and topographic data. *Geomorphology*, 201, pp.135–147.

Motagh, M., Wetzel, H.-U., Roessner, S. & Kaufmann, H., (2013). A TerraSAR-X InSAR study of landslides in southern Kyrgyzstan, Central Asia. *Remote Sens. Lett.*, 4(7), pp.657–666.

Mueller, M. & Segl, K., (1999). Simulation of high resolution imagery. In G. J. A. Nieuwenhuis, R. A. Vaughan, & M. Molenaar, eds. *Operational Remote Sensing for Sustainable Development*. Rotterdam: Balkema, pp. 331–338.

Murillo-Garcia, F.G., Alcantara-Ayala, I., Ardizzone, F., Cardinali, M., Fiourucci, F. & Guzzetti, F., (2015). Satellite stereoscopic pair images of very high resolution: a step forward for the development of landslide inventories. *Landslides*, 12(2), pp.277–291.

Nadim, F., Kjekstad, O., Peduzzi, P., Herold, C. & Jaedicke, C., (2006). Global landslide and avalanche hotspots. *Landslides*, 3(2), pp.159–173.

NEAU, (2015a). *Landslides and Displacement Situation Update*, Kathmandu, Nepal: Nepal Earthquake Assessment Unit (NEAU).

NEAU, (2015b). *Landslides and Flash Floods in the Monsoon*, Kathmandu, Nepal: Nepal Earthquake Assessment Unit (NEAU).

Nefeslioglu, H.A., Gokceoglu, C., Sonmez, H. & Gorum, T., (2011). Medium-scale hazard mapping for shallow landslide initiation: the Buyukkoy catchment area (Cayeli, Rize, Turkey). *Landslides*, 8(4), pp.459–483.

Nichol, J. & Wong, M.S., (2005). Satellite remote sensing for detailed landslide inventories using change detection and image fusion. *Int. J. Remote Sens.*, 26(9), pp.1913–1926.

OCHA, (2015). *Humanitarian Bulletin Nepal Earthquake Issue 04 (Final Issue) | 1 – 30 September 2015*, Kathmandu, Nepal: United Nations Office for the Coordination of Humanitarian Affairs (OCHA).

Ojala, T., Pietikainen, M. & Maenpaa, T., (2002). Multiresolution gray-scale and rotation invariant texture classification with local binary patterns. *IEEE Trans. Pattern Anal. Mach. Intell.*, 24(7), pp.971–987.

Othman, A.A. & Gloaguen, R., (2013). Automatic Extraction and Size Distribution of Landslides in Kurdistan Region, NE Iraq. *Remote Sens.*, 5(5), pp.2389–2410.

Parker, R.N., Densmore, A.L., Rosser, N.J., Michele, M. de, Li, Y., Huang, R., Whadcoat, S. & Petley, D.N., (2011). Mass wasting triggered by the 2008 Wenchuan earthquake is greater than orogenic growth. *Nat. Geosci.*, 4(7), pp.449–452.

Park, N. -W. & Chi, K. -H., (2008). Quantitative assessment of landslide susceptibility using high-resolution remote sensing data and a generalized additive model. *Int. J. Remote Sens.*, 29(1), pp.247–264.

Peruccacci, S., Brunetti, M.T., Luciani, S., Vennari, C. & Guzzetti, F., (2012). Lithological and seasonal control on rainfall thresholds for the possible initiation of landslides in central Italy. *Geomorphology*, 139, pp.79–90.

Petley, D., (2012). Global patterns of loss of life from landslides. *Geology*, 40(10), pp.927–930.

Petley, D.N., (2010). On the impact of climate change and population growth on the occurrence of fatal landslides in South, East and SE Asia. *Q J Eng. Geol. Hydroge.*, 43(4), pp.487–496.

Plank, S., Hölbling, D., Eisank, C., Friedl, B., Martinis, S. & Twele, A., (2015). Comparing object-based landslide detection methods based on polarimetric SAR and optical satellite imagery–a case study in Taiwan. In *7th International Workshop on Science and Applications of SAR Polarimetry and Polarimetric Interferometry, POLinSAR 2015*. pp. 27–30.

Pourghasemi, H.R., Pradhan, B., Gokceoglu, C., Mohammadi, M. & Moradi, H.R., (2013). Application of weights-of-evidence and certainty factor models and their comparison in landslide susceptibility mapping at Haraz watershed, Iran. *Arab. J. Geosci.*, 6(7), pp.2351–2365.

Pradhan, B., (2013). A comparative study on the predictive ability of the decision tree, support vector machine and neuro-fuzzy models in landslide susceptibility mapping using GIS. *Comput. Geosci.*, 51, pp.350–365.

Pradhan, B. & Lee, S., (2010a). Delineation of landslide hazard areas on Penang Island, Malaysia, by using frequency ratio, logistic regression, and artificial neural network models. *Environ. Earth Sci.*, 60(5), pp.1037–1054.

Pradhan, B. & Lee, S., (2010b). Landslide susceptibility assessment and factor effect analysis: backpropagation artificial neural networks and their comparison with frequency ratio and bivariate logistic regression modelling. *Environ. Modell. Softw.*, 25(6), pp.747–759.

Puissant, A., Hirsch, J. & Weber, C., (2005). The utility of texture analysis to improve per-pixel classification for high to very high spatial resolution imagery. *Int. J. Remote Sens.*, 26(4), pp.733–745.

Rabus, B., Eineder, M., Roth, A. & Bamler, R., (2003). The shuttle radar topography mission - a new class of digital elevation models acquired by spaceborne radar. *ISPRS-J. Photogramm. Remote Sens.*, 57(4), pp.241–262.

Rau, J.-Y., Jhan, J.-P. & Rau, R.-J., (2014). Semiautomatic Object-Oriented Landslide Recognition Scheme From Multisensor Optical Imagery and DEM. *IEEE Trans. Geosci. Remote Sensing*, 52(2), pp.1336–1349.

Reigber, C., Michel, G.W., Galas, R., Angermann, D., Klotz, J., Chen, J.Y., Papschev, A., Arslanov, R., Tzurkov, V.E. & Ishanov, M.C., (2001). New space geodetic constraints on the distribution of deformation in Central Asia. *Earth Planet. Sci. Lett.*, 191(1-2), pp.157–165.

Richter, R. & Schlapfer, D., (2002). Geo-atmospheric processing of airborne imaging spectrometry data. Part 2: atmospheric/topographic correction. *Int. J. Remote Sens.*, 23(13), pp.2631–2649.

Riegler, G., Hennig, S.D. & Weber, M., (2015). Worlddem - a Novel Global Foundation Layer. In U. Stilla & C. Heipke, eds. *Pia15+hrigi15 - Joint Isprs Conference, Vol. I*. Gottingen: Copernicus Gesellschaft Mbh, pp. 183–187.

Roessner, S., Wetzel, H.U., Kaufmann, H. & Sarnagoev, A., (2005). Potential of satellite remote sensing and GIS for landslide hazard assessment in southern kyrgyzstan (Central Asia). *Nat. Hazards*, 35(3), pp.395–416.

Rosin, P.L. & Hervas, J., (2005). Remote sensing image thresholding methods for determining landslide activity. *Int. J. Remote Sens.*, 26(6), pp.1075–1092.

Rossi, M., Witt, A., Guzzetti, F., Malamud, B.D. & Peruccacci, S., (2010). Analysis of historical landslide time series in the Emilia-Romagna region, northern Italy. *Earth Surf. Proc. Land.*, 35(10), pp.1123–1137.

Saba, S.B., van der Meijde, M. & van der Werff, H., (2010). Spatiotemporal landslide detection for the 2005 Kashmir earthquake region. *Geomorphology*, 124(1–2), pp.17–25.

Scaioni, M., Longoni, L., Melillo, V. & Papini, M., (2014). Remote Sensing for Landslide Investigations: An Overview of Recent Achievements and Perspectives. *Remote Sens.*, 6(10), pp.9600–9652.

Schlögel, R., Torgoev, I., De Marneffe, C. & Havenith, H.-B., (2011). Evidence of a changing size–frequency distribution of landslides in the Kyrgyz Tien Shan, Central Asia. *Earth Surf. Proc. Land.*, 36(12), pp.1658–1669.

Shibayama, T. & Yamaguchi, Y., (2014). A Landslide Detection Based on the Change of Scattering Power Components Between Multi-Temporal Polsar Data. In *2014 Ieee International Geoscience and Remote Sensing Symposium (igarss)*. New York: Ieee.

Shimada, M., Watanabe, M., Kawano, N., Ohki, M., Motooka, T. & Wada, Y., (2014). Detecting Mountainous Landslides by SAR Polarimetry: A Comparative Study Using Pi-SAR-L2 and X-band SARs. *T. Jpn. Soc. Aeronaut. S.*, 12(ists29), p.Pn_9–Pn_15.

Song, C., Woodcock, C.E., Seto, K.C., Lenney, M.P. & Macomber, S.A., (2001). Classification and change detection using Landsat TM data: When and how to correct atmospheric effects? *Remote Sens. Environ.*, 75(2), pp.230–244.

Stolle, A., Langer, M., Bloethe, J.H. & Korup, O., (2015). On predicting debris flows in arid mountain belts. *Glob. Planet. Change*, 126, pp.1–13.

Storey, J., Choate, M. & Lee, K., (2008). Geometric performance comparison between the OLI and the ETM+. In *Proceedings of the PECORA 17 Conference, November 18-20,2008*. Denver, Colorado.

Strahler, A.N., (1952). Hypsometric (Area-Altitude) Analysis of Erosional Topography. *Geol. Soc. Am. Bull.*, 63(11), p.1117.

Stumpf, A. & Kerle, N., (2011). Object-oriented mapping of landslides using Random Forests. *Remote Sens. Environ.*, 115(10), pp.2564–2577.

Stumpf, A., Lachiche, N., Malet, J.-P., Kerle, N. & Puissant, A., (2014). Active Learning in the Spatial Domain for Remote Sensing Image Classification. *IEEE Trans. Geosci. Remote Sens.*, 52(5), pp.2492–2507.

Stumpf, A., Malet J.-P., Kerle, N., Tofani, V., Segoni, S., Casagli, N., Michoud, C., Jaboyedoff, M., Fornaro, G., Peduto, D., Cascini, L., Baron, I., Supper, R., Oppikofer, T., L'Heureux, J.-S., Van Den Eeckhaut, M., Hervás, J., Moya, J., Raucoules, D.& Carman M. (2011). *Guidelines for the selection of appropriate remote sensing technologies for monitoring different types of landslides.* Report: SafeLand Deliverable D4.4.

Sundaresan, A., Varshney, P. & Arora, M., (2007). Robustness of change detection algorithms in the presence of registration errors. *Photogramm. Eng. Remote Sens.*, 73(4), pp.375–383.

Tachikawa, T., Hato, M., Kaku, M. & Iwasaki, A., (2011). Characteristics of Aster Gdem Version 2. In *2011 Ieee International Geoscience and Remote Sensing Symposium (igarss)*. New York: Ieee, pp. 3657–3660.

Tan, K.C., Lim, H.S., MatJafri, M.Z. & Abdullah, K., (2012). A comparison of radiometric correction techniques in the evaluation of the relationship between LST and NDVI in Landsat imagery. *Environ. Monit. Assess.*, 184(6), pp.3813–3829.

Teshebaeva, K., Roessner, S., Echtler, H., Motagh, M., Wetzel, H.-U. & Molodbekov, B., (2015). ALOS/PALSAR InSAR Time-Series Analysis for Detecting Very Slow-Moving Landslides in Southern Kyrgyzstan. *Remote Sens.*, 7(7), pp.8973–8994.

Tofani, V., Raspini, F., Catani, F. & Casagli, N., (2013). Persistent Scatterer Interferometry (PSI) Technique for Landslide Characterization and Monitoring. *Remote Sens.*, 5(3), pp.1045–1065.

Torgoev, I., Aleshin, Y.G. & Ashirov, G.E., (2008). Influence of Climatic Conditions on the Origin of Landslides in Kyrgyzstan (Central Asia). In *International Conference on Management of landslide hazard in the Asia-Pacific Region*. Sendai, Japan.

Townshend, J., Justice, C., Gurney, C. & Mcmanus, J., (1992). The Impact of Misregistration on Change Detection. *IEEE Trans. Geosci. Remote Sens.*, 30(5), pp.1054–1060.

Tsai, F., Hwang, J.-H., Chen, L.-C. & Lin, T.-H., (2010). Post-disaster assessment of landslides in southern Taiwan after 2009 Typhoon Morakot using remote sensing and spatial analysis. *Nat. Hazards Earth Syst. Sci.*, 10(10), pp.2179–2190.

Udelhoven, T., (2011). TimeStats: A Software Tool for the Retrieval of Temporal Patterns From Global Satellite Archives. *IEEE J. Sel. Top. Appl. Earth Observ. Remote Sens.*, 4(2), pp.310–317.

USGS, (1947). USGS - National Geospatial Data Standards - United States National Map Accuracy Standards.

Van Den Eeckhaut, M. & Hervás, J., (2012). State of the art of national landslide databases in Europe and their potential for assessing landslide susceptibility, hazard and risk. *Geomorphology*, 139–140(0), pp.545–558.

Van Den Eeckhaut, M., Reichenbach, P., Guzzetti, F., Rossi, M. & Poesen, J., (2009). Combined landslide inventory and susceptibility assessment based on different mapping units: an example from the Flemish Ardennes, Belgium. *Nat. Hazards Earth Syst. Sci.*, 9(2), pp.507–521.

Varnes, D.J., (1984). *Landslide hazard zonation: a review of principles and practice*. Natural Hazard Series (3), Paris: Unesco. pp. 63.

Varnes, D.J., (1978). Slope movement types and processes. *Transportation Research Board Special Report*, (176).

Verbesselt, J., Hyndman, R., Newnham, G. & Culvenor, D., (2010). Detecting trend and seasonal changes in satellite image time series. *Remote Sens. Environ.*, 114(1), pp.106–115.

Wan, S., Lei, T.-C. & Chou, T.-Y., (2012). A landslide expert system: image classification through integration of data mining approaches for multi-category analysis. *Int. J. Geogr. Inf. Sci.*, 26(4), pp.747–770.

Wan, S., Yen, J.Y., Lin, C.Y. & Chou, T.Y., (2015). Construction of knowledge-based spatial decision support system for landslide mapping using fuzzy clustering and KPSO analysis. *Arab. J. Geosci.*, 8(2), pp.1041–1055.

Wasowski, J. & Bovenga, F., (2014). Investigating landslides and unstable slopes with satellite Multi Temporal Interferometry: Current issues and future perspectives. *Eng. Geol.*, 174, pp.103–138.

Weng, M.-C., Wu, M.-H., Ning, S.-K. & Jou, Y.-W., (2011). Evaluating triggering and causative factors of landslides in Lawnon River Basin, Taiwan. *Eng. Geol.*, 123(1–2), pp.72–82.

van Westen, C.J., Castellanos, E. & Kuriakose, S.L., (2008). Spatial data for landslide susceptibility, hazard, and vulnerability assessment: An overview. *Eng. Geol.*, 102(3-4), pp.112–131.

Wetzel, H.-U., Roessner, S. & Sarnagoev, A., (2000). Remote sensing and GIS based geological mapping for assessment of landslide hazard in Southern Kyrgyzstan (Central Asia). *Management information systems*, pp.355–366.

Wieczorek, G.F., (1983). Preparing a detailed landslide-inventory map for hazard evaluation and reduction. *Bull. Assoc. Eng. Geol.*, 21(3), p.6.

Wu, C.Y. & Chen, S.C., (2013). Integrating spatial, temporal, and size probabilities for the annual landslide hazard maps in the Shihmen watershed, Taiwan. *Nat. Hazards Earth Syst. Sci.*, 13(9), pp.2353–2367.

Wulder, M.A., Masek, J.G., Cohen, W.B., Loveland, T.R. & Woodcock, C.E., (2012). Opening the archive: How free data has enabled the science and monitoring promise of Landsat. *Remote Sens. Environ.*, 122, pp.2–10.

Yang, X. & Chen, L., (2010). Using multi-temporal remote sensor imagery to detect earthquake-triggered landslides. *Int. J. Appl. Earth Obs. Geoinf.*, 12(6), pp.487–495.

Yerokhin, S.A., (1998). *Landslide Activity in Southern Kyrgyzstan*, Bishkek, Kyrgyzstan: Ministry of Emergency Situations of the Kyrgyz Republic.

Yonezawa, C., Watanabe, M. & Saito, G., (2012). Polarimetric Decomposition Analysis of ALOS PALSAR Observation Data before and after a Landslide Event. *Remote Sens.*, 4(8), pp.2314–2328.

Zitova, B. & Flusser, J., (2003). Image registration methods: a survey. *Image Vis. Comput.*, 21(11), pp.977–1000.

Zubovich, A.V., Wang, X., Scherba, Y.G., Schelochkov, G.G., Reilinger, R., Reigber, C., Mosienko, O.I., Molnar, P., Michajljow, W., Makarov, V.I., Li, J., Kuzikov, S.I., Herring, T.A., Hamburger, M.W., Hager, B.H., Dang, Y., Bragin, V.D. & Beisenbaev, R.T., (2010). GPS velocity field for the Tien Shan and surrounding regions. *Tectonics*, 29, p.TC6014.

Appendix

A - (Semi-)Automated Landslide Mapping Approaches – An Extensive Overview

Table App-1. Overview of (semi-)automated approaches for the derivation of landslide inventory maps.

	Method							Area						Sensors		
	Acquisitions			Element		Additional				Scale [d]						
	mono-temporal	bi-temporal [a]	multi-temporal	pixel based	object based	DEM derivatives	texture		Size (km²)	detailed	large	medium	small	mono-sensor	multi-sensor	
historical inventory																
(Othman & Gloaguen 2013)	●			●		●		Iraq	220		●			●		Quickbird
(Wan et al. 2012)	●			●		●		Taiwan	750		●			●		SPOT 4
(Danneels et al. 2007)	●			●	●	●	●	Kyrgyzstan	135		●					ASTER
(Moine et al. 2009)	●				●			France	200		●			●[b]		SPOT 5, aerial
(Barlow et al. 2006)	●				●	●		Canada	440		●			●		SPOT 5
(Aksoy & Ercanoglu 2012)	●				●	●		Turkey	300		●			●		Landsat ETM+
(Hölbling et al. 2012)	●				●	●		Italy	70		●			●		SPOT 5
(Blaschke et al. 2014)	●				●	●	●	Iran	100		●				●	SPOT 5, IRS-ID P6 (pan)
(Dou et al. 2015)	●				●	●	●	China	N/A	●				●		Quickbird
(Martha et al. 2010)	●				●	●	●	India	81		●			●		IRS Resourcesat-1 LISS IV
event-based inventory																
hydrometeorological trigger																
(Wan et al. 2015)	●			●		●		Taiwan	9	●				●		SPOT 4
(Borghuis et al. 2007)	●			●		●		Taiwan	115		●			●		SPOT 5
(Mondini et al. 2013)	●	[c]		●		●		Taiwan	117		●			●		Formosat-2
(Rau et al. 2014)	●				●	●		Taiwan	81, 64, 13		●			●[b]		Formosat-2, aerial (ZI/DMC)
(Lahousse et al. 2011)	●				●	●	●	Taiwan	40		●			●		SPOT 5
(Mondini et al. 2011a)		1/2		●				Taiwan	31.8, 760		●			●		Formosat-2
(Mondini et al. 2011b)		1		●				Italy	9.4	●				●		Quickbird
(Nichol & Wong 2005)		2		●				Hong Kong	36		●			●		SPOT 2/3
(Tsai et al. 2010)		1		●		●		Taiwan	2500			●		●		Formosat-2
(Cheng et al. 2004)		1		●		●		Taiwan	333		●			●		SPOT (N/A)
(Lu et al. 2011)		1		●	●	●	●	Italy	1.8, 8.1	●				●		Quickbird
(Park & Chi 2008)		1			●			Korea	10	●					●	IKONOS, Quickbird
(Hölbling et al. 2015)		1			●	●	●	Taiwan	16		●			●		SPOT 5

seismic trigger																	
(Parker et al. 2011)	●	-		●	●	●		China	13000				●			●	EO-1 ALI (pan), SPOT 5
(Lodhi 2011)	●	2		●				Pakistan	N/A		●			●			ASTER
(Yang & Chen 2010)		1		●				China	400		●					●	Landsat-TM, ASTER
(Lacroix et al. 2013)		1		●		●		Peru	27000				●	●			SPOT 5
both																	
(Stumpf et al. 2014)	●	-			●	●	●	Brazil, China	10, 36		●			●[b]			Landsat-TM,SPOT 5,GeoEye-1, IKONOS
(Stumpf & Kerle 2011)		1			●	●	●	Haiti, China, Italy, France	ca. 1 (per test site)	●				●[b]			IKONOS, Quickbird, Geoeye-1, aerial
multi-temporal inventory																	
(Martha et al. 2012)	●	1			●	●	●	India	81		●					●	IRS-1D (pan), Cartosat-1 (pan)
(Martha et al. 2013)	●	1			●	●	●	India	81		●					●	IRS-1D (pan), Cartosat-1 (pan) Resourcesat-1 LISS-IV
thesis [e]		1	●	●	●	●		Kyrgyzstan	2500,7500, 12000			●	●			●	Landsat-(E)TM, SPOT 1 & 5, IRS-1C (LISS3), ASTER, RapidEye

[a] 1 – statistical bi-temporal change detection or 2 – post-classification comparison (two mono-temporal image classifications and subsequent comparison)

[b] monotemporal classification approach tested on different sensors

[c] compared post-event results to an existing pre-event inventory

[d] after Cascini (2008): detailed (< 10km²); large (10-1000km²); medium (1000-10000km²); small (>10000km²)

[e] landslide mapping approach presented in this thesis

B - Identification of Pre-Cursors of Hazardous Landslides – An Example

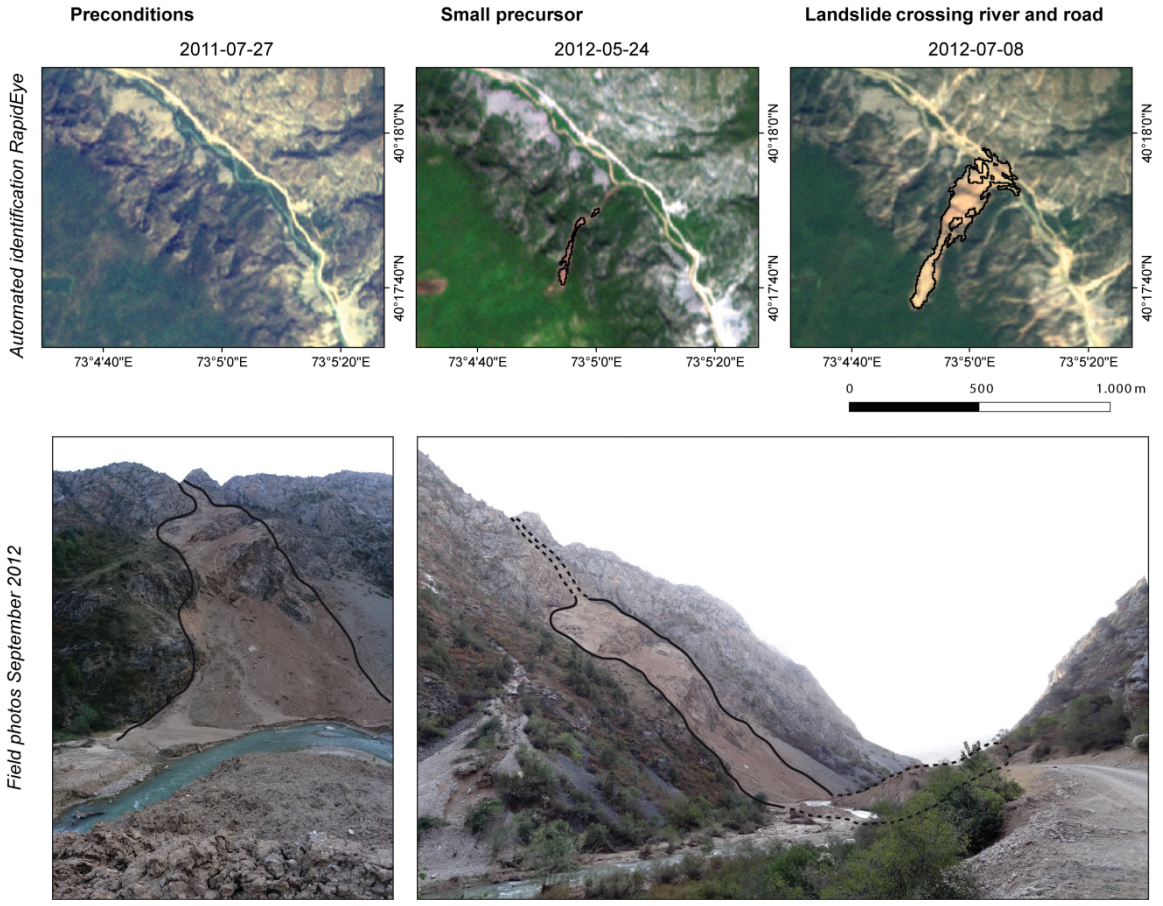

Figure App-1. Evolution of a landslide. Automatic identification of a small precursor and of a subsequent hazardous landslide that crossed the valley and for a short time blocked the river and the road on the other side of the valley.

C - RapidEye-Based Landslide Mapping Results – Complete Study Area

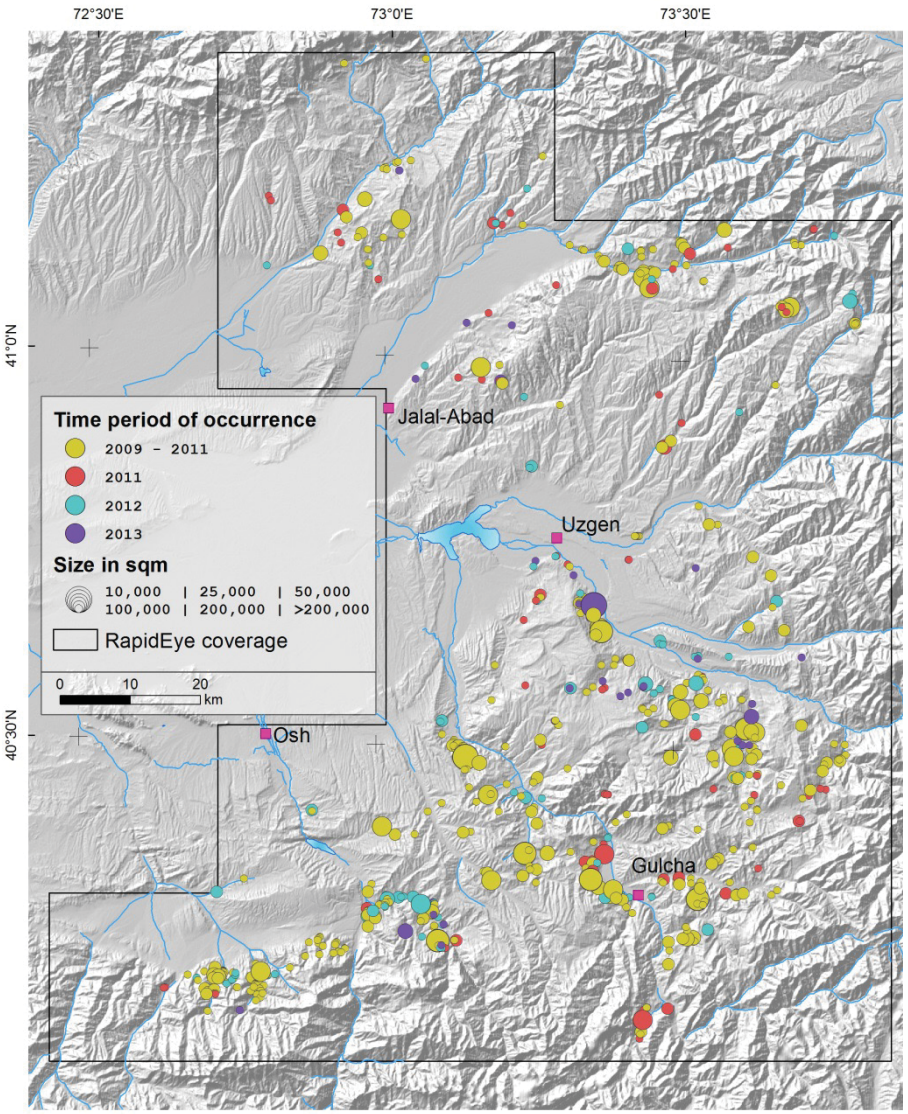

Figure App-2. Identified landslide objects for the complete study area based on RapidEye data coverage between 2009 and 2013.

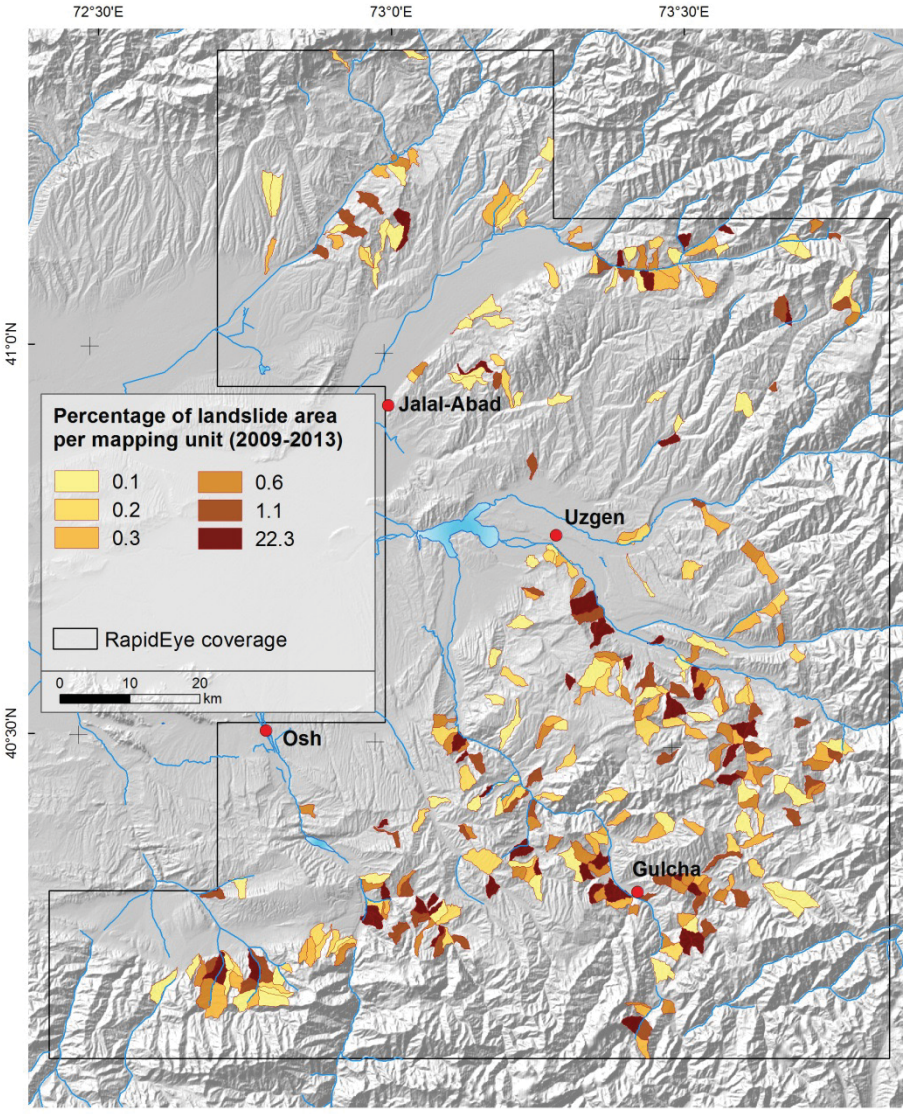

Figure App-3. Percentage of landslide-affected area per mapping unit.

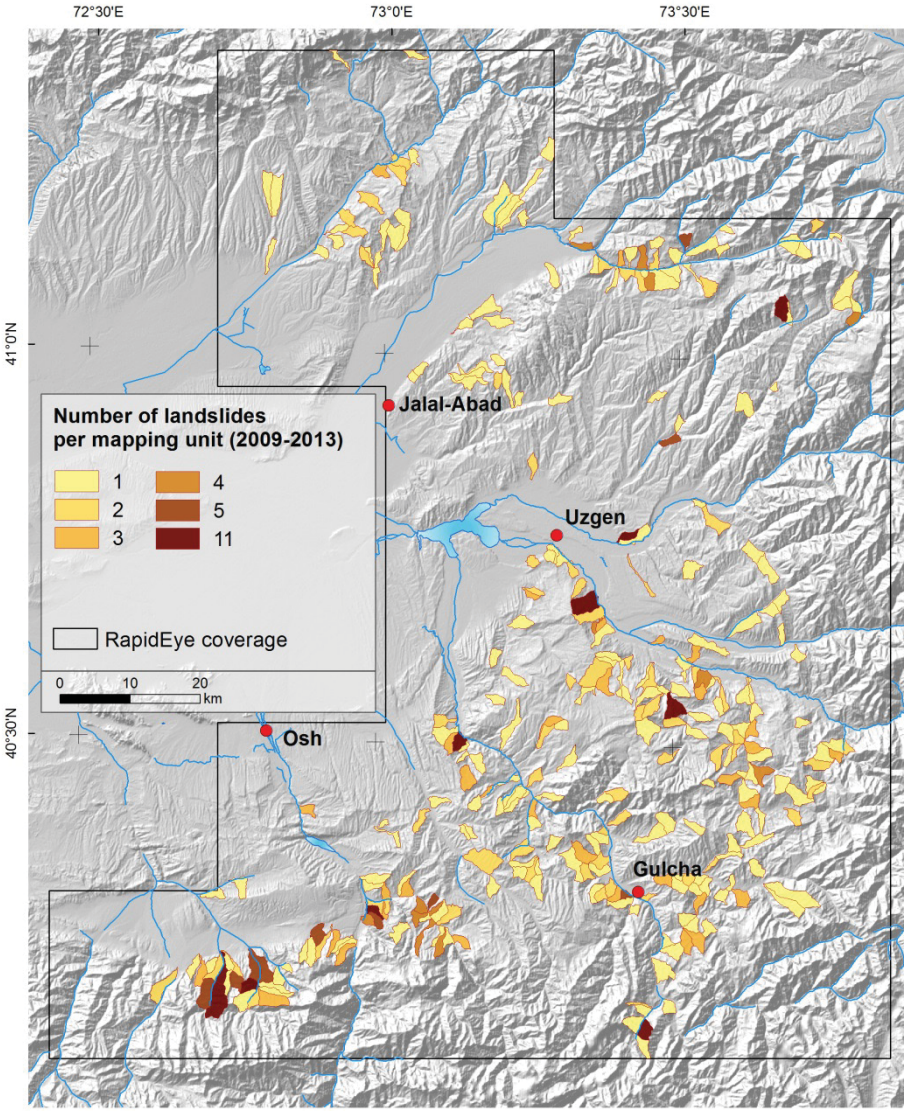

Figure App-4. Number of landslide failures per mapping unit.

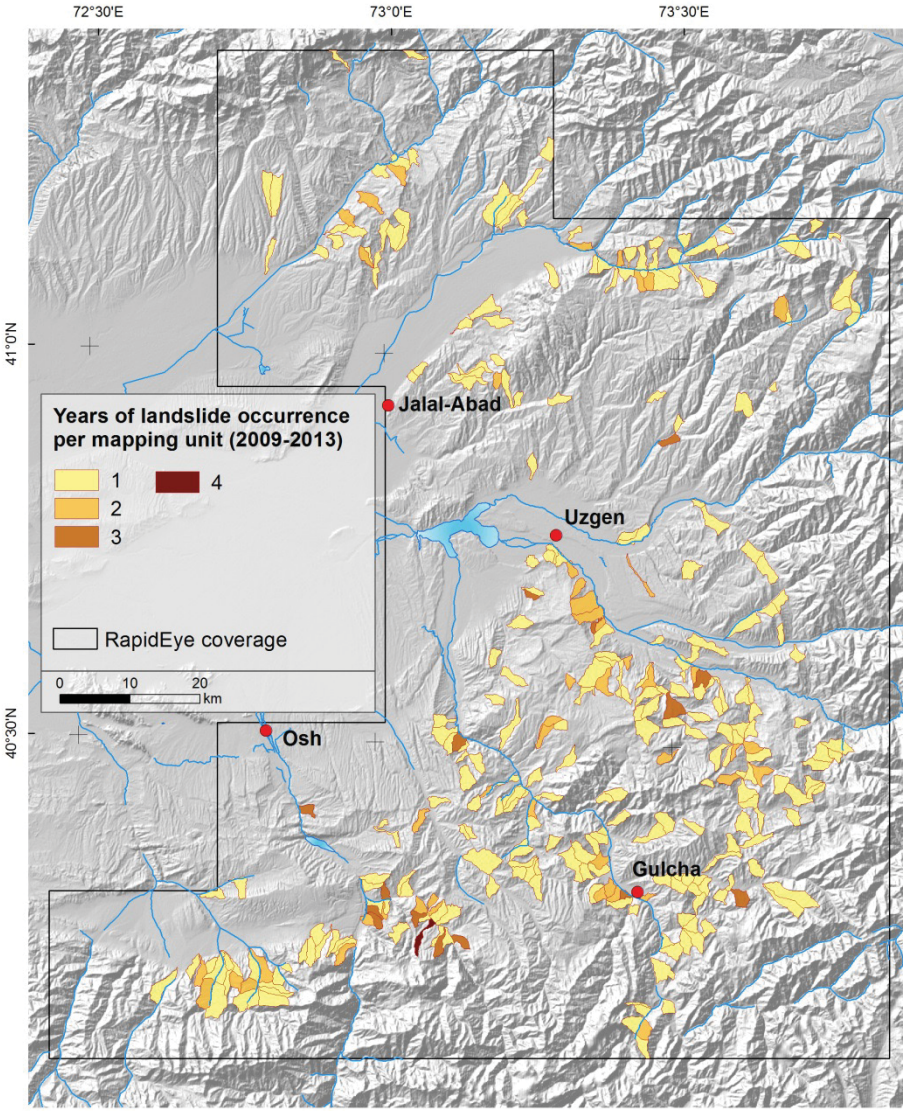

Figure App 5. Number of years with detected landslide activity per mapping unit.

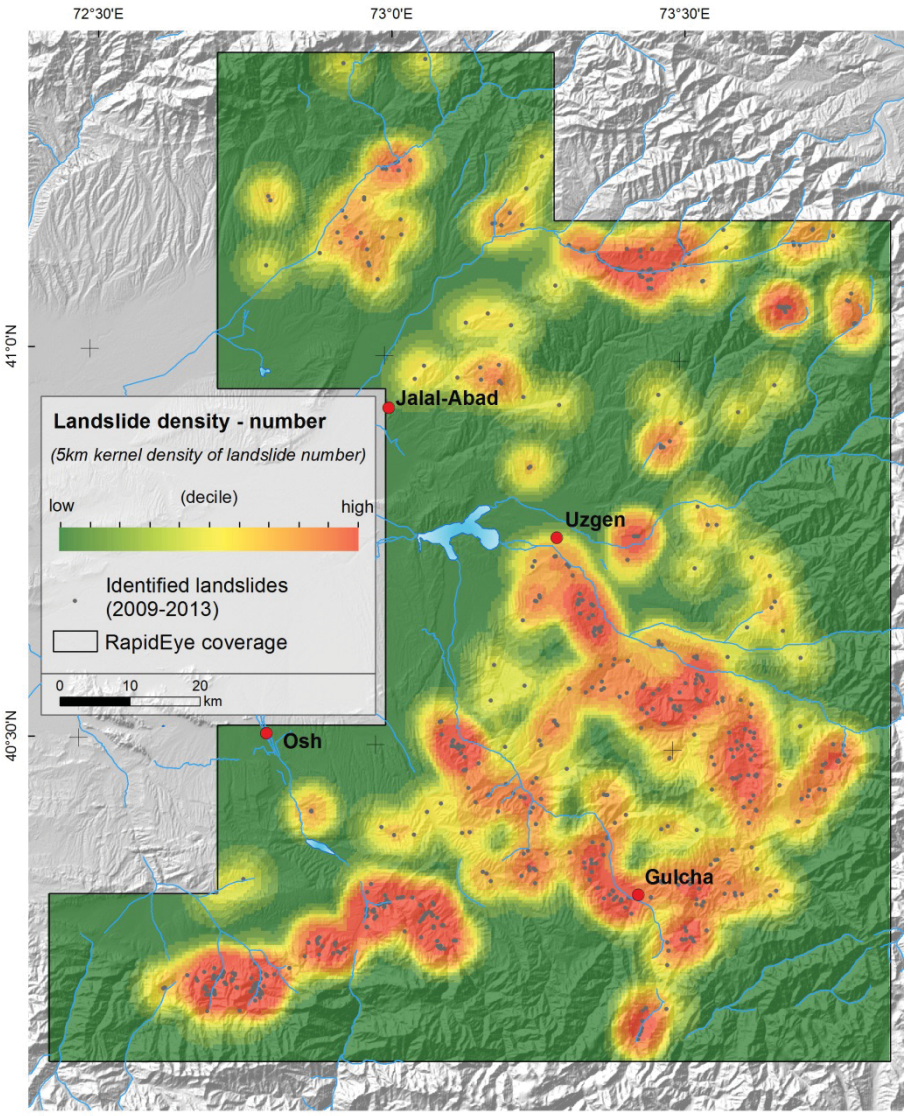

Figure App-6. Spatiotemporal landslide density. Figure represents sum of landslide failures for a moving quadratic-weighted kernel of 5km size.

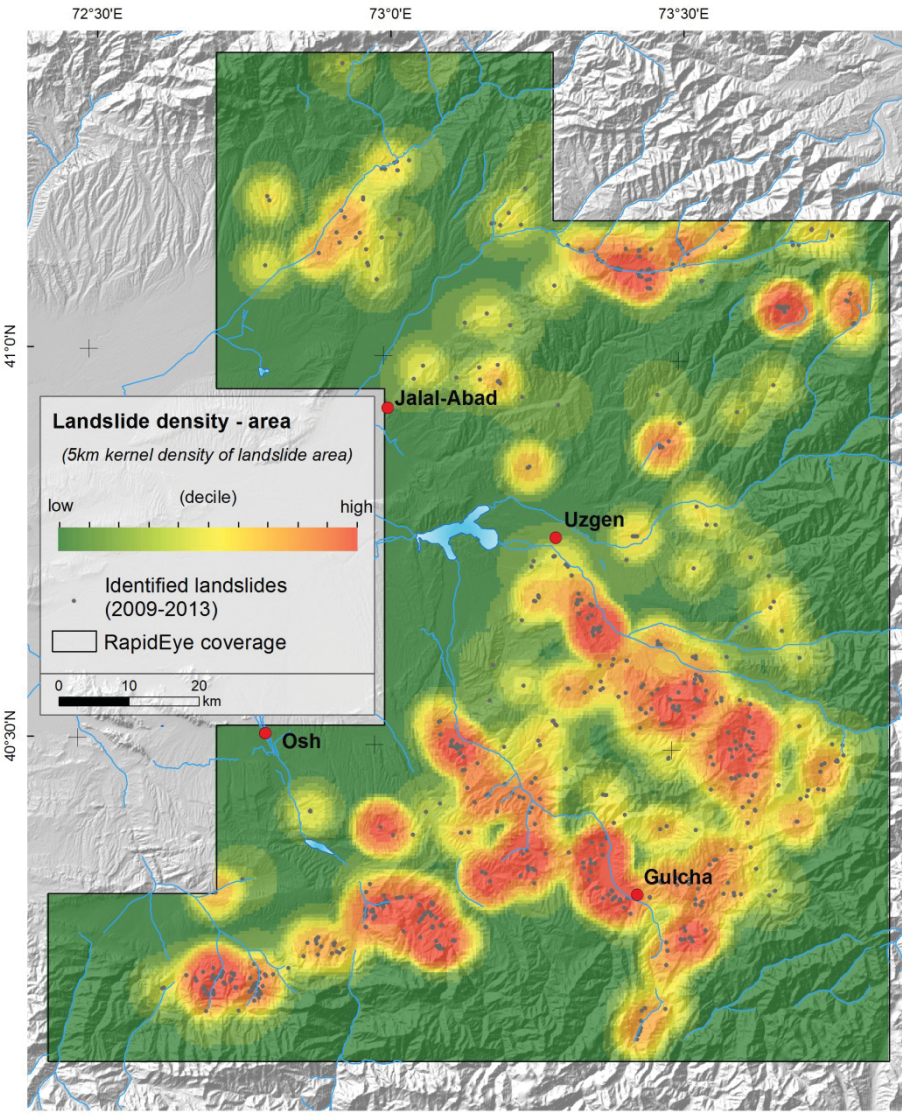

Figure App-7. Spatiotemporal landslide density weighted by landslide size. Figure represents sum of landslide area for a moving quadratic-weighted kernel of 5km size.

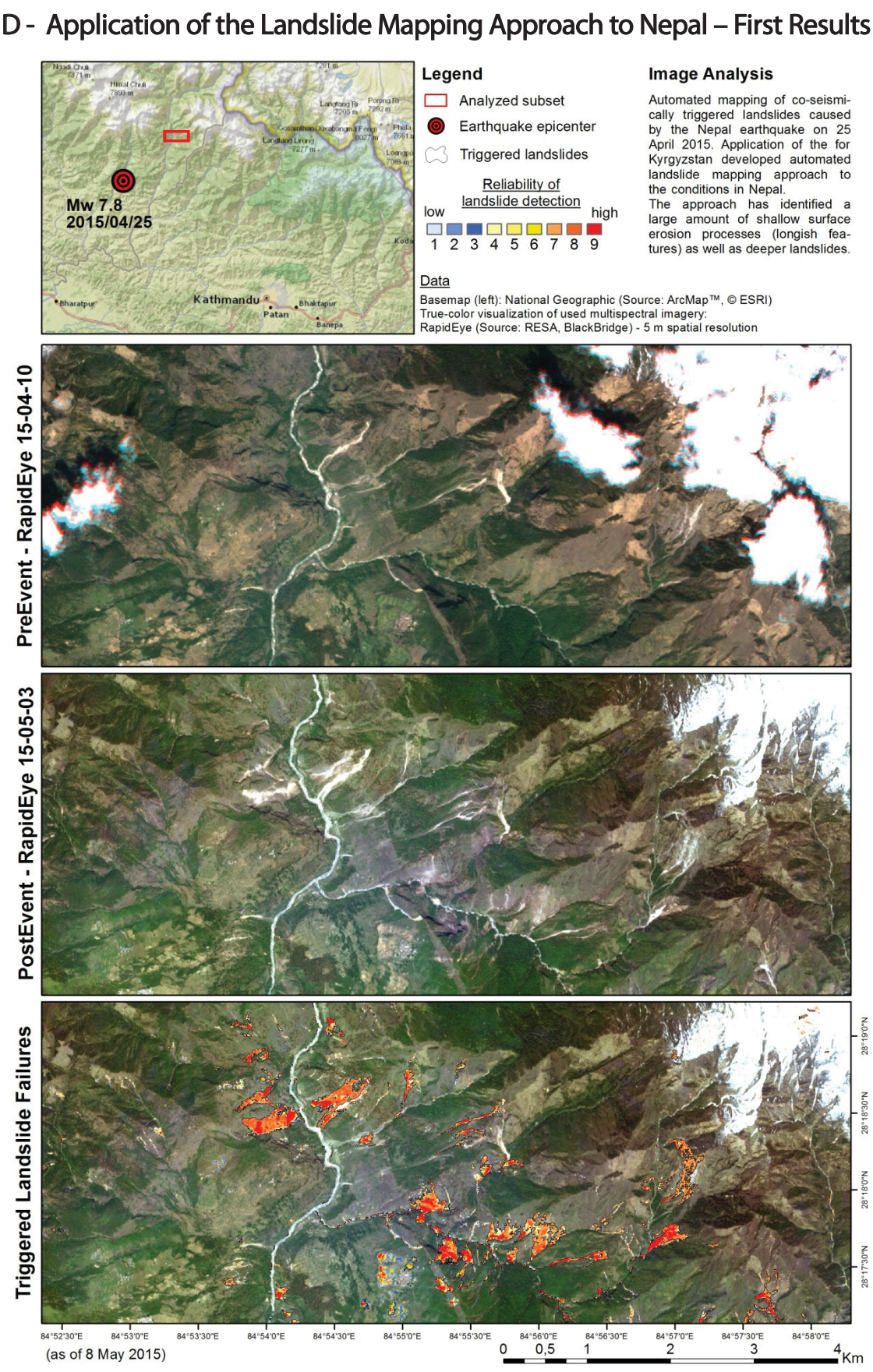

Figure App-8. RapidEye-based application of the landslide mapping approach (example 1).

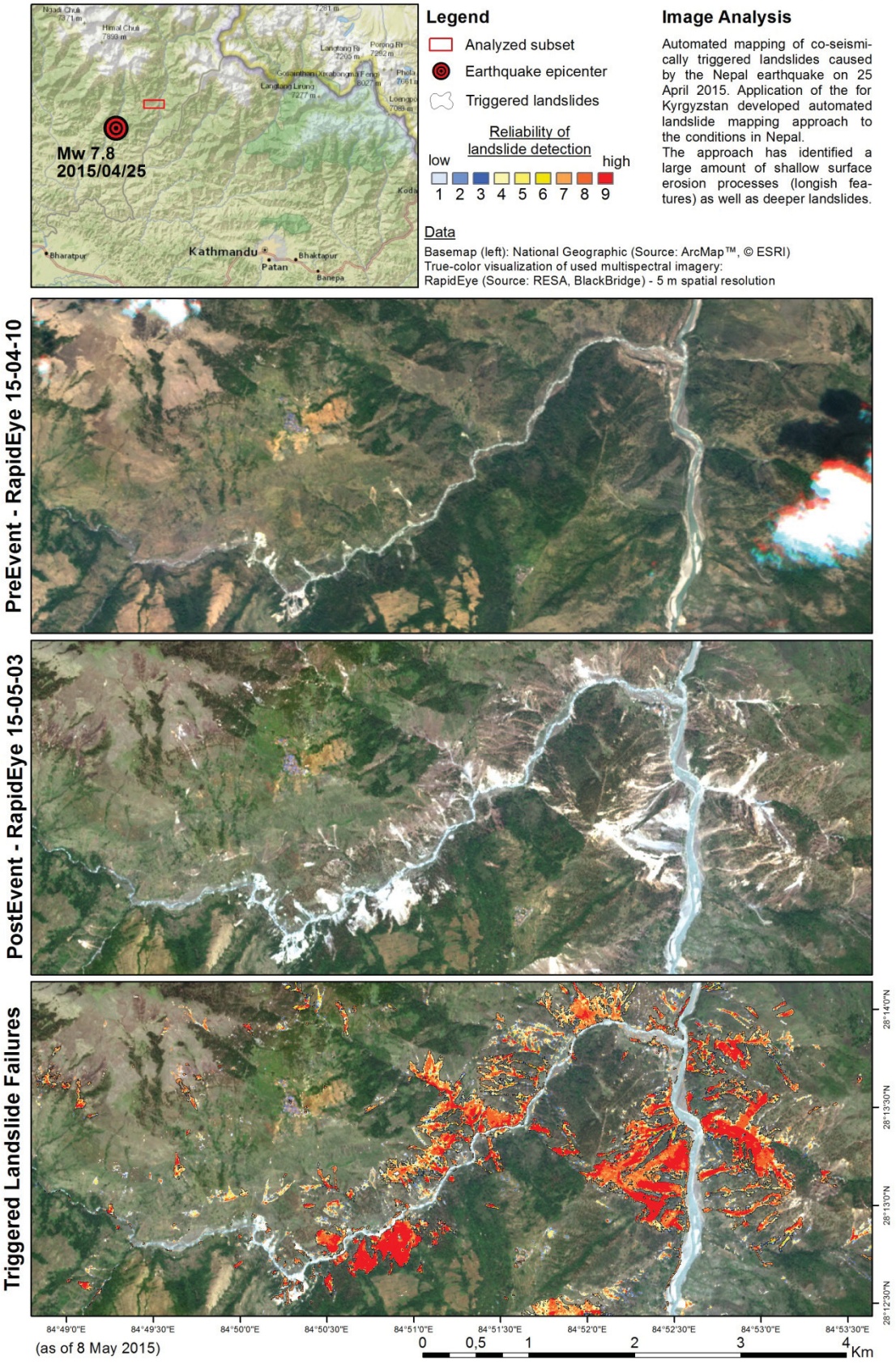

Figure App-9. RapidEye-based application of the landslide mapping approach (example 2).

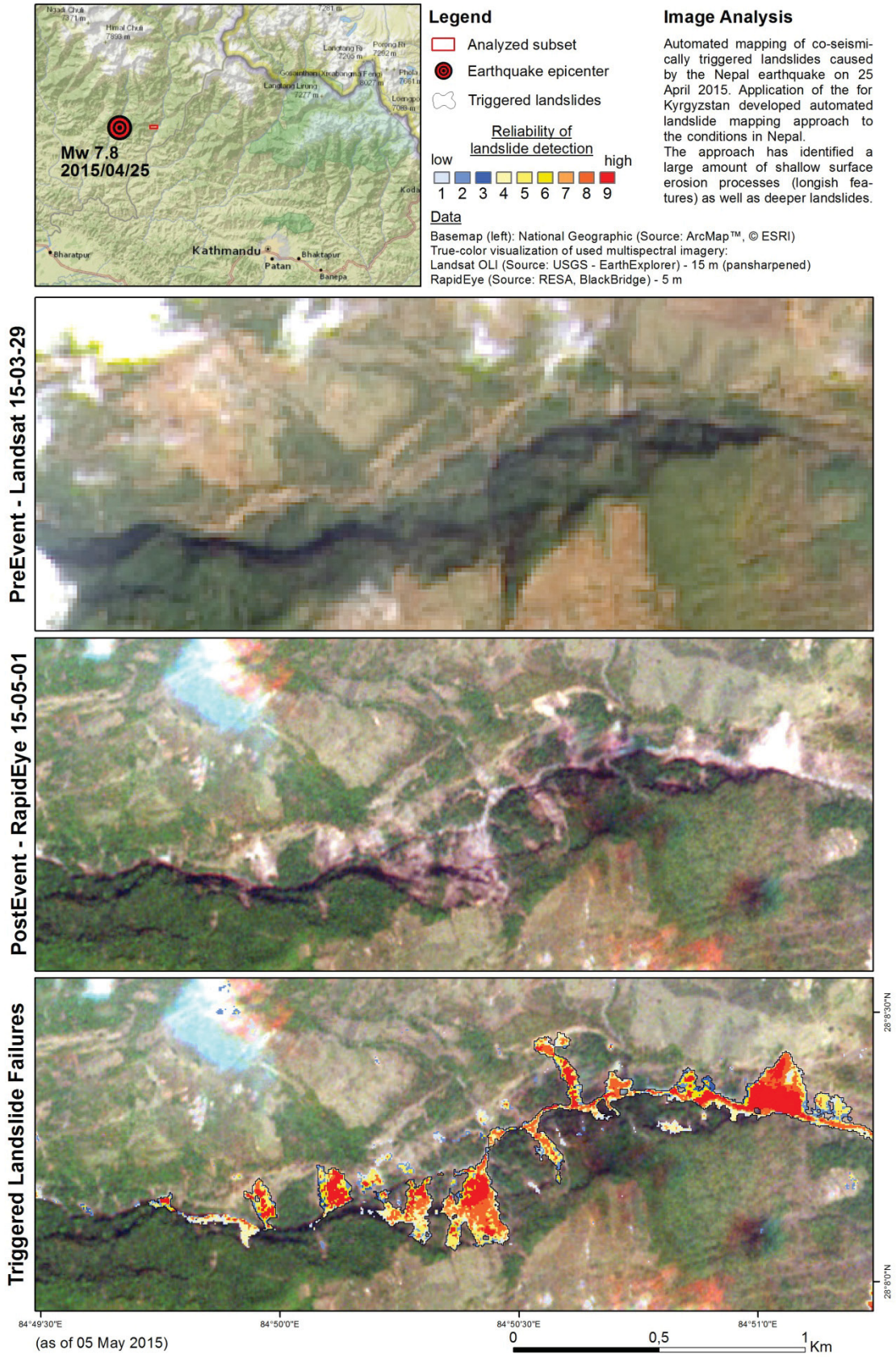

Figure App-10. Application of the landslide mapping approach to multi-sensor scenario (Landsat & RapidEye) (example 1).

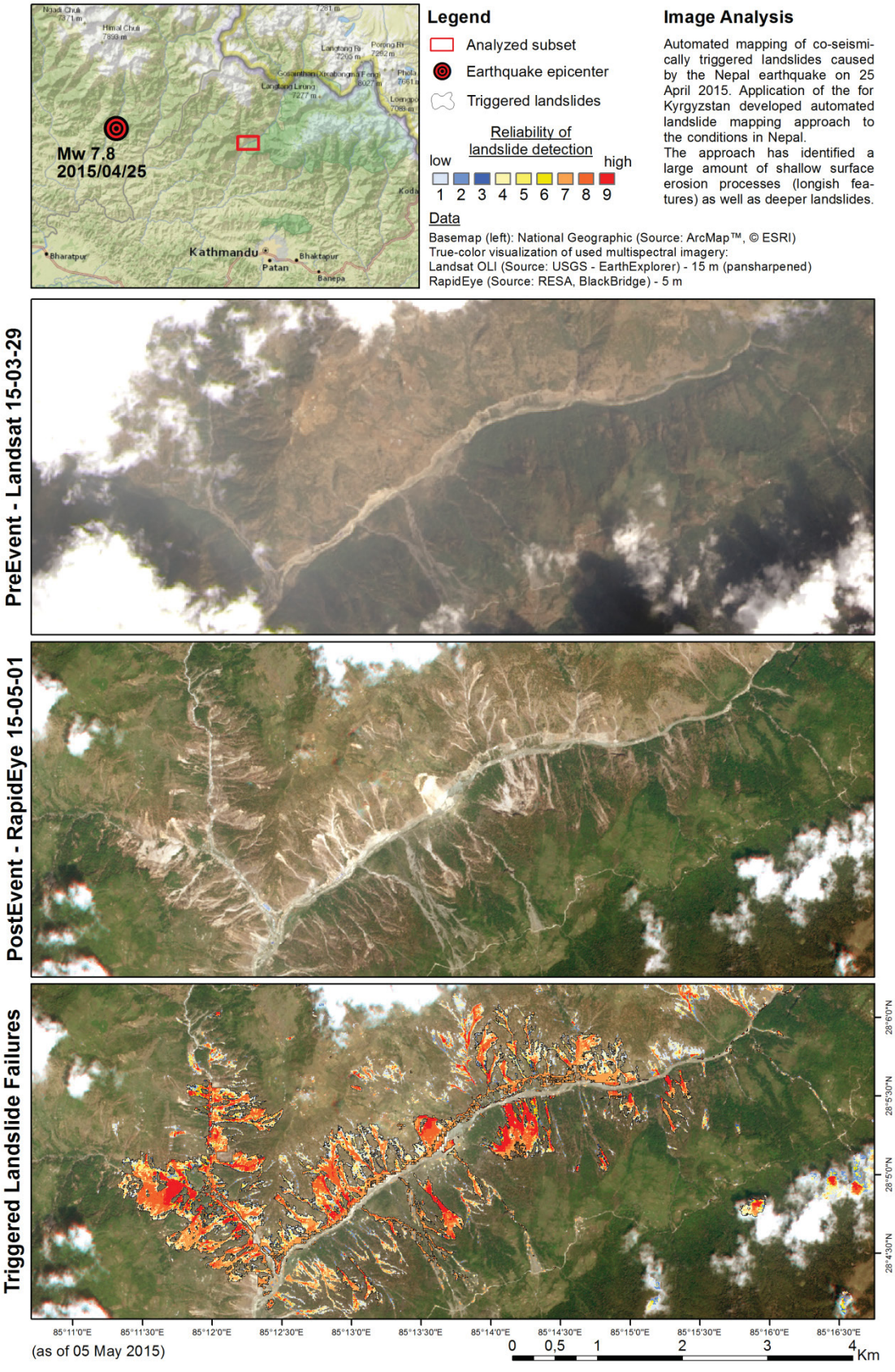

Figure App-11. Application of the landslide mapping approach to multi-sensor scenario (Landsat & RapidEye) (example 2).

E - Publications Related to the Thesis

Peer-reviewed articles

Behling, R., Roessner, S., Segl, K., Kleinschmit, B. & Kaufmann, H., (2014b). Robust Automated Image Co-Registration of Optical Multi-Sensor Time Series Data: Database Generation for Multi-Temporal Landslide Detection. *Remote Sens.*, 6(3), pp.2572–2600.

Behling, R., Roessner, S., Kaufmann, H. & Kleinschmit, B., (2014a). Automated Spatiotemporal Landslide Mapping over Large Areas Using RapidEye Time Series Data. *Remote Sens.*, 6(9), pp.8026–8055.

Behling, R., Roessner, S., Golovko, D. & Kleinschmit, B., (submitted on 02 September 2015). Derivation of Long-Term Spatiotemporal Landslide Activity–An Automated Multi-Sensor Time Series Approach. Remote Sens. Environ.

Golovko, D., Roessner, S., **Behling, R.**, Wetzel, H.-U. & Kleinschmit, B., (2015). Development of Multi-Temporal Landslide Inventory Information System for Southern Kyrgyzstan Using GIS and Satellite Remote Sensing. *Photogramm. Fernerkund. Geoinf.*, (2), pp.157–172.

Roessner, S., **Behling, R.**, Segl, K., Golovko, D., Wetzel, H.-U. & Kaufmann, H., (2014). Automated Remote Sensing Based Landslide Detection for Dynamic Landslide Inventories. In K. Sassa, P. Canuti, & Y. Yin, eds. *Landslide Science for a Safer Geoenvironment: Volume 2: Methods of Landslide Studies*. Cham: Springer International Publishing, pp. 345 – 350.

Golovko, D., Roessner, S., **Behling, R.**, Wetzel, H.-U. & Kaufmann, H., (2014). GIS-Based Integration of Heterogeneous Data for a Multi-temporal Landslide Inventory. In K. Sassa, P. Canuti, & Y. Yin, eds. *Landslide Science for a Safer Geoenvironmen: Volume 2: Methods of Landslide Studies.t*. Cham: Springer International Publishing, pp. 799 – 804.

Pilz, M., Roessner, S., Janssen, C., **Behling, R.**, Parolai, S., Saponaro, A., Schäbitz, M., (2013). Massenbewegungen in Zentralasien : Lawinen aus Boden und Gestein. *System Erde*, 3(2), pp.32 – 37. ISSN: 2191-8589

Conference paper

Behling, R., Roessner, S., Segl, K., Rogass, C., Wetzel, H.U. & Kaufmann, H., (2012). Automatische geometrische Koregistrierung multitemporaler Satellitendaten zur Inventarisierung von Hangrutschungen. In E. Borg, H. Daedelow, & R. Johnson, eds. *Vom Algorithmus zum Produkt - 4. RESA Workshop*. Neustrelitz, Germany, pp. 35–50. ISBN 978-3-942183-61-1.

Behling, R., Roessner, S., Wetzel, H.U. & Kaufmann, H., (2013). Automated Multi-temporal Landslide Identification in Kyrgyzstan Using Satellite Remote Sensing Data. In E. Seifert, ed. *Publikationen der Deutschen Gesellschaft für Photogrammetrie, Fernerkundung und Geoinformation (33. Wissenschaftlich-Technische Jahrestagung der DGPF*), Freiburg i. B., Germany, pp. 244–255. ISSN 0942-2870.

Behling, R., Roessner, S., Segl, K. & Kaufmann, H., (2013). Automated Landslide Detection Using Multi-temporal RapidEye Data. In E. Borg, H. Daedelow, & R. Johnson, eds. *From the Basics to the Service. 5th RESA Workshop*. Neustrelitz, Germany, pp. 239–257. ISBN 978-3-95545-002-1.

Roessner, S., **Behling, R.**, Golovko, D., Motagh, M., Teshebaeva, K. & Wetzel, H.-U., (2014). Multi-temporal satellite remote sensing for dynamic landslide hazard assessment in Southern Kyrgyzstan. In *Publikationen der Deutschen Gesellschaft für Photogrammetrie und Fernerkundung*. Hamburg, Germany. p. 8. ISSN 0942-2870.

Behling, R., Roessner, S., Golovko, D., Wetzel, H.-U., (2014). Automated Spatiotemporal Landslide Mapping in Kyrgyzstan Using Long-Term Optical Satellite Multi-Sensor Time Series Data. In *ISEO 2014, 2nd International Symposium on Earth Observation for Arid and Semi-Arid Environments.* Issyk-kul, Kyrgyzstan. p. 7.

Golovko, D., Roessner, S., **Behling, R.**, Wetzel, H.-U. (2014). Remote Sensing Contribution to Landslide Hazard Assessment in Southern Kyrgyzstan. In *ISEO 2014, 2nd International Symposium on Earth Observation for Arid and Semi-Arid Environments.* Issyk-kul, Kyrgyzstan. p. 5.

Conference presentations (oral, poster)

Behling, R., Roessner, S., Segl, K., Roga\s s, C., Wetzel, H.-U. & Kaufmann, H., (2011). Development of pre-processing strategies for automated identification of landslide events in Southern Kyrgyzstan within a multi-temporal and multi-sensor change detection approach. In *4th Workshop on Land Use & Land Cover - EARSel (Prague 2011)*. Prague, Czech Republic.

Roessner, S., Motagh, M., **Behling, R.**, Teshebaeva, K., Wetzel, H.-U. & Kaufmann, H., (2011). Optical and radar remote sensing for quantitative analysis of landslide activity in Southern Kyrgyzstan, Central Asia. In *Geophysical Research Abstracts Vol. 13, EGU2011-8607-1, 2011. EGU General Assembly 2011.* Vienna, Austria.

Behling, R., Roessner, S., Segl, K., Roga\s s, C., Wetzel, H.-U. & Kaufmann, H., (2012). Multitemporal Trajectory-Based Change Detection for Automated Landslide Identification in Kyrgyzstan Using Satellite Remote Sensing Data. In *1st International Workshop on "Temporal Analysis of Satellite Images"* Mykonos Island, Greece.

Golovko, D., Roessner, S., **Behling, R.**, Wetzel, H.-U. & Kaufmann, H., (2013). Development of a Dynamic Landslide Inventory Information System for Southern Kyrgyzstan. In *Geophysical Research Abstracts, Vol. 15, EGU2013-9198, 2013. EGU General Assembly 2014.*Vienna, Austria.

Golovko, D., Roessner, S., **Behling, R.**, Wetzel, H.-U. & Kaufmann, H., (2013). Using Remote Sensing and GIS for Dynamic Landslide Hazard Assessment in Southern Kyrgyzstan. In *International Conference MOUNTAINHAZARDS 2013 - Natural Hazards, Climate Change and Water in Mountain Areas.* Bishkek, Kyrgyzstan. p. 81.

Behling, R., Roessner, S., Segl, K., Kleinschmit, B. & Kaufmann, H., (2014). Automated landslide identification using temporal NDVI-trajectories in long-term optical multi-sensor time-series data. In *Geophysical Research Abstracts Vol. 16, EGU2014-15679-2, 2014. EGU General Assembly 2014.* Vienna, Austria.

Golovko, D., Roessner, S., **Behling, R.**, Wetzel, H.-U. & Kaufmann, H., (2014). Open-Source GIS Tool for Landslide Hazard Assessment in Southern Kyrgyzstan. In *FOSSGIS 2014*. Berlin, Germany 2014.

Behling, R., Roessner, S., Segl, K., Wetzel, H.U. & Kaufmann, H., (2014). Automated landslide identification at a regional scale using long-term optical multi-sensor time-series data. In *First joint Workshop of the EARSeL Special Interest Group on Land Use & Land Cover and the NASA LCLUC Program on "Frontiers in Earth Observation for Land System Science"*. Berlin, Germany.

Behling, R., Roessner, S., Segl, K., Kleinschmit, B. & Kaufmann, H. (2014). Potential of Optical Satellite Time Series Data as Contribution to an Operational Spatiotemporal Mapping of Backdated and Recent Landslide Activity for Large Areas. In *Vom Potential zur Lösung - 3.gemeinsamer Workshop der Aks Auswertung von Fernerkundungsdaten der DGPF e.V. Fernerkundung der DGfG e.V.* Berlin, Germany.

Roessner, S., **Behling, R.**, Golovko, D., Motagh, M., Teshebaeva, K. & Wetzel, H.-U., (2015). RESA priority area Central Asia – Fergana: multisensor analysis of landslide activity in Kyrgyzstan. In *Nutzung von RapidEye-Daten im Kontext der Synergie mit anderen Sensoren und in Vorbereitung auf künftige Missionen – 7th RESA Workshop*. Bonn, Germany.

Andermann, C., **Behling, R.**, Cook, K.L., Emberson, R., Hovius, N., Marc, O., Motagh, M., Roessner, S., Sens-Schoenfelder, C. & Turowski, J. M., (2015). Landscape Response To The Mw7.9 Gorkha Earthquake. In *GSA Annual Meeting*. Baltimore, Maryland, USA.

F - Acknowledgment

I would like to take the chance to thank all the people who contributed to the completion of my doctoral thesis.

The thesis was written at the remote sensing section of the GFZ German Research Centre for Geosciences. I want to thank Prof. Dr. Hermann Kaufmann and Prof. Dr. Luis Guanter, the heads of the remote sensing section during the time of my thesis, for providing a professional and well-structured scientific environment. They gave me the freedom to develop my own ideas and to present and discuss them at international conferences. They are also thanked for acting as second and third reviewer of my thesis.

I want to thank Prof. Dr. Birgit Kleinschmit enabling with her supervision the realization of the thesis at the TU-Berlin. Thank you for acting as first reviewer, for helping at official formalities, and for your effective comments and advices in the context of writing my thesis.

My supervisor at the GFZ, Dr. Sigrid Roessner, assisted me in writing my papers and helped me with words and deeds whenever needed. Sigrid thank you for that very much.

I also want to thank all my co-authors contributing with their ideas, advices, and motivation to the presented manuscripts. The technical help of Dr. Karl Segl for the first paper is also much appreciated. Not mentioned yet is Dr. Hans-Ulrich Wetzel, who contributed to the thesis with helpful comments and his long-year expertise in the Kyrgyz landslide situation.

I thank Dr. Sabine Chabrillat for giving me the freedom and support to work on my thesis aside the tasks of the "GeoArchives" project I was working on the last year of my thesis.

Special thanks go to all my proofreaders, which helped to "optimize" the final thesis. Darya, Carsten, Sigrid, and Juliane thanks for your time, care, and effort.

The colleagues of the remote sensing section always provided a fruitful and inspiring atmosphere with scientific and non-scientific conversations. Thanks to Sigrid, Uli, Darya, and Kanayim for the productive teamwork at the GFZ and at the interesting field work in Kyrgyzstan. I would also like to thank my "roommate" Carsten for the pleasant time at work (especially in the afternoon) and the colleagues joining the (afternoon) coffee break for off-topic discussions.

Finally, I want to thank my family and friends for moral and emotional support during the long period of my thesis and for taking my mind of the thesis whenever it was necessary. A big thank you goes to my parents for the support during my studies as well as for the freedom and trust in all my life decisions.

G - Author's Declaration

I prepared this dissertation without illegal assistance. This work is original except where indicated by special reference in the text and no part of the dissertation has been submitted for any other degree. This dissertation has not been presented to any other University for examination, neither in Germany nor in another country.

Berlin, November 2015 (Robert Behling)